Resource Allocation and Positioning of Power-Autonomous Portable Access Points

Babu, Nithin

DOI (link to publication from Publisher):
10.54337/aau494412529

Publication date:
2022

Document Version
Publisher's PDF, also known as Version of record

RESOURCE ALLOCATION AND POSITIONING OF POWER-AUTONOMOUS PORTABLE ACCESS POINTS

BY
NITHIN BABU

DISSERTATION SUBMITTED 2022

AALBORG UNIVERSITY
DENMARK

Resource Allocation and Positioning of Power-Autonomous Portable Access Points

Ph.D. Dissertation

Nithin Babu

Aalborg University
Department of Electronic Systems
Fredrik Bajers Vej 7B
DK-9220 Aalborg

Dissertation submitted: July, 2022

PhD supervisor: Prof. Petar Popovski
Aalborg University

Assistant PhD Supervisor: Dr. Constantinos B. Papadias
Adjunct Prof. Aalborg University, Prof. Alba,
The American College of Greece

PhD committee: Associate Professor Gilberto Berardinelli (chairman)
Aalborg University, Denmark

Associate Professor Anna Tzanakaki
National and Kapodistrian University of Athens, Greece

Professor Rui Zhang
National University of Singapore, Singapore

PhD Series: Technical Faculty of IT and Design, Aalborg University

Department: Department of Electronic Systems

ISSN (online): 2446-1628
ISBN (online): 978-87-7573-865-6

Published by:
Aalborg University Press
Kroghstræde 3
DK – 9220 Aalborg Ø
Phone: +45 99407140
aauf@forlag.aau.dk
forlag.aau.dk

Printed in Denmark by Stibo Complete, 2022

Abstract

The feasibility of providing cellular connectivity in remote areas in future generations of wireless networks depends on the availability of a reliable power grid. Similar issues arise in emergency network deployment for rapid connectivity provisioning in disaster areas and broadband provisioning in massive-scale social events such as sports events and concerts, where access to a power grid is limited. Furthermore, future cellular communication systems are expected to cut their CO_2 emissions by at least 50% by 2030 as the first step to achieving net-zero networks. Grid-independent energy-neutral (EN) communication networks that are portable and use green energy for their operation provide a critical solution to the above.

In this thesis, we realize an EN system using an unmanned aerial vehicle (UAV)-based power-autonomous portable access point (PAP) system in which UAVs will be carrying radio access nodes to serve a set of ground nodes. The energy required to recharge the UAVs is generated using an off-grid charging station (CS) comprising energy generation and storage modules. This thesis proposes a framework for energy- and cost-efficient deployment of a power-autonomous PAP system. The proposed framework incorporates realistic power generation, storage, and consumption models directly into the wireless network optimization. The contributions are grouped into 3 categories. The initial works propose stationary PAP deployment policies that maximize the number of bits or area covered per Joule of energy consumed. To start with, we determine energy-efficient hovering altitudes for a PAP considering orthogonal and non-orthogonal resource allocation schemes. Later, a multi-level circle packing algorithm determines energy-efficient 3D hovering locations for PAPs deployed to serve a given region. Since a PAP consumes less power while flying, a subset of works design energy-efficient trajectories for a PAP, forming the second group. The trajectory design starts by considering a simple fly-hover-communicate policy to serve the users in which the hovering locations, the flying velocity of the UAV, and the battery parameters are optimized to maximize the energy efficiency and minimize the operational cost of the system. These are then extended to a fly-communicate protocol in the presence of intelligent reflecting surfaces (IRS) placed on the facade of buildings to improve the channels between a PAP and ground nodes. Then, we propose a deep-reinforcement learning-based 3D trajectory pol-

icy that maximizes the number of bits transmitted per Joule of energy consumed while ensuring service fairness among the users. The work considers a pragmatic non-linear battery discharge profile of UAV batteries according to the Peukert effect. Finally, the third group includes methodologies for a cost-efficient design of an energy-neutral PAP system that configures a hybrid CS as a function of the load profile generated by the PAPs. We consider two types of hybrid CS; the first uses a combination of photovoltaic (PV) panels and batteries, whereas the second configuration harvests energy from wind and solar and stores the excess energy in a ground battery unit. Numerical evaluations show that the exclusion of realistic energy generation, consumption, and storage models results in sub-optimal or obsolete solutions.

Resumé

Muligheden for cellulært netværk at levere forbindelse til fjerntliggende områder i fremtidige generationers trådløst netværk afhænger af tilgængeligheden til et pålideligt el net. Lignende udfordringer opstår i nødsituations netværksimplementering, for at opnå hurtig provision af forbindelse til katastrofeområder og bredbånds provisionering til sociale begivenheder af massiv skala, så som sportsbegivenheder og koncerter hvor adgang til et elnet er begrænset. Ydermere, fremtidig cellulære kommunikationssystemer forventes at begrænse deres CO_2 udslip med mindst 50% inden 2030, som det første skridt mod at opnå netto nul netværk. Net-uafhængig energi-neutralt (EN) kommunikationsnetværk som er transporterbar, og bruger grøn energi til deres drift, skaber en kritisk løsning for det overstående.

I denne afhandling opnår vi et EN system, ved brug af ubemandet luftfartøj (UAV)-baseret energi-autonom transportabel access point (PAP), hvor UAV'er bærer radio adgangsknudepunkter til at servicere en gruppe grund noder. Den nødvendige energi til opladning af UAV'er generes ved brug af 'off-grid' opladningsstationer (CS), bestående af energi generation og lager moduler. Denne afhandling foreslår en struktur for energi- og pris-effektiv implementering af et energi-autonomt PAP system. Den forslået struktur inkorporerer realistisk energi generation, lager, og konsumeringsmodeller direkte ind i den trådløse netværksoptimering. Bidragende er opdelt i 3 kategorier. Det initiale værk foreslår stationær PAP implementeringspolitikker, som optimerer antallet af bits eller område dækket per Joule energi konsumeret. Til at starte med, fastslog vi energi-effektiv svævende højder for et PAP, med overvejelser af ortogonal og ikke-ortogonal ressource allokeringsordninger. Senere, bestemmer en cirkel paknings algoritme på flere niveauer, energi-effektiv 3D svæve lokationer for PAP'er implementeret til at servicere i en given region. Siden et PAP forbruger mindre energi imens den flyver, så designer en delmængde af værkerne energi-effektiv trajektorier for et PAP, som danner den anden gruppe værker. Trajektorie designet begynder med overvejelser af en simpel flyve-svæve-kommuniker politik til at servicere brugerne, hvoraf svæve lokationerne, flyve hastigheden for UAVen og batteri parametre er optimeret til at maximere energieffektiviteten, og minimere systemets operationelle pris. Disse udvides til en flyve-kommuniker protokol i tilstedeværelsen af en Intelligent refleksiv overflade (IRS), som

er placeret på facaden af bygninger, for at forbedre kanalerne mellem en PAP og grund noder. Efterfølgende foreslår vi en deep-reinforcement learning baseret 3D trajektorie politik, som maksimerer antallet af bits transmitteret pr. Joule energi konsumeret, imens serviceretfærdighed blandt brugerne sikres. Værket overvejer en pragmatisk ikke-lineær batteri udledningsprofil for UAV batterier ifølge Peukert effekten. Endeligt, så inkludere den tredje gruppe værker, metoder for pris-effektivt design af et energi-neutralt PAP system, som konfigurerer en hybrid CS som en funktion af belastningsprofilen generet af PAP'er. Vi overvejer to typer hybrid CS; den første bruger en kombination af fotovoltaisk (PV) paneler og batterier, hvorimod den anden konfiguration høster energi fra vind og sol og lagrer den overskydende energi i en grund batterienhed. Numerisk evaluering viser at ekskludering af realistisk energi generation, forbrug, og lagre model resulterer i sub-optimale, og forældet løsninger.

Contents

List of Papers

The main contributions of the thesis are contained in the following list of papers whose contents are included in Part II of the thesis.

[A] N. Babu, K. Ntougias, C. B. Papadias and P. Popovski, "Energy Efficient Altitude Optimization of an Aerial Access Point," in *IEEE 31st Annual International Symposium on Personal, Indoor and Mobile Radio Communications (PIMRC),* 2020, pp. 1-7.

[B] N. Babu, C. B. Papadias and P. Popovski, "Energy-Efficient Deployment of a Non-Orthogonal Multiple Access Unmanned Aerial System," in *IEEE International Conference on Communications Workshops (ICCWorkshops),* 2021, pp. 1-6.

[C] N. Babu, C. B. Papadias and P. Popovski, "Energy-Efficient 3-D Deployment of Aerial Access Points in a UAV Communication System," *IEEE Communications Letters,* vol. 24, no. 12, pp. 2883-2887, Dec. 2020.

[D] N. Babu, M. Virgili, C. B. Papadias, P. Popovski and A. Forsyth, "Cost- and Energy-Efficient Aerial Communication Networks with Interleaved Hovering and Flying," *IEEE Transactions on Vehicular Technology,* vol. 70, no. 9, pp. 9077-9087, Sept. 2021.

[E] N. Babu, M. Virgili, M. Al-jarrah, X. Jing, E. Alsusa, P. Popovski, A. J. Forsyth, C. Masouros, and C. B. Papadias,"Energy-Efficient Trajectory Design of a Multi-IRS Assisted Portable Access Point," submitted to *IEEE Transactions on Vehicular Technology* (Major Revision).

[F] N. Babu, I. Donevski, A. Valcarce, J. J. Nielsen, and C. B. Papadias, "Fairness Based Energy-Efficient 3D Path Planning of a Portable Access Point : A Deep Reinforcement Learning Approach," submitted to *IEEE Open Journal of the Communications Society* (Major Revision).

[G] M. Virgili, N. Babu, M. Javidsharifi, I. Valiulahi, C. Masouros, A. J. Forsyth, T. Kerekes, C. B. Papadias, "Cost-Efficient Design of an Energy-Neutral UAV-Based

Mobile Network," submitted to *IEEE Transactions on Communications* (Major Revision).

[H] I. Donevski, M. Virgili, N. Babu, J. J. Nielsen, P. Popovski, A. J. Forsyth, and C. B. Papadias, "Sustainable and Persistent Wireless Services with UAV Swarms for Off-Grid Applications : CAPEX Efficient Coverage Maximization," submitted to *IEEE Transactions on Smart Grid* (Major Revision).

Acknowledgment

This thesis section is incomplete without thanking my supervisors, Dr. Constantinos B. Papadias and Prof. Petar Popovski, who were always there when I needed professional and personal advice. The research freedom they gave me while ensuring quality research output is the part I enjoyed the most in my Ph.D. study. The detailed comments and feedback I received from them helped me a lot to evolve as a mature researcher.

I thank Dr. Alvaro Valcarce of Nokia Bell Labs, France, for hosting me as a visiting researcher in his group. Even though it was done virtually, the regular weekly meetings helped me plan and finish the work timely. A special acknowledgment to the project PAINLESS, which has received funding from the European Union's Horizon 2020 research and innovation program under grant agreement No 812991, for providing an excellent platform for my research. The numerous summer and winter schools arranged by the consortium helped me improve my technical knowledge and soft skills, many thanks to the organizers. Many novel aspects of the proposed works would not be there if there were no collaboration with other peer-researchers of the project, a special thanks to them. I am grateful to the Connectivity team for the hospitality I received during my stay at the section. I would like to also express my gratitude to my colleagues in the SWIFT lab, who were always there to support me during my difficult times. Being away from family for three years was expected to be difficult, especially during the pandemic, a special acknowledgment to my family for making it less intense.

Finally, I would like to thank Prof. Rui Zhang, Dr. Anna Tzanakaki, and Dr. Gilberto Berardinelli for accepting to be members of my Ph.D. assessment committee and for taking their time to evaluate my work.

Nithin Babu
Aalborg University

Part I

Introductory Chapters

Chapter 1

Introduction

1 Motivation

Various technologies are envisioned for the energy-efficient deployment of future cellular networks [1]: improving the coverage area and reducing the link power budgets by increasing the number of infrastructure nodes per unit area, forming dense heterogeneous networks (HetNets) [2]; increasing the number of base station (BS) antennas to cope with the increased service demand from the users [3]. The above solutions imply high-deployment costs, and the availability of reliable power grids decides its possible deployment. Many countries cannot contain the expansion of cellular networks due to the limited power grid infrastructure. For instance, in Africa, only 10% of individuals have access to the electrical grid [4]. Furthermore, the conventional cellular infrastructure would fail to meet the sporadic service demands from natural disaster/special event scenarios.

A candidate cost-and energy-efficient, easily-deployable solution to overcome the above-mentioned problems is to deploy a UAV(s)-based green and power-autonomous portable access point (PAP) system. A PAP system contains UAV(s) that will be hovering or moving over the service required area carrying radio access node(s) to serve ground users and a ground charging station (CS) that harvests the energy needed for the operation from renewable sources such as solar and wind. When a natural disaster happens, UAVs can be deployed quickly to survey the area for search and rescue, deliver supplies for first aid, and provide emergency communications. The use of UAVs to provide internet access in earthquake-hit regions in Japan [5] and Nokia's F-cell technology to extend cellular coverage extension using drone-based base stations are proven applications of portable access points [6]. Accordingly, UAVs are expected to dominate applications in remote/under-served areas and applications requiring temporary high bandwidth communications infrastructure. UAV use cases are booming, with recent

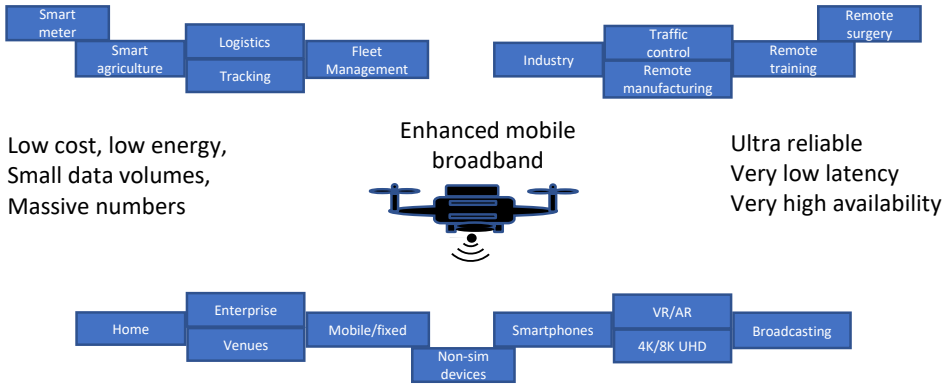

Fig. 1.1: UAV use cases [7].

forecasts indicating a $100 billion market opportunity over the coming years [7]. The use case varies from photography to precision farming as well as inspection and mapping in industries. In white paper [7], Ericsson proposed the 5G use cases of UAVs shown in Fig. 1.1.

A PAP system can achieve an efficient power-autonomous operation through a combination of energy-efficient deployment of PAPs and a cost-efficient configuration of the CS. The works linked to a conventional cellular infrastructure design consider energy efficiency and harvesting aspects separately. The existing frameworks are unsuitable for a PAP system due to: a) the wireless network optimization should incorporate realistic power generation, storage, and consumption models; b) the network deployment planning and the CS configuration should be done jointly. Furthermore, the limited on-board energy of the UAV should be efficiently spent among the UAV-related and communication-related energy consumption parts.

The quality of the air-to-ground channel from a PAP at a given position to a user is a function of the elevation angle and the 3D distance between them [8]. The energy consumed by the UAV is very high compared to the consumption of the on-board access point. Hence, the PAP deployment policy should aim, for instance, at maximizing the number of bits transmitted per Joule of energy which is distinct from maximizing the throughput or minimizing the energy consumption separately. Furthermore, the cost per bit can be minimized by: a) minimizing the number of UAVs through efficient PAP deployment policies; b) minimizing the number of harvesting and storage modules by configuring the CS as a function of the load profile generated by the PAP deployment policy. The load profile should reflect UAVs' charging and discharging schedules, which is application-specific. For instance, a single PAP is enough to collect data from nodes in a delay tolerant network, which stores the data and transmits it when a reliable communication link is available. On the contrary, a broadband application requires one PAP per cell where the hovering altitude of the PAP defines the cell boundary. Hence,

the load to the CS varies largely among these two scenarios. The above-mentioned characteristics and trade-offs associated with an efficient design of a power-autonomous PAP system open up many challenges. We address the challenges in this thesis by achieving the research objectives defined in Section 2.

2 Research Objectives

This thesis **envisions a grid-independent network of portable access points capable of replacing the power-grid restricted base station topologies**. The thesis objective is achieved by addressing the challenges discussed in the previous section through the following research objectives:

> **[RO1]:** Develop realistic power generation, storage, and consumption models, and incorporate them directly into the PAP deployment optimization;
>
> **[RO2]:** Introduce energy-efficiency metrics that represent the trade-offs between coverage and energy, throughput and power, cost and coverage, and cost and throughput;
>
> **[RO3]:** Propose energy-efficient placement policies for a PAP system;
>
> **[RO4]:** Build optimization framework that minimizes the cost of the system by balancing the energy generation and consumption.

Since the thesis objective involves improving the system's energy efficiency and achieving power autonomy, accurate energy generation models of harvesting units such as PV panels and windmills, exact energy storage model for batteries used at the CS and the UAV, and precise energy consumption model of the UAV, are required ([**RO1**]). The lifetime of a PAP system will be a critical performance indicator that is not explicitly accounted for by the current 5G performance metrics. Accordingly, the definition of new metrics to represent the trade-offs associated with a PAP system, such as coverage vs. power, throughput vs. energy, and cost vs. data rate, is paramount ([**RO2**]). Using the developed energy models, energy- and cost-efficient policies need to be developed that ensure the power autonomy of the system ([**RO3**] and [**RO4**]). The objectives are achieved through a number of submitted and published scientific papers.

The papers that share a common system setup are grouped into three groups, as shown in Fig. 1.2:

> [G1]: Static PAPs: Energy-Efficient Positioning and Communication;
>
> - Papers A, B, and C are grouped as [G1] that propose deployment policies to determine energy-efficient hovering locations for PAPs considering realistic power consumption models and different multiple access schemes.

		[RO1]	[RO2]	[RO3]	[RO4]
[G1]	PAPER A		✓	✓	
	PAPER B		✓	✓	
	PAPER C			✓	
[G2]	PAPER D	✓		✓	
	PAPER E	✓		✓	
	PAPER F	✓	✓	✓	
[G3]	PAPER G	✓	✓	✓	✓
	PAPER H	✓	✓	✓	✓

Fig. 1.2: Grouping of scientific papers.

[G2]: Dynamic PAPs: Energy Efficient Path Planning and Resource Allocation;

- Papers D, E, and F form [G2] that develop a framework to improve the system's energy efficiency by moving a PAP through an optimal path while ensuring service fairness among the users. The optimization framework includes realistic power consumption and storage models.

[G3]: Energy-Neutral System Optimization: Cost Efficient CS design;

- [G3] consists of Papers G and H that achieve energy-neutrality by configuring the CS based on the load demanded by the PAPs. The proposed algorithms use realistic power generation, storage, and consumption models.

In Chapter 2 of Part I, we give an extensive summary of the papers and the trade-offs considered in each group.

3 Thesis Outline and Assumptions

The remainder of the thesis is organized as follows. Chapter 2 describes the trade-offs considered while developing optimal placement solutions for static, dynamic, and energy-neutral PAP systems. It also provides an extensive summary of the scientific papers contributing to achieving the objective of the thesis. As mentioned in the previous section, Papers A, B, and C propose energy-efficient placement policies for a static PAP system, whereas Papers D, E, and F offer solutions for energy-efficient trajectory design of a dynamic PAP system. Finally, Papers G and H design an energy-neutral PAP system. In Chapter 3, we summarize the contributions and discuss the future scope of the work. Part II of the thesis includes the published and submitted scientific papers that form the core part of the thesis.

The assumptions that are common to all the works that constitute this thesis are,

- The system is deployed as a stand-alone unit to serve a set of outdoor-ground users located in areas having no cellular service from the conventional cellular infrastructure.
- We model the air-to-ground channel by considering two propagation groups: the first group corresponds to a favorable Line-of-Sight (LoS) condition, or near-Line-of-Sight condition to a ground user, while the second group generally corresponds to Non-Line-of-Sight (NLoS), but still receiving coverage via strong reflections. This is a reasonable and justifiable model, as radio signals emitted by a PAP propagate in free space until reaching the environment where they incur shadowing and scattering caused by the man-made structures, introducing additional loss in the air-to-ground link [8]. For a given elevation angle between a user and a PAP at a given location, this additional loss has a Gaussian distribution [9], and it depends on the building profile of the region. However, from [9], the change in the additional path loss within a particular propagation group (LoS/NLoS) is insignificant compared to the change in path loss value from one group to the other: the NLoS path loss value depends on the scattering and reflections from the surrounding buildings, which in turn rely primarily on the frequency of operation and the building profile of the region. Since the proposed policies are used in the planning phase of the PAP deployment, we consider the long-term channel variation rather than short-term random behavior due to the dynamic propagation environment.
- The optimal placement policy is developed offline at the ground station prior to the PAP deployment. This requires the ground station to be aware of the positions of the users, which can be done, for instance, using the new radio positioning protocol (NRPPa).

- The backhaul link for the PAP is achievable with the new integration of low earth orbit (LEO) satellites [10]; hence, not considered in the analysis.

References

[1] F. Boccardi et al, "Five Disruptive Technology Directions for 5G," *IEEE Commun. Mag.,* vol. 52, no. 2, pp. 74, Feb. 2014.

[2] J. G. Andrews, "Seven Ways that HetNets are a Cellular Paradigm Shift," *IEEE Commun. Mag.,* vol. 51, no. 3, pp. 136–144, May 2013.

[3] E. G. Larsson, et al, "Massive MIMO for Next Generation Wireless Systems," *IEEE Commun. Mag.,* vol. 52, no. 2, pp. 186–195, Feb. 2014.

[4] S. Kumar, "Size of Global Off-Grid and Gad-Grid Telecom Towers," in *Bi-Annual Report, Green Power for Mobile,* August 2014, p.14.

[5] "National institute of Information and Communication Technology, Japan, Development of UAV wireless communication systems in NICT," in *13th Broadsky Workshop,* Japan, 2015

[6] A. Fotouhi, H. Qiang, M. Ding, M. Hassan, L. G. Giordano, A. Garcia Rodriguez, and J. Yuan, "Survey on UAV Cellular Communications: Practical Aspects, Standardization Advancements, Regulation, and Security Challenges," *IEEE Communications Surveys Tutorials,* pp. 1–1, 2019.

[7] Takacs, Attila, et al. "Drones and networks: Ensuring safe and secure operations." *Ericsson White Paper 14* (2018).

[8] A. Al-Hourani, S. Kandeepan and S. Lardner, "Optimal LAP Altitude for Maximum Coverage," *IEEE Wireless Communications Letters,* vol. 3, no. 6, pp. 569-572, Dec. 2014.

[9] A. Al-Hourani, S. Kandeepan, and A. Jamalipour, "Modeling Air-to Ground Path Loss for Low Altitude Platforms in Urban Environments," in *Globecom 2014, Symposium on Selected Areas in Communications: Satellite & Space Communication,* Austin, USA, Dec. 2014.

[10] Soret, Beatriz, et al. "5G Satellite Networks for Internet of Things: Offloading and Backhauling," *International Journal of Satellite Communications and Networking*, 39.4 (2021): 431-444.

Chapter 2

Summary of Contributions

1 Static PAPs: Energy-Efficient Positioning and Communication

This section summarizes the works considering PAP deployment policies in which the PAPs hover at optimal locations to serve the users. Fig. 2.1 shows the architecture of a static PAP system. As shown in the figure, the PAPs and the users are connected to a centralized system called unmanned aerial system (UAS) traffic management system (UTM) through orthogonal control channels. These links can be used by the pilot to send maneuver control signals to the PAP or by the users to request the service of the PAP. The operators will connect to the UTM to get flight approval and periodically report the status of the flights [1]. The main motivation for such a static deployment is from Fig. 2.2 that contains plots of the LoS probability as a function of the elevation angle θ, for different deployment regions [2]. As seen in the figure, an elevation angle greater than 20^o guarantees an LoS link between a PAP and a user in a suburban region. Consequently, the LoS coverage area of a PAP can be modelled as a circle of radius,

$$R_p = h_{\mathrm{p}} \tan(\theta_{\mathrm{los}}), \tag{2.1}$$

where h_p is the hovering altitude, and θ_{los} is the minimum elevation angle between a user and a PAP required to guarantee an LoS link, obtained from Fig. 2.2. Thus, the LoS coverage area increases as the hovering altitude increases, but the corresponding link quality decreases due to a larger propagation distance. Additionally, there is an increase in the UAV power consumption as the PAP ascents axially due to the variation in air density and pressure. The optimal hovering locations for the PAPs, considering the trade-offs between the coverage area, link quality, and the UAV energy consumption, are determined through policies proposed in Papers A-C.

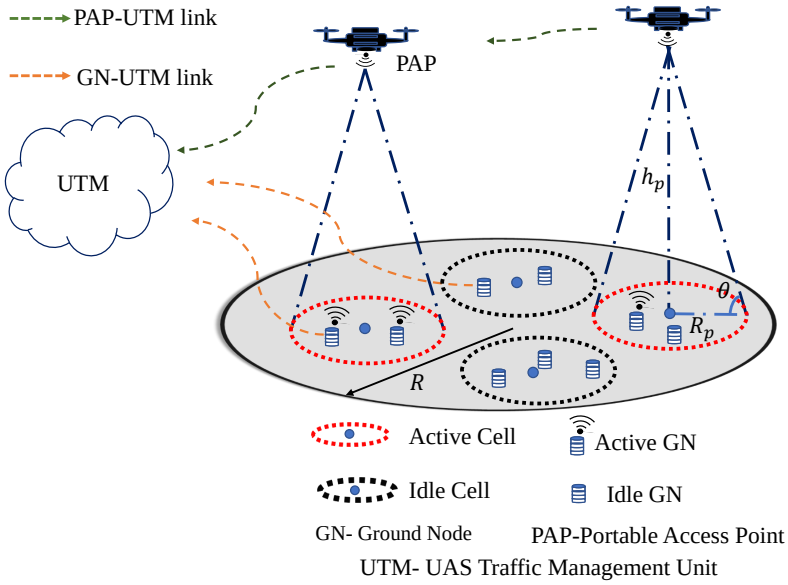

Fig. 2.1: [G1]: PAPs hover at optimal 3D locations to serve the users.

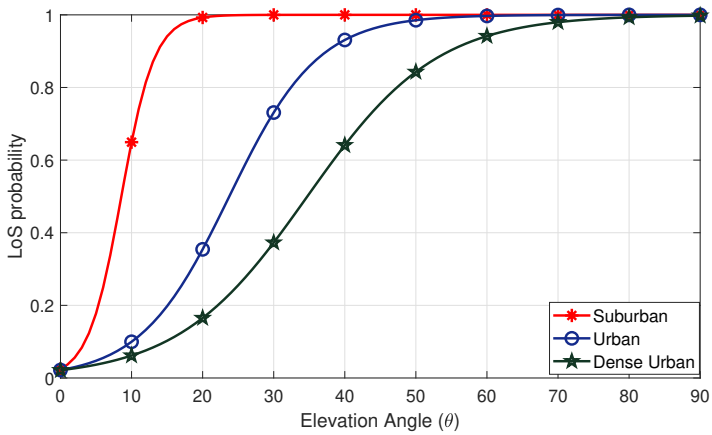

Fig. 2.2: LoS probability versus elevation angle for different deployment regions [2].

Paper A: "Energy Efficient Altitude Optimization of an Aerial Access Point"

This paper considers an unmanned aerial vehicle carrying a radio access node called an aerial access point (AAP) deployed to serve a set of ground users. The objective is to determine the optimal hovering altitude for the AAP that maximizes the total number of bits transmitted per Joule of energy consumed, measured as the global energy efficiency (GEE) of the system. The work considers a downlink communication between the AAP and the users. The numerator of the GEE is estimated by assuming a uniform distribution of the users along the line-of-sight (LoS) coverage area of the AAP. The altitude and a minimum elevation angle, a function of the environment, determine the LoS coverage area. The AAP serves the users through the frequency-division-multiple-access (FDMA) scheme, where the availability of a sufficient number of orthogonal channels is assumed. The total energy consumption (the denominator of the GEE) is modelled as the sum of the propulsion energy consumption of the UAV and the energy consumed by the communication equipment. With an increase in the hovering altitude, the LoS coverage area as well as the UAV energy consumption increase, whereas the channel gain to a user decreases. Therefore, the proposed algorithm determines an energy-efficient hovering altitude for the AAP by exploiting this tradeoff between the total number of bits transmitted and the total energy consumed.

The objective is translated into a non-convex optimization problem of maximizing the GEE of the system, subject to altitude and minimum individual data rate constraints. The problem is solved using the sequential convex programming (SCP) optimization technique. The fundamental idea of SCP is to iteratively solve a sequence of convex approximated problems of the original non-convex problem so that the feasible solution points converge to the KKT point of the original non-convex problem. The initial feasible solution required to solve the problem using the SCP technique is taken as the minimum altitude. The obtained solution using the SCP technique cannot be claimed as the global optimum. Hence, the work compares the obtained solution to the global optimum obtained by solving the same problem using the polyblock outer approximation (PA) algorithm. Numerical results show that the optimal altitude obtained using the SCP technique lies close to the global optimum found using the PA algorithm. Moreover, neglecting the communication-related energy consumption has a negligible impact on the optimal hovering altitude.

Paper B: "Energy-Efficient Deployment of a Non-Orthogonal Multiple Access Unmanned Aerial System"

This work proposes an algorithm to determine the energy-efficient hovering altitude of an AAP deployed to collect data from a set of ground users (uplink communication). The algorithm maximizes a new energy efficiency metric called area energy efficiency (AEE)

of the system. The AEE of the system is defined as the ratio between the geographical area covered by the AAP and the total energy consumption. The system set up assumes the AAP to be equipped with a directional antenna. The users send their collected data to the AAP using an uplink power-domain non-orthogonal multiple access (P-NOMA) scheme. According to the P-NOMA scheme, the users send data using the same time and frequency resources but with different power levels. The receiver at the AAP removes the inter-user interference from the co-channel users through the successive interference cancellation (SIC) technique.

The SIC receiver at the AAP requires diverse received powers from the users to decode the messages successfully, guaranteed through the proposed uplink-P-NOMA scheme. Each user is assigned an index of the decoding order following the path loss value: a user with a higher path loss value is assigned a higher index value. The users then follow a power-reduction scheme for transmitting data. The scheme ensures that the received powers from the n^{th} and $(n+1)^{\text{th}}$ user differs by a power reduction factor δ, where n is the index of decoding order. The AEE maximization objective is formulated as a non-convex optimization problem subject to altitude and minimum data rate constraints. As the altitude increases, the coverage area of the AAP increases along with the energy consumption. Hence, the numerator and the denominator of the objective function are increasing functions of the hovering altitude. Consequently, the optimal altitude is determined using a bisection-based algorithm. Numerical evaluations show that the proposed P-NOMA scheme outperforms an equivalent orthogonal multiple access (OMA) scheme in terms of the AEE.

Paper C: "Energy-Efficient 3D Deployment of Aerial Access Points in a UAV Communication System"

While Papers A and B consider the altitude optimization of a single-UAV system, this work proposes an energy-efficient 3D placement of multiple AAPs. The paper considers an uplink communication from a set of users. The positioning of the AAPs is done to maximize the GEE of the system. The users are assumed to be uniformly distributed across the geographical region. The AAPs follow a universal frequency reuse policy, and the total bandwidth available at an AAP is equally divided among users in its coverage area. For an AAP hovering at a given altitude, all the users with an LoS probability greater than a threshold value are considered covered by the AAP. This makes the coverage region of an AAP circular in shape, for which the radius depends on the hovering altitude and the LoS threshold value. The universal frequency reuse policy causes inter-cell interference from the co-channel users in the neighboring cells. Finally, each user chooses the transmit power according to the uplink power control so that the received power values at an AAP from all the users in its coverage area are equal to a target power value.

The GEE of the system depends on the locations of the AAPs; as the altitude

increases, the coverage area and the propulsion energy consumption of an AAP increase, thereby affecting the GEE. The proposed algorithm decouples the 3D placement problem into vertical and horizontal positioning sub-problems. The horizontal positioning of the AAPs determines the fraction of the total area covered by the AAPs. In the presence of inter-cell interference, the optimal altitude that maximizes the GEE is derived as the minimum permitted altitude. The horizontal positions of the AAPs, which maximize the total area covered by the AAPs, are determined by modelling it as a circle packing problem. The optimal altitude value determines the radius of the circle. The work then proposes a novel regular polygon-based AAP placement algorithm that gives the horizontal position coordinates of the AAPs. The algorithm allows for determining the maximum number of non-interfering AAPs placed in the desired area. From the numerical evaluations, it is observed that a set of AAP hovering locations, determined using the proposed algorithm, covers around 78% of the total area on average. Also, neglecting the energy consumption of the aerial vehicle will result in a sub-optimal solution.

2 Dynamic PAPs: Energy Efficient Path Planning and Resource Allocation

This section summarizes the works considering a PAP flying to serve the users. The primary motivation to move a PAP above the region to serve the users is from Fig. 2.4. The figure has two plots showing the variations of power consumption as a rotary-wing PAP takes a level forward flight with different payloads. As seen in the figure, a PAP consumes less power as it starts moving from hovering up to a certain velocity, increasing afterward: the total power consumed by a PAP has three parts, the first part to overcome the drag of the fuselage, the second to oppose the rotor-induced drag force, and the third to compensate the profile drag force of the rotors. The magnitude of power required to overcome the rotor-induced drag force decreases with the PAP velocity; in the low-speed regime, it dominates the power consumed to overcome the fuselage and rotor profile drag forces. Hence, a flying PAP can have more air-time, defined as the duration it remains aloft, compared to a hovering one by optimally selecting the flight velocity.

The air-time of a PAP is a non-linear function of the power drawn from the battery. A usual approach to estimate the air-time is to find the ratio of the initial on-board energy to the sum of instantaneous power consumption values [3]- [5]. Mathematically, if a PAP draws P_1 Watts for T_1 seconds (s), it can draw P_2 W for $\frac{P_1 T_1}{P_2}$ s, which is not the case in practice. This observation is termed the Peukert effect in the literature [7]. Practically, a battery is useful until the terminal voltage or the remaining discharge time becomes lower than the corresponding threshold values, whichever happens first, as shown in

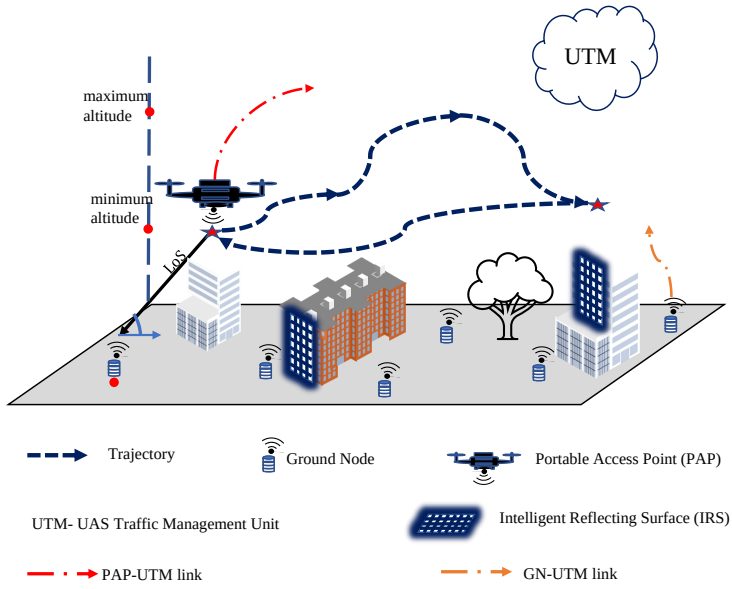

Fig. 2.3: [G2]: PAPs flying to maximize the energy efficiency of the system while ensuring service fairness among the users.

Fig. 2.5. The figure shows that neglecting the Peukert effect overestimates the air-time, causing an early landing of the PAP without completing the mission. Therefore, the trajectory of a PAP should be designed considering the non-linear discharge behavior of the PAP battery. Fig. 2.3 shows the system setup of a dynamic PAP system. The main design variables are the flying velocity of the PAP and the scheduling of users for completing the mission. For tractability, the trajectory of the PAP is discretized in the time/space domain. The velocity with which the PAP covers a segment of the trajectory and the corresponding scheduling of the users are determined to maximize the system's energy efficiency. Papers D-F propose policies for energy-efficient trajectory design of a PAP while considering pragmatic battery discharge profile (Papers E and F).

Paper D: "Cost- and Energy-Efficient Aerial Communication Networks with Interleaved Hovering and Flying"

Paper D optimizes the system for both the uplink and downlink communication between an AAP and a set of ground users. The AAP follows a fly-hover-communicate protocol

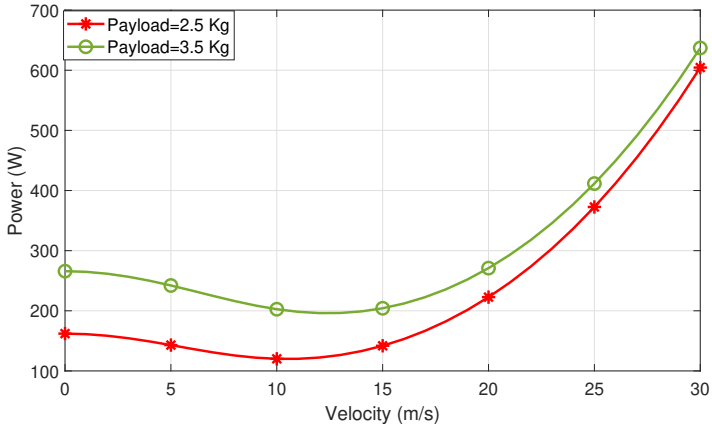

Fig. 2.4: Variation of the PAP power consumption Vs velocity.

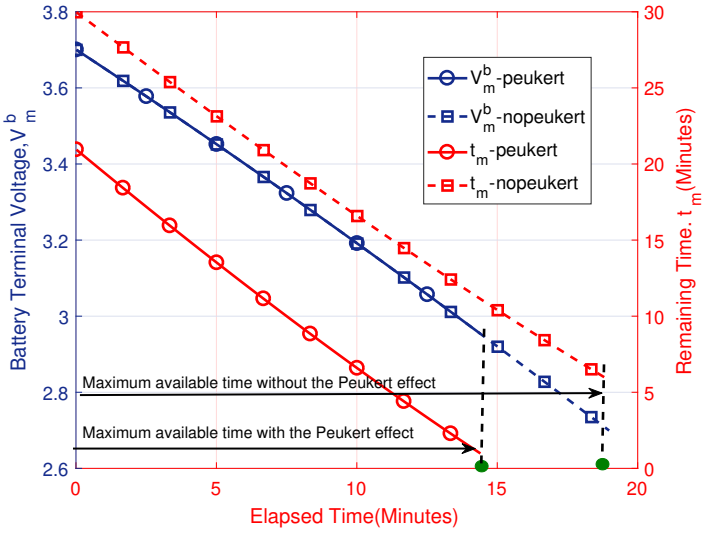

Fig. 2.5: Air-time with and without considering the Peukert effect for constant 200W power-draw until the battery discharges completely.

to serve the users. As the name indicates, it will fly from one hovering point (HP) to another, hovers for the time needed to exchange the data packets, then moves on to the following HP. Additionally, each user must send/receive a file of a given size to/from the AAP. The objective is to deploy a single moving AAP in an energy- and cost-efficient way so that all the users are served at the end of the trajectory. The system is operated for a given duration in a day, and if the active time of the AAP is less than the service duration, then a fully charged AAP from the ground station replaces the out-of-power AAP. The AAP is equipped with a directional antenna of a given beamwidth, whereas all the users have omni-directional antennas. The users in the coverage area are allocated with orthogonal frequency bands to each other. The uplink communications from the users follow the power control mechanism, as explained in Paper C.

Firstly, the paper models a multi-rotor UAV's hovering and flying power consumption. The power consumption model used in Papers A-C applies only to a specific UAV type. It is then used to find the optimal number and locations of the hovering points required to cover a given set of users. The coverage region of the AAP while hovering at an HP is a circular region centered around the HP whose radius is a function of the hovering altitude and the beamwidth of the AAP antenna. Similar to Paper C, the proposed algorithm decouples the 3D HP determination problem into vertical and horizontal positioning problems. Since the AAP serves only the set of users associated with one HP at a time, the co-channel interference is neglected in the analysis. Through Proposition 1, the uplink and downlink GEE are increasing functions of the hovering altitude. Consequently, the vertical coordinates of the HPs are fixed to the maximum altitude determined by the minimum data rate constraint. By Proposition 2, the uplink GEE is an increasing function of the antenna's beamwidth, whereas the downlink GEE is neither an increasing nor a decreasing function of the beamwidth. Therefore, the antenna beamwidth that maximizes the GEE is obtained using a ternary search algorithm (Algorithm 1). Similar to Paper C, the problem of finding the horizontal projection coordinates of the HPs takes the form of a circle packing problem. Recall that the circles placed according to the regular-polygon-based algorithm proposed in Paper C cover only 78% of the geographical region. Hence, this work presents a regular-pentagon-based multi-level circle packing algorithm that gives the set of HPs covering all the users (Algorithm 2). The algorithm's first part determines the group of circles centered at HPs covering the given geographical area entirely. In the second part, the circles that do not cover users are discarded. The AAP serves the users taking the shortest path through the set of HPs.

The later part of the paper determines the values of depth-of-discharge (DOD), defined as the portion of battery capacity consumed during a discharge cycle, and horizontal flying velocity, which minimize the annualized cost of the system (ACS). The ACS is the sum of the capital, maintenance, and replacement costs. The capital cost is contributed by the purchasing prices of the AAPs and the charging station, whereas the maintenance cost is the cost of the electricity consumed to recharge the batteries. The

replacement cost is incurred when we replace a battery after its lifetime. The capital cost can be decreased by increasing the DOD since it decreases the number of AAPs by increasing the active time of an AAP. The maintenance cost is relatively less sensitive to the DOD and can be reduced by setting a high DOD value. Conversely, the lifetime of a battery can be increased by setting a low DOD value. Considering these trade-offs, the work determines the optimal DOD and horizontal flying velocity values that minimize the ACS numerically.

Paper E: "Energy-Efficient Trajectory Design of a Multi-IRS Assisted Portable Access Point"

This work considers the possibility of using intelligent reflecting surfaces (IRSs) to improve the GEE of a UAV-based system. The system set up considers a PAP deployed to deliver a file of a given size to a set of ground users. The PAP is assumed to serve the users through the time division multiple access scheme (TDMA). Paper D estimates the active time of the PAP as a linear function of the energy available at the beginning of the mission and the total power consumption. Unlike Papers A-D, this work considers a pragmatic battery discharge profile for the PAP's battery unit called the Peukert effect. Through numerical evaluations, it is observed that neglecting the Peukert effect overestimates the active time of a PAP, which could affect the mission planning. The work starts by proposing an algorithm to determine the available flight time of the PAP considering the Peukert effect. Later, this is put as a constraint in the optimization problem. The objective is to determine an efficient 2D trajectory for the PAP and allocate time slots to the users so that the GEE of the system is maximized, subject to the flight time, data delivery, TDMA, altitude, and IRS phase shift constraints. The additional phase shift values introduced by the elements of the IRSs should be selected to maximize the GEE of the system. This makes the IRS phase shift optimization a direct function of the trajectory. The main challenge in adding IRSs to a PAP system is finding optimal locations for the IRSs and then determining the optimal phase shift values introduced by their elements, considering the interdependence of amplitude and phase values of a re-radiated wave from an IRS element. The work models the PAP and a user channel using the probabilistic LoS-NLoS path loss model, whereas the PAP-IRS and IRS-GN are modelled using the 3GPP air-to-ground channel model, considering the IRSs placed at the height of 10 m.

The proposed methodology solves the GEE maximization problem in two phases. The first phase determines the optimal locations of the IRSs using the proposed multi-tier circle packing algorithm in which the radius of the circle is 20 m, which guarantees an LoS link between a user located at the edge of the circle and an IRS whose horizontal plane coordinates are the same as the center of the circle. The multi-tier packing algorithm is an extension of the regular-pentagon-based multi-level circle packing algorithm proposed in Paper D. In the multi-tier packing algorithm, instead of considering

the 5- circle packing alone, each level of the packing considers all the available packing patterns. Accordingly, each tier of the packing selects the packing that gives the least number of circles required to cover the given area. Once the multi-tier packing algorithm determines the locations of the IRSs, the PAP path is selected as the shortest path between the locations. The flying altitude of the PAP is the one that guarantees an LoS channel to all the IRSs. The continuous path is then segmented into smaller segments so that the path loss values between the PAP and each GN while the PAP is in a given path segment remain stationary. Using the segmented paths and locations of the users and the IRSs, the expected spectral efficiency for each user while the PAP is in a given path segment is estimated and is repeated for all the path segments.

The second phase calculates the flying velocity of the PAP and the scheduling of the users using a novel multi-lap trajectory algorithm that maximizes the GEE of the system. The formulated problem is convex and is solved using available solvers such as MATLAB's CVX. The numerical evaluation section investigates the effect of adding more battery units on the available flight time. It is observed that increasing the battery size beyond a certain threshold reduces the available flight time since the power consumption increases with the weight. The presence of IRSs improves the GEE of the system by providing additional controllable channels between the PAP and the users. Finally, the proposed multi-lap trajectory is compared with a single lap and fly-hover-communicate (Paper D) baselines. The proposed scheme outperforms the baselines and could improve the GEE by 30%.

Paper F: "Fairness Based Energy-Efficient 3D Path Planning of a Portable Access Point: A Deep Reinforcement Learning Approach"

This paper optimizes the 3D trajectory of a PAP that provides wireless service to a set of ground nodes. In contrast to Papers D and E, the proposed policy designs the trajectory without decoupling the problem in horizontal and vertical dimensions. The paper introduces a new energy efficiency metric called fair energy efficiency (FEE) that puts importance on both energy efficiency and user fairness. One can maximize the GEE metric used in Papers A and C-E by flying the PAP above a sub-set of users to increase the sum rate (the numerator of the GEE). On the other hand, the FEE metric is a weighted energy efficiency metric, where the weight is the fairness index (FI). If the PAP sends an equal number of bits to all the users by the end of the trajectory, the fairness index will be 1. To maximize the FEE, the PAP will follow a 3D trajectory that maximizes energy efficiency and per-user fairness. Similar to Paper E, the proposed algorithm considers the Peukert effect to determine the air-time of the PAP. The PAP returns to a destination when it has only enough energy left on-board to fly to the destination from the latest location. Consequently, the objective function depends on the Peukert effect, which was not the case in Paper E. The PAP serves

the users following the TDMA scheme in which the time allocated to each user while the PAP is in a given path segment is proportional to the respective expected spectral efficiency. The proposed FEE metric and the heuristic TDMA scheme are optimal for an IoT application scenario in which the PAP is deployed to deliver a file of a given size to all the users by the end of the trajectory. Suppose the PAP flies near to a user in a given time instant. In that instant, it is more efficient to allocate more resources to that user since the communication channel to the user, as well as the throughput, will improve. However, to guarantee a high long-term user fairness, the later segments of the trajectory should be closer to the remaining users.

The paper formulates the FEE maximization objective as an optimization problem subject to altitude, 3D movement, and the Peukert constraints. The problem takes the form of a non-convex problem with non-tractable constraints. Therefore, it is represented as a Markov Decision Process (MDP) with continuous state and action spaces. A state of the PAP has entries related to its 3D coordinates, the total energy consumed up to the current position, the 3D distance to the users, and the total number of bits transmitted to the users up to the current segment of the trajectory. The action space represents the action taken by the PAP, which is modelled as a 3D vector representing the velocity of the PAP. The reward space is mapped to the FEE value of the system using the reward shaping technique. Since the state and action spaces are continuous, the proposed methodology uses the twin delayed deep deterministic policy gradient (TD3) actor-critic deep reinforcement learning (DRL) framework to learn a policy that maximizes the FEE of the system. The actor takes the current state of the PAP as the input and suggests an action (velocity vector). The PAP moves from the current state to the next after taking the recommended action. The critic network takes the current state and the action as the inputs and gives the Q-value of the action after observing the next state and the reward. The parameters of the networks are updated in the improving direction of the Q-value.

The work completes the training of the networks following two approaches: the first approach is suitable for applications where the users' positions remain stationary, whereas the second approach generalizes the learned policy to any arrangement of users. It does so by changing the users' positions after each training episode. At the end of the training, the actor can be used as a standalone unit that gives the movement commands to the flight controller of the PAP. Numerical evaluations show that neglecting the Peukert effect overestimates the air-time of the PAP and can be addressed by optimally selecting the PAP's flying speed. Moreover, the user fairness, energy efficiency, and hence the FEE value of the system can be improved by efficiently moving the PAP above the GNs. The proposed policy gives massive FEE improvements over stop-and-hover baseline scenarios of up to 33.31%, 197.87%, 215.92% for suburban, urban, and dense urban environments, respectively.

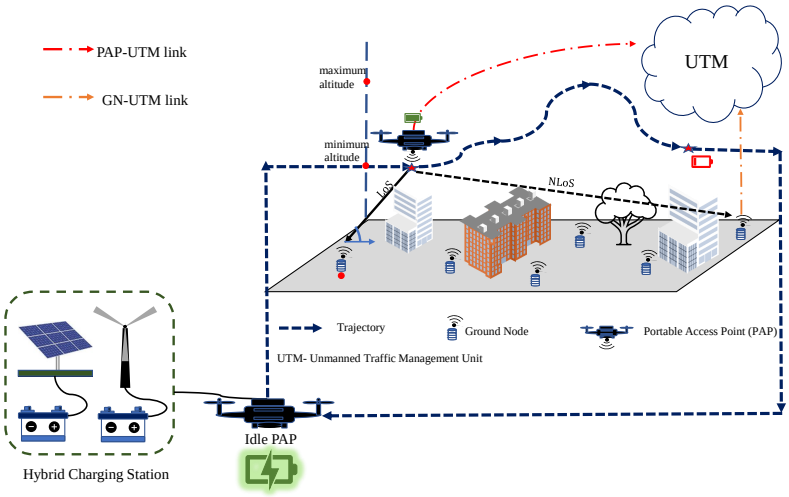

Fig. 2.6: [G3]: The power-autonomy of the system is achieved by harvesting the required energy from renewable energy sources.

3 Energy-Neutral System Optimization: Cost Efficient CS design

This section includes summary of papers that consider the cost-efficient design of a grid-independent PAP system. Fig. 2.6 shows the architecture of a energy-neutral PAP system. The energy required to recharge the PAPs is derived from renewable energy sources such as wind and solar. When a PAP runs out of the on-board battery capacity, it flies back to the CS and enters the idle mode. Meanwhile, a fully recharged PAP ascends to continue serving the users. The PV and the windmill modules at the CS harvest energy from solar irradiation and wind, respectively. If there is a surplus in energy, it is stored in a ground battery unit at the CS. The battery unit supplements the harvesting modules when there is a deficit in the harvested energy to meet the load.

The configuration of the CS and the number of PAPs minimize the cost of the system if they are determined as a function of the mission-related variables. For instance, Fig. 2.7 shows the load profile for three scenarios. Case 1 represents a flying PAP deployed to collect data from a set of ground nodes, whereas Case 2 characterizes the load demand from a set of PAPs serving the users by hovering all the time [9]. Case 2 models the load generated by two tethered PAPs serving the users [8]. For a given load profile, PV panels, batteries, and windmill units are selected to ensure the zero-sum balance between energy harvested, stored, and consumed during the system's operation. The shape of the load profile changes according to the distribution of the users and the PAP deployment policy, as seen in the figure. Furthermore, the power generation depends

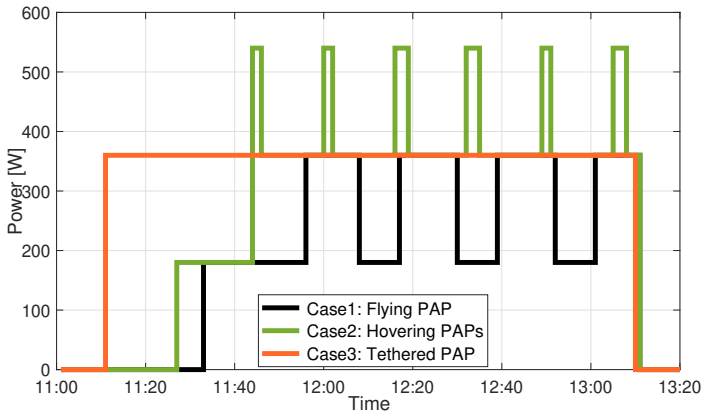

Fig. 2.7: Load profiles for different PAP deployment scenarios.

on the availability of solar irradiation and the wind profile of the serving region at the time of year. Careful consideration of these factors is required to avoid over or under-provisioning the charging station. Hence, Papers G and H minimize the cost of the charging station by configuring it as a function of the load profile generated using the mission-specific parameters.

Paper G: "Cost-Efficient Design of an Energy-Neutral UAV-Based Mobile Network"

This work proposes a cost-efficient design of a grid-independent PAP system. Recall that Paper D minimizes the operational cost of a PAP system by optimizing the flying velocity of the PAP and the DOD value of the on-board battery. However, the cost associated with the charging station was assumed to be a constant value. The investment cost of the system can be reduced by imposing an energy neutrality condition, which refers to the zero-sum balance between energy harvested, stored, and consumed for the system operation. This work considers a hybrid charging station consisting of PV panels and batteries. The batteries supplement the panels if the harvested energy is insufficient to meet the load. If the panels harvest more energy than required, the additional energy is stored in the batteries. Hence, the work minimizes the cost by configuring the number of panels and batteries as a function of the load to the charging station. As mentioned above, the load varies with the type of application for which the PAP is deployed. The system set up considers the PAP deployed to harvest data from a set of internet-of-things (IoT) nodes. The system's cost comprises the purchase cost related to the PV panels, the batteries, and the UAVs. The number of PAPs depends on the time-difference-of-arrival (TDOA) of the network and the available flight time of the PAP.

The cost minimization problem subject to the energy neutrality, data harvesting, TDMA, and velocity constraints cannot be solved using conventional convex optimization tools due to a non-tractable form of the energy-neutrality constraint. The proposed wave-based method tackles this issue by representing the load profile as a proportional function of the required number of AAPs. The method allows representing the cost as a function of the number of AAPs, which is minimized by designing an efficient path. The path design uses the mean-shift clustering algorithm to identify service hotspots. As in Paper E, the shortest continuous path between the cluster centers is discretized to do the TDMA user scheduling. Using the trajectory variables, the time to recharge each AAP is determined and is used to generate the load profile using the wave-based method. A constrained search algorithm then finds the cost-efficient configuration of the CS that meets the energy-neutrality constraint. The results indicate that the off-grid CS is particularly advantageous in rural areas, while in urban areas, its cost is comparable to that of a grid-connected alternative. Please note that the proposed framework can also be used to configure the CS for AAP placement policies offered in Papers A-F, using the corresponding trajectory parameters as the input to the wave-based method.

Paper H: "Sustainable Wireless Services with UAV Swarms Tailored to Renewable Energy Sources"

Paper H considers an off-grid scenario in which a swarm of UAVs is deployed to serve a region. The hovering points of the UAVs are determined based on the desired service rate to be provided to the whole area. The proposed method models the service rate as zonal datarate density (ZDD), which represents data rate per unit of area for an hour of the day and for the entire region. The ZDD is modelled as a random variable for a stochastic process whose expected value is the hourly average of the incoming traffic. The energy required for the system's operation is derived from two renewable energy sources, solar and wind, and the excess generation is stored in a ground battery unit. The work estimates the quantity of the harvested energy using the solar irradiation and wind speed data from the European Commission's Photovoltaic Geographical Information System. A nearly out-of-power UAV flies back to the CS, whose battery is replaced with a fully charged one; hence, the load to the CS is the set of depleted batteries. The area covered by the UAV swarm can be increased by increasing the swarm size, which implies a larger CS. The work aims to configure the system to maximize the area covered per unit of cost.

The paper maximizes the cost-efficiency of the system by modelling it as a combinatorial optimization problem. It is then solved using the proposed greedy and sparse search (GSS) algorithm, which solves the problem by solving two sub-problems. The first sub-problem sparsely searches for a solution where the coverage per energy efficiency is improving and drops the cases where an increase in the area does not yield an improvement in the efficiency. The second sub-problem finds the cost-efficient combination

of the energy generation and storage units that meets the load generated by the UAV swarm required to cover the coverage-efficient solution from the first sub-problem. The best results are achieved in areas with mild wind and reliable solar irradiation; regions with strong winds and unreliable solar intensity require higher capital expenditure.

References

[1] Takacs, Attila, et al. "Drones and Networks: Ensuring Safe and Secure Operations," *Ericsson white paper 14* (2018).

[2] A. Al-Hourani, S. Kandeepan and S. Lardner, "Optimal LAP Altitude for Maximum Coverage," *IEEE Wireless Communications Letters,* vol. 3, no. 6, pp. 569-572, Dec. 2014.

[3] W. Shi, J. Li, H. Wu, C. Zhou, N. Cheng and X. Shen, "Drone-Cell Trajectory Planning and Resource Allocation for Highly Mobile Networks: A Hierarchical DRL Approach," *IEEE Internet of Things Journal,* vol. 8, no. 12, pp. 9800-9813, June 15, 2021.

[4] Wu, H., Lyu, F., Zhou, C., Chen, J., Wang, L., & Shen, X., "Optimal UAV Caching and Trajectory in Aerial-Assisted Vehicular Networks: A Learning-Based Approach," *IEEE Journal on Selected Areas in Communications,* 38(12), 2783-2797, 2020.

[5] Y. Zeng, J. Xu and R. Zhang, "Energy Minimization for Wireless Communication with Rotary-Wing UAV," *IEEE Trans. on Wireless Commun.*, vol. 18, no. 4, pp. 2329-2345, April 2019.

[6] Y. Zeng and R. Zhang, "Energy-Efficient UAV Communication With Trajectory Optimization," *IEEE Trans. on Wireless Commun.*, vol. 16, no. 6, pp. 3747-3760, June 2017.

[7] Khan, K. A., et al. "PKL electrochemical cell and the Peukert's law," in *IJARIIE* 4.2 (2018): 4219-4227.

[8] Amorosi, L.; Chiaraviglio, L.; Galan-Jimenez, J. "Optimal energy management of UAV-based cellular networks powered by solar panels and batteries: Formulation and solutions," *IEEE Access 2019, 7:* 53698–53717.

[9] Galán-Jiménez J, Moguel E, García-Alonso, J, Berrocal J, "Energy-efficient and solar powered mission planning of UAV swarms to reduce the coverage gap in rural areas: The 3D case," in *Ad Hoc Netw. 2021, 118, 102517.*

Chapter 3

Conclusions and Future Work

Through this thesis, we provide solutions for cost-and energy-efficient deployment of a power-autonomous portable access point system. The system consists of UAVs carrying radio access nodes called portable access points (PAPs) deployed to serve ground users and a hybrid charging station that derives the energy required for the system's operation from renewable sources such as solar and wind. The thesis objective is achieved through a number of scientific papers. In the following, we summarize the main takeaways.

The energy efficiency metric to evaluate the performance of the proposed PAP deployment policy should be selected based on the available information. Paper A proposes an energy efficiency metric called global energy efficiency (GEE) of the system, defined as the ratio of the sum rate to the sum of the energy consumed by the aerial vehicle and the communication equipment. The GEE metric, measuring bits/Joule, is ideal for scenarios where the users' locations are available at the planning phase of the PAP deployment. For systems in which the user locations are unavailable, the area energy efficiency (AEE) proposed in Paper B, which measures the area covered by a PAP per Joule of energy consumed, is ideal. The proposed GEE and AEE metrics do not emphasize service fairness among the users. The fair energy efficiency (FEE), a weighted energy efficiency metric with the weight equal to the fairness index, proposed in Paper F encompasses both the user fairness and the system's energy efficiency.

The system's energy efficiency behavior varies with the underlying resource allocation scheme. For instance, Paper A considers an orthogonal frequency allocation with the total available power for the downlink communication equally divided among the users. The system's downlink GEE follows a bell-shaped behavior with regard to the hovering altitude. On the contrary, in Paper B, the uplink GEE of a multi-PAP system, considering inter-cell interference from the co-channel users in the neighboring cells, is a decreasing function of the altitude. The work in Paper D considers orthogonal frequency and constant power allocation schemes subject to a total power constraint. The results

show that both the uplink and downlink GEEs are increasing functions in the absence of inter-cell interference. Hence, the energy-efficient placement policy of PAP(s) varies with the system's resource allocation scheme.

The numerical evaluations in the included papers show that the consideration of the PAP energy consumption in developing energy-efficient deployment policies for a PAP system has a significant impact, neglecting the same results in sub-optimal deployment policies. The energy-efficient hovering altitudes from the proposed algorithms in Papers A and C, neglecting the PAP energy consumption, are offset from the optimal altitude by a considerable margin. In Paper D, a zero PAP energy consumption value inverted the behavior of the GEE. Hence, the inclusion of the aerial vehicle's power consumption is paramount while developing an energy-efficient deployment policy for a PAP system. Moreover, the Peukert effect, which models the non-linear discharge behavior of a PAP battery, becomes significant if a PAP is deployed to remain aloft until its battery capacity is sufficient to return to the charging station. A PAP deployment policy developed neglecting the Peukert effect causes an early landing of the PAP. The effect can be ignored for short-term deployments since there will be sufficient leftover energy in the PAP battery.

From Papers D, E and F, a flying PAP can increase the GEE of the system compared to a hovering PAP. But, the choice depends on the target application. For instance, a PAP system for provisioning continuous broadband connectivity in a rural area requires hovering PAPs, for which the policies developed in Papers A-C and H can be used. On the other hand, if the users in the network can tolerate a delay in service, such as data collection from a delay-tolerant IoT network, deploying a single PAP according to the policy proposed in Paper F is a cost-and energy-efficient solution.

A cost-efficient energy-neutral PAP system is feasible in rural areas with mild wind and a reliable solar irradiation profile. The service continuity of a PAP system beyond the active time of a PAP can be achieved by having backup PAPs in the system, one of which could replace an out-of-power PAP. The feasibility of such a power-autonomous PAP system depends on the availability of power sources to meet the load from the PAPs. The wave-based method proposed in Paper G can be used to model the load to the charging station as a function of the corresponding PAP deployment policy. Later, the load profile is used to find the most economical combination of the energy generation and storage units using the algorithms proposed in Papers G and H.

1 Future Work

The non-terrestrial network (NTN) architecture containing non-terrestrial stations, including UAVs, High Altitude Platforms (HAPs), and satellites, is envisioned to complement the terrestrial infrastructures to provide ubiquitous and high-capacity global connectivity [1]. Integrating the proposed power-autonomous PAP system as a segment

of the NTN could be an exciting extension of the thesis. Papers A-H consider standalone deployment of a power-autonomous PAP system with the assumption of availability of a reliable backhaul link. Including the PAP system in the NTN architecture invites many challenges, namely the development of efficient spectrum sharing techniques, new physical layer procedures to compensate for the large propagation delays, mobility, and constellation management to ensure reliable and continuous inter-module connectivity, etc. Furthermore, dense deployment of PAP systems for different use cases requires the development of aerial corridors for the safe flight of the PAPs.

References

[1] Giordani, Marco, and Michele Zorzi, "Non-Terrestrial Networks in the 6G Era: Challenges and Opportunities," *IEEE Network* 35.2 (2020): 244-251.

Part II

Papers

Paper A

Energy Efficient Altitude Optimization of an Aerial Access Point

Nithin Babu, Konstantinos Ntougias, Constantinos B. Papadias, and Petar Popovski

Published in
IEEE 31st Annual International Symposium on Personal, Indoor and Mobile Radio Communications, pp. 1-7, 2020, doi: 10.1109/PIMRC48278.2020.9217265.

Abstract

In this paper, we propose an energy-efficient optimal altitude for an aerial access point (AAP), which acts as a flying base station to serve a set of ground user equipment (UE). Since the ratio of total energy consumed by the aerial vehicle to the communication energy is very large, we include the aerial vehicle's energy consumption in the problem formulation. After considering the energy consumption model of the aerial vehicle, our objective is translated into a non-convex optimization problem of maximizing the global energy efficiency (GEE) of the aerial communication system, subject to altitude and minimum individual data rate constraints. At first, the non-convex fractional objective function is solved by using sequential convex programming (SCP) optimization technique. To compare the result of SCP with the global optimum of the problem, we reformulate the initial problem as a monotonic fractional optimization problem (MFP) and solve it using the polyblock outer approximation (PA) algorithm. Numerical results show that the candidate solution obtained from SCP is the same as the global optimum found using the monotonic fractional programming technique. Furthermore, the impact of the aerial vehicle's energy consumption on the optimal altitude determination is also studied.

1 Introduction

The role of uninhabited AAP in the deployment of emergency networks such as deploying aerial base stations to provide reliable connectivity in disaster areas [1] or in social events such as concerts is vital. In Japan, earthquake affected areas were provided with internet access with the help of unmanned aerial vehicles (UAV) [2]. Cellular coverage extension using drone deployed base stations by Nokia's F-cell technology is another proven application of portable access points [3]. The mobility and ability of aerial vehicles to adjust their altitude to improve the probability of line-of-sight (LoS) communication channel to the ground UEs makes them suitable for acting as relays in the internet of things (IoT) applications [4]. Despite all these applications, the efficiency of an aerial communication system (ACS) is highly dependent on the limited energy available at the aerial vehicle [5]. Any improvement in the energy efficiency of ACS implies longer aerial vehicle hovering, hence more information bits transmitted to UEs.

Compared to the conventional cellular communication systems, the total energy required by ACS is very high. This is because, in ACS, in addition to the communication-related energy, the aerial vehicle consumes energy during vertical climb and hovering. Most of the works in the literature only consider communication-related energy, which is suboptimal in the case of an ACS. In [6], the authors present an analytical approach to optimize the altitude of low altitude aerial platforms to maximize the radio coverage area. The authors of [7] jointly optimize the flying altitude and the antenna beamwidth for throughput maximization. A new 3-dimensional deployment plan for the drone-base

station to serve the users based on their service requirements, while minimizing the number of drones, is presented in [8]. The work in [9] proposes a new polynomial-time complex spiral mobile base station placement algorithm in UAV-UE communications. The works in [10], [11] find the optimal altitude for UAV-base stations that maximizes the number of covered users using the minimum transmit power.

None of the above works consider the energy consumption of the aerial vehicle in the optimization problem. Since the ratio of communication energy to the total energy consumed by the aerial vehicle is negligible, the results proposed in the above works are suboptimal for the GEE maximization of ACS. When the altitude of an AAP increases, the LoS coverage area increases, the LoS channel gain decreases and the energy consumed by the aerial vehicle also increases. With these facts, we can say that the GEE of an ACS, defined as the ratio of the total number of data bits transmitted to the total energy consumed, will not be maximum either at maximum or minimum permitted AAP altitudes. We exploit this tradeoff between the total number of bits transmitted and the energy consumed to determine an energy-efficient hovering altitude for the AAP. Some of the works which consider the aerial vehicle's energy consumption include [12], [13], [14]. An energy-efficient 3D trajectory of a UAV deployed to serve a set of IoT nodes is investigated in [15]. Optimal trajectories, which minimize the fixed and rotary-wing UAV associated energy are designed in [13] and [14] respectively. The authors in [12] maximizes the minimum average rate and energy efficiency through joint optimization of trajectory, velocity, and acceleration of UAV flying at a fixed altitude. An altitude-dependent energy consumption model is used by the authors of [16] to find drone locations that minimize the cost while ensuring the surveillance of all the targets.

To the best of our knowledge, we are the first to determine an optimal altitude which maximizes the GEE for an ACS considering both the energy required for communication and energy consumed by the aerial vehicle. The rest of the paper is organized as follows. In section 2, we model the system. The energy consumption of the aerial vehicle and GEE are explained in section 3. Section 4 formulates the optimization problem and solves it using SCP and MFP techniques. The numerical results are discussed in section 5. Finally, our findings are concluded in section 6.

In this paper, scalars are represented by lowercase letters. Boldface lowercase letters are used to denote vectors and $\mathbb{R}^M$ denotes the set of M dimensional real-valued vectors.

2 System Model

2.1 System Model

We consider an orthogonal multiple access downlink broadcast transmission scenario enabled by an AAP acting as a flying base station, where each user is allocated a fixed bandwidth. We assume there is always a sufficient number of orthogonal channels (e.g., narrowband frequency division multiple access systems [17]). As shown in Fig. A.1,

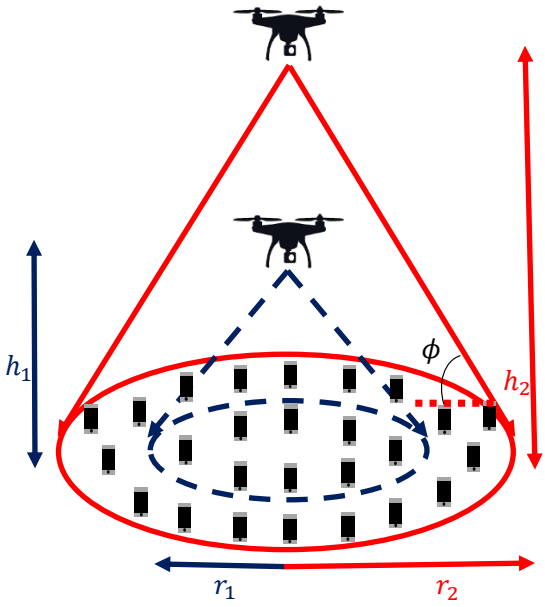

Fig. A.1: AAP enabled downlink broadcast transmission scenario.

we assume a uniform distribution of N UEs in the AAP coverage area $A_{\text{ue}} = \pi\overline{r}^2$ such that $N = \rho_{\text{ue}} * A_{\text{ue}}$, where ρ_{ue} and $\overline{r} = h_{\text{A}}\text{cot}(\phi)$ represent the density of UEs and the radius of the AAP coverage area respectively, and ϕ represents the minimum elevation angle required for the LoS channel between the edge UE and the AAP [6]. The AAP is employed at an altitude of h_{A} meters (m) with the horizontal plane coordinates the same as the center of A_{ue}. In addition to this, we consider the deployment of this system in rural areas where the channel between the AAP and UE is dominated by the LoS link. In real life, this represents the access segment of an ACS in which an AAP is deployed for cellular coverage extension in a rural area. Given this, the LoS channel gain between the UE located at a distance r from the center of the coverage area and the AAP is given by

$$h(r) = \frac{h_0}{r^2 + h_{\text{A}}^2}, \tag{A.1}$$

where h_0 represents the channel gain at a reference distance of 1m. The signal-to-noise ratio (SNR) $\gamma_{\overline{r}}$, at the edge UE is given by

$$\gamma_{\overline{r}} = \frac{P_T h_0}{N(\overline{r}^2 + h_{\text{A}}^2)\sigma^2}, \tag{A.2}$$

where the total data transmission power P_{T} available at the AAP is divided equally among the N UEs and σ^2 represents the variance of the zero-mean additive white Gaussian noise at the corresponding receiver.

Hence, the total number of bits transmitted per unit Hz of bandwidth from the AAP to the considered UE through a channel of bandwidth W in T seconds is expressed as

$$R(\overline{r}) = T\log_2(1+\gamma_{\overline{r}}). \tag{A.3}$$

Through (A.3) and (A.2), the data rate of a UE depends on distance r from the center of the coverage area. Because of the inverse relationship between γ_{r} and r, the data rate of any UE is lower bounded by the data rate of the edge UE. That is,

$$R(r) \geq R(\overline{r}) = R(h_{\mathrm{A}}), \qquad \forall r \ \leq \ \overline{r}. \tag{A.4}$$

Since maximizing $R(r)$ is equivalent to maximizing $R(\overline{r})$ and for ease of explanation, we consider the sum of minimum rate, $R(\overline{r})$, in the definition of the GEE of the considered ACS in Section 3. The algorithm developed in Section 4 applies to the maximization of GEE defined in terms of the sum of actual rate $R(r)$.

3 Global Energy Efficiency of the ACS

The global energy efficiency of the considered ACS is given by

$$\mathrm{GEE[bits/Joule.Hz]} = \frac{\overline{R}(h_{\mathrm{A}})[\mathrm{bits/Hz}]}{E(h_{\mathrm{A}},T)[\mathrm{Joule}]}, \tag{A.5}$$

where $\overline{R}(h_{\mathrm{A}})$ is the sum of the minimum number of data bits transmitted per Hz from the AAP to the N UEs in T seconds; $E(h_{\mathrm{A}},T) = E_{\mathrm{A}}(h_{\mathrm{A}},T)+E_{\mathrm{C}}(T)$ is the total energy consumed by the AAP, in which $E_{\mathrm{C}}(T)$ is the energy required for data communication and $E_{\mathrm{A}}(h_{\mathrm{A}},T)$ given by (A.12), is the total energy consumed by the mechanical parts of the aerial vehicle during vertical climb and hovering. We consider a climb-hover communicate scheme in which the AAP climbs at a specific altitude and then communicates with N UEs while hovering.

3.1 Sum of the Minimum Number of Data Bits Transmitted, $\overline{R}(h_{\mathrm{A}})$

Considering the uniform distribution of UEs over A_{ue}, the sum of the minimum number of data bits transmitted per Hz from the AAP to the N UEs in T seconds through

orthogonal channels of bandwidth W Hz is expressed as

$$\overline{R}(h_{\mathrm{A}}) = T \int_0^{2\pi} \int_0^{\bar{r}} \rho_{\mathrm{ue}} R(\overline{r}) r dr d\theta, \tag{A.6}$$

$$= T\rho_{\mathrm{ue}}\pi h_{\mathrm{A}}^2 \mathrm{cot}^2\phi \mathrm{log}_2\left(1 + \frac{P_{\mathrm{T}} h_0}{N(\overline{r}^2 + h_{\mathrm{A}}^2)\sigma^2}\right), \tag{A.7}$$

$$= T\rho_{\mathrm{ue}}\pi h_{\mathrm{A}}^2 \mathrm{cot}^2\phi \mathrm{log}_2\left(1 + \frac{\beta}{h_{\mathrm{A}}^4}\right), \tag{A.8}$$

where $\beta = \dfrac{P_{\mathrm{T}} h_0 \mathrm{sin}^2\phi}{\pi\rho_{\mathrm{ue}}\mathrm{cot}^2\phi\sigma^2}$.

3.2 Aerial Vehicle Energy Consumption

The total energy consumed by an aerial vehicle ($E(h_{\mathrm{A}}, T)$) is composed of three main parts:

1. Energy required for data communication ($E_{\mathrm{C}}(T)$);
2. Energy consumed by the rotor of the aerial vehicle during climbing from ground to an altitude of h_{A} ($E_{\mathrm{cl}}(h_{\mathrm{A}})$);
3. Energy consumed by rotor during hovering at altitude h_{A} ($E_{\mathrm{ho}}(h_{\mathrm{A}}, T)$).

The energy required for data communication is given by

$$E_{\mathrm{C}}(T) = (P_{\mathrm{T}} + P_{\mathrm{H}})T, \tag{A.9}$$

where P_{T} is the total power used for the symbol transmission and P_{H}, is the total power consumption by all the hardware circuits in the transmitter section of the AAP. The energy parts $E_{\mathrm{cl}}(h_{\mathrm{A}})$ and $E_{\mathrm{ho}}(h_{\mathrm{A}}, T)$ follow the energy consumption model presented by the authors of [18]. In [18], the authors presented different power/energy consumption factors based on the field experiments performed on the Intel Aero Ready to Fly Drone. Unlike fixed and rotary-wing unmanned aerial vehicles [13], [14], the energy consumed by the rotor of a quadropter/drone during hovering is dependent on the hovering altitude [18], [16]. According to [18], the energy consumed by the quadropter during climbing from the ground to an altitude of h_{A} with a constant climb rate is given by

$$E_{\mathrm{cl}}(h_{\mathrm{A}}) = \alpha_{\mathrm{cl}} h_{\mathrm{A}} + \beta_{\mathrm{cl}}, \tag{A.10}$$

and the energy consumed during hovering at an altitude h_{A} for T seconds is given by

$$E_{\mathrm{ho}}(h_{\mathrm{A}}, T) = (\alpha_{\mathrm{ho}} h_{\mathrm{A}} + \beta_{\mathrm{ho}})T, \tag{A.11}$$

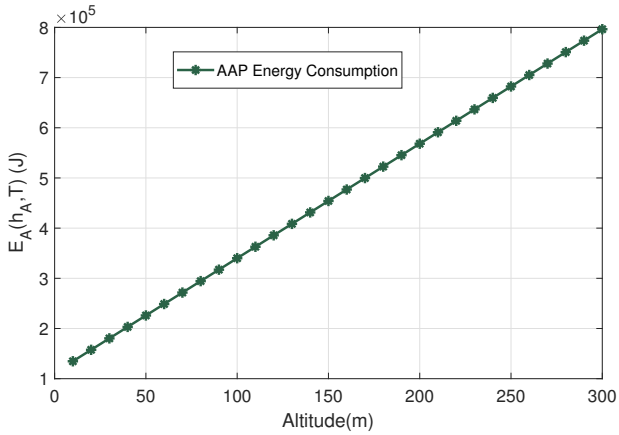

Fig. A.2: Total energy consumed by the rotor of the aerial vehicle.

where the constants $\alpha_{\text{cl}}, \beta_{\text{cl}}, \alpha_{\text{ho}}, \beta_{\text{ho}}$ are determined from the curve fitting performed on the measured power/energy values from the field experiments.

Hence the total energy consumed by the rotor of the AAP to climb to an altitude of h_{A} m and hover for T seconds is given by

$$E_{\text{A}}(h_{\text{A}}, T) = E_{\text{cl}}(h_{\text{A}}) + E_{\text{ho}}(h_{\text{A}}, T). \tag{A.12}$$

Fig. A.2 shows the increasing nature of $E_{\text{A}}(h_{\text{A}}, T)$ with altitude for a fixed time of operation with constants $\alpha_{\text{cl}=315,\beta_{cl}} = -211.261, \alpha_{\text{ho}=4.917,\beta_{ho}} = 275.204$ [18] and $T = 400s$. It is because as the altitude increases, the air temperature and pressure decreases. The decrease in the air pressure reduces the upward thrust provided by the air, to balance the downward force produced by the weight of the aerial vehicle. Hence, at higher hovering altitudes, to balance the weight, the propeller of the aerial vehicle needs to generate an additional force, which results in increased energy consumption.

Hence the total energy consumed by the AAP is given by

$$E(h_{\text{A}}, T) = E_{\text{cl}}(h_{\text{A}}) + E_{\text{ho}}(h_{\text{A}}, T) + E_{\text{C}}(T). \tag{A.13}$$

4 Problem Formulation

Our objective is to find the optimum altitude for the AAP, which maximizes the system's global energy efficiency (GEE) subject to minimum data rate and altitude constraints. By using (A.5),(A.8) and (A.13), our main objective is formulated as an optimization

problem and is expressed as follows:

$$\text{(A:P1)} : \underset{h_{\mathrm{A}}}{\text{maximize}} \quad \frac{\overline{R}(h_{\mathrm{A}})}{E(h_{\mathrm{A}}, T)},$$

$$\text{s.t.} \quad h_{\min} \leq h_{\mathrm{A}} \leq h_{\max}, \tag{A.14}$$

$$W \log_2 \left(1 + \frac{\beta}{h_{\mathrm{A}}^2(\bar{r}^2 + h_{\mathrm{A}}^2)}\right) \geq R_0, \tag{A.15}$$

where (A.14) represents the permitted AAP altitude range specified by the aviation regulatory board and R_0 is the minimum data rate required by the UE in bits-per-second (bps).

The objective function of (A:P1) belongs to the class of fractional programming problems [19]. It can be globally solved using Dinkelbach's algorithm [20], provided $\overline{R}(h_{\mathrm{A}})$ is concave, and $E(h_{\mathrm{A}}, T)$, (A.14), (A.15) are convex functions of h_{A}. From (A.13), (A.14), we find that the denominator of the objective function and AAP altitude constraint are a convex function of h_{A} while the numerator $\overline{R}(h_{\mathrm{A}})$ in (A.8), is neither convex nor concave in nature. Also, the minimum individual data rate constraint (A.15) is non-convex in nature. Hence (A:P1) cannot be globally solved with polynomial time complexity. As a means to obtain an efficient solution that fulfills the Karush Kuhn Tucker (KKT) conditions of (A:P1), we use the polynomial-time complex sequential convex programming (SCP) technique [21]. Besides, to obtain the global optimum of (A:P1), we exploit the monotonic structure of the objective function in the general framework of monotonic fractional programming (MFP) optimization [22] [23].

4.1 GEE Maximization Using SCP

In this part, we find the optimal altitude of the AAP, which maximizes the GEE of the ACS using sequential convex programming. The fundamental idea of SCP is to iteratively solve a sequence of convex approximated problems of the original non-convex problem so that the feasible solution points converge to the KKT point of the original non-convex problem [21]. Here we approximate the non-concave numerator, $\overline{R}(h_{\mathrm{A}})$ of (A:P1) as a concave function using a first-order Taylor approximation technique.

For the k^{th} iteration, let h_k be the feasible solution from the previous iteration. Then the first order Taylor approximation of $\overline{R}(h_{\mathrm{A}})$ about h_k is

$$\overline{R}(h_{\mathrm{A}}) \approx \overline{R}(h_k) + \overline{R}'(h_k)(h_{\mathrm{A}} - h_k), \tag{A.16}$$

where

$$\overline{R}'(h_k) = T\rho_{\mathrm{ue}}\pi\cot^2\phi 2h_k \log_2\left(1 + \frac{\beta}{h_k^4}\right) - T\rho_{\mathrm{ue}}\pi\cot^2\phi \frac{4\beta h_k}{\log_e(2)\left(\beta + {h_k}^4\right)}. \tag{A.17}$$

Similarly, the non-convex nature of (A.15) is tackled with the following Taylor approximation:

$$W\log_2\left(1+\frac{\beta}{h_k^4}\right)-\frac{4W\beta(h_{\mathrm{A}}-h_k)}{h_k(\beta+h_k^4)\log_e 2}\geq R_0. \tag{A.18}$$

Using (A.16) and (A.18), (A:P1) can be reformulated as

$$\begin{aligned}\text{(A:P2)}: \underset{h_{\mathrm{A}}}{\text{maximize}} \quad & \frac{\overline{R}(h_k)+\overline{R}'(h_k)(h_{\mathrm{A}}-h_k)}{E(h_{\mathrm{A}},T)},\\ \text{s.t.} \quad & \text{(A.14)}, \text{(A.18)}.\end{aligned} \tag{A.19}$$

Algorithm A.1: GEE Maximization using SCP.

1 Initialize h_1, $l_1^s=\dfrac{S(h_1,h_1)}{E(h_1,T)}$, $k=1$;
2 **while** (1) **do**
3 $\quad h_{\mathrm{opt}}^s=h_k$;
4 $\quad$ Determine the optimal solution h_k^{s*} by solving

$$\underset{h_{\mathrm{A}}}{\text{maximize}} \quad S(h_{\mathrm{A}},h_k)-l_k^sE(h_{\mathrm{A}},T)$$
$$s.t \quad \text{(A.14)}, \text{(A.18)};$$

5 $\quad l_{k+1}^s=\dfrac{S(h_k^{s*},h_k)}{E(h_k^{s*},T)}$;
6 $\quad$ **if** $((l_{k+1}^s-l_k^s)/l_{k+1}^s)<\zeta$ **then**
7 $\quad\quad$ break;
8 $\quad h_{k+1}=h_k^{s*}$;
9 $\quad k=k+1$;
10 **Output**: Optimal AAP Altitude= h_{opt}^s.

Note that (A:P2) is a single ratio fractional maximization problem with a concave numerator $S(h_{\mathrm{A}},h_k)=\overline{R}(h_k)+\overline{R}'(h_k)(h_{\mathrm{A}}-h_k)$, convex denominator $E(h_{\mathrm{A}},T)=E_{\mathrm{A}}(h_{\mathrm{A}},T)+E_{\mathrm{C}}(T)$ and convex constraints. Therefore (A:P2) can be efficiently solved by using polynomial time complex Algorithm A.1. In every iteration of Algorithm A.1, the optimal solution in step 4 is determined by using standard convex optimization tools like CVX [24]. In Section 5, we show that the efficient solution of (A:P1) obtained by solving (A:P2) through Algorithm A.1 matches the global optimum obtained using the monotonic fractional program optimization technique.

4.2 GEE Maximization Using MFP

Algorithm A.2: GEE Maximization using MFP.

1 Initialize h_1, $l_1^m = \dfrac{\overline{R}(h_1)}{E(h_1, T)}$, $k = 1$.
2 **while** (1) **do**
3 $\quad h_{\text{opt}}^m = h_k$
4 $\quad$ Determine the optimal solution h_k^{m*} by solving the monotonic optimization problem (A:P6) using Algorithm A.3
5 $\quad l_{k+1}^m = \dfrac{\overline{R}(h_k^{m*})}{E(h_k^{m*}, T)}$
6 $\quad$ **if** $((l_{k+1}^m - l_k^m)/l_{k+1}^m) < \zeta$ **then**
7 $\quad\quad$ break;
8 $\quad h_{k+1} = h_k^{m*}$
9 $\quad k = k + 1$
10 **Output**: Optimal AAP Altitude= h_{opt}^m

The candidate solution obtained from SCP cannot be considered as the global optimum of (A:P1). Therefore, to obtain the global optimum of (A:P1), we exploit the monotonic behavior of the objective function using the monotonic fractional programming technique [22] [23]. The key idea is that the global optimum of an increasing objective function of a maximization problem lies in the outer boundary of the feasible set formed by the constraints. Following the fundamental definitions from [23], a maximization problem takes the canonical form of a monotonic optimization problem, if it can be formulated as

$$\begin{aligned} \text{(A:P3)} : \underset{\mathbf{v}}{\text{maximize}} \quad & f(\mathbf{v}), \\ \text{s.t.} \quad & \mathbf{v} \in \mathcal{G} \cap \mathcal{H}, \end{aligned}$$

where $f : \mathbb{R}^M \to \mathbb{R}$ is an increasing function of $\mathbf{v}$, $\mathcal{G} \subset [\mathbf{0}, \mathbf{a}]$ is a compact normal set with nonempty interior, and $\mathcal{H}$ is a closed conormal set on $[\mathbf{0}, \mathbf{a}]$. For exact definitions of monotonicity, normal and co-normal sets please refer to [23].

The optimization problem (A:P1) fits in the class of fractional problems, which can be globally solved by Algorithm A.2. For a given positive l_k^m, in every k^{th} iteration of Algorithm A.2, we need to solve the following maximization problem in step 4:

$$\text{(A:P4)} : \underset{h_{\text{A}}}{\text{maximize}} \quad \overline{R}(h_{\text{A}}) - l_k^m \left\{ E_{\text{A}}(h_{\text{A}}, T) + E_{\text{C}}(T) \right\}, \tag{A.20}$$

$$\text{s.t.} \quad \text{(A.14)} - \text{(A.15)}. \tag{A.21}$$

It should be noted that, at first look, (A:P4) doesn't take the canonical form of monotonic optimization problem defined in (A:P3). However, (A:P4) can be expressed as the maximization of differences of increasing functions of h_{A}, which allows us to reformulate (A:P4) as a monotonic optimization problem. For the ease of reformulation, we equivalently represent the minimum individual data rate constraint as

$$h_{\max} = \left[\frac{\beta}{2^{\frac{R_0}{W}} - 1} \right]^{1/4}. \tag{A.22}$$

Note that (A.20) can be rewritten as

$$\text{(A:P5)} : \underset{h_{\mathrm{A}}}{\text{maximize}} \;\; \overline{R}_1(h_{\mathrm{A}}) - \overline{R}_2(h_{\mathrm{A}}, l_k^m), \tag{A.23}$$

$$\text{s.t.} \quad \text{(A.14)}, \tag{A.24}$$

where

$$\begin{aligned} \overline{R}_1(h_{\mathrm{A}}) &= T\rho_{\mathrm{ue}}\pi\cot^2\phi h_{\mathrm{A}}^2 \log_2\left(\beta + h_{\mathrm{A}}^4\right), \\ \overline{R}_2(h_{\mathrm{A}}, l_k^m) &= T\rho_{\mathrm{ue}}\pi\cot^2\phi h_{\mathrm{A}}^2 \log_2\left(h_{\mathrm{A}}^4\right) + l_k^m(E(h_{\mathrm{A}}, T)), \end{aligned} \tag{A.25}$$

are monotonically increasing functions of h_{A}, and $h_{\max}$ of (A.14) is given by (A.22). In order to write (A:P5) in canonical form, we introduce the additional variable $t = \overline{R}_2(h_{\max}, l_k^m) - \overline{R}_2(h_{\mathrm{A}}, l_k^m)$, which allows (A:P5) to be reformulated as

$$\text{(A:P6)} : \underset{h_{\mathrm{A}}, t}{\text{maximize}} \;\; \overline{R}_1(h_{\mathrm{A}}) + t, \tag{A.26}$$

$$\text{s.t.} \quad (h_{\mathrm{A}}, t) \in \mathcal{G} \cap \mathcal{H}, \tag{A.27}$$

where

$$\mathcal{G} = \left\{ \begin{matrix} (h_{\mathrm{A}}, t) : h_{\mathrm{A}} \le h_{\max}, \\ t \le \overline{R}_2(h_{\max}, l_k^m) - \overline{R}_2(h_{\mathrm{A}}, l_k^m), \end{matrix} \right\} \tag{A.28}$$

$$\mathcal{H} = \left\{ (h_{\mathrm{A}}, t) : h_{\mathrm{A}} \ge h_{\min}, t \ge 0 \right\}. \tag{A.29}$$

By the monotonically increasing behavior of $\overline{R}_2(h_{\mathrm{A}}, l_k^m)$ we can relate

$$\overline{R}_2(h_{\min}, l_k^m) \le \overline{R}_2(h_{\mathrm{A}}, l_k^m). \tag{A.30}$$

By [Proposition 2, [22]], (A.28) defines a normal set and (A.29) defines a co-normal set in the polyblock

$$[h_{\min}, h_{\max}] \times \left[0, \overline{R}_2(h_{\max}, l_k^m) - \overline{R}_2(h_{\min}, l_k^m)\right], \tag{A.31}$$

with the vertex set $\mathcal{V}$. Hence by using (A.26)-(A.29) we represent (A:P4) in the canonical form of monotonic optimization problem with $f(\mathbf{v}) = \overline{R}_1(\mathbf{v}(1))+\mathbf{v}(2)$, $\forall \mathbf{v} \in \mathcal{V}$, which can be globally solved by using the polyblock outer approximation algorithm as explained in Algorithm A.3 [23]. Even though the complexity of this global optimization algorithm is exponential in the number of variables, it is much lower compared to other global optimization techniques, which exhaustively search over the entire feasible set. Hence the globally optimal AAP altitude is obtained by solving (A:P1) using Algorithm A.2 in which, at each iteration, step 4 is solved by using Algorithm A.3.

Algorithm A.3: PA Algorithm [25].

1 Initialize $i = 1$, $\mathcal{V}_i$ as the vertexset of polyblock (A.31)
2 Set $\mathbf{v}_{\min} = \text{argmin}\{f(\mathbf{v}) \mid \mathbf{v} \in \mathcal{V}_i\}$
3 Set $\mathbf{v}_{\max} = \text{argmax}\{f(\mathbf{v}) \mid \mathbf{v} \in \mathcal{V}_i\}$
4 Set $f_{\max} = \max_{\mathbf{v}\in\mathcal{V}_i} f(\mathbf{v})$ and $f_{\min} = f(\mathbf{v}_{\min})$
5 **while** $[(f_{\max} - f_{\min})/f_{\max} > e]$ **do**
6 Obtain $\mathbf{v}_o$, the intersecting point of the line drawn from $\mathbf{v}_{\min}$ to $\mathbf{v}_{\max}$ with the normal region $\mathcal{G}$ using bisection method [Algorithm 1 [25]]
7 Update the vertex set, $\mathcal{V}_{i+1}$ according to Lemma 2.16 of [25]
8 **if** $f(\mathbf{v}_o) > f_{\min}$ **then**
9 $f_{\min} = f(\mathbf{v}_o)$
10 $\mathbf{v}_{\min} = \mathbf{v}_o$
11 set $i = i + 1$
12 remove all $\mathbf{v} \in \mathcal{V}_i$ with $f(\mathbf{v}) \leq f_{\min} + e$
13 Set $f_{\max} = \max_{\mathbf{v}\in\mathcal{V}_i} f(\mathbf{v})$
14 **Output**: $h_k^{m*} = \mathbf{v}_o(1)$.

5 Numerical Evaluation

In this section, we compare the optimal altitude values obtained through SCP and MFP optimization techniques. Furthermore, the convergence behavior of the PA algorithm; the impact of aerial vehicle's energy consumption on GEE; the variation of GEE with minimum data rate requirement are discussed. We consider $h_0 = 1.42 \times 10^{-4}$, $P_{\mathrm{T}} = 10$ dBm, $W = 20$MHz, $\sigma_0^2 = -169$dBm/Hz , $\phi = 43°$, $\rho = 0.005$UEs/m^2, $P_{\mathrm{H}} = 5$W, $T = 400$s, $R_o = 20$Mbps and $h_{\min} = 10$m.

Fig. A.3 shows the accurate plot of GEE with the altitude of aerial vehicle, h_{A}, along with the optimal points obtained through SCP and MFP techniques. From the plot, it is observed that GEE decreases when h_{A} is very low or very high. The reason for this behavior is that, at low h_{A}, the number of UEs covered ($N = \rho_{\mathrm{ue}}\pi h_{\mathrm{A}}^2 \cot^2\phi$) by

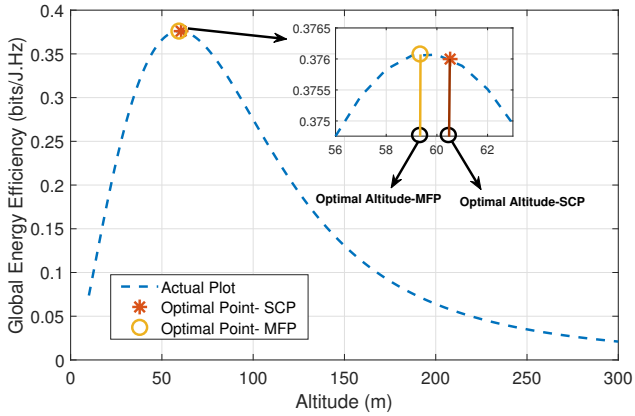

Fig. A.3: Optimal solutions obtained from SCP and MFP.

the AAP decreases with decreasing h_{A}, leading to a decrease in the total number of bits transmitted, thereby to reduced GEE. At high altitude regions, the LoS channel gain between the UE and AAP decreases, the number of UEs covered by AAP increases, and $E(h_{\mathrm{A}}, T)$ increases. In addition to this, with an increase in the number of users, power alloted for a single UE decreases. So in the high altitude region, the increase in the number of UEs is highly compensated by the combined effect of the decrease in channel gain, decrease in power per UE and increase in $E(h_{\mathrm{A}}, T)$, which result in a low GEE. Fig. A.3 also shows that the optimal AAP altitude obtained by the SCP is very close to the globally optimal altitude obtained from the monotonic fractional programming technique. Hence the global optimum of our objective can be obtained by the polynomial-time complex sequential convex optimization technique.

Fig. A.4 shows the convergence behavior of the PA algorithm in the last iteration of MFP. The converging nature of upper($f_{\max}$) and lower($f_{\min}$) bounds of the PA algorithm guarantees the evaluation of the global optimum of GEE in a finite number of convex evaluations; with the number of convex evaluations much greater than that required by SCP. The optimal altitude plots of MFP and SCP says that the locally optimal altitude value obtained using SCP is equal to the globally optimal altitude obtained using MFP. In addition to this, Fig. A.4 shows the error in determining the optimal altitude without considering the rotor energy consumption, $E_{\mathrm{A}}(h_{\mathrm{A}}, T)$. It is observed that the optimal altitude determined with $E_{\mathrm{A}}(h_{\mathrm{A}}, T) = 0$, is 18.23m higher than the actual optimal altitude value. Hence, according to Fig. A.3, hovering at an altitude higher than the actual optimal value yields low GEE. Therefore, to achieve the maximum GEE value, the rotor energy consumption of the aerial vehicle should be considered while formulating the optimization problem.

Fig. A.5 depicts the variation of GEE with the minimum data rate requirement. The two GEE plots correspond to the variation of GEE with R_o when the aerial vehicle

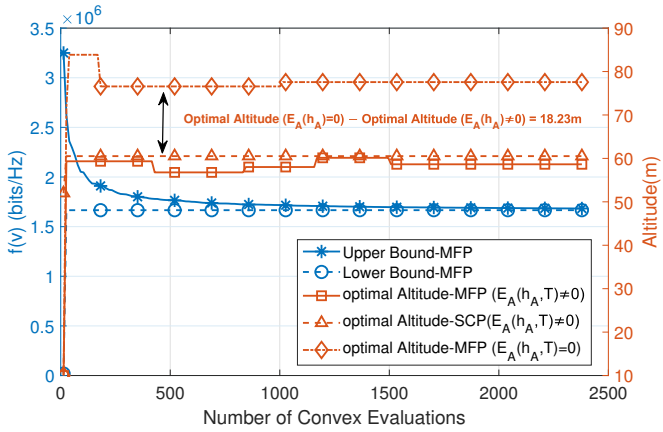

Fig. A.4: Convergence behavior of the PA algorithm.

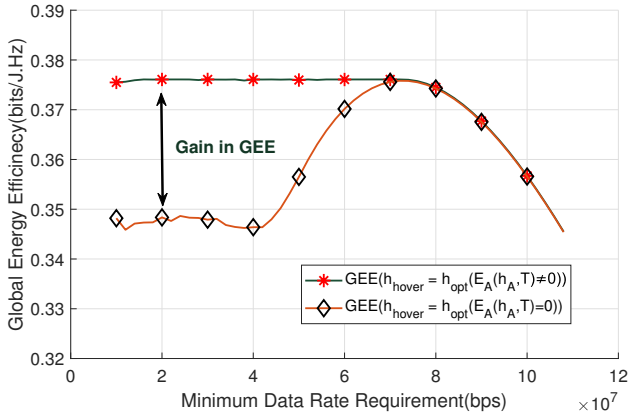

Fig. A.5: Global energy efficiency versus minimum individual data rate requirement.

is hovering at the optimal altitude obtained: (a) with zero energy consumed by the rotor of the aerial vehicle($h_{\text{hover}} = h_{\text{opt}}(E_{\text{A}}(h_{\text{A}}, T) = 0)$); (b) with non-zero energy consumed by the rotor of the aerial vehicle ($h_{\text{hover}} = h_{\text{opt}}(E_{\text{A}}(h_{\text{A}}, T) \neq 0)$). As said before, the GEE of the ACS with $h_{\text{hover}} = h_{\text{opt}}(E_{\text{A}}(h_{\text{A}}, T) \neq 0)$ is more than that with $h_{\text{hover}} = h_{\text{opt}}(E_{\text{A}}(h_{\text{A}}, T) = 0)$. This gain in GEE reflects the effect of considering the aerial vehicle's rotor energy consumption in altitude optimization, showcasing the novel aspect of this paper. In the plot, the value of GEE is constant for a range of R_o and then it starts decreasing with an increase in R_o. From (A.22), the value of the maximum allowed altitude, $h_{\max}$ decreases with increase in R_o. It is because a higher minimum individual data rate is achieved by increasing the LoS channel gain obtained by decreasing the hovering altitude of the aerial vehicle. When $h_{\max}(R_o)$ is greater than the h_{A} corresponding to the global optimum of GEE ($\text{GEE}_{\text{global}}$), the optimal altitude is equal to $h_{\text{A}}(\text{GEE}_{\text{global}})$ and GEE remains constant; for $h_{\max}(R_o) \leq h_{\text{A}}(\text{GEE}_{\text{global}})$, optimal altitude is equal to $h_{\max}$, results in decrease in GEE with increase in R_o. The decrease in GEE with increase in R_o(decrease in $h_{\max}$) shows the monotonically increasing property of GEE which is exploited in MFP.

6 Conclusion

In this work, we found the optimal energy-efficient altitude of an aerial access point which acts as a flying base station for an orthogonal multiple access downlink broadcast transmission scenario. The modeled energy consumption is the sum of energy consumed by the aerial vehicle and the energy required for the communication between the AAP and the UEs. An efficient solution to the formulated GEE maximization problem with individual data rate constraint and altitude constraint is obtained using sequential convex programming and is compared to the global optimum achieved by the monotonic fractional programming technique. One can see that the optimal altitude value from the polynomial-time complex SCP matches the globally optimal altitude value obtained from the monotonic fractional programming. Further, we observed that there is a gain in the GEE when the aerial access point is hovering at an optimal altitude determined by considering the non-zero rotor energy consumption of the aerial vehicle. In addition to this, the optimal altitude, and hence GEE, decrease with an increase in the minimum individual data rate constraint. Joint altitude and power optimization in a non-orthogonal multiple access transmission scheme with multiple AAPs is left as our future work.

References

[1] M. Erdelj and E. Natalizio, "UAV-Assisted Disaster Management: Applications and Open Issues," in *International Conference on Computing, Networking and Commu-*

nications (ICNC), Feb 2016, pp. 1–5.

[2] "National institute of Information and Communication Technology, Japan, Development of UAV wireless communication systems in NICT," *13th Broadsky Workshop, Japan,* 2015.

[3] A. Fotouhi, H. Qiang, M. Ding, M. Hassan, L. G. Giordano, A. Garcia-Rodriguez, and J. Yuan, "Survey on UAV Cellular Communications: Practical Aspects, Standardization Advancements, Regulation, and Security Challenges," *IEEE Communications Surveys Tutorials,* pp. 3417-3442, 2019.

[4] N. H. Motlagh, M. Bagaa, and T. Taleb, "UAV-Based IoT Platform: A Crowd Surveillance Use Case," *IEEE Communications Magazine,* vol. 55, no. 2, pp. 128–134, February 2017.

[5] Y. Zeng, R. Zhang, and T. J. Lim, "Wireless Communications with Unmanned Aerial Vehicles: Opportunities and Challenges," *IEEE Communications Magazine,* vol. 54, no. 5, pp. 36–42, May 2016.

[6] A. Al-Hourani, S. Kandeepan, and S. Lardner, "Optimal LAP Altitude for Maximum Coverage," *IEEE Wireless Communications Letters,* vol. 3, no. 6, pp. 569–572, Dec 2014.

[7] H. He, S. Zhang, Y. Zeng, and R. Zhang, "Joint Altitude and Beamwidth Optimization for UAV-Enabled Multiuser Communications," *IEEE Communications Letters,* vol. 22, no. 2, pp. 344–347, Feb 2018.

[8] E. Kalantari, H. Yanikomeroglu, and A. Yongacoglu, "On the Number and 3D Placement of Drone Base Stations in Wireless Cellular Networks," in *IEEE 84th Vehicular Technology Conference (VTC-Fall), IEEE,* pp. 1–6, 2016.

[9] J. Lyu, Y. Zeng, R. Zhang, and T. J. Lim, "Placement Optimization of UAV-Mounted Mobile Base Stations," *IEEE Communications Letters,* vol. 21, no. 3, pp. 604–607, 2016.

[10] M. Alzenad, A. El-Keyi, F. Lagum, and H. Yanikomeroglu, "3-D Placement of an Unmanned Aerial Vehicle Base Station (UAV-BS) for Energy Efficient Maximal Coverage," *IEEE Wireless Communications Letters,* vol. 6, no. 4, pp. 434–437, 2017.

[11] M. Mozaffari, W. Saad, M. Bennis, and M. Debbah, "Drone Small Cells in the Clouds: Design, Deployment and Performance Analysis," in *IEEE Global Communications Conference (GLOBECOM), IEEE,* pp. 1–6, 2015.

[12] S. Eom, H. Lee, J. Park, and I. Lee, "UAV-Aided Wireless Communication Designs with Propulsion Energy Limitations," *IEEE Transactions on Vehicular Technology,* 69.1: 651-662, 2019.

[13] Y. Zeng, J. Xu, and R. Zhang, "Energy Minimization for Wireless Communication with Rotary-Wing UAV," *IEEE Transactions on Wireless Communications,* vol. 18, no. 4, pp. 2329–2345, April 2019.

[14] Y. Zeng and R. Zhang, "Energy-Efficient UAV Communication with Trajectory Optimization," *IEEE Transactions on Wireless Communications,* vol. 16, no. 6, pp. 3747–3760, June 2017.

[15] M. Mozaffari, W. Saad, M. Bennis, and M. Debbah, "Mobile Unmanned Aerial Vehicles (UAVs) for Energy-Efficient Internet-of-Things Communications," *IEEE Transactions on Wireless Communications,* vol. 16, no. 11, pp. 7574–7589, Nov 2017.

[16] D. Zorbas, L. Di Puglia Pugliese, T. Razafindralambo, and F. Guerriero, "Optimal Drone Placement and Cost-Efficient Target Coverage," *Journal of Network and Computer Applications,* vol. 75, no. C, pp. 16–31, 2016.

[17] A. Goldsmith, Wireless communications. Cambridge university press, 2005.

[18] H. V. Abeywickrama, B. A. Jayawickrama, Y. He, and E. Dutkiewicz, "Comprehensive Energy Consumption Model for Unmanned Aerial Vehicles, Based on Empirical Studies of Battery Performance," *IEEE Access,* vol. 6, pp. 58 383–58 394, 2018.

[19] A. Zappone and E. Jorswieck, "Energy Efficiency in Wireless Networks via Fractional Programming Theory," *Foundations and Trends® in Communications and Information Theory*, 11.3-4, 185-396, 2015.

[20] J.-P. Crouzeix and J. A. Ferland, "Algorithms for Generalized Fractional Programming," *Mathematical Programming* 52.1 (1991): 191-207.

[21] B. R. Marks and G. P. Wright, "A General Inner Approximation Algorithm for Nonconvex Mathematical Programs," *Operations Research* 26.4 (1978): 681-683.

[22] A. Zappone, E. Björnson, L. Sanguinetti, and E. Jorswieck, "Globally Optimal Energy-Efficient Power Control and Receiver Design in Wireless Networks," *IEEE Transactions on Signal Processing,* vol. 65, no. 11, pp. 2844–2859, June 2017.

[23] Y. J. A. Zhang, L. Qian, and J. Huang, "Monotonic Optimization in Communication and Networking Systems," *Foundations and Trends® in Networking,* 7.1: 1-75, 2013.

[24] M. Grant and S. Boyd, "CVX: Matlab Software for Disciplined Convex Programming," version 2.1." (2014).

[25] E. Björnson, E. Jorswieck et al., "Optimal Resource Allocation in Coordinated Multi-Cell Systems," *Foundations and Trends® in Communications and Information Theory,* vol. 9, no. 2–3, pp. 113–381, 2013.

Paper B

Energy-Efficient Deployment of a Non-Orthogonal Multiple Access Unmanned Aerial System

Nithin Babu, Constantinos B. Papadias, and Petar Popovski

Published in
IEEE International Conference on Communications Workshops (ICCWorkshops), pp. 1-6, 2021, doi: 10.1109/ICCWorkshops50388.2021.9473727.

The layout has been revised.

Abstract

In this work, we propose a methodology for the energy-efficient placement of an unmanned aerial system (UAS) deployed to collect data from a set of ground user equipments (UEs). The data-communication between the UEs and the UxNB, a radio access node carried by an unmanned aerial vehicle (UAV), of the UAS follows a non-orthogonal multiple-access (NOMA) scheme; in which all the UEs share the same time and frequency resources. The receiver removes the inter-UE interference from the co-channel UEs through joint implementation of a power-reduction technique at the UEs and the successive interference cancellation (SIC) at the receiver. Firstly, a new energy-efficiency metric, area energy efficiency (AEE) representing the total area covered by a UxNB per Watt-Hour (Wh) of energy consumed, is introduced. Then, the optimal hovering altitude of the UxNB that maximizes the AEE is determined using the proposed algorithm. Numerical evaluations show that the obtained solution using the proposed algorithm matches the globally optimal solution, and the proposed NOMA scheme prevails over an equivalent orthogonal multiple access (OMA) scheme, in terms of the AEE.

1 Introduction

Next-generation wireless networks are expected to support high data rates and a larger number of user devices [1]. Standardization bodies like the 3rd generation partnership project (3GPP) has been considering meeting these demands with non-orthogonal multiple access (NOMA) schemes [2]. The NOMA scheme supports users by differentiating them in power or space domains, thereby allowing them to share the same time and frequency resources. The NOMA scheme that separates the users in the power domain, called power-domain NOMA (P-NOMA), requires a successive interference cancellation (SIC) receiver [4]. The SIC receiver exploits the diversity in the received signal-to-interference-plus-noise ratio (SINR) from the user equipments (UEs): the message from the strongest UE (highest received SINR) is decoded treating all the other UE's messages as noise; then, the message from the second-strongest UE is decoded after subtracting the strongest UE's message from the received signal. This continues until the SIC receiver decodes the message from the UE with the lowest received SINR value.

UAV-assisted networks deployed to provide cellular service for applications having temporary/emergency nature such as frequent data collection from a set of Internet-of-Things (IoT) nodes or assisting the rescue operation during a natural disaster, is considered as one of the promising application of the next-generation wireless networks [3]. Here, we consider such a UAV-assisted network in which the UAV carries a NOMA-based radio access node to the service-required area. The latest 3GPP report, [15], has enlisted various technical specifications of a UAV-assisted network.

The concept of a UAV-assisted NOMA system has been considered in the works [5]-

[14]. [4] presents a survey on the existing studies that have considered the integration of the P-NOMA scheme with the enabling communications schemes and technologies, which are expected to meet the various requirements of next-generation wireless networks. In [5], the authors study the P-NOMA scheme for the energy-efficient placement of a UAV- base station using the user-pairing method. The individual users in a pair will be using the same time and frequency resources; whereas, the resources allocated to two different user pairs will be orthogonal. The placement and power allocation that maximize the downlink sum rate of a NOMA-UAV network is proposed in [6]. The work in [7] maximizes the minimum downlink throughput of a UAV network by jointly optimizing multi-user communication scheduling and the UAV trajectory. The joint optimization problem is decoupled into two blocks (the scheduling and the UAV trajectory blocks) and is solved using the block coordinate descent method. The authors of [8], propose a solution to the max-min rate optimization problem of a UAV-enabled NOMA communication system. The optimization problem is formulated subject to total power, bandwidth, altitude, and beamwidth constraints, and is solved using the sequential convex programming technique. In [9], the authors present a joint UAV trajectory design and resource allocation algorithm that maximizes the minimum average rate among the ground users of a UAV communication system. The formulated max-min downlink data rate problem is solved using the penalty dual decomposition method. The work in [10] minimizes the transmit power of a UAV-NOMA system subject to the minimum achievable rate requirements; whereas, the sum rate a similar system is maximized in [11] by jointly optimizing the UAV trajectory and the NOMA precoding. The authors of [12] aim to maximize the system capacity of a UAV-NOMA system by jointly optimizing the subchannel assignment, the uplink transmit power, and the flying heights of the UAVs using the K-means clustering method and the matching theory. [13] considers a different application scenario in which a UAV system co-exists with a set of ground users; the authors maximize both the data rate from the UAV to the base stations and the data rate of the co-channel ground users to their associated base stations by optimizing the precoding vectors at the multi-antenna UAV. [14] discusses the possibility of using a UAV as a full-duplex relay to aid the communication between a base station and two NOMA users. Considering a simultaneous wireless information and power transfer technique, the authors aim at maximizing the sum throughput of the whole system and the harvested energy at the UAV based on the inner approximation method.

The works in [5]- [10] consider a downlink-NOMA communication between a single- or multi- UAV system and a set of ground users. Except [5], none of the above works maximize the energy-efficiency of a NOMA-UAV system considering both the communication and the UAV energy consumption. Additionally, the user-pairing method considered in [5] exploits only partial non-orthogonality (between two user pairs) to maximize the number of bits transmitted per Joule of energy consumed. However, [12] and [13] consider an uplink data transmission between a set of users and a UAV, but the energy-efficiency aspect remains unstudied in these works. Being an energy-limited system, we

believe that the energy-efficient placement of a UAS is of paramount importance. In our previous works, [18] and [19], we have considered the energy-efficient placement of a single- and multi-UAV system, respectively. [18] considers a downlink OMA scheme, whereas in [19], we consider an uplink OMA scheme with the universal frequency reuse among the UAVs. The placement optimization of a NOMA-UAS that maximizes the proposed area energy efficiency (AEE) metric considering both the communication and the UAV energy consumption has, to the best of our knowledge, not been considered in the literature.

Section 2 explains the system architecture and the assumptions alongside the definitions of the proposed AEE metric and the power-reduction scheme. Our objective here is to find an energy-efficient hovering altitude for the UxNB part of a UAS considering an uplink P-NOMA scheme. As the altitude increases, the area covered by the UxNB increases, the time taken by the ground users to complete the uplink data transmission increases, and the power consumed by the UAV increases. Intending to capture these effects, we introduce a new energy-efficiency metric in Section 2.3, the AEE. The AEE of a UAS is neither maximum at a low altitude value nor at a high altitude value. In Section 3, we determine the area energy-efficient hovering altitude for a NOMA-UAS. All our main findings from the numerical evaluations are discussed in Section 4.

2 System Model and Definitions

We consider a UxNB, a radio access node carried in the air by a UAV, deployed to collect independent data from a set of uniformly distributed ground UEs with a density ρ_u. The UxNB with the ground controller, as shown in Fig. B.1, forms the UAS model proposed in the latest 3GPP report [15]. The UxNB is assumed to be equipped with a directional antenna of half-power beamwidth 2θ with antenna gain in direction (ψ, ω) given by [20],

$$g_{\mathrm{u,a}} = \begin{cases} \dfrac{g_{\mathrm{o,a}}}{\theta^2} & -\theta \leq \psi \leq \theta, -\theta \leq \omega \leq \theta, \\ \approx 0 & \text{otherwise}, \end{cases} \tag{B.1}$$

where $g_{\mathrm{o,a}} \approx 2.2846$. All the UEs are equipped with an omnidirectional antenna. Also, the UEs send their collected data to the UxNB using the same time and frequency resources, but with different power levels, thereby forming an uplink P-NOMA scheme. The transmitted data packets are successfully decoded using the successive interference cancellation technique at the UxNB. In practice, this maps to the data-collection phase of an IoT network.

2.1 Propagation Channel

The ground-to-air channel between a UE and the UxNB falls either to the line-of-sight (LoS) or the non-LoS group depending on its relative position to the UxNB. The LoS

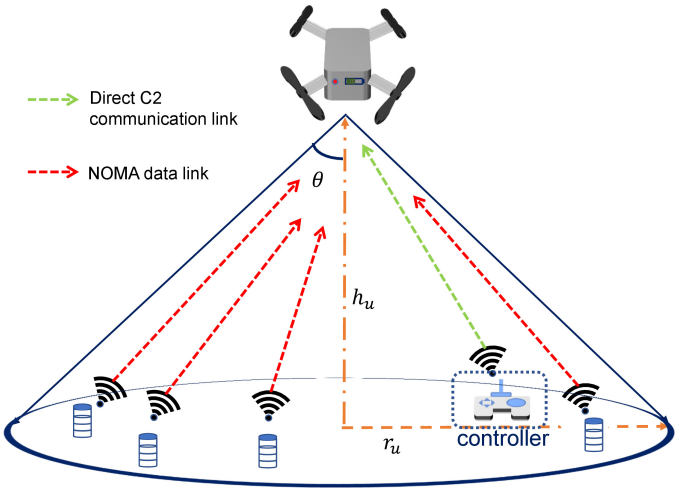

Fig. B.1: Unmanned Aerial System Architecture.

probability of a UE-UxNB channel link is expressed as [21],

$$P_1(\phi_i) = \frac{1}{\{1 + a\exp\left[-b(\phi_i - a)\right]\}}, \tag{B.2}$$

where $\phi_i = (180/\pi)\tan^{-1}(h_\mathrm{u}/r_i)$ is the elevation angle between the i^{th} UE located at a distance of r_i from the center of the UxNB's coverage area, and the UxNB hovering at an altitude h_u; a, b are the environment-dependent parameters that depend on the building profile of the deploying area. Hence, the probabilistic mean path loss is given by [19],

$$\overline{L}_i(h_\mathrm{u}) = P_1(\phi_i) \times L_{1,i} + P_2(\phi_i) \times L_{2,i}, \tag{B.3}$$

$$= \frac{(r_i^2 + h_\mathrm{u}^2)}{h_\mathrm{o}} \left\{P_1(\phi_i)\mu_1^2 + [1 - P_1(\phi_i)]\mu_2^2\right\}, \tag{B.4}$$

where, μ_1^2 and μ_2^2 are the mean values of the additional path loss due to the long-term random channel variations associated with the respective LoS and NLoS links; h_o is the channel gain at a reference distance of 1 m.

2.2 Uplink P-NOMA Scheme

The uplink power control mechanism in LTE systems require that the received powers from different UEs equal the same target power, p_u [22]. Hence, the power transmitted by a UE assuming full channel-loss compensation is given by,

$$p(h_\mathrm{u}) = p_\mathrm{u}\overline{L}_i(h_\mathrm{u}). \tag{B.5}$$

For successful decoding of the received messages in the presence of co-channel interference, the SIC receiver at the UxNB requires different received powers per UE. First of all, the UEs send individual control messages to the UxNB with the same transmit power using orthogonal control channels. The UxNB then assigns indices of the decoding order to the UEs based on the corresponding path loss values: a higher index value to a UE with a higher path loss value. That is, in an instance with N UEs in the coverage region of the UxNB, the closest UE to the center of the coverage region is assigned the index 1, whereas the farthest UE the index N. Next, the UxNB informs the UEs of their corresponding index of the decoding order through the associated control channels. Now, the UEs follow a power-reduction scheme for the concurrent transmission of the messages using the same frequency resource. Accordingly, the UE with the index of decoding order i transmits its message with a power given by [16],

$$p_i(h_{\mathrm{u}}) = \frac{p_{\mathrm{u}} \overline{L}_i(h_{\mathrm{u}})}{\delta^{i-1}}, \tag{B.6}$$

where, δ is the power-reduction factor. (B.6) guarantees the required power diversity at the SIC receiver of the UxNB unit. Consider the UxNB hovering at an altitude h_{u} covering $N(h_{\mathrm{u}}) = \rho_{\mathrm{u}} \pi h_{\mathrm{u}}^2 \tan^2\theta$ uniformly distributed UEs. Then, the received signal at the UxNB, from the UEs transmitting the messages with the P-NOMA scheme, is expressed as,

$$y_{\mathrm{u}} = \sum_{i=1}^{N(h_{\mathrm{u}})} \sqrt{\frac{p_i(h_{\mathrm{u}})}{\overline{L}_i(h_{\mathrm{u}})}} x_i + \sigma_{\mathrm{n}}^2, \tag{B.7}$$

where, x_i is the message transmitted by the i^{th} UE, and $\sigma_{\mathrm{n}}^2 = \sigma_0^2 W$ is the zero-mean additive white Gaussian noise power with a power spectral density σ_0^2 over a channel bandwidth W. Using the diverse received power from the UEs, the SIC receiver starts decoding the message from the first UE (the UE with the index 1) considering the messages from the remaining $(N(h_{\mathrm{u}}) - 1)$ UEs as co-channel interference. Correspondingly, the i^{th} UE's message is decoded only after decoding the prior $(i-1)$ UEs' messages; hence, the received SINR value from the i^{th} UE is given by,

$$\Gamma_i^{\mathrm{n}}(h_{\mathrm{u}}) = \frac{\frac{p_i(h_{\mathrm{u}})}{\overline{L}_i(h_{\mathrm{u}})}}{\sum_{j=i+1}^{N(h_{\mathrm{u}})} \frac{p_j(h_{\mathrm{u}})}{\overline{L}_j(h_{\mathrm{u}})} + \sigma_{\mathrm{n}}^2}. \tag{B.8}$$

(B.8) assumes successful decoding of the messages from the first to the $(i-1)^{\mathrm{th}}$ UE; an additional noise term in the denominator of $\Gamma_i^{\mathrm{n}}(h_{\mathrm{u}})$ represents the co-channel interference from the remaining $(N(h_{\mathrm{u}}) - i)$ UEs. In Section 3, we incorporate the above-mentioned condition as quality-of-service (QoS) constraints: $\Gamma_i^{\mathrm{n}}(h_{\mathrm{u}}) \geq \Gamma_{\mathrm{m}}\ \forall i \in \mathcal{N} = \{1, 2, ..., N(h_{\mathrm{u}})\}$; Γ_{m} is the minimum SINR required at the receiver for the successful decoding of the message from a UE. Therefore, the achievable data rate of the i^{th} UE in

bits-per-second (bps) assuming perfect channel modulation, coding scheme, and known channel state information (CSI) at the transmitter is given by (B.9):

$$R_i^{\mathrm{n}}(h_{\mathrm{u}}) = W \log_2 \left[1 + \Gamma_i^{\mathrm{n}}(h_{\mathrm{u}})\right] \ \forall i \in \mathcal{N}. \tag{B.9}$$

2.3 Area Energy Efficiency

We define the area energy-efficiency of a UAS as the ratio between the geographical area covered by the UAS, and the total energy consumption:

$$\mathrm{AEE}_{\mathrm{n}}(h_{\mathrm{u}}) \ [\mathrm{m}^2/\mathrm{Wh}] = \frac{\pi r_{\mathrm{u}}^2(h_{\mathrm{u}}) \, [\mathrm{m}^2]}{T_{\mathrm{u}} P_{\mathrm{t}}(h_{\mathrm{u}}) \kappa \, [\mathrm{Wh}]}, \tag{B.10}$$

where, $P_{\mathrm{t}}(h_{\mathrm{u}}) = P_{\mathrm{u}}(h_{\mathrm{u}}) + P_{\mathrm{c}}$ is the total power consumed by the UxNB in Watts with $P_{\mathrm{u}}(h_{\mathrm{u}}) = \alpha_{\mathrm{u}} h_{\mathrm{u}} + \beta_{\mathrm{u}}$, the power consumed by the UAV while hovering at an altitude h_{u}, and P_{c} is the communication-related power consumed by the radio-access node; T_{u} is the time during which the UxNB remains aloft; $\kappa = 2.78 \times 10^{-}4$ is the Joule to Wh conversion factor. Furthermore, the UAV's power consumption is modelled as an increasing function of the hovering altitude to capture the effect of increased air pressure and temperature, which demands the UAV to generate more power to maintain a stable hovering position at higher altitudes [17], [19]; α_{u}, β_{u} are the UAV-dependent parameters obtained through the empirical study on the UAV's hovering energy consumption reported in [17]; $r_{\mathrm{u}}(h_{\mathrm{u}}) = h_{\mathrm{u}} \tan\theta$ is the radius of the UxNB's circular coverage region. The AEE, defined in (B.10), represents the trade-off between an increase in the coverage area and the associated increase in the total energy spent to cover the area. Since available energy-efficiency metrics like the global energy efficiency (GEE), which represents the number of bits transmitted per Joule of energy consumed, do not capture this trade-off, we believe that the proposed AEE metric is well suited for energy-efficient placement of a UAS deployed for rural applications, where the coverage area and the energy consumption factors are of great importance.

3 Optimal Hovering Altitude of the UxNB

In this section, we determine the hovering altitude of the UxNB that maximizes the AEE subject to the altitude and minimum QoS constraints. All the UEs follow the P-NOMA scheme to transmit D bits of data to the UxNB. The corresponding optimization

problem can be written as;

$$\text{(B:P1)} : \underset{h_{\mathrm{u}}}{\text{maximize}} \quad \frac{\pi h_{\mathrm{u}}^2 \tan^2\theta}{T_{\mathrm{u}}^{\mathrm{n}}(h_{\mathrm{u}}) P_t(h_{\mathrm{u}}) \kappa}, \tag{B.11}$$

$$\text{s.t.} \quad h_{\min} \leq h_{\mathrm{u}} \leq h_{\max}, \tag{B.12}$$

$$\Gamma_i^{\mathrm{n}}(h_{\mathrm{u}}) \geq \Gamma_{\mathrm{m}} \quad \forall i \in \mathcal{N}, \tag{B.13}$$

$$T_{\mathrm{u}}^{\mathrm{n}}(h_{\mathrm{u}}) = \frac{D}{\min\{R_i^{\mathrm{n}}(h_{\mathrm{u}}) : \forall i \in \mathcal{N}\}}. \tag{B.14}$$

The objective function of (B:P1) is the AEE as defined in (B.10); (B.12) is the altitude constraint with $h_{\min}$ and $h_{\max}$, the respective lower and upper limits of the hovering altitude specified by the regulatory board. (B.13) represents the QoS constraints that ensure the successful decoding of the received messages from the UEs hence validating (B.8) and (B.9). (B.14) represents the maximum time taken among the UEs in the UxNB's circular coverage region, to complete the uplink data transmission of D bits of data. (B.13) can be equivalently written as,

$$\text{minimum}\,[\Gamma_i^{\mathrm{n}}(h_{\mathrm{u}})] \geq \Gamma_{\mathrm{m}}. \tag{B.15}$$

From (B.8), the received SINR from a UE depends on both the received and the interference-plus-noise (IN) power values. Considering the first UE, with an increase in the number of UEs in the coverage region of the UxNB, even though the number of interfering UEs increases, the magnitude of interference from each of the $(N-1)$ UEs decreases; whereas, for the N^{th} UE, the received power decreases exponentially. Hence, to find minimum $[\Gamma_i^{\mathrm{n}}(h_{\mathrm{u}})]$, we propose the UxNB to cover a minimum number of UEs as reported in (B.16).

Proposition B1. *For given $\gamma_{\mathrm{n}} = p_{\mathrm{u}}/\sigma_{\mathrm{n}}^2$, ρ_{u}, δ, and θ values, the inequality $\Gamma_1^{\mathrm{n}}(h_{\mathrm{u}}) > \Gamma_2^{\mathrm{n}}(h_{\mathrm{u}}) > ... > \Gamma_N^{\mathrm{n}}(h_{\mathrm{u}})$ is satisfied when the UxNB covers a minimum number of UEs given by (B.16):*

$$N_{min}(h_{min}^{'}) = 1 + \frac{1}{\Delta} log_2\left(\frac{\gamma_{\mathrm{n}}}{\delta - 1}\right), \tag{B.16}$$

where $\Delta = log_2\delta$.

Proof. Substituting (B.6) in (B.8), the SINR expression of the i^{th} UE can be rewritten as,

$$\Gamma_i^{\mathrm{n}}(h_{\mathrm{u}}) = \frac{\frac{\gamma_{\mathrm{n}}}{\delta^{i-1}}}{\sum_{j=i+1}^{N(h_{\mathrm{u}})} \frac{\gamma_{\mathrm{n}}}{\delta^{j-1}} + 1}, \tag{B.17}$$

$$= \frac{\gamma_{\mathrm{n}}}{\frac{\gamma_{\mathrm{n}}}{\delta}\left[\frac{1-1/\delta^{N(h_{\mathrm{u}})-i}}{1-1/\delta}\right] + \delta^{i-1}} \tag{B.18}$$

From (B.18), $\Gamma_1^{\mathrm{n}}(h_{\mathrm{u}}) > \Gamma_N^{\mathrm{n}}(h_{\mathrm{u}})$ is equivalently written as,

$$\frac{\gamma_{\mathrm{n}}}{\frac{\gamma_{\mathrm{n}}}{\delta}\left[\frac{1-1/\delta^{N(h_{\mathrm{u}})-1}}{1-1/\delta}\right]+1} > \frac{\gamma_{\mathrm{n}}}{\delta^{N(h_{\mathrm{u}})-1}}, \tag{B.19}$$

rearranging (B.19) with $N(h_{\mathrm{u}})$ on the left-hand side gives (B.16). □

$N(h_{\mathrm{u}}) = \rho_{\mathrm{u}}\pi h_{\mathrm{u}}^2 \tan^2\theta$ in (B.16) gives the minimum hovering altitude of the UxNB to cover $N_{\min}(h_{\min}^{'})$ UEs as,

$$h_{\min}^{'} = \frac{1}{\tan\theta\sqrt{\rho_{\mathrm{u}}\pi}}\sqrt{1+\frac{1}{\Delta}\log_2\left(\frac{\gamma_{\mathrm{n}}}{\delta-1}\right)}. \tag{B.20}$$

Using Proposition B1, (B.13) and (B.14) are rewritten as (B.21) and (B.22), respectively:

$$\Gamma_N^{\mathrm{n}}(h_{\mathrm{u}}) \geq \Gamma_{\mathrm{m}}, \tag{B.21}$$

$$T_{\mathrm{u}}^{\mathrm{n}}(h_{\mathrm{u}}) = \frac{D}{R_N^{\mathrm{n}}(h_{\mathrm{u}})}. \tag{B.22}$$

Substituting (B.6) in (B.8), and using it in (B.21) gives,

$$\frac{p_{\mathrm{u}}}{\delta^{[N(h_{\mathrm{u}})-1]}\sigma_{\mathrm{n}}^2} \geq \Gamma_{\mathrm{m}}, \tag{B.23}$$

$$N(h_{\mathrm{u}}) \leq 1+\frac{1}{\Delta}\log_2\left(\frac{\gamma_{\mathrm{n}}}{\Gamma_{\mathrm{m}}}\right) = Q(\Gamma_{\mathrm{m}}). \tag{B.24}$$

(B.24) converts the minimum QoS constraints, (B.13), into the altitude constraint, $h_{\mathrm{u}} \leq \frac{1}{\tan\theta}\sqrt{\frac{Q(\Gamma_{\mathrm{m}})}{\rho_{\mathrm{u}}\pi}} = h_{\max}^{\mathrm{Q}}$. Hence, (B:P1) is reformulated as,

$$\text{(B:P2)}: \underset{h_{\mathrm{u}}}{\text{maximize}} \quad \frac{\pi h_{\mathrm{u}}^2\tan^2\theta}{\left[\frac{D}{R_N^{\mathrm{n}}(h_{\mathrm{u}})}\right]P_{\mathrm{t}}(h_{\mathrm{u}})\kappa}, \tag{B.25}$$

$$\text{s.t.} \quad \underbrace{\max\{h_{\min}, h_{\min}^{'}\}}_{\overline{h}_{\min}} \leq h_{\mathrm{u}} \leq \underbrace{\min\{h_{\max}, h_{\max}^{\mathrm{Q}}\}}_{\overline{h}_{\max}}, \tag{B.26}$$

Both the numerator and the denominator of the objective function of (B:P2), $\mathrm{AEE}_{\mathrm{n}}(h_{\mathrm{u}})$, are increasing functions of the hovering altitude, h_{u}. The optimal altitude that maximizes $\mathrm{AEE}_{\mathrm{n}}(h_{\mathrm{u}})$ is determined using the bisection method as detailed in Algorithm B.1.

For a given, θ, ρ_{u}, γ_{n}, δ, and Γ_{m} values, the algorithm takes $\overline{h}_{\min}$ and $\overline{h}_{\max}$ as the input parameters. Algorithm B.1 makes use of the first derivative property of

Algorithm B.1: Optimal Hovering altitude of the UxNB.

Input:$\overline{h}_{\max}$, $\overline{h}_{\min}$;
Find: $l = \mathrm{AEE}_{\mathrm{d,n}}(\overline{h}_{\min})$, $u = \mathrm{AEE}_{\mathrm{d,n}}(\overline{h}_{\max})$ using (B.27); ;
while *1* **do**
  if $l > 0$ *&* $u > 0$ **then**
    $h_{\mathrm{u,opt}} = \overline{h}_{\max}$;
    break.
  if $l < 0$ *&* $u < o$ **then**
    $h_{\mathrm{u,opt}} = \overline{h}_{\min}$;
    break.
  $m = \left[\overline{h}_{\min} + \overline{h}_{\max}\right]/2$;
  if $AEE_{\mathrm{d,n}}(\overline{h}_{min}) \times AEE_{\mathrm{d,n}}(m) < 0$ **then**
    $\overline{h}_{\max} = m$;
  else
    $\overline{h}_{\min} = m$;
  if $|\overline{h}_{min} - \overline{h}_{max}| \leq \eta$ **then**
    $h_{\mathrm{u,opt}} = \overline{h}_{\min}$;
    break.
Output: Optimal hovering altitude $h_{\mathrm{u,opt}}$.

$\mathrm{AEE_n}(h_\mathrm{u})$: $\mathrm{AEE_{d,n}}(h_{\mathrm{u,opt}}) = 0$; $\mathrm{AEE_{d,n}}(h_\mathrm{u}) > 0 \ \forall h_\mathrm{u} \in [h_{\min}, h_{\mathrm{u,opt}})$; $\mathrm{AEE_{d,n}}(h_\mathrm{u}) < 0 \ \forall h_\mathrm{u} \in (h_{\mathrm{u,opt}}, h_{\max}]$, where,

$$\begin{aligned}\mathrm{AEE_{d,n}}(h_\mathrm{u}) = &\frac{W\pi\tan^2\theta}{D\kappa P_\mathrm{t}(h_\mathrm{u})}\left[2h_\mathrm{u}\log_2\left(1+\frac{\gamma_\mathrm{n}}{\delta^{N(h_\mathrm{u})-1}}\right)\right] \\ &- \frac{W\pi\tan^2\theta}{D\kappa P_\mathrm{t}(h_\mathrm{u})}\left[\frac{2h_\mathrm{u}^3\gamma_\mathrm{n}\pi\rho_\mathrm{u}\tan^2\theta\ln(\delta)}{\ln(2)\left(\delta^{N(h_\mathrm{u})-1}+\gamma_\mathrm{n}\right)}\right] \\ &- \frac{W\pi\tan^2\theta\alpha_\mathrm{u}}{D\kappa P_\mathrm{t}^2(h_\mathrm{u})}h_\mathrm{u}^2\log_2\left(1+\frac{\gamma_\mathrm{n}}{\delta^{N(h_\mathrm{u})-1}}\right), \end{aligned} \tag{B.27}$$

and $h_{\mathrm{u,opt}}$ is the optimal altitude. The algorithm starts with a larger interval supposedly containing the optimal altitude: $h_\mathrm{u} \in \left[\overline{h}_{\min}, \overline{h}_{\max}\right]$. In every iteration, if the altitude corresponding to the midpoint of the interval maps to an $\mathrm{AEE_n}(h_\mathrm{u})$ value that lies on the falling (rising) edge of the $\mathrm{AEE_n}(h_\mathrm{u})$ curve, the upper (lower) limit of the interval is changed to the midpoint. This process continues until the interval width is negligible. The interval width after the k^{th} iteration is $(\overline{h}_{\min} - \overline{h}_{\max})/2^k$; therefore, the complexity of the algorithm is $\mathcal{O}\left\{\log_2[\,(h_{\min} - h^{'}_{\max})/\eta\,]\right\}$.

OMA-UAS

To compare the AEE performance of the NOMA-UAS with an uplink OMA scheme, we consider that the total available bandwidth, W, is equally divided among $N(h_\mathrm{u})$ UEs. Consequently, the bandwidth allocated to each UE and the noise power will be a function of the hovering altitude. Thus, for given, h_u, ρ_u, and θ values, the achievable data rate of the i^{th} UE using the OMA scheme is evaluated using the following expression:

$$R_i^\mathrm{o}(h_\mathrm{u}) = \frac{W}{N(h_\mathrm{u})}\log_2\left[1+\frac{\gamma_\mathrm{n}N(h_\mathrm{u})}{\delta^{i-1}}\right] \ \forall i \in \mathcal{N}. \tag{B.28}$$

From (B.28), it is evident that for a given h_u, the inequality $R_1^\mathrm{o}(h_\mathrm{u}) > R_2^\mathrm{o}(h_\mathrm{u}) > ... > R_N^\mathrm{o}(h_\mathrm{u})$ is satisfied. Therefore, the corresponding AEE is expressed as,

$$\mathrm{AEE_o}(h_\mathrm{u}) = \frac{\pi h_\mathrm{u}^2\tan^2\theta}{T_\mathrm{u}^\mathrm{o}(h_\mathrm{u})P_t(h_\mathrm{u})\kappa}, \tag{B.29}$$

where $T_\mathrm{u}^\mathrm{o}(h_\mathrm{u}) = \frac{D}{R_N^\mathrm{o}(h_\mathrm{u})}$.

4 Numerical Results and Discussion

In this section, we provide and discuss our main findings obtained through the numerical evaluation. The considered simulation parameters are $h_0 = 1.42 \times 10^{-4}$, $\mu_1 = 1.0116$,

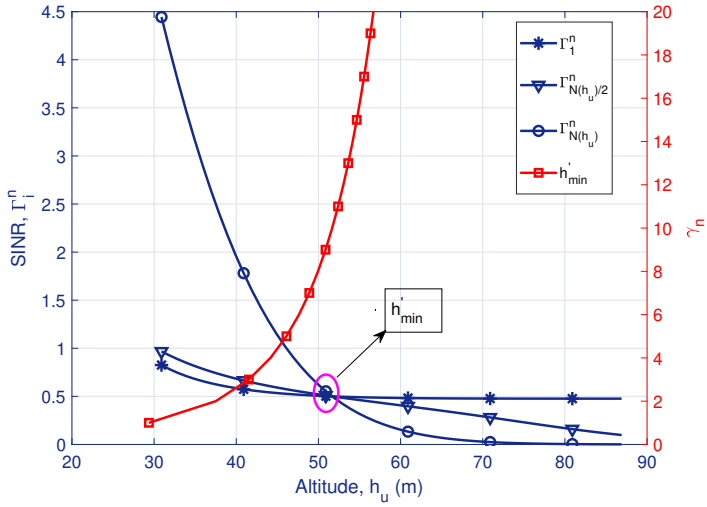

Fig. B.2: SINR vs Altitude for $\rho_u = 10^-3, \delta = 1.5, \gamma_n = 10$.

$\mu_2 = 11.2202$, $a = 4.88$, $b = 0.43$ [19], $W = 80$MHz, $h_{max} = 300$m, $h_{min} = 10$m, $\Gamma_m = 8.668 \times 10^-4$(100Kbps), $D = 10^{10}$ bits, $\alpha_u = 4.917$, and $\beta_u = 275.204$ [17], $\eta = 0.5$, $\theta = 45^o$, $P_c = 10$W.

Fig. B.2 shows the variations of the SINR values of the first, the middle, and the last UEs, with regards to the hovering altitude of the UxNB. As proved in Proposition B1, in the figure, the SINR value of the last UE (with the index N) is greater than the first UE (with the index 1) up to the altitude value equal to the right-hand side of (B.20), beyond which the inequality, $\Gamma_1^n(h_u) > \Gamma_N^n(h_u)$, is satisfied. Moreover, the h'_{min} increases with the signal-to-noise (SNR) ratio value, γ_n, to guarantee a positive difference between the SINR values of the first and the last UEs.

Fig. B.3 shows the variations of the achievable AEE values with the underlying P-NOMA and OMA schemes, plotted using (B.25) and (B.29), respectively. The plots are shown against the hovering altitude of the UxNB for $\delta = 1.5$ and $\gamma_n = 10$. As expected, the AEE is neither maximum at a lower altitude value nor at a higher altitude value. In the low-altitude regime, the smaller area covered by the UxNB (the numerator of the AEE) overcompensates the reduced UxNB's energy consumption resulting in a low AEE value. Similarly, in the high-altitude regime, the UxNB takes more time to complete the uplink data transmission from the UEs demanding a longer UAV endurance; hence, the increased UAV energy consumption at a higher altitude reduces the AEE value despite the increased coverage area. As shown in the figure, the combined effect of the above-mentioned trade offs makes the AEE function a bell-shaped curve. Also, the optimal points obtained through Algorithm B.1, are the global optima of the AEE plots. Furthermore, the figure shows that the maximum AEE value considering the NOMA

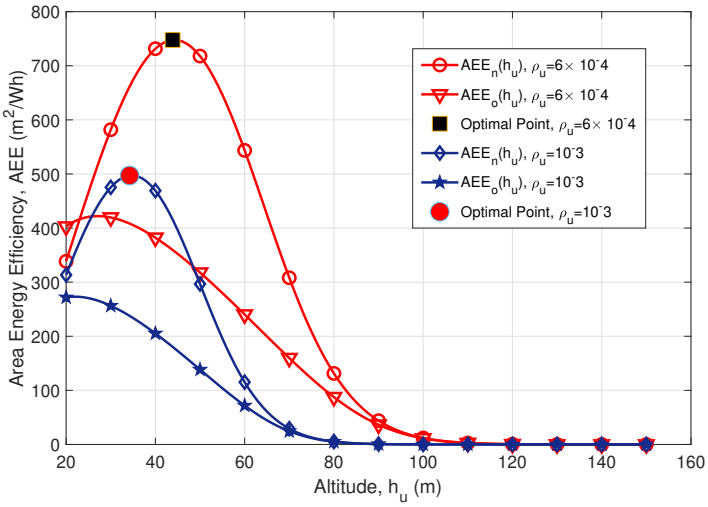

Fig. B.3: AEE versus Altitude: $\delta = 1.5, \gamma_{\mathrm{n}} = 10$.

scheme is always higher than the corresponding value obtained using the OMA scheme.

The effect of the UE density over the maximum AEE value is shown in Fig. B.4. For both the NOMA and the OMA schemes, the respective maximum AEE values decrease with an increase in the UE density: the $T_{\mathrm{u}}(h_{\mathrm{u}})$ factor increases because of the decrease in the received SINR from the edge-UE owing to the increase in the number of the UEs in the coverage area; this increases the energy consumption (the denominator of the AEE) thereby reducing the respective maximum AEE values. The figure has three sets of plots, each corresponding to a particular power-reduction factor, δ. For each set, the maximum AEE value achieved through the NOMA scheme prevails over the corresponding value of the OMA scheme. Also, the margin between maximum AEE values decreases with an increase in the user density. Furthermore, the gain in the AEE value achieved using the NOMA scheme, over the OMA scheme, decreases with the increase in the δ value. From the above discussions, it is clear that the proposed NOMA scheme is more energy-efficient when the power-reduction factor associated with the edge-UE lying in the coverage region, δ^{N-1}, is relatively small. The factor either increases with an increase in the number of UEs (ρ_{u}) or with the δ value. Hence, the proposed scheme is recommended to use with a low δ value in applications where the user density is small. The lower-bound of the δ value is decided by the ability of the SIC receiver to successively decode the messages using the diversity in power received from the UEs.

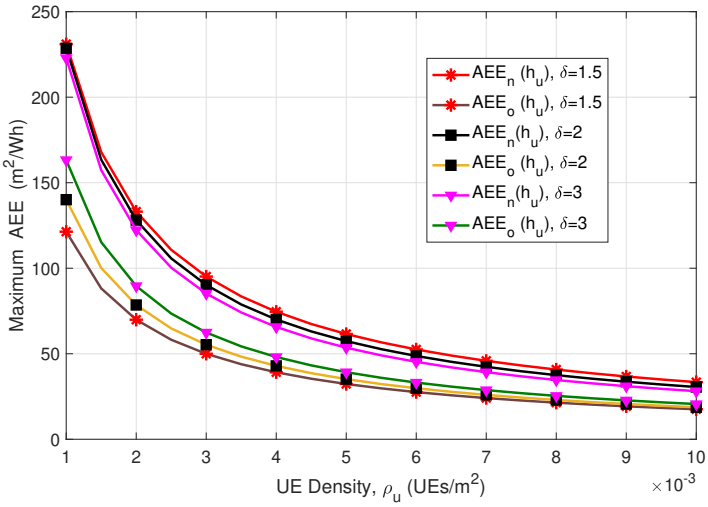

Fig. B.4: Maximum AEE versus UE density: $\gamma_{\mathrm{n}} = 6$.

5 Conclusion

In this work, we determined the optimal hovering altitude of a UAS deployed for a non-orthogonal multiple access uplink transmission scenario. The necessary power diversity required at the SIC receiver was ensured through the uplink power-reduction scheme that forms the basis of the P-NOMA scheme. The optimization problem maximized the proposed area energy efficiency metric while satisfying the altitude and the QoS constraints. The AEE-performance of the UAS with the underlying P-NOMA scheme is compared to the OMA scheme. It is observed that the P-NOMA scheme outperforms the OMA scheme and the corresponding achievable gain depends on the UE density and the power-reduction factor. The gain is inversely proportional with regard to the UE density and the power-reduction factor. The downlink-AEE analysis considering multiple UAS is left as future work.

References

[1] K. B. Letaief, W. Chen, Y. Shi, J. Zhang, and Y. A. Zhang, "The Roadmap to 6G: AI Empowered Wireless Networks," *IEEE Communications Magazine,* vol. 57, no. 8, pp. 84–90, Aug. 2019

[2] Y. Chen, A. Bayesteh, Y. Wu, B. Ren, S. Kang, S. Sun, Q. Xiong, C. Qian, B. Yu, Z. Ding, S. Wang, S. Han, X. Hou, H. Lin, R. Visoz, and R. Razavi, "Toward the

Standardization of Non-Orthogonal Multiple Access for Next Generation Wireless Networks," *IEEE Communications Magazine,* vol. 56, no. 3, pp. 19–27, Mar. 2018.

[3] A. Fotouhi, H. Qiang, M. Ding, M. Hassan, L. G. Giordano, A. Garcia-Rodriguez, and J. Yuan, "Survey on uav Cellular Communications: Practical Aspects, Standardization Advancements, Regulation, and Security Challenges," *IEEE Communications Surveys Tutorials,* pp. 1–1, 2019.

[4] Maraqa O, Rajasekaran AS, Al-Ahmadi S, Yanikomeroglu H, Sait SM, "A Survey of Rate-Optimal Power Domain NOMA with Enabling Technologies of Future Wireless Networks," *IEEE Communications Surveys and Tutorials*, 2020 Aug 3;22(4):2192-235.

[5] M. F. Sohail, C. Y. Leow and S. Won, "Energy-Efficient Non-Orthogonal Multiple Access for UAV Communication System," *IEEE Transactions on Vehicular Technology,* vol. 68, no. 11, pp. 10834-10845, Nov. 2019.

[6] X. Liu et al., "Placement and Power Allocation for NOMA-UAV Networks," *IEEE Wireless Communications Letters," vol. 8, no. 3, pp. 965-968, June 2019.*

[7] J. Sun, Z. Wang and Q. Huang, "Cyclical NOMA Based UAV-Enabled Wireless Network," *IEEE Access,* vol. 7, pp. 4248-4259, 2019.

[8] A. A. Nasir, H. D. Tuan, T. Q. Duong and H. V. Poor, "UAV-Enabled Communication Using NOMA," *IEEE Transactions on Communications,* vol. 67, no. 7, pp. 5126-5138, July 2019.

[9] F. Cui, Y. Cai, Z. Qin, M. Zhao and G. Y. Li, "Multiple Access for Mobile-UAV Enabled Networks: Joint Trajectory Design and Resource Allocation," *IEEE Transactions on Communications,* vol. 67, no. 7, pp. 4980-4994, July 2019.

[10] D. Hu, Q. Zhang, Q. Li and J. Qin, "Joint Position, Decoding Order, and Power Allocation Optimization in UAV-Based NOMA Downlink Communications," *IEEE Systems Journal,* vol. 14, no. 2, pp. 2949-2960, June 2020.

[11] N. Zhao et al., "Joint Trajectory and Precoding Optimization for UAV-Assisted NOMA Networks," *IEEE Transactions on Communications,* vol. 67, no. 5, pp. 3723-3735, May 2019.

[12] R. Duan, J. Wang, C. Jiang, H. Yao, Y. Ren and Y. Qian, "Resource Allocation for Multi-UAV Aided IoT NOMA Uplink Transmission Systems," *IEEE Internet of Things Journal,* vol. 6, no. 4, pp. 7025-7037, Aug. 2019.

[13] X. Pang et al., "Uplink Precoding Optimization for NOMA Cellular-Connected UAV Networks," *IEEE Transactions on Communications,* vol. 68, no. 2, pp. 1271-1283, Feb. 2020.

[14] Mu, Guangchen. "Joint Beamforming and Power Allocation for Wireless Powered UAV-Assisted Cooperative NOMA systems," *EURASIP Journal on Wireless Communications and Networking*, 2020.1 (2020): 1-14.

[15] 3GPP; Technical Specification Group Services and System Aspects; Unmanned Aerial System (UAS) support in 3GPP; Stage 1; Release 17

[16] Zhang N, Wang J, Kang G, Liu Y, "Uplink Non Orthogonal Multiple Access in 5G Systems," *IEEE Communications Letters,* 2016 Jan 25;20(3):458-61.

[17] H. V. Abeywickrama, B. A. Jayawickrama, Y. He and E. Dutkiewicz, "Comprehensive Energy Consumption Model for Unmanned Aerial Vehicles, Based on Empirical Studies of Battery Performance," *IEEE Access,* vol. 6, pp. 58383-58394, 2018.

[18] N. Babu, K. Ntougias, C. B. Papadias and P. Popovski, "Energy Efficient Altitude Optimization of an Aerial Access Point," in *IEEE 31st Annual International Symposium on Personal, Indoor and Mobile Radio Communications (PIMRC),* 2020, pp. 1-7.

[19] N. Babu, C. B. Papadias and P. Popovski, "Energy-Efficient 3-D Deployment of Aerial Access Points in a UAV Communication System," *IEEE Communications Letters,* vol. 24, no. 12, pp. 2883-2887, Dec. 2020.

[20] H. He, S. Zhang, Y. Zeng and R. Zhang, "Joint Altitude and Beamwidth Optimization for UAV-Enabled Multiuser Communications," *IEEE Communications Letters,* vol. 22, no. 2, pp. 344-347, Feb. 2018.

[21] A. Al-Hourani, S. Kandeepan and S. Lardner, "Optimal LAP Altitude for Maximum Coverage," *IEEE Wireless Communications Letters,* vol. 3, no. 6, pp. 569-572, Dec. 2014.

[22] 3GPP, "Physical Layer Procedures," , TR 36.213, Sep. 2015, v 10.12.0

Paper C

Energy-Efficient 3D Deployment of Aerial Access Points in a UAV Communication System

Nithin Babu, Constantinos B. Papadias, and Petar Popovski

Published in
IEEE Communications Letters, Vol. 24, pp. 2883-2887, 2020, doi: 10.1109/LCOMM.2020.3017559.

The layout has been revised.

Abstract

In this letter, we propose an energy-efficient 3-dimensional placement of multiple aerial access points (AAPs), in the desired area, acting as flying base stations for uplink communication from a set of ground user equipment (UE). The globally optimal energy-efficient vertical position of AAPs is derived analytically by considering the inter-cell interference and AAP energy consumption. The horizontal position of AAPs which maximize the packing density of the AAP coverage area are determined using a novel regular polygon-based AAP placement algorithm. We also determine the maximum number of non-interfering AAPs that can be placed in the desired area. The effect of the AAP energy consumption on the optimal placement and the analytic findings are verified via numerical simulations.

1 Introduction

The aerial coverage provided for temporary data demand events with the help of unmanned aerial vehicles (UAVs) acting as flying base stations is considered as one of the essential components of fifth-generation (5G) and beyond-5G wireless networks. Unlike the conventional approach of fixed base stations, the portable feature of the UAV-based aerial communication system not only increases the probability of line-of-sight (LoS) links between the UEs and the AAP but also could be dynamically deployed in natural disaster areas [1] or social events such as concerts. One of the major limitations of the UAV communication system is it's limited lifetime proportional to the available onboard energy. So the UAVs should be deployed in such a way as to increase the number of bits successfully transmitted per joule of energy consumed, defined as global energy efficiency (GEE). The GEE of the UAV-based system depends on the 3-D coordinates of the UAV location; as the altitude increases, the coverage area of the UAV increases and the UAV energy consumption increases [2], thereby affecting the GEE. The horizontal positioning of the UAVs determines the fraction of the total number of users in the desired area covered by the UAV; the higher the fraction, the higher the GEE. The authors of [3] propose an energy-efficient 3-D placement of an unmanned aerial vehicle base station for maximal coverage under the orthogonal multiple access (OMA) scheme. The work in [4] proposes an optimal 3-D deployment of three UAV-base stations in a given urban area for maximum coverage under the OMA scheme. In [5], an online method for proper 3D deployment of UAV base stations to maximize the lifetime of the network is proposed. None of the above works consider the energy consumption of the mechanical parts of the aerial vehicle and the co-channel interference from the neighboring cells. In our previous work [6] we have determined the energy-efficient hovering altitude for a standalone AAP deployed for orthogonal downlink broadcast transmission. The energy-efficient 3-D deployment of multiple AAPs in a given geographical

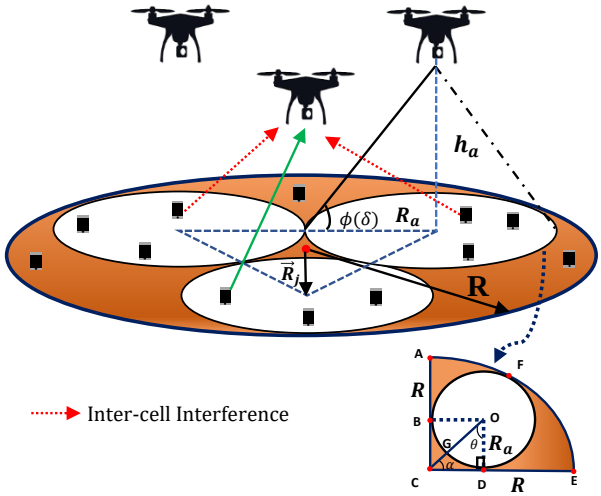

Fig. C.1: System setup.

area considering both the communication-related energy and UAV energy consumption in the presence of inter-cell interference has, to the best of our knowledge, not been investigated in the literature.

In this letter, we analytically determine the optimal vertical position of AAPs by solving the GEE maximization of identical and independent single AAP systems with the altitude and the individual UE power constraints. Then the horizontal coordinates of the AAPs with non-overlapping coverage areas are determined by posing it as a problem of non-overlapping circle packing and solved using the proposed multilevel regular polygon-based placement algorithm.

2 System Model

We consider a circular geographical area of radius R, containing a set of N_{u} uniformly distributed stationary ground UEs with a density ρ_{u}, such that $N_{\mathrm{u}} = \rho_{\mathrm{u}}\pi R^2$. As shown in Figure C.1, the given geographical area is covered by multiple AAPs positioned in a way that their coverage areas do not overlap and the horizontal plane coordinates of the AAP are assumed to be those of the center of the AAP coverage area. A universal frequency reuse among the AAPs is assumed, in which the total bandwidth W is equally divided among $N_{\mathrm{u}}^{'} = \rho_{\mathrm{u}}\pi R_{\mathrm{a}}^2$ UEs lying in the circular coverage area of an AAP of radius R_{a}. Since the UEs in the neighboring cells use the same set of frequencies, the receiver at

the AAP experiences inter-cell interference from the co-channel UEs in the neighboring cells. Let $\mathcal{U}^{'}$ be the subset of UEs covered by the AAP, such that $|\mathcal{U}^{'}| = \rho_{\mathrm{u}}\pi R_{\mathrm{a}}^2$.

2.1 Optimal Vertical Positioning of the AAPs

Considering AAPs with non-overlapping coverage areas, the problem of finding the optimal vertical positioning of the AAPs breaks down to identical and independent single AAP vertical positioning problems. Hence all the AAPs will be hovering at the energy-efficient altitude obtained by solving the independent AAP vertical positioning problem [5]. Here we consider an orthogonal uplink communication between the UEs and the associated AAP.

Channel Model

We consider the channel model proposed by authors in [7], in which the communication channel between the UEs and the AAP can be modelled either as a line-of-sight (LoS) or a non-line-of-sight (N-LoS) link. Since the planning phase of the base station deployment considers long-term channel variation rather than short-term random behavior, we neglect the small scale channel variations due to the dynamic propagation environment [7]. The environment-dependent long-term channel variations due to shadowing and scattering referred to as additional path loss have a Gaussian distribution [7]; however, in this letter, we only use the mean value of this distribution and not its random behavior [3], [5], [7]. Hence η_{l} and η_{nl} are the mean value of the additional path loss for LoS and N-LoS links. Then the path loss for the LoS and N-LoS links between a UE located at a distance of r_i from the center of the coverage area is given by

$$L_x = \frac{\eta_x d_i^2}{g_0} \quad \text{for } x \in \{l, nl\}, \tag{C.1}$$

where $g_0 = (c/4\pi f_{\mathrm{c}})^2$ represents the channel gain at a reference distance of 1m; c, f_{c} are the velocity of light and carrier frequency of the radio signal; $d_i = \sqrt{r_i^2 + h_{\mathrm{a}}^2}$, is the distance between the i^{th} UE and the AAP. The LoS probability, P_{l} between a UE and it's associated AAP is given by [7];

$$P_{\mathrm{l}} = \frac{1}{1 + a\exp\left[-b(\phi_i - a)\right)]}, \tag{C.2}$$

where a, b are environment-dependent parameters given in [7] and $\phi_i = (180/\pi)\tan^{-1}(h_{\mathrm{a}}/r_i)$ is the elevation angle between the i^{th} UE and associated AAP. Hence, the N-LoS link probability, P_{nl} associated with the same UE-AAP pair is $1 - P_{\mathrm{l}}(r_i, h_{\mathrm{a}})$. Because of

the non-availability of the terrain knowledge, we consider a probabilistic mean path loss given by

$$\begin{aligned}\overline{L}(r_i, h_\mathrm{a}) &= P_\mathrm{l} \times L_\mathrm{l} + P_\mathrm{nl} \times L_\mathrm{nl}, \\ &= \frac{d_i^2}{g_0} \times [\eta_\mathrm{l} P_\mathrm{l} + \eta_\mathrm{nl}(1 - P_\mathrm{l})], \\ &= \underbrace{\frac{d_i^2}{g_0}}_{\mathrm{FSPL}} \times \underbrace{[\eta_\mathrm{nl} + P_\mathrm{l}(\eta_\mathrm{l} - \eta_\mathrm{nl})]}_{\eta_\mathrm{m},\ \text{mean additional path loss}}. \end{aligned} \tag{C.3}$$

AAP Coverage Region

In this letter, we consider the GEE as the performance matrix for the AAP deployment. Since the GEE of the considered system might not be maximum at the altitude corresponding to the minimum required SNR value [7], [3], we define the coverage region of an AAP based on the P_l threshold, δ. For a given AAP altitude, all the UEs having a LoS probability greater than δ are considered to be covered by the AAP. This threshold translates into a circular coverage region with radius, $R_\mathrm{a} = h_\mathrm{a}\cot(\phi(\delta))$ and all the UEs at distance $r_i \leq R_\mathrm{a}$ are considered to be lying in the AAP coverage area.

Uplink Power Control

Each user chooses the transmit power according to the uplink power control specified in the 3GPP technical report [8]. Then the transmit power for the i^{th} UE (in Watts) is given by

$$P_i = \min\left\{P_\mathrm{max}, P_\mathrm{a} B(\overline{L}(r_i, h_\mathrm{a}))^\beta\right\}, \tag{C.4}$$

where P_max is the maximum transmit power; P_a is the target arrived power at the AAP; B is the number of allocated resource blocks and β is the path loss attenuation factor of fractional transmission power control (TPC) [8] [9]. The information about the target power and the AAP location is sent to the UEs through the control signaling. Since B and β do not depend on the AAP position, we assume they are both equal to 1. However, the algorithm developed in Section 2.2 is applicable for any B, β values. Hence the average transmit power transmitted by the i^{th} UE is given by

$$\overline{P}_i = P_\mathrm{a}\overline{L}(r_i, h_\mathrm{a}), \quad \forall\ i\ \in \mathcal{U}^{'}. \tag{C.5}$$

Thus the expectation of the sum of the powers transmitted by all the UEs in the AAP coverage area is obtained by taking an expectation over the uniformly distributed UEs with a density ρ_u:

$$\overline{P}_{\mathrm{t}} = \rho_{\mathrm{u}} \int_0^{R_{\mathrm{a}}} 2\pi P_{\mathrm{a}} \overline{L}(r_i, h_{\mathrm{a}}) r_i dr_i,$$
$$\leq \frac{2\pi\rho_{\mathrm{u}} P_{\mathrm{a}} \eta_{\mathrm{m}} \cot^2(\phi(\delta)) h_{\mathrm{a}}^4 (\cot^2(\phi(\delta)) + 2)}{4g_0}. \tag{C.6}$$

The free space path loss (FSPL) and the P_{l} variable of η_{m}, of $\overline{L}(r_i, h_{\mathrm{a}})$ depend on r_i. By (C.2), $P_{\mathrm{l}}(r_j) \geq P_{\mathrm{l}}(r_k)$ for all $r_j \leq r_i$. Because of the complex P_{l} expression, for the remaining analytical derivation, we approximate P_{l} for all the UEs in the AAP coverage area to be equal to the P_{l} of the edge UE ($r_i = R_{\mathrm{a}}$). Assuming no interference cancellation techniques at the AAP surrounded by M AAPs, the upper bound of the data rate of the i^{th} UE in bits per seconds (bps) is given by

$$D_i = W_i \log_2 \left\{ 1 + \frac{\dfrac{\overline{P}_i}{\overline{L}(r_i, h_{\mathrm{a}})}}{\Sigma_{j=1}^{M} \dfrac{\overline{P}_{i,j}}{\overline{L}(r_{i,j}, h_{\mathrm{a}})} + \dfrac{\sigma_0^2 W}{N'_{\mathrm{u}}}} \right\}, \tag{C.7}$$

$$= W_i \log_2 \left\{ 1 + \frac{P_{\mathrm{a}} N_{\mathrm{u}'}}{M P_{\mathrm{a}} N_{\mathrm{u}'} + \sigma_0^2 W} \right\}, \tag{C.8}$$

where σ_o^2 is the power spectral density of the zero-mean additive white Gaussian noise at the corresponding receiver; $W_i = W/N_{\mathrm{u}'}$. Since the inter-cell interference is a decreasing function of the distance from the receiver, in (C.8), we consider the case of maximum interference from the co-channel UEs in the neighboring cells lying close to the cell edge UEs. Because of the uplink power control, all the UEs in the coverage region will have the same data rate upper bounded by (C.8). Assuming optimal (capacity-achieving) coding, we consider that these bounds will be attained. Then, the sum of the data rate will be:

$$D_{\mathrm{u}'}(h_{\mathrm{a}}) = \underbrace{\rho_{\mathrm{u}} \pi h_{\mathrm{a}}^2 \cot^2 \phi(\delta)}_{N_{\mathrm{u}'}} \times D_i. \tag{C.9}$$

The sum of the data rates of the ground UEs, the data transmission energy, and the AAP energy consumption are the three major factors affecting the GEE of the system. The GEE of the considered system is defined as;

$$\mathrm{GEE}(h_{\mathrm{a}}) = \frac{S_{\mathrm{u}'}(h_{\mathrm{a}})}{E(h_{\mathrm{a}})}, \tag{C.10}$$

where $S_{\mathrm{u}'}(h_{\mathrm{a}}) = T D_{\mathrm{u}'}(h_{\mathrm{a}})$ is the total number of data bits transmitted by the UEs in the AAP coverage area in T seconds; $E(h_{\mathrm{a}})$ is the total energy consumed by the AAP. The energy consumed by the AAP is the sum of the energy required for data

communication and the energy consumed by the mechanical parts of the UAV during climbing and hovering, and is given by:

$$E(h_{\mathrm{a}}) = \underbrace{(\alpha_{\mathrm{cl}} h_{\mathrm{a}} + \beta_{\mathrm{cl}})}_{E_{\mathrm{a,climb}}} + \underbrace{(\alpha_{\mathrm{ho}} h_{\mathrm{a}} + \beta_{\mathrm{ho}})\, T}_{E_{\mathrm{a,hover}}} + \underbrace{\overline{P}_{\mathrm{D}} T}_{\mathrm{E_{data}}}, \tag{C.11}$$

where $\overline{P}_{\mathrm{D}} = \overline{P}_{\mathrm{t}} + P_{\mathrm{C}}$ is the total data communication power, with P_{C} being the total hardware circuit power consumption and where $\overline{P}_{\mathrm{t}}$ is given by (C.6). $\alpha_{\mathrm{cl}}, \beta_{\mathrm{cl}}, \alpha_{\mathrm{ho}}, \beta_{\mathrm{ho}}$ are the constants related to the UAV [2]. The aerial vehicle's energy consumption, $E_{\mathrm{a}}(h_{\mathrm{a}})$ increases with an increase in the altitude, because the reduced air pressure at higher altitudes demands the generation of an additional force by the propeller of the aerial vehicle, which results in increased energy consumption [2] [10]. The problem of determining the optimal hovering altitude of the AAP which maximizes the GEE while satisfying the altitude and the individual UE power constraints can be formulated as:

$$\begin{aligned} (\mathrm{C{:}P1}) : \underset{h_{\mathrm{A}}}{\text{maximize}} \quad & \mathrm{GEE}(h_{\mathrm{a}}), \\ \text{s.t.} \quad & h_{\min} \leq h_{\mathrm{a}} \leq h_{\max}, && \text{(C.12)} \\ & P_i \leq P_{\max}, && \text{(C.13)} \end{aligned}$$

where $P_{\max}$ is the maximum power available at each UE, $h_{\min}$ and $h_{\max}$ are the minimum and maximum permitted AAP altitude specified by the aviation regulatory board respectively. (C.13) can be equivalently translated into the altitude constraint, $h_{\mathrm{a}} \leq h'_{\max} = \sqrt{\dfrac{P_{\max} g_0}{P_{\mathrm{a}} \eta_{\mathrm{m}} (1 + \cot^2(\phi(\delta)))}}$. (C:P1) is solved by using Proposition C1.

Proposition C1. *For a given ρ_{u}, P_{max}, δ, P_{a}, GEE(h_{a}) is a decreasing function of the hovering altitude of the AAP.*

Proof. To prove the decreasing nature of GEE(h_{a}), the numerator, $S_{\mathrm{u}'}(h_{\mathrm{a}})$ and the denominator, $E(h_{\mathrm{a}})$ should be a non-increasing and increasing function of h_{a}, respectively. From (C.11), $E(h_{\mathrm{a}})$ is an increasing function of h_{a} and it remains to prove that $\frac{\mathrm{d}S_{\mathrm{u}'}(h_{\mathrm{a}})}{\mathrm{d}h_{\mathrm{a}}} \leq 0 \; \forall \, h_{\mathrm{a}} \in \left\{ h_{\min}, \min(h_{\max}, h'_{\max}) \right\}$, which is shown below:

$$\frac{\dfrac{\mathrm{d}S_{\mathrm{u}'}(h_{\mathrm{a}})}{\mathrm{d}h_{\mathrm{a}}}}{TW} = \frac{2\kappa(\phi(\delta)) h_{\mathrm{a}} \log_2 e}{\kappa(\phi(\delta)) h_{\mathrm{a}}^2 + \dfrac{\sigma_o^2 W}{M+1}} - \frac{2\kappa(\phi(\delta)) h_{\mathrm{a}} \log_2 e}{\kappa(\phi(\delta)) h_{\mathrm{a}}^2 + \dfrac{\sigma_o^2 W}{M}}, \tag{C.14}$$

where $\kappa(\phi(\delta)) = P_{\mathrm{a}} \rho_{\mathrm{u}} \pi \cot^2(\phi(\delta))$. From (C.14), since $\dfrac{1}{TW} \dfrac{\mathrm{d}S_{\mathrm{u}'}(h_{\mathrm{a}})}{\mathrm{d}h_{\mathrm{a}}} \approx 0$ for $P_{\mathrm{a}} >> \sigma_o^2 W$, the numerator of the GEE is proved to be a non-increasing function of h_{a}. Hence

according to Proposition C1, the solution of (C:P1), the optimal vertical position of AAPs for maximum GEE, is the minimum altitude $h_{\min}$. Then the optimal LoS threshold value δ_o corresponding to $h_{\min}$ is determined numerically in Section 3. The corresponding radius of the individual AAP coverage region is $R_{\mathrm{a}} = h_{\min}\cot(\phi(\delta_o))$. □

2.2 Optimal Horizontal Positioning of the AAPs

In this section, we aim to determine the optimal horizontal positioning of the AAPs in the given desired circular region of radius R so that the packing density, defined as the ratio of area covered by the AAPs to the given desired area, is maximized. We consider an equal coverage region for all the AAPs with optimal radius $R_{\mathrm{a}} = h_{\min}\cot(\phi(\delta_o))$. We propose a multi-level regular polygon-based placement algorithm to determine the optimal horizontal positioning of the AAPs in the desired area. In the first level of Algorithm C.1, $N_{\mathrm{a},1}$ AAPs with non-overlapping coverage areas are placed along the boundary of the desired area. In the next level, $N_{\mathrm{a},2}$ AAPs are placed along the boundary of the void circle, of radius R_2, formed at the center of the desired area after the first level arrangement. The $N_{\mathrm{a},l}$ value is determined by Proposition C2.

Proposition C2. *The maximum number of non-overlapping circles, $N_{\mathrm{a},l}(\geq 3)$, of radius R_{a} that can be placed along the boundary of a larger circle of radius R_{l} should satisfy the following inequality:*

$$N_{\mathrm{a},l}\left[\pi + \alpha(1+sec\theta)^2 - \sqrt{3}(\frac{\pi+2\alpha}{\pi}) - \theta\right] \leq \frac{\pi R_{\mathrm{l}}^2}{R_{\mathrm{a}}^2}, \tag{C.15}$$

where $\alpha = \left(\frac{\pi}{2} - \theta\right)$ and $\theta = \frac{(N_{\mathrm{a},l}-2)\,\pi}{2N_{\mathrm{a},l}}$ are the angles associated with the polygon whose vertices are the center of the AAPs coverage regions as marked in Figure C.1.

Proof. Consider Figure C.1; the void around a circle along the boundary of the desired area is given by

$$\begin{aligned} \mathrm{V}_{\mathrm{Edge}} &= \mathrm{A}_{\mathrm{ABODEFA}} - \mathrm{A}_{\mathrm{BFDOB}}, \\ &= R_{\mathrm{a}}^2\left[\alpha\,(1+\sec\theta)^2 - \tan\theta - \frac{\sqrt{3}\,(\pi+2\alpha)}{\pi}\right], \end{aligned} \tag{C.16}$$

in which $\mathrm{A}_{\mathrm{BFDOB}}$ is the space claimed by the sector BFDOB of angle $\pi + 2\alpha$ [11]; the void at the center of the desired area is given by

$$\mathrm{V}_{\mathrm{center}} = \underbrace{R_{\mathrm{a}}^2\tan\theta}_{\mathrm{A}_{\mathrm{BODCB}}} - \underbrace{R_{\mathrm{a}}^2\theta}_{\mathrm{A}_{\mathrm{BODGB}}}. \tag{C.17}$$

The inequality (C.15) is based on the constraint that the sum of areas covered by $N_{\mathrm{a},l}$ AAPs and the void area should be less than the desired area. □

Algorithm C.1: Multilevel regular polygon based AAP placement algorithm.

Input: R_{a}, R, $l = 1$;
Find $N_{\mathrm{a},l}$ using (C.15) with $R_l = R$;
while (1) **do**
  $l = l + 1$;
  if $\{[R - 2(l-1)R_{\mathrm{a}}] \geq 2.1547R_{\mathrm{a}}\}$ **then**
    Find $N_{\mathrm{a},l}$ using (C.15) with $R_l = R - 2(l-1)R_{\mathrm{a}}$;
  else
    break;
if *($R_l \geq R_{\mathrm{a}}$) & ($R_l < 2R_{\mathrm{a}}$)* **then**
  $N_{\mathrm{a},l} = 1$;
if *($R_l \geq 2R_{\mathrm{a}}$) & ($R_l < 2.1547R_{\mathrm{a}}$)* **then**
  $N_{\mathrm{a},l} = 2$;
Output: Obtain the horizontal coordinates of the AAP location using $N_{\mathrm{a},l}$ value.

In each level of the AAP placement, the packing density maximization problem can be equivalently modeled as

$$\text{(C:P2)}: \underset{\vec{R}_j, j\in\{1,\ldots,N_{\mathrm{a},l}\}}{\text{maximize}} \quad \frac{N_{\mathrm{a},l}R_{\mathrm{a}}^2}{R_l^2}, \tag{C.18}$$

$$\text{s.t.} \quad \left\|\vec{R}_j - \vec{R}_k\right\| \geq 2R_{\mathrm{a}} \;\; \forall\, j \neq k \in \{1,\ldots,N_{\mathrm{a},l}\}, \tag{C.19}$$

$$\left\|\vec{R}_j\right\| + R_{\mathrm{a}} \leq R_l \quad \forall\, j \in \{1,\ldots,N_{\mathrm{a},l}\}, \tag{C.20}$$

$$R_l \geq R_{\mathrm{a}} = h_{\min}\cot[\phi(\delta_o)], \tag{C.21}$$

where $\vec{R}_j$ is the vector representing the location of the center of the coverage region of the j^{th} AAP in the given geographical area. The maximum packing density is achieved when the AAPs coverage areas are non-overlapping and lie inside the desired area, and the voids between the coverage area are minimized. The constraint (C.19) guarantees the zero overlapping between the AAPs coverage areas; (C.20) restricts the center of the AAP coverage region to be inside the void area. The constraint (C.21) restricts the minimum geographical area to be covered greater than the coverage region of a single AAP. (C:P2) takes the form of a circle packing problem [11] and is solved using Algorithm C.1. In Algorithm C.1, (C.19) is satisfied by placing the center of the inner circles of radius R_{a} on the vertices of a regular polygon of $N_{\mathrm{a},l}$ sides of side length equal to $2R_{\mathrm{a}}$ so that the tangency between the inner circles is achieved. The maximum value of $N_{\mathrm{a},l}$ satisfying (C.15) maximizes the objective function of (C:P2) while satisfying (C.20); $N_{\mathrm{a},l} \geq 3$ implies $R_l \geq R_{\mathrm{a}}(1 + \sec 30^o) = 2.1547R_{\mathrm{a}}$.

In step 2 of Algorithm C.1, the maximum number of non-interfering circles, $N_{\mathrm{a},1}$,

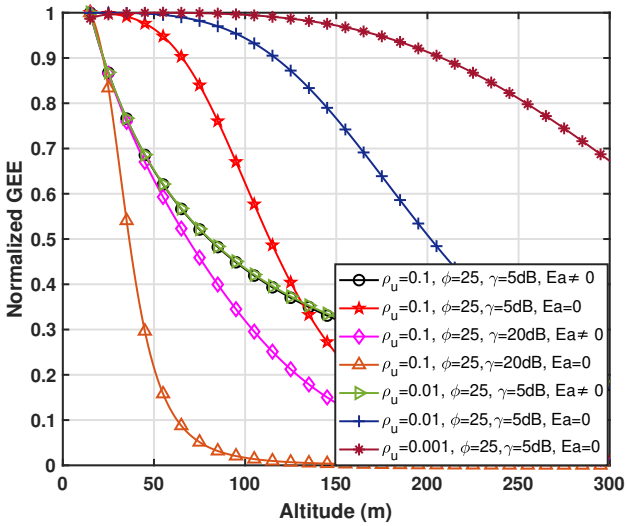

Fig. C.2: GEE variation with the hovering altitude.

that can be placed along the boundary of the desired area is determined using (C.15). In step 5, if the void formed at the center of the desired area after the l^{th} level circle arrangement contains a circle of radius $R - 2lR_{\mathrm{a}} \geq 2.1547R_{\mathrm{a}}$, then in the next level, $N_{\mathrm{a},l+1}$ circles can be placed in the center, where $N_{\mathrm{a},l+1}$ is determined using (C.15) with $R_{l+1} = R - 2lR_{\mathrm{a}}$. This multilevel circle packing continues until the maximum radius of the void circle at the center of the desired area is less than $2.1547R_{\mathrm{a}}$. In the l^{th} level, the coordinates of the horizontal location of the AAPs, which is same as the coordinates of the vertices of the regular polygon of $N_{\mathrm{a},l}$ sides can be obtained as $\left[R^{'}\cos\left(\frac{2\pi m}{N_{\mathrm{a},l}}\right), R^{'}\sin\left(\frac{2\pi m}{N_{\mathrm{a},l}}\right)\right]$ where $R^{'} = R - \frac{l(l+1)R_{\mathrm{a}}}{2}$, $m \in \{0, 1, .., N_{\mathrm{a},l} - 1\}$.

3 Simulation Result and Analysis

In this section, we provide some representative simulation results in support of our analysis. The considered simulation parameters are $g_0 = 1.42 \times 10^{-4}, \eta_{\mathrm{l}} = 0.1\mathrm{dB}, \eta_{\mathrm{nl}} = 21\mathrm{dB}, a = 4.88, b = 0.43$ [7], $W = 20\mathrm{MHz}, M = 6, P_{\mathrm{C}} = 5\mathrm{W}, T = 500\mathrm{s}, P_{\max} = 1\mathrm{mW}, h_{\max} = 300\mathrm{m}, h_{\min} = 15\mathrm{m}, \alpha_{\mathrm{cl}} = 315, \beta_{\mathrm{cl}} = -211.261, \alpha_{\mathrm{ho}} = 4.917, \beta_{\mathrm{ho}} = 275.204$ [2].

Figure C.2 contains the plots of the GEE with the hovering altitude of the AAP. The negative slope of the plots with non-zero AAP energy consumption ($E_{\mathrm{a}} \neq 0$) verifies the monotonically decreasing nature of the GEE with the hovering altitude. This is

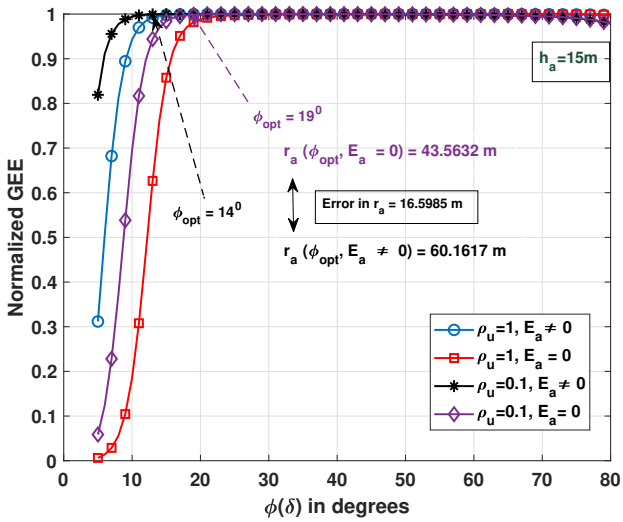

Fig. C.3: GEE variation for different $\phi(\delta)$ threshold.

because an increase in the number of UEs covered is highly compensated by an increase in the communication-related and AAP energy consumption. As seen in Figure C.2, in low signal-to-noise ratio ($\gamma = P_{\mathrm{a}}/\sigma_0^2 W$) regions, with the energy consumed by the aerial vehicle $E_{\mathrm{a}} = 0$, the GEE remains constant in low altitude region and then decreases leading to an error in determining the optimal hovering altitude. Since $E_{\mathrm{a}}(h_{\mathrm{a}}) >> E_{\mathrm{data}}$ in low UE density regions, the exclusion of aerial vehicle's energy consumption while defining the GEE will results in a non-optimal solution. On the other hand, with non-zero E_{a}, the GEE is a decreasing function of altitude. This explains the significance of E_{a} in the energy-efficient placement of AAPs, a novel aspect of this letter.

Figure C.3 shows the variation of the GEE with different P_{l} threshold δ, for a given AAP hovering altitude. Because of the saturation of P_{l}, and the proportional decrease in the number of covered UEs and the total transmit power, all the plots of Figure C.3 saturate after a particular $\phi(\delta)$ value. The saturation point shifts towards the left with non-zero E_{a} value, because of the additional energy term in the denominator of the GEE.

Figure C.4 gives the maximum packing density that can be achieved for the different radii of the desired area. It is observed that using Algorithm C.1, for $R = 180.48$m ($N_{\mathrm{a},1} = 6, N_{\mathrm{a},2} = 1$), a packing density almost equal to the Groemer's upper bound on the maximum density of packing of n equal circles in a circle [11] is achieved, For the remaining higher R values, the AAPs placed using Algorithm C.1 covers around 78 % of the desired area.

Figure C.5 shows the sample multi-level AAP placement pattern obtained through

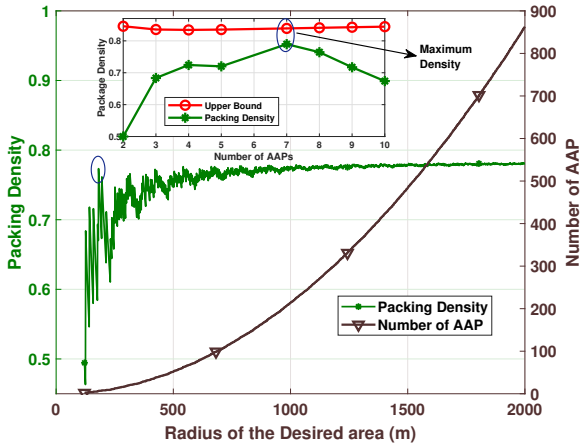

Fig. C.4: Packing Density for different desired area.

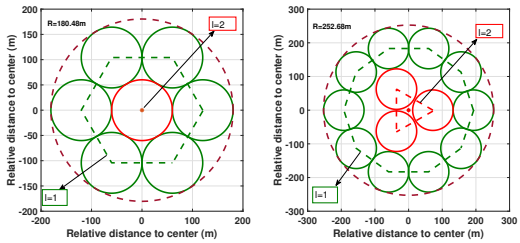

Fig. C.5: Horizontal Positioning of AAPs.

Algorithm C.1 for two different values of the desired area. Considering the origin as the center of the desired area, for $R = 180.48$m, the center coordinate set of the AAPs placed in the first level, forms the vertices of a regular hexagon and the next level contains a single AAP placed directly above the center of the desired region providing the packing density of 78.96%. For $R = 252.68$m, the first level of AAP placement follows an octagon, whereas the second level of AAP placement follows an equilateral triangle covering 68.44% of the desired area. The packing density can be further improved by controlled overlapping between AAP coverage regions.

4 Conclusion

In this letter, we proposed the 3-D placement of a set of AAPs deployed for an energy-efficient uplink communication considering the inter-cell interference and AAP energy

consumption. The energy-efficient hovering altitude of AAPs is analytically derived and the optimal horizontal positioning problem takes the form of a circle packing problem for maximum packing density, and solved using the multilevel regular polygon-based placement algorithm. The extension of our analysis to a downlink UAV-communication with non-uniformly distributed UEs along with the full coverage of the desired area by controlled overlapping between AAP coverage regions is left as future work.

References

[1] M. Erdelj and E. Natalizio, "UAV-Assisted Disaster Management: Applications and Open Issues," in *International Conference on Computing, Networking and Communications (ICNC),* Feb 2016, pp. 1–5.

[2] H. V. Abeywickrama, B. A. Jayawickrama, Y. He, and E. Dutkiewicz, "Comprehensive Energy Consumption Model for Unmanned Aerial Vehicles, Based on Empirical Studies of Battery Performance," *IEEE Access,* vol. 6, pp. 58 383–58 394, 2018.

[3] M. Alzenad, A. El-Keyi, F. Lagum, and H. Yanikomeroglu, "3-D Placement of an Unmanned Aerial vehicle Base Station (UAV-BS) for Energy Efficient Maximal Coverage," *IEEE Wireless Communications Letters,* vol. 6, no. 4, pp. 434–437, 2017.

[4] M. Mozaffari, W. Saad, M. Bennis, and M. Debbah, "Efficient Deployment of Multiple Unmanned Aerial Vehicles for Optimal Wireless coverage," *IEEE Communications Letters,* vol. 20, no. 8, pp. 1647–1650, 2016.

[5] J. Lu, S. Wan, X. Chen, and P. Fan, "Energy-Efficient 3D UAV-BS Placement Versus Mobile Users' Density and Circuit Power," in *IEEE Globecom Workshops (GC Wkshps),*pp. 1–6, 2017.

[6] N. Babu, K. Ntougias, C. B. Papadias and P. Popovski, "Energy Efficient Altitude Optimization of an Aerial Access Point," in *IEEE 31st Annual International Symposium on Personal, Indoor and Mobile Radio Communications,* pp. 1-7, 2020.

[7] A. Al-Hourani, S. Kandeepan, and S. Lardner, "Optimal LAP Altitude for Maximum Coverage," *IEEE Wireless Communications Letters,* vol. 3, no. 6, pp. 569–572, Dec 2014.

[8] 3GPP, "Physical layer procedures," , TR 36.213, Sep. 2015, v 10.12.0.

[9] N. Zhang, J.Wang, G. Kang, and Y. Liu, "Uplink Non-Orthogonal Multiple Access in 5g Systems," *IEEE Communications Letters,* vol. 20, no. 3, pp. 458–461, 2016.

[10] M. F. Sohail, C. Y. Leow, and S. Won, "Energy-Efficient Non-Orthogonal Multiple Access for UAV Communication System," *IEEE Transactions on Vehicular Technology,* vol. 68, no. 11, pp. 10 834–10 845, 2019.

[11] Z. Gáspár and T. Tarnai, "Upper Bound of Density for Packing of Equal Circles in Special Domains in the Plane," in *Periodica Polytechnica Civil Engineering,* vol. 44, no. 1, pp. 13–32, 2000.

Paper D

Cost- and Energy-Efficient Aerial Communication Networks with Interleaved Hovering and Flying

Nithin Babu, Marco Virgili, Constantinos B. Papadias, Petar Popovski, and Andrew Forsyth

Published in
IEEE Transactions on Vehicular Technology, vol. 70, no. 9, pp. 9077-9087, Sept. 2021, doi: 10.1109/TVT.2021.3100255.

The layout has been revised.

Abstract

This work proposes a methodology for the energy-and cost-efficient 3-D deployment of an unmanned aerial vehicle (UAV)-based aerial access point (AAP), that exchanges a given amount of independent data with a set of ground user equipment (UE). Considering a fly-hover-communicate transmission scheme, the most energy-efficient 3-D hovering points (HPs) of the AAP are determined by decoupling the problem in the horizontal and vertical dimensions. First, we derive analytically the optimal hovering altitude that jointly maximizes the downlink and uplink global energy efficiency (GEE) of the system. Next, we propose the multilevel circle packing (MCP) algorithm to determine the minimal number of HPs and their associated horizontal coordinates, such that the AAP covers all the UEs in the given geographical area. A cost analysis is carried out to observe the variation of both fixed and variable costs; these are then minimized by suitably selecting the AAP's battery parameters, like the depth of discharge (DOD), defined as the portion of battery capacity that is consumed during a discharge cycle, and the velocity of the UAV. Simulation results show that: the UAV energy consumption has a significant impact on the 3-D HPs of the AAP; the time spent during the substitution swap of an out of power AAP has a major influence on the operational cost; the cost of the system can be optimized by suitably selecting the onboard battery and the UAV flight parameters.

1 Introduction

The use of unmanned aerial vehicles (UAVs) deployed for providing temporary telecommunication services in a disaster-affected area or a special situation event is considered as an important application of the 5G and beyond technology [1], [2]. The mobile feature of UAV-based communication systems provides opportunities for better communication channels to the UEs as compared to conventional systems. The improved channel gain is due to the higher line-of-sight (LoS) probability [4], shorter distance between the aerial access point (AAP) and the pieces of user equipment (UEs), and ability to choose a preferred link. On the other hand, the service time of a UAV-based AAP is determined by the available onboard energy. Due to this energy constraint, the deployment of the AAP should be done in an energy-efficient way to maximize the number of bits transmitted per Joule of energy consumed, as captured by the global energy efficiency (GEE) of the network [3]. As defined in [3], the GEE of an aerial communication network is the ratio of the sum rate in bits per second to the total power consumed. The total power consumed is the sum of the communication-related power and the power required by the UAV for flying and hovering.

The placement optimization of a UAV-based base station with the objective of optimizing communication-related parameters, such as sum rate and coverage, is well

investigated in the literature. For instance, the authors of [4] present an analytical approach to optimize the altitude of a UAV-based base station for a given maximum allowed path loss. A joint altitude and beam-width optimization for throughput maximization is considered in [5]. A method to find the optimal 3-D location of a UAV base station is developed in [6], which maximizes the coverage region and optimizes the transmission power. In [7], the authors have developed a learning-based Intent-aware Upper Confidence Bound (IUCB) algorithm that could be used for offloading tasks in an air-ground integrated vehicular edge computing system. Works studying the deployment of a multi-UAV system for optimal wireless coverage and throughput maximization include [9], [10]. The work in [8] maximizes the revenue of the mobile crowd-sensing (MCS) carrier and the UAV via a joint optimization of route planning and task assignment subject to practical constraints of battery capacity and sensing latency. A 3-D deployment plan for a flying base station that serves the users according to their service requirements is presented in [11]. The placement optimization of dynamic standalone drones equipped with a steerable antenna is proposed in [12].

In [13], the authors maximize the minimum average rate and individual uplink energy-efficiency of multiple ground nodes supported by a UAV. The works [17], [18] maximize the downlink GEE of a UAV-based communication system flying at a constant altitude using the sequential convex programming-based trajectory optimization techniques. The trajectory optimizations considered in [14], [15], and [16] maximize the downlink throughput. In our previous work [3], we have determined the energy-efficient hovering altitude for a standalone AAP deployed for orthogonal downlink broadcast transmission. In another work [19], we have optimized the 3-D locations of a multi-UAV system which maximize the uplink GEE of the system in the presence of inter-cell interference. A detailed survey on the works that consider energy-efficient UAV deployment is available in [20].

Besides the placement optimization of the AAP, cost minimization is of great importance for the effective deployment of the aerial communication network. In order to minimize the installation cost of UAVs and charging stations, an efficient mixed-infrastructure placing was proposed in [21]. In [22], an economic analysis aimed at optimizing both coverage and capital cost is carried out, while [23] provides a novel technical solution for a sensor network and provides information on the price of all its components. However, the capital cost is just one part of the total expenses, which depend on how the system operates: parameters such as the number of UAVs, the UAV swap time, and the depth of discharge (DOD) need to be optimized.

The works [4]- [16] position UAVs for optimizing communication-related parameters such as sumrate, transmit power, or coverage region without considering the energy-consumption factors of the UAVs. [13], [17], and [18] maximize the GEE by considering a simple line-of-sight (LoS) single UAV system. Furthermore, from [20], none of the existing works, to the best of our knowledge, have considered a UAV placement problem that jointly maximizes the uplink and downlink GEE by considering both the com-

munication and UAV-related energy consumption factors. Moreover, the UAV energy consumption models used are not directly applicable to a multi-rotor UAV-based system. In addition to this, operational cost minimization by optimizing the system parameters of a UAV network has, to the best of our knowledge, not yet been considered in the literature.

1.1 Main Contributions and Paper Organization

The work proposes an energy- and cost-efficient rotary-wing UAV-assisted aerial communication network deployed to provide temporary service to a set of ground UEs. The main contributions are:

- We propose and use hovering and flying power consumption models that apply to any multi-rotor UAV. The power consumption models used in [17] cannot be applied directly to a multi-rotor UAV since they are based on the axial momentum theory applied to a single-rotor UAV.
- The altitude and beamwidth optimization considering both the communication-related and UAV energy consumption factors that maximize both the uplink and the downlink GEE has, to the best of our knowledge, not been investigated in the literature.
- A general framework for the optimal horizontal positioning of UAV in a target area is proposed through the polynomial-time complex multi-level circle packing (MCP) algorithm. The algorithm applies to the maximization of different objectives in which the coverage radius depends on the objective function to be maximized. We consider the GEE as the performance matrix and determine the UAV coverage radius which maximizes both the uplink and downlink GEE of the system.
- A detailed economic analysis of the aerial network is provided; furthermore, the operational cost minimization by optimizing the number of UAVs, the UAV swap time, the UAV flying velocity, and the depth of discharge of the UAV battery has, to the best of our knowledge, not yet been considered in the literature.

Section 2 describes the system setup and assumptions taken for this study, while in subsection 2.3, we derive the expression to estimate the power consumed by a multi-rotor UAV during its hovering, horizontal and vertical movements. The optimal altitude and beamwidth that maximize both the uplink and the downlink GEE are determined in Section 3.1 and Section 4, respectively. Using the optimal altitude and beamwidth determined from Section 3.1, in Section 3.2 we propose a general framework for determining the minimum number and location of hovering points (HPs) to cover all the UEs in a given geographical region, using a polynomial-time complex MCP algorithm. The different factors that affect the deployment and operational cost of the considered

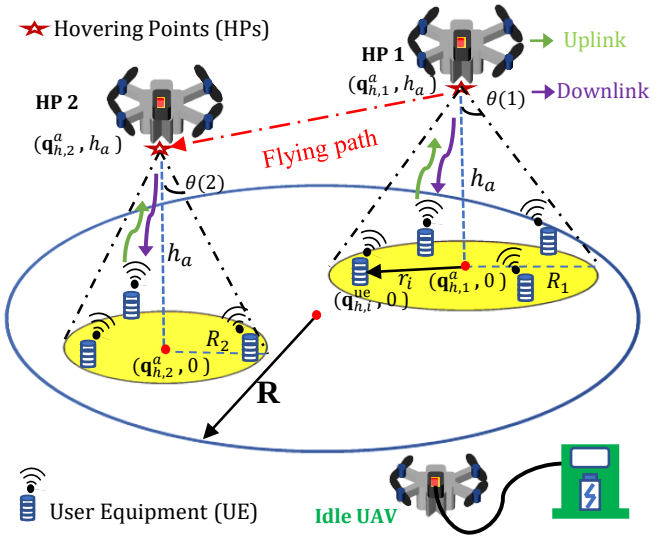

Fig. D.1: System setup.

network are discussed in Section 4[1]. The annualized cost of the system is minimized by suitably selecting the onboard battery parameter and the optimal horizontal flying velocity of the UAV. A detailed discussion of the main findings and the future scopes of work are provided in Sections 5 and 6. In this paper, boldface lowercase letters are used to denote vectors.

2 System Modelling and Definitions

We consider a delay-tolerant network consisting of a set of uniformly distributed UEs with a density of λ_{u}UEs/m^2 over a circular geographical area of radius R m. We assume that each UE needs to send/receive data bits to/from the AAP every T_{n} seconds (s). Our objective is to deploy a single moving AAP in an energy- and cost-efficient way so that all the UEs are served by the AAP once every T_{n} s. In order to do so, the AAP will follow a *fly-hover-communicate* protocol, meaning it will fly from one HP to another, hovers for the time needed to exchange the data packets, then moves on to the next destination as shown in Fig. D.1. The AAP is deployed to serve the UEs for t_{miss} hrs/day and, if the active time (t_{active}) of the serving-UAV is less than t_{miss}, then the idle UAV will replace the out-of-power UAV while the latter descends to recharge.

[1]This work considers the GEE HPs determination problem and the DOD optimization problem not jointly, but sequentially; the later one takes the set of energy-efficient HPs as the input to find the cost-efficient DOD.

We assume the AAP is equipped with a directional antenna with the antenna gain in the direction $(\epsilon, \kappa,)$ given by,

$$G_{\mathrm{a}} = \begin{cases} \dfrac{G_{\mathrm{o}}}{\theta^2} & -\theta \leq \epsilon \leq \theta, -\theta \leq \kappa \leq \theta, \\ g \approx 0 & \text{otherwise}, \end{cases} \tag{D.1}$$

where $G_{\mathrm{o}} \approx 2.2846$ [5], and since the side lobe gain of the antenna is assumed very small compared to the main lobe gain, we can also assume $g \approx 0$. The half-power beamwidth of the antenna in the elevation and the azimuth plane is 2θ. The UEs are equipped with an omnidirectional antenna of unitary gain. Hence the coverage area of a single AAP hovering at an altitude h_a will be a circular region of radius $R_{\mathrm{a}} = h_{\mathrm{a}}\tan\theta$ as shown in Fig. D.1. In addition, we assume an orthogonal multiple access transmission scenario between the AAP and its served UEs, where each UE in the geographical area is allocated a fixed bandwidth (e.g., in a narrowband frequency division multiple access system [26]).

The line-of-sight (LoS) and non-LoS (NLoS) air to ground channel links are considered to model the probabilistic mean path loss between the AAP and the UEs [4], given by [19]:

$$\overline{L}_i = P_{\mathrm{l}}(\phi_i) \times \frac{d_i^2 \eta_{\mathrm{l}}^2}{g_{\mathrm{o}}} + (1 - P_{\mathrm{l}}(\phi_i)) \times \frac{d_i^2 \eta_{\mathrm{nl}}^2}{g_{\mathrm{o}}}, \tag{D.2}$$

$$= \frac{d_i^2}{g_{\mathrm{o}}} \underbrace{\left[P_{\mathrm{l}}(\phi_i)\left(\eta_{\mathrm{l}}^2 - \eta_{\mathrm{nl}}^2\right) + \eta_{\mathrm{nl}}^2\right]}_{L_{\mathrm{m}}(\phi_i)}, \tag{D.3}$$

where $P_{\mathrm{l}}(\phi_i) = 1/\left\{1 + a\exp\left[-b(\phi_i - a)\right)\right]\}$ is a modified Sigmoid function that closely represents the LoS probability between the AAP and the i^{th} UE located at a distance of r_i from the center of the AAP coverage area, corresponding to an elevation angle of $\phi_i = (180/\pi)\tan^{-1}(h_{\mathrm{a}}/r_i)$ with the AAP hovering at an altitude h_{a}; the parameters a and b are directly linked to the environment variables such as the mean number of buildings, their height distribution, and the ratio of built-up land area to the total land area using the two variable surface fitting [4]; g_{o} is the channel gain at a reference distance of 1m; $d_i = \sqrt{r_i^2 + h_{\mathrm{a}}^2}$. Since the work considers the planning phase of the AAP deployment, we consider long term channel random variation rather than the small scale fading component [4], [6], [19]; η_{l} and η_{nl} are the mean values of the excess loss due to the man-made structures associated with the LoS and NLoS links, respectively.

2.1 Downlink Data Rate

Consider an AAP deployed to send independent information to a set of UEs through orthogonal channels be hovering at the HP1 position as shown in Fig. D.1. The equivalent average SNR defined as the ratio of average received signal power to the noise

power, received by a UE located at a distance of r_i from the center of the coverage region is $\gamma_i^{\mathrm{d}} = \dfrac{G_{\mathrm{a}} P_i^{\mathrm{d}}}{\Gamma_i \sigma^2 \overline{L}_i}$; $\Gamma_i \geq 1$ represents the gap between the channel capacity and the achievable rate due to the practical coding scheme and modulation scheme used; σ^2 is the variance of the zero-mean additive white Gaussian noise; P_i^{d} is the power allocated for the i^{th} UE. Hence the corresponding achievable data rate of the UE in bits per second is given by:

$$S_i^{\mathrm{d}} = B\log_2\left(1+\gamma_i^{\mathrm{d}}\right), \tag{D.4}$$

where B is the bandwidth allocated to each UE. The average sum rate, $\overline{S}_{\mathrm{d}}$, defined as the expectation of the sum of the achievable rate by all the UEs in the AAP coverage area is obtained by taking an expectation over the uniformly distributed UEs with a density λ_{u}:

$$\overline{S}_{\mathrm{d}} = B\lambda_{\mathrm{u}} \int_0^{R_{\mathrm{a}}} 2\pi S_i^{\mathrm{d}} r_i dr_i, \tag{D.5}$$

where $R_{\mathrm{a}} = h_{\mathrm{a}}\tan\theta$. The integral in (D.5) is difficult to evaluate because of the excess path loss factor, $L_{\mathrm{m}}(\phi_i)$. Since the LoS probability is a decreasing function of r_i, we approximate $P_{\mathrm{l}}(\phi_i) \approx P_{\mathrm{l}}(\phi_{\mathrm{edge}})\,\forall i$, where $P_{\mathrm{l}}(\phi_{\mathrm{edge}})$ is the LoS probability of the edge UE [19] with $\phi_{\mathrm{edge}} = 90^o - \theta$ (in deg). Thus the average rate value evaluated using (D.5) with $L_{\mathrm{m}}(\phi_i) = L_{\mathrm{m}}(\phi_{\mathrm{edge}})\,\forall i$ is the lower bound of the actual rate value expressed as,

$$\overline{S}_{\mathrm{d}} = 2\pi\lambda_{\mathrm{u}} B \int_0^{R_{\mathrm{a}}} \log_2\left(1+\frac{G^{'}}{(r_i^2+h_{\mathrm{a}}^2)}\right) r_i dr_i, \tag{D.6}$$

$$\begin{aligned} &= B^{'}\left(G^{'}+h_{\mathrm{a}}^2\sec^2\theta\right)\log(G^{'}+h_{\mathrm{a}}^2\sec^2\theta) \\ &- B^{'}\left(G^{'}+h_{\mathrm{a}}^2\right)\log(G^{'}+h_{\mathrm{a}}^2) \\ &- B^{'}\left[\left(h_{\mathrm{a}}^2\sec^2\theta\right)\log(h_{\mathrm{a}}^2\sec^2\theta) - h_{\mathrm{a}}^2\log(h_{\mathrm{a}}^2)\right], \end{aligned} \tag{D.7}$$

where $G^{'} = \dfrac{G_{\mathrm{a}} P_i^{\mathrm{d}} g_{\mathrm{o}}}{\Gamma_i \sigma^2 L_{\mathrm{m}}(\theta)}$, $B^{'} = B\pi\lambda_{\mathrm{u}}\log_2 e$.

2.2 Uplink Data Rate

A different deployment scenario in which the AAP hovering at HP1 of Fig. D.1 is deployed to collect independent data from a set of ground UEs is considered in this section. We consider the uplink power control implemented according to the 3GPP technical report [24], through which each UE chooses its uplink transmit power so that the received SNRs at the AAP from all the UEs in the coverage region are equal. Hence,

the average transmit power chosen by a UE located at a distance of d_i from the AAP location in the uplink power control scheme is represented in its basic form as $P_i^{\mathrm{u}} = P_{\mathrm{a}}\overline{L}_i$; where P_{a} is the target power to be received at the AAP. Because of the uplink power control, the received SNR from all the UEs will be the same: $\gamma_i^{\mathrm{u}} = \dfrac{G_{\mathrm{a}}P_{\mathrm{a}}}{\Gamma_i\sigma^2}$ and the uplink data rate will be different from the downlink data rate:

$$S_i^{\mathrm{u}} = B\log_2\left(1+\gamma_i^{\mathrm{u}}\right). \tag{D.8}$$

In addition to this, all the UEs lying in the coverage area of the AAP will have the same data rate given by (D.8); hence the sum of the data rate is given by,

$$\overline{S}_{\mathrm{u}} = B\pi\lambda_{\mathrm{u}}h_{\mathrm{a}}^2\tan^2\theta S_i^{\mathrm{u}}. \tag{D.9}$$

2.3 UAV Power Consumption Model

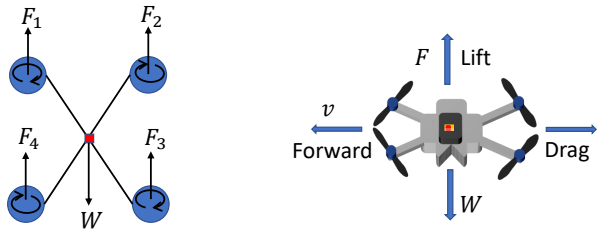

Fig. D.2: Forces acting on a multi-rotor UAV ($N_R = 4$).

The UAV carrying the radio access node ascends vertically to a HP, hovers there, and then moves horizontally from one HP to another. In this section, we provide the general expressions to calculate the total power consumed by a UAV during its hovering, horizontal and vertical movements. The definitions and values of all the variables used in this section are given in Table D.1. From the free-body diagram, as shown in Fig. D.2, of the considered multi-rotor UAV,

$$\sum_{n=1}^{N_{\mathrm{R}}} F_n - W = 0. \tag{D.10}$$

The total power consumed by the UAV during its horizontal flying from one HP to another, as shown in Fig. D.1, is derived using the axial momentum theory [17], [30]. Applying (D.10) in (67) of [17], the power required for forward flight, by assuming

Table D.1: UAV Parameters [30].

Label	Definition	Value
W	Weight of the UAV in Newton	35.28 N
N_{R}	Number of rotors	4
F_{n}	Upward thrust by the n^{th} rotor	-
v	UAV's horizontal flying velocity	-
v_{tip}	Tip speed of the rotor	102 m/s
A_{f}	Fuselage area	0.2113 m^2
$\rho(h_a)$	Air density	-
C_D	Drag Co-efficient	0.022
A_r	Rotor disc area	0.083 m^2
Δ	Profile drag coefficient	0.012
s	Rotor solidity	0.05

identical rotors ($F_n = F\ \forall n$), is given by,

$$P_{\mathrm{hfly}}(v) = \underbrace{N_{\mathrm{R}} P_{\mathrm{b}} \left(1 + \frac{3v^2}{v_{\mathrm{tip}}^2}\right)}_{P_{\mathrm{blade}}} + \underbrace{\frac{1}{2} C_D A_{\mathrm{f}} \rho(h_{\mathrm{a}}) v^3}_{P_{\mathrm{fuselage}}} + \underbrace{W \left(\sqrt{\frac{W^2}{4N_{\mathrm{R}}^2 \rho^2(h_{\mathrm{a}}) A_{\mathrm{r}}^2} + \frac{v^4}{4}} - \frac{v^2}{2}\right)^{1/2}}_{P_{\mathrm{induce}}}, \tag{D.11}$$

where $P_{\mathrm{b}} = \frac{\Delta}{8} \rho(h_{\mathrm{a}}) s A_{\mathrm{r}} v_{\mathrm{tip}}^3$, $\rho(h_{\mathrm{a}}) = (1 - 2.2558.10^{-5} h_{\mathrm{a}})^{4.2577}$. P_{blade} and P_{fuselage} are the powers required to overcome the profile drag forces of the rotor blades and the fuselage of the aerial vehicle that oppose its forward movement, respectively, while P_{induce} represents the power required to lift the payload. The hovering power is obtained by substituting $v = 0$ in (D.11):

$$P_{\mathrm{hov}}(h_{\mathrm{a}}) = N_{\mathrm{R}} P_{\mathrm{b}} + \frac{W^{3/2}}{\sqrt{2N_{\mathrm{R}} \rho(h_{\mathrm{a}}) A_{\mathrm{r}}}}. \tag{D.12}$$

Using (12.35) of [30], the power required by the aerial vehicle to climb vertically with a rate v_c m/s is expressed as,

$$P_{\mathrm{vfly}} = \frac{W}{2} \left(v_{\mathrm{c}} + \sqrt{v_{\mathrm{c}}^2 + \frac{2W}{N_{\mathrm{R}} \rho(h_{\mathrm{a}}) A_{\mathrm{r}}}}\right) + N_{\mathrm{R}} P_{\mathrm{b}}. \tag{D.13}$$

The effect of reduced air density at higher altitudes, which demands additional force to the propeller of the UAV, is captured by modeling the hovering power as an increasing

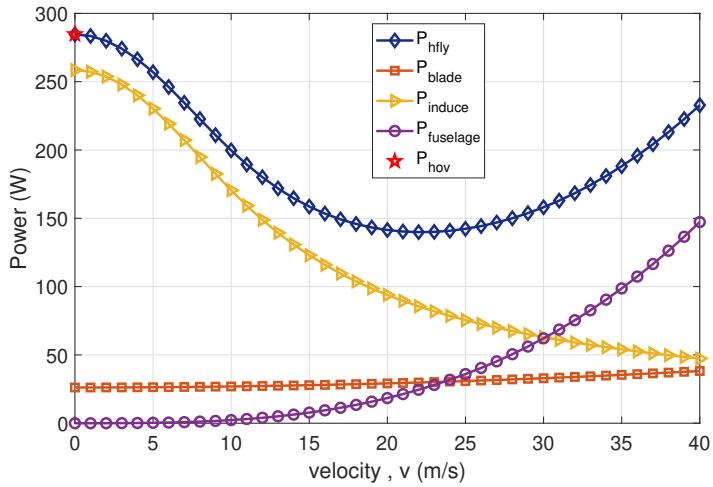

Fig. D.3: UAV Power consumption components.

function of the altitude, as reported in (D.12). It is known from (D.11) that the drag forces are increasing functions of v, and are the power components that oppose them. On the other hand, the P_{induce} is a decreasing function of v; hence, there exists an optimal velocity that minimizes $P_{\text{hfly}}(v)$, as shown in Fig. D.3.

3 Energy Efficient Hovering Points

In this section we find the energy-efficient 3-D HPs of the AAP in the given geographical area which maximize the uplink and the dowlink GEE subject to minimum Quality-of-Service (QoS), altitude, and power constraints. The corresponding downlink GEE maximization problem is formulated as follows:

$$\text{(D:P1)} : \underset{\{\mathbf{q}_{\text{a},j}\}}{\text{maximize}} \quad \frac{\sum\limits_{j\in\mathcal{A}} \alpha_j \sum\limits_{i\in\mathcal{U}} t_{\text{h}} \beta_i^j S_i^{\text{d}}}{\sum\limits_{j\in\mathcal{A}} t_{\text{h}} \left(P_{\text{hov}}(h_{\text{a}}) + \sum\limits_{i\in\mathcal{U}} \beta_i^j P_i^{\text{d}} \right) + t_{\text{f}} P_{\text{fly}}(v)},$$

$$\text{s.t.} \quad h_{\min} \le q_{v,j}^{\text{a}} \le h_{\max}, \ \forall j \in \mathcal{A}, \tag{D.14}$$

$$S_i^{\text{d}} \ge S_{\text{o}}^{\text{d}} \ \forall i \in \mathcal{U}, \tag{D.15}$$

$$\sum_{i\in\mathcal{U}} \beta_i^j P_i^{\text{d}} \le P_{\max}^{\text{d}} \ \forall j \in \mathcal{A}, \tag{D.16}$$

$$\sum_{j\in\mathcal{A}} \beta_i^j = 1 \qquad \forall i \in \mathcal{U}, \tag{D.17}$$

$$\|\mathbf{q}_{\text{h},j}^{\text{a}} - \beta_i^j \mathbf{q}_{h,i}^{\text{ue}}\| \le |q_{\text{v},j}^{\text{a}}| \tan\theta \ \forall j \in \mathcal{A}. \tag{D.18}$$

The numerator of (D:P1) is the sum of the data rate of all the UEs in the given geographical area. The binary indicator variable α_j is equal to 1 if the AAP is hovering at the j^{th} HP with coordinates $(\mathbf{q}^{\text{a}}_{h,j}, q^{\text{a}}_{\text{v},j})$, or to 0 otherwise; β^j_i is equal to 1 if the i^{th} UE located at $(\mathbf{q}^{\text{ue}}_{\text{h},i}, 0)$ is covered by the AAP while hovering at the j^{th} HP; $\mathcal{A}$ and $\mathcal{U}$ are the sets of the HPs and UEs, respectively. (D.14), (D.15), and (D.16) are the altitude, QoS and power constraints; $h_{\min}$ and $h_{\max}$ are the minimum and maximum permitted AAP altitudes. (D.17) expresses that each UE should be covered by the AAP while hovering at any of the $|\mathcal{A}|$ HPs. (D.18) is the coverage region constraint that couples the horizontal and vertical coordinates of a HP. The denominator of the ratio in (D:P1) is the sum of the hovering and the flying energy consumption, with t_{h} and t_{f} being the hovering time at a HP and the total flying time respectively. (D:P1) has the form of a mixed-integer non-linear fractional problem (MINLFP), which is exponentially complex to solve due to the constraint (D.18). Considering the uplink GEE to be jointly maximized with the downlink GEE would enhance the complexity further; hence we decouple the AAP placement problem in the vertical and horizontal dimensions [5], [19].

3.1 Optimal Vertical Coordinates of the Hovering Points

The energy-efficient hovering altitude of the AAP considering both the uplink and downlink communication between the AAP and the UEs is analytically derived in this section. Here we consider the instant in which the AAP is hovering at HP1 as shown in Fig. D.1 with 3-D coordinates $(\mathbf{q}^{\text{a}}_{\text{h},1}, q^{\text{a}}_{\text{v},1}) = (0, 0, h_{\text{a}})$. The problem that finds the optimal altitude that maximizes both the uplink and downlink GEE of the considered aerial communication network subject to the altitude, power, and QoS constraints can be formulated as,

$$\begin{aligned}
\text{(D:P2)}: \underset{h_{\text{a}}}{\text{maximize}} \quad & \left(\text{GEE}_{\text{d}}, \text{GEE}_{\text{u}}\right), \\
\text{s.t.} \quad & h_{\min} \leq h_{\text{a}} \leq h_{\max}, && \text{(D.19)} \\
& S^{\text{d}}_i \geq S^{\text{d}}_{\text{o}}; S^{\text{u}}_i \geq S^{\text{u}}_{\text{o}} \quad \forall i : r_i \leq R_{\text{a}}, && \text{(D.20)} \\
& P^{\text{d}}_t \leq P^{\text{d}}_{\max}, && \text{(D.21)} \\
& P^{\text{u}}_i \leq P^{\text{u}}_{\max} \quad \forall i : r_i \leq R_{\text{a}}, && \text{(D.22)}
\end{aligned}$$

where, $\text{GEE}_{\text{d}} = \overline{S}_{\text{d}}/P^{\text{d}}_{\text{t}}$ and $\text{GEE}_{\text{u}} = \overline{S}_{\text{u}}/P^{\text{u}}_{\text{t}}$ are the uplink and downlink GEE of the system, respectively, with P^{d}_{t}, P^{u}_{t} being the respective total downlink and uplink AAP power consumption while hovering, expressed by (D.23) and (D.24):

$$P^{\text{d}}_{\text{t}} = \underbrace{\pi \lambda_{\text{u}} h^2_{\text{a}} \tan^2\theta P^{\text{d}}_i}_{P^{\text{d}}_{\text{com}}} + P_{\text{hov}}(h_{\text{a}}), \tag{D.23}$$

$$P^{\text{u}}_{\text{t}} = \underbrace{\frac{2\pi \lambda_{\text{u}} P_{\text{a}} L_{\text{m}}(\theta) \tan^2\theta h^4_{\text{a}} [\tan^2\theta + 2]}{4 g_{\text{o}}}}_{P^{\text{u}}_{\text{com}}} + P_{\text{hov}}(h_{\text{a}}), \tag{D.24}$$

where $P_{\text{com}}^{\text{d}}$ and $P_{\text{com}}^{\text{u}}$ are the respective total communication-related power consumption values; $P_{\text{com}}^{\text{u}}$ of (D.24), is obtained by averaging the power profile over a uniform distribution of density λ_{u}, with the approximation $L_{\text{m}}(\phi_i) \approx L_{\text{m}}(\phi_{\text{edge}})\ \forall i : r_i \leq R_{\text{a}}$ [19]. (D.19) and (D.20) are the altitude and QoS constraints with $S_{\text{o}}^{\text{d}}, S_{\text{o}}^{\text{u}}$ being the respective minimum downlink and uplink data rates in bps; (D.21) and (D.22) are the total downlink and individual UE uplink power constraints. Considering the edge UE ($r_i = R_{\text{a}}$), the uplink QoS constraint becomes $P_{\text{a}} = \delta_{\text{u}}\Gamma_i\sigma^2/G_{\text{a}}$; furthermore, the downlink QoS constraint, (D.20), and the power constraints, (D.21) and (D.22), can be equivalently represented as the altitude constraints in (D.25), (D.26), and (D.27):

$$h_{\text{a}} \leq h_{\text{max},\delta_{\text{d}}}^{\text{d}} = \cos\theta\sqrt{\frac{G'}{\delta_{\text{d}}}}, \tag{D.25}$$

$$h_{\text{a}} \leq h_{\text{max},P}^{\text{d}} = \sqrt{\frac{P_{\text{max}}^{\text{d}} - P_{\text{hov}}}{\pi\lambda_{\text{u}}\tan^2\theta P_i^{\text{d}}}}, \tag{D.26}$$

$$h_{\text{a}} \leq h_{\text{max},P}^{\text{u}} = \cos\theta\sqrt{\frac{g_{\text{o}}P_{\text{max}}^{\text{u}}}{P_{\text{a}}L_{\text{m}}(\theta)}}, \tag{D.27}$$

where $\delta_{\text{d}} = 2^{S_{\text{o}}^{\text{d}}/B} - 1$ and $\delta_{\text{u}} = 2^{S_{\text{o}}^{\text{u}}/B} - 1$. Hence, (D:P2) can be reformulated as

$$\begin{aligned}(\text{D:P2.1}) : \underset{h_{\text{a}}}{\text{maximize}} \quad & (\text{GEE}_{\text{d}}, \text{GEE}_{\text{u}}), \\ \text{s.t.} \quad & h_{\text{min}} \leq h_{\text{a}} \leq \min\left\{h_{\text{max}}, h_{\text{max},\delta_{\text{d}}}^{\text{d}}, h_{\text{max,P}}^{\text{d}}, h_{\text{max,P}}^{\text{u}}\right\}.\end{aligned} \tag{D.28}$$

Proposition D.1. *For given θ, S_{o}^{d}, and S_{o}^{u} values;*
Statement A: The GEE of the system considering the downlink communication between the AAP and the ground UEs lying in the AAP coverage region is an increasing function of the hovering altitude.
Statement B: The GEE of the system considering the uplink communication between the AAP and the ground UEs lying in the AAP coverage region is an increasing function of the hovering altitude.

Proof. The derivative of the numerator and the denominator of the downlink GEE with respect to h_{a} are given by:

$$\frac{\overline{S}_{\text{d}}'}{2h_{\text{a}}B'} = \sec^2\theta\log\left(\frac{G' + h_{\text{a}}^2\sec^2\theta}{h_{\text{a}}^2\sec^2\theta}\right) - \log\left(\frac{G' + h_{\text{a}}^2}{h_{\text{a}}^2}\right), \tag{D.29}$$

$$P_t^{'\mathrm{d}} = 2\pi\lambda_{\mathrm{u}} h_{\mathrm{a}} \tan^2\theta P_i^{\mathrm{d}} + P_{\mathrm{hov}}^{'}(h_{\mathrm{a}}), \tag{D.30}$$

where $P_{\mathrm{hov}}^{'}(h_{\mathrm{a}}) = N_{\mathrm{R}} \dfrac{\Delta}{8} \rho^{'}(h_{\mathrm{a}}) s A_{\mathrm{r}} v_{\mathrm{tip}}^3 - \dfrac{W^{3/2} \rho^{'}(h_{\mathrm{a}})}{\sqrt{8 N_{\mathrm{R}} A_{\mathrm{r}}} \rho^{3/2}(h_{\mathrm{a}})}$ with $\rho^{'}(h_{\mathrm{a}}) = -9.6.10^{-5}(1 - 2.2558.10^{-5} h_{\mathrm{a}})^{3.2577}$. Hence the derivative of the downlink GEE with respect to h_{a} is

$$\begin{aligned} \left(P_{\mathrm{t}}^{\mathrm{d}}\right)^2 \left(\frac{\overline{S}_{\mathrm{d}}}{P_{\mathrm{t}}^{\mathrm{d}}}\right)^{'} &= \overline{S}_{\mathrm{d}}^{'} P_{\mathrm{t}}^{\mathrm{d}} - P_{\mathrm{t}}^{'\mathrm{d}} \overline{S}_{\mathrm{d}}, \\ &> 0 \quad \forall h \in \{h_{\min}, h_{\max}\}. \end{aligned} \tag{D.31}$$

The increasing nature of the uplink GEE with respect to h_{a} can be proved using similar steps used in the proof of Statement A with the following numerator and denominator derivatives:

$$\overline{S}_{\mathrm{u}}^{'} = 2B\pi\lambda_{\mathrm{u}} \tan^2\theta S_i^{\mathrm{u}} h_{\mathrm{a}}, \tag{D.32}$$

$$P_t^{'\mathrm{u}} = \frac{2\pi\lambda_{\mathrm{u}} P_{\mathrm{a}} L_{\mathrm{m}}(\theta) \tan^2\theta [\tan^2\theta + 2] h_{\mathrm{a}}^3}{g_{\mathrm{o}}} + P_{\mathrm{hov}}^{'}(h_{\mathrm{a}}). \tag{D.33}$$

Thus, by Proposition D.1, the globally energy-efficient hovering altitude for the AAP that maximizes both the uplink and downlink GEE (the objective function of (D:P2)) is $h_{\mathrm{opt}} = \min\left\{h_{\max}, h_{\max,\delta_{\mathrm{d}}}^{\mathrm{d}}, h_{\max,\mathrm{P}}^{\mathrm{d}}, h_{\max,\mathrm{P}}^{\mathrm{u}}\right\}$.

Optimal Beamwidth

For a given altitude, both the uplink and downlink GEE of the system vary with the beamwidth of the antenna at the UAV. As the beamwidth increases, the coverage area increases, the effective antenna gain given by (D.1) decreases, and the additional path loss factor, $L_{\mathrm{m}}(\theta)$, increases. Here we find the optimal beamwidth that jointly maximizes the uplink and downlink GEE of the system.

Proposition D.2. *For a given QoS constraint, the uplink-GEE is an increasing function of the beamwidth.*

Proof. The derivative of the uplink sum rate is given by:

$$\frac{d\overline{S}_{\mathrm{u}}}{d\theta} = 2B\pi\lambda_{\mathrm{u}} h_{\mathrm{a}}^2 \tan\theta \sec^2\theta \log_2(1 + \delta_{\mathrm{u}}) > 0. \tag{D.34}$$

Since $P_{\mathrm{com}}^{\mathrm{u}} << P_{\mathrm{hov}}(h_{\mathrm{a}})$, $P_{\mathrm{t}}^{\mathrm{u}} \approx P_{\mathrm{hov}}$ makes the denominator of the uplink GEE an independent function of θ. Hence, the optimal beamwidth that maximizes the uplink-GEE of the considered system is $\theta_{\mathrm{opt}}^{\mathrm{u}} = \theta_{\max}$. □

Using (D.7) and $P_{\mathrm{t}}^{\mathrm{u}} \approx P_{\mathrm{hov}}$, it can be pointed out that the downlink GEE is neither an increasing function nor a decreasing function of θ. Hence, for a given hovering altitude, the optimal θ that maximizes the downlink GEE can be determined using the ternary search method, as detailed in Algorithm D.1. Therefore, the antenna beamwidth

Algorithm D.1: Optimal Beamwidth.

Input: $\theta_{\min}$,$\theta_{\max}$;
Take any two points θ_1, and θ_2 : $\theta_{\min} < \theta_1 < \theta 2 < \theta_{\max}$. Calculate $\mathrm{GEE_d}(\theta_{\min})$, $\mathrm{GEE_d}(\theta_1)$, $\mathrm{GEE_d}(\theta_2)$, $\mathrm{GEE_d}(\theta_{\max})$;
if $GEE_{\mathrm{d}}(\theta_1) < GEE_{\mathrm{d}}(\theta_2)$ **then**
    $\theta_{\mathrm{opt}} \notin [\theta_{\min}, \theta_1)$:$\theta_{\min} = \theta_1$;
if $GEE_{\mathrm{d}}(\theta_1) > GEE_{\mathrm{d}}(\theta_2)$ **then**
    $\theta_{\mathrm{opt}} \notin (\theta_2, \theta_{\max},]$:$\theta_{\max} = \theta_2$;
if $GEE_{\mathrm{d}}(\theta_1) == GEE_{\mathrm{d}}(\theta_2)$ **then**
    $\theta_{\min} = \theta_1$; $\theta_{\max} = \theta_2$;
Repeat Step 2 to Step 7 until $|\theta_{\min} - \theta_{\max}| \leq \psi$.
Output: $\theta_{\mathrm{opt}}^{\mathrm{d}} = \theta_{\min}$.

that maximizes both the uplink and the downlink GEE is $\theta_{\mathrm{opt}} = \min(\theta_{\mathrm{opt}}^{\mathrm{u}}, \theta_{\mathrm{opt}}^{\mathrm{d}})$. Hence, the corresponding radius of the coverage region is given by $R_{\mathrm{opt}} = h_{\mathrm{opt}} \tan\theta_{\mathrm{opt}}$.

3.2 Optimal Horizontal Coordinates of the HPs

In this section, we determine the horizontal coordinates of the optimal HPs for the AAP $\left(\left\{\mathbf{q}_{\mathrm{h},j}^{\mathrm{a}}\right\}\right)$ so that all the UEs in the given geographical region will be covered by the AAP once every T_{n} s. The vertical coordinate of all the HPs will be equal to the optimal altitude determined from Section 3.1, i.e. $q_{\mathrm{v},j}^{\mathrm{a}} = h_{\mathrm{opt}}\ \forall j \in \mathcal{A}$. Since the coverage region of the considered AAP is circular in shape, a full coverage of the given area is only achievable through the controlled overlapping among the coverage regions centered at $\left\{\left(\mathbf{q}_{\mathrm{h},j}^{\mathrm{a}}, 0\right)\right\}$. The two main related challenges are finding the minimum number of HPs and their horizontal coordinates so that the given area is fully covered. We propose a MCP algorithm for doing so, using the circle packing theory. With the optimal coverage radius R_{opt} from Section 3.1, the problem takes the form of a circle packing problem, in which the given circle of radius R needs to be covered by smaller circles of radius R_{opt}. A regular-pentagon-based 5-circle packing pattern is considered in the proposed novel MCP algorithm. As shown in Fig. D.7, the 5-circle packing covers a circle of radius ΛR_{opt} by placing five equi-radius smaller circles of radius R_{opt} about the center of the larger circle, where $\Lambda = 1.618$ is the golden ratio [25]. The smaller circles are placed according to the solution of the 5-disks problem, which guarantees the least overlapping

between the adjacent circles [25]. The centers of the smaller circles arranged this way form the vertices of a regular pentagon of side length $2\sin(36^o)\Lambda\ R_{\text{opt}}$, with vertices located at $\left\{(x_k^l, y_k^l)\right\}$ where,

$$x_k^l = x^{l-1} + R_l \cos\left(\frac{2\pi k}{5}\right) \quad \text{for } k \in \{0, 1, ...4\}\,, \tag{D.35}$$

$$y_k^l = y^{l-1} + R_l \sin\left(\frac{2\pi k}{5}\right) \quad \text{for } k \in \{0, 1, ...4\}\,, \tag{D.36}$$

with (x^{l-1}, y^{l-1}) as the center of the pentagon and $R_l = R_{\text{opt}}$. Thus, to cover a circular region with $R > \Lambda R_{\text{opt}}$, we initially place this 5-circle pattern in multiple levels as shown in Fig. D.4, and then the radius of each circle is adjusted according to the farthest UE's position in the circle.

Proposition D.3. *Using the multi-level 5 circle packing method, the maximum number of HPs required to cover a given circular region of radius R by a fly-hover communicating AAP with a coverage radius of R_{opt} is given by 5^{M_p}, where $M_p = \left\lceil \frac{1}{log_2(\Lambda)} log_2\left(\frac{R}{R_{opt}}\right)\right\rceil$.*

Proof. According to the multi-level 5 circle packing method, the radius of the circle to be covered in each level is $1/\Lambda$ times the radius of the circle of the previous level. This multi-level packing continues until the radius of the circle to be covered is less than or equal to the coverage radius of the AAP, giving the inequality:

$$R\frac{1}{\Lambda^{M_p}} \leq R_{\text{opt}}. \tag{D.37}$$

Thus, the total number of levels required is given by:

$$M_{\text{p}} = \left\lceil \frac{1}{\log_2(\Lambda)} \log_2\left(\frac{R}{R_{\text{opt}}}\right)\right\rceil. \tag{D.38}$$

Hence the maximum number of smaller circles (HPs) of radius R_{opt} required to cover the given geographical region of radius R by the 5-circle multi-level packing is 5^{M_p}. □

MCP Algorithm

The MCP algorithm given in Algorithm D.2 can be grouped into two parts: in the first part (line 1 to line 10), the locations of the HPs are determined using the multi-level 5-circle packing method; in the second part (lines 11 to 16), the beamwidth of the antenna at each HP is adjusted based on the UE positions in the coverage area so that the constraints (D.17) and (D.18) are satisfied. Consider $R = 733$m, $h_{\text{opt}} = 102$m and $\theta = 70^o$; using (D.38), the total number of circle packing levels required to cover the

Algorithm D.2: Multilevel circle packing (MCP).

Input: R_{opt}, R, $l = 1$;
Find the number of required levels using (D.38);
while $l \leq M_p$ **do**
    if *l==1* **then**
        Find the center of circles using (D.35) & (D.36) with $(x^{l-1}, y^{l-1}) = (0, 0)$ & $R_l = R/\Lambda$;
    else
        $R_l = R_{l-1}/\Lambda$
        For each of the (x_k^{l-1}, y_k^{l-1}), find the center of 5 circles using (D.35) & (D.36) with $(x^{l-1}, y^{l-1}) = (x_k^{l-1}, y_k^{l-1})$;
    l=l+1;
$\mathcal{A} = \left\{(x_k^{M_p}, y_k^{M_p}, h_{\text{opt}})\right\}$;
For each $j \in \mathcal{A}$, find the unique set of UEs covered, $\mathcal{U}_j$;
if *isempty(* $\mathcal{U}_j$ *)* **then**
    $\mathcal{A} = \mathcal{A} - \{j\}$;
else
    $\theta(j) = \arctan\left(\frac{[\max(r_i), i \in \mathcal{U}_j]}{h_{\text{opt}}}\right)$;
Output: $\mathcal{A}$, the set optimal HPs to cover the UEs in the given geographical area.

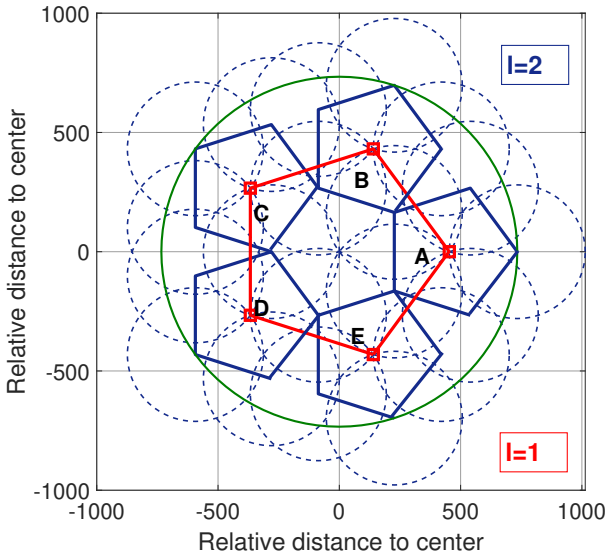

Fig. D.4: AAP coverage circles positioned using the first part of the MCP algorithm for $R = 733$m.

given area is 2. As shown in Fig. D.4, in the first level of placement ($l = 1$), the location of the centers of 5 smaller circles of radius $R_1 = R/\Lambda$ are determined using step 5 of the MCP algorithm (A,B,C,D,E of Fig. D.4). In the next level, step 8 is used to determine the location of the centers of 5 smaller circles of radius $R_2 = R_1/\Lambda$ that cover the circle of radius R_1. This step is repeated for each of the 5 determined centers from the first level. The centers of the smaller circles of radius R_2 are the HPs that cover the given geographical area. As seen in Fig. D.4, the determined HPs lie on the vertices of 5 smaller pentagons with circumcenters A, B, C, D, E. For any given R, this multi-level circle packing continues until the radius of the circle to be covered is less than, or equal to, the coverage radius of the AAP, or until $l = M_p$. In the second part, redundant coverage of the same UE by multiple HPs and the HPs without any UEs in the coverage region are removed. The coverage radius associated with each HP is readjusted as the radial distance of the farthest UE lying in the respective coverage areas by adjusting the antenna beamwidth using step 15. It should be noted that, with given R and R_{opt}, the first part takes a total running time of $O\left[\log_2\left(R/R_{\text{opt}}\right)\right]$ to find the initial set of HPs, whereas the second part needs to perform a total of $\sum_{f=0}^{|\mathcal{A}|-1}(|\mathcal{A}|-f)(|\mathcal{A}|-f-1)$ pair checks to remove the redundant UE coverage where $|\mathcal{A}| = 5^{M_{\text{P}}}$. Hence the complexity of the proposed MCP algorithm is, at worst $O\left[\log_2\left(R/R_{\text{opt}}\right) + 5^{\omega \log_2(R/R_{\text{opt}})}\right]$, a polynomial quantity of the input parameters R and R_{opt}; where $\omega = 2/\log_2\Lambda$. It should be noted that this algorithm could maximize different objective functions in which the coverage

radius of the AAP will be determined by the very objective function. Also, it can be adapted to different packing patterns by replacing the equations in step 5 and 8.

4 Economic Analysis and Cost Optimisation

In this section, we describe the cost optimization method developed for an aerial network and the parameters it uses. The total aerial network deployment cost consists of two parts: a) the cost of purchasing the required number of UAVs and recharging stations, called the capital cost; b) the maintenance and replacement cost associated with the long-term operation of the network, represented by the operational cost. The UAV is equipped with two TB47D LiPo Battery, for a total capacity $E_{\text{batt}} = 199.8$ Wh. Our objective is to minimize the network deployment cost by optimally planning the operational parameters.

The financial analysis is based on the annualized cost of the system (ACS), defined as the sum of the annualized capital, maintenance, and replacement costs [27]:

$$\text{ACS} = C_{\text{cap,a}} + C_{\text{main,a}} + C_{\text{rep,a}}. \tag{D.39}$$

The annualization is needed in order to report different expenses to the same time interval (year of reference) so that expenses happening at different times can be compared. $C_{\text{cap,a}}$ is given by (D.40), where the capital cost is multiplied by the capital recovery factor (CRF), i.e., the portion of capital that is paid back every year to the financier:

$$C_{\text{cap,a}} = \underbrace{(n_{\text{u}} C_{\text{u}}) + (n_{\text{s}} C_{\text{s}})}_{C_{\text{cap}}} \cdot \underbrace{\frac{I\,(1+I)^{\text{lt}}}{(1+I)^{\text{lt}} - 1}}_{\text{CRF}}, \tag{D.40}$$

with C_{u} and C_{s} being the purchasing cost per unit of, respectively, UAV and charging station. The financing method is based on debt, with a duration of 15 years (lifetime of the system), a nominal interest rate of 4% [28] and an inflation rate of 2%, meaning a real interest rate $I \approx 2\%$. n_{s} is the number of charging stations and n_{u}, the number of UAVs in the system (both active and idle), determined as:

$$n_{\text{u}} = \left(\frac{t_{\text{dead}}}{t_{\text{active}}} + 1\right) \left\lceil \min\left(|\mathcal{A}|, \frac{t_{\text{lap}}(v)}{T_{\text{n}}}\right)\right\rceil, \tag{D.41}$$

where t_{dead} represents all the *dead time* an AAP spends recharging and ascending/descending, as expressed in (D.42); t_{active} is the total *active time* of a UAV; $t_{\text{lap}}(v)$ is the time needed to complete a lap, stopping at all the HPs. Given (D.40) and (D.41), for a low T_{n} value, the number of UAVs, and thus the capital cost, is determined by the number of HPs ($|\mathcal{A}|$). Hence, by finding the minimum number of HPs required to cover all the UEs (Algorithm D.2), we minimize the capital cost. The t_{dead} value is calculated

assuming a maximum charging power $P_{\mathrm{ch,max}}$, a DOD that can go from 5% to 95%, and a fixed charging efficiency η_{ch}, as follows:

$$t_{\mathrm{dead}} = \frac{E_{\mathrm{batt}}\mathrm{DOD}}{P_{\mathrm{ch,max}}}\eta_{\mathrm{ch}} + t_{\mathrm{ex}}, \tag{D.42}$$

where t_{ex} is the unproductive time spent by the UAV climbing to take its position in the network and descending for recharge. The cost of the electricity consumed to recharge the batteries is given by the product of the energy provided by the charging station and the cost of electricity in the network deployment region (in the UK, $C_{\mathrm{el}} = 0.14$£/kWh):

$$C_{\mathrm{ch}} = \frac{t_{\mathrm{miss}}}{t_{\mathrm{active}}} C_{\mathrm{el}} \frac{E_{\mathrm{UAV}}(v, h_{\mathrm{a}})}{\eta_{\mathrm{ch}}}, \tag{D.43}$$

where $E_{\mathrm{UAV}}(v, h_{\mathrm{a}}) = |\mathcal{A}| t_{\mathrm{h}} P_{\mathrm{hov}}(h_{\mathrm{a}}) + t_{\mathrm{f}} P_{\mathrm{hfly}}(v) + t_{\mathrm{ex}} P_{\mathrm{vfly}}$ and $t_{\mathrm{miss}} = 2$hr is the duration of an entire mission. $C_{\mathrm{main,a}}$ represents both the yearly maintenance cost (assumed equal to 1% of the capital cost) and the cost of a recharge, adjusted for inflation f after n years using $C_{\mathrm{main,a}} = (C_{\mathrm{ch}} + 1\% C_{\mathrm{cap}})\,(1+f)^n$. The last element of (D.39) is represented by the annualized cost of battery replacement, $C_{\mathrm{rep,a}}$, calculated using,

$$C_{\mathrm{rep,a}} = C_{\mathrm{bat}} \frac{I}{(1+I)^{l_{\mathrm{bat}}} - 1}, \tag{D.44}$$

with l_{bat} being the lifetime of the battery and C_{bat} its replacement cost (£155). For simplicity, the lifetime of the battery is assumed to depend solely on the DOD, and it is simulated using the model presented in [29], reported in (D.45):

$$n_{\mathrm{c}} = 8.131 e^{4(-0.03809\mathrm{DOD})} + 2.151 e^{-8(0.2433\mathrm{DOD})}. \tag{D.45}$$

This returns the number of cycles n_{c} a $LiFePO_4$ battery can withstand at a certain DOD, which is then converted into years using the mission duration and its frequency.

$C_{\mathrm{cap,a}}$, $C_{\mathrm{main,a}}$, and $C_{\mathrm{rep,a}}$ can be minimized by suitably selecting the DOD value and the velocity of the UAV. $C_{\mathrm{cap,a}}$ can be minimized by increasing the DOD, since this increases t_{active}. It can be noted that t_{dead} also grows with the DOD, but at a slower rate, due to the attenuation effect of t_{ex}. However, (D.41) is a step function, so the variations in these parameters do not always affect n_{u}. By (D.43), $C_{\mathrm{main,a}}$ can be reduced by increasing t_{active} through the selection of a high DOD value. On the contrary, since the lifetime of the battery is increased by a low DOD value, the battery replacement cost $C_{\mathrm{rep,a}}$ can only be minimized by selecting a low DOD value. For a fixed network delay tolerance, T_{n}, the UAV velocity affects both the power consumption and the number of UAVs: though the minimum power consumption is reached at an average speed of 20 m/s (Fig. D.3), the minimum cost is expected to be achieved when the UAV is operated at its maximum velocity because a higher velocity minimizes the capital cost by reducing the $t_{\mathrm{lap}}(v)$ value. Considering these trade-offs, the values of DOD and horizontal flying velocity that minimize the ACS will be numerically determined in the next section.

Table D.2: Simulation Parameters.

Parameter	Value	Parameter	Value
g_{o}	1.42×10^{-4}	B	10^6 Hz
$h_{\max}$	120m	λ_{u}	$0.001\mathrm{UEs}/m^2$
$\delta_{\mathrm{d}}, \delta_{\mathrm{u}}$	9 dB	$h_{\min}$	10 m
$\Gamma_i \ \forall i \in \mathcal{U}$	1.2	$P^{\mathrm{d}}_{\max}$	500W
$P^{\mathrm{u}}_{\max}$	1W	C_{u}	£2000
C_{s}	£1000	C_{bat}	£155
η_{ch}	0.95	$P_{\mathrm{ch,max}}$	180W

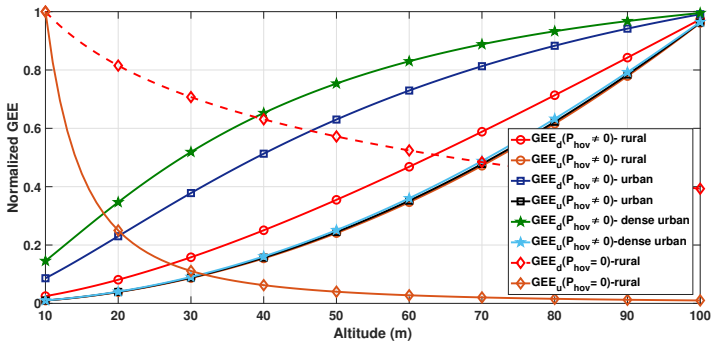

Fig. D.5: GEE variation with the hovering altitude.

5 Numerical Results and Discussion

In this section, we provide the results of the numerical evaluation in support of our analysis. The considered simulation parameters are given in Table D.2.

5.1 Energy Efficient Hovering Points

Fig. D.5 shows the variation of the normalized GEE with the hovering altitude for both the uplink and downlink communication parts, plotted using (D.7), (D.23), (D.9), and (D.24). The $(a, b, \eta_{\mathrm{l}}, \eta_{\mathrm{nl}})$ parameters used for rural, urban, and dense-urban regions are, respectively, $(4.83, 0.43, 1.01, 11.22)$, $(9.6, 0.16, 1.12, 10)$, $(12.08, 0.11, 1.2, 14.12)$ [4]. As proved in Proposition D.1, both the uplink and downlink GEE are increasing functions of the hovering altitude in the three geographical regions considered. As the altitude increases, the received SNR at each UE (downlink) decreases because of the increasing d_i value. In contrast, the received SNR at the AAP from the UEs (uplink) is independent of the hovering altitude because of the uplink power control mechanism. Nevertheless, a higher hovering altitude demands the UEs to transmit more power to deliver the target power (P_{a}) at the AAP. However, this increase in the communication-related power

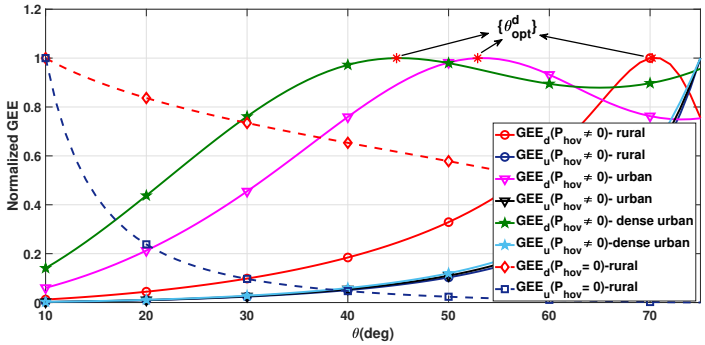

Fig. D.6: GEE variation with the antenna beamwidth.

consumption is negligible, if compared to the UAV hovering power ($P_{\text{hov}}(h_{\text{a}})$)). Both the AAP coverage area and the UAV power consumption increase with the altitude, but the effect of the larger area (higher number of covered UEs) is more relevant in both cases, which makes the downlink and uplink GEE monotonically increasing functions of the hovering altitude. It should be noted that, in both cases, if $P_{\text{hov}}(h_{\text{a}})$ is neglected, the increase in the communication power becomes significant and the GEE becomes in fact a decreasing function of the altitude. Thus $h_{\text{opt}}(P_{\text{hov}}(h_{\text{a}}) = 0) = h_{\min}$, which is not only energy-inefficient, but also requires more HPs to cover the given area (cost-inefficient).

Fig. D.6 shows the variation of the GEE with half of the half-power beamwidth, θ, in rural, urban, and dense-urban scenarios. As said in Section 4, the coverage radius is an increasing function of θ; however, for a given height, Fig. D.6 shows that the downlink GEE increases with θ up to $\theta^{\text{d}}_{\text{opt}}$ (obtained using Algorithm D.1), then decreases. This is because the LoS probability is a decreasing function of θ and, after $\theta^{\text{d}}_{\text{opt}}$, the high path loss NLoS links become dominant; hence, the gain in sum rate achieved by a greater number of covered UEs is overcompensated by a drop in the received SNR. On the other hand, the uplink GEE is an increasing function of θ: because of the power control mechanism, the uplink sum-rate grows with the number of UEs in the coverage region, which is, in turn, an increasing function of θ. However, the maximum value of θ will be decided by the $P^{\text{u}}_{\max}$ of the edge UE. Furthermore, the optimal beamwidth decreases as we move from rural to dense-urban regions due to the presence of taller and more numerous buildings. In both the uplink and downlink scenarios, the plots with $P_{\text{hov}}(h_{\text{a}}) = 0$ are decreasing functions of θ, forcing the elevation angle between the UEs and the AAP to be 0^o. This means that, with $P_{\text{hov}}(h_{\text{a}}) = 0$, the AAP should hover directly above the UE locations to maximize the GEE. This would be a sub-optimal result, as the number of HPs would be equal to that of UEs.

Fig. D.8 shows the final HP locations in the given geographical area of $R = 453$m, determined using the proposed MCP algorithm of Section. 3.2. The simulation considers 10 UEs randomly distributed in the given geographical area. As explained in Section

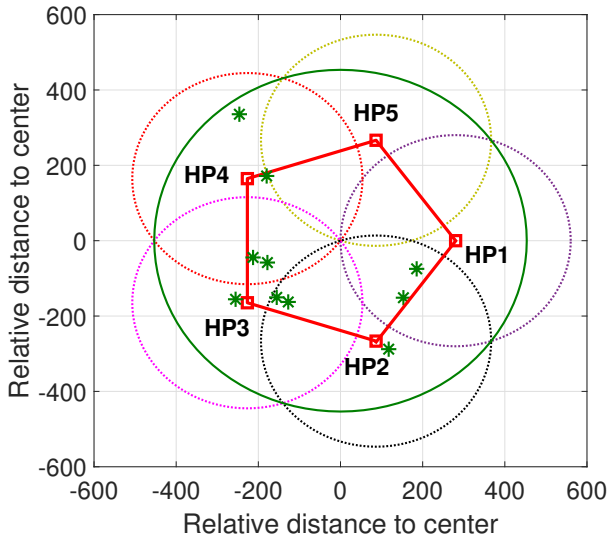

Fig. D.7: AAP coverage circles positioned using the first part of the MCP algorithm for $R = 453$m.

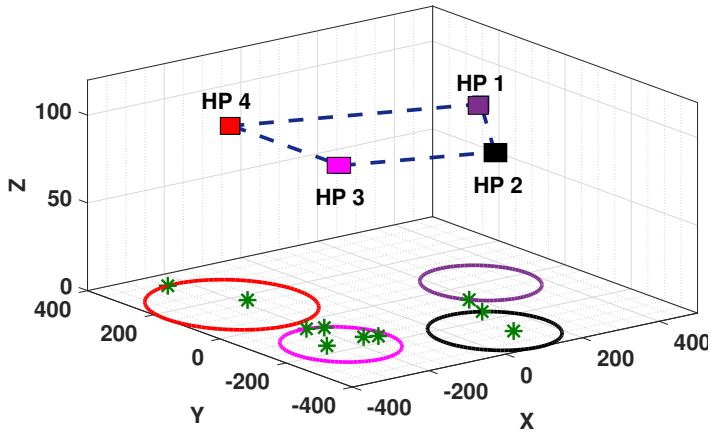

Fig. D.8: 3-D HPs using the MCP algorithm for $R = 453$m.

3.2 and shown in Fig. D.7, $R = 455$m requires one level of circle packing. Using the HPs from the first part of Algorithm D.2 as the input, the second part removes the redundant coverage of a UE by different HPs and then discards the HPs with no UEs in its coverage region. As seen in Fig. D.8, each UE is covered by only one of the HPs and one of these (HP5, in Fig. D.7), having no UEs in its coverage area, is removed, reducing the total number of HPs from 5 to 4. In addition, the coverage radius, hence the beamwidth, of each HP is adjusted considering the position of the farthest UE in each coverage region.

5.2 Cost Analysis Results

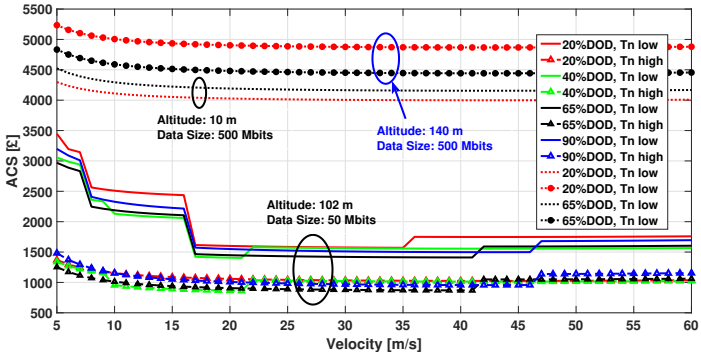

Fig. D.9: Cost evaluation with $T_{\mathrm{n}} = 100s$ and $T_{\mathrm{n}} = 10000s$.

Fig. D.9 shows the variations of the ACS with the UAVs velocity, the DOD of their batteries, the hovering altitude, the data packet sizes (D) to be exchanged between the UAV and the users, and the maximum allowed time between two UAV passages T_{n}. The cost analysis is carried out using the set of HPs from the previous section as input. The hovering time at an HP is determined as the time required to complete the uplink and the downlink transmission: $t_{\mathrm{h}=} D/S^{\mathrm{u}}_{\mathrm{edge}} + D/S^{\mathrm{d}}_{\mathrm{edge}}$. The DOD value that minimizes the annualized cost of the system described in (D.39) depends on the UAV velocity and t_{ex}. As the curves within the lower black circle in Fig. D.9 show, with a small data size (50 Mbits) the velocity should be kept just above 17m/s, due to the decrease of $t_{\mathrm{lap}}(v)$ in (D.41), which in turn decreases the number of UAVs. As velocity increases further, ACS keeps decreasing, albeit with a slowing pace, due to the flying time decreasing, while the hovering time is constant. At even higher velocity the power consumption grows, draining the battery quickly enough to require the deployment of extra UAVs and greater electricity consumption, affecting (D.40) and (D.43), and ultimately the ACS. If T_{n} is large enough (curves with triangles in Fig. D.9), then $t_{\mathrm{lap}}(v)/T_{\mathrm{n}} < 1$; hence, the number of active UAVs does not vary with the velocity. Nevertheless, the

first component of (D.41) is velocity-dependant, so the total number of UAVs still varies, although by a small margin. The upper curves in Fig. D.9 show what happens with larger data size: the hovering time increases, thus the flying time becomes negligible and so does the velocity, resulting in horizontal curves. These curves also show the effect of altitude: since every UAV swap represents a waste of energy and time proportional to t_{ex}, which, in turn, has a positive relationship with the altitude, a higher altitude negatively affects both the number of UAVs and the energy consumption, raising the cost. This effect is more relevant if the DOD is low, as swaps happen more often. The negative effect of higher swap frequency is represented by the gap between the black and the red curve at different altitudes: when the altitude is low (upper black circle) a low DOD results more advantageous, whereas the opposite is true at a higher altitude (blue circle). Therefore, the optimal DOD becomes higher as the mission altitude rises. With reference to (D.39), the trade-off to determine the optimal DOD is between two opposite forces: maximization of battery lifetime (l_{bat} in (D.44)) with low DOD; minimization of UAV fleet (n_{u} in (D.41)) and UAV swaps with high DOD. The latter effects become more relevant as altitude rises, and t_{ex} with it. Still, since the two forces are comparable, the optimal DOD is unlikely to be extremely high or low, and it must be determined as a function of the given T_{n}, D, and h_{opt} parameters. With the user distribution shown in Section 5.1, $T_{\mathrm{n}} = 100s$, and a data size of 50 Mbits, the overall cost is minimized when $v = 33\mathrm{m/s}$ and the DOD is 50%, resulting in an ACS of £1388.

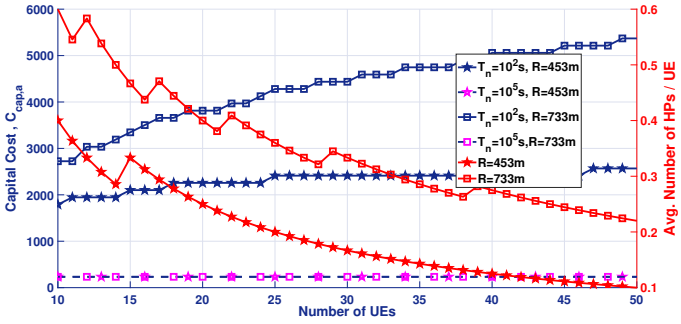

Fig. D.10: Capital Cost evaluation with 500 Mbits.

Fig. D.10 shows the variation of $C_{\mathrm{cap,a}}$ with regards to the number of UEs for different values of R. As seen in the figure, the capital cost depends mainly on the delay tolerance of the network: for a high T_{n}value, $C_{\mathrm{cap,a}}$ is independent of the number of UEs or the R-value since a single AAP could fly-hover communicate with the UEs sequentially. Furthermore, the average number of HPs does not increase linearly with the number of UEs because of the efficient MCP algorithm. Additionally, for a low T_{n} value, $C_{\mathrm{cap,a}}$ increases with a decrease in UE density since it needs more HPs to cover widely separated UEs. Hence the system is more cost-efficient when it is deployed to

cover a smaller geographical region with a relatively high number of UEs. The 3-D trajectory optimization of an AAP that communicates to a set of mobile users [31], [32] while flying is left for future work.

6 Conclusion

In this work, we carried out a cost and energy optimization of a UAV-based aerial communication network by taking into account both telecommunications and energy parameters. Observing that the GEE becomes an increasing function of the hovering altitude, the 3-D hovering locations of an AAP that maximize the uplink and downlink GEE are determined using the proposed MCP algorithm. The coordinates generated this way are used as input for the cost analysis, which calculates the number of UAVs needed and how deeply they should exploit their batteries (optimal DOD) and flying parameter (optimal velocity), in order to minimize the annualized total cost of the system. The optimal DOD showed to have an indirect dependency with the altitude, as this extends the UAV swap time (t_{ex}). The optimal UAV velocity was calculated for a low data size because its effect becomes less relevant at a higher data size.

References

[1] Erdelj, Milan, and Enrico Natalizio, "UAV-Assisted Disaster Management: Applications and Open Issues," in *2016 ICNC Kauai, HI, USA; 1-5.*

[2] Fotouhi, Azade, et al. "Survey on UAV Cellular Communications: Practical Aspects, Standardization Advancements, Regulation, and Security Challenges," *IEEE Commun. Surv. and Tut. 21.4 (2019)*: 3417-3442.

[3] N. Babu, K. Ntougias, C. B. Papadias and P. Popovski, "Energy Efficient Altitude Optimization of an Aerial Access Point," *IEEE 31st Annual International Symposium on Personal, Indoor and Mobile Radio Communications (PIMRC),* 2020, pp. 1-7.

[4] A. Al-Hourani, S. Kandeepan and S. Lardner, "Optimal LAP Altitude for Maximum Coverage," *IEEE Wireless Commun. Lett.*, vol. 3, no. 6, pp. 569-572, Dec. 2014.

[5] H. He, S. Zhang, Y. Zeng and R. Zhang, "Joint Altitude and Beamwidth Optimization for UAV-Enabled Multiuser Communications," *IEEE Commun. Lett.*, vol. 22, no. 2, pp. 344-347, Feb. 2018.

[6] M. Alzenad, A. El-Keyi, F. Lagum and H. Yanikomeroglu, "3-D Placement of an Unmanned Aerial Vehicle Base Station (UAV-BS) for Energy-Efficient Maximal Coverage," *IEEE Wireless Commun. Lett.*, vol. 6, no. 4, pp. 434-437, Aug. 2017.

[7] H. Liao et al., "Learning-Based Intent-Aware Task Offloading for Air-Ground Integrated Vehicular Edge Computing," in *IEEE Trans. on Intell. Transp. Syst.*. 2020 Oct 29.

[8] Z. Zhou et al., "When Mobile Crowd Sensing Meets UAV: Energy-Efficient Task Assignment and Route Planning," *IEEE Trans. on Commun.*, vol. 66, no. 11, pp. 5526-5538, Nov. 2018

[9] M. Mozaffari, W. Saad, M. Bennis and M. Debbah, "Efficient Deployment of Multiple Unmanned Aerial Vehicles for Optimal Wireless Coverage," *IEEE Commun. Lett.*, vol. 20, no. 8, pp. 1647-1650, Aug. 2016.

[10] Liu, Xiao, et al. "Trajectory design and power control for multi-UAV assisted wireless networks: A machine learning approach," *IEEE Trans. on Veh. Technol.* 68.8 (2019): 7957-7969

[11] E. Kalantari, H. Yanikomeroglu, and A. Yongacoglu, "On the Number and 3D Placement of Drone Base Stations in Wireless Cellular Networks," in *2016 IEEE 84th VTC-Fall, IEEE*, 2016, pp. 1–6.

[12] I. Donevski and J. J. Nielsen, "Dynamic Standalone Drone-Mounted Small Cells," in *2020 EuCNC, Dubrovnik, Croatia*, 2020, pp. 342-347.

[13] S. Eom, H. Lee, J. Park, and I. Lee, "UAV-Aided Wireless Communication Designs with Propulsion Energy Limitations," *IEEE Trans. on Veh. Technol.*, 2019.

[14] J. Lyu, Y. Zeng, and R. Zhang, "Cyclical Multiple Access in UAV-Aided communications: A throughput-Delay Tradeoff," *IEEE Wireless Commun. Lett.*, vol. 5, no. 6, pp. 600–603, Dec 2016.

[15] Wu, Qingqing, and Rui Zhang, "Common Throughput Maximization in UAV-Enabled OFDMA Systems with Delay Consideration," *IEEE Trans. on Commun. 66.12 (2018)*: 6614-6627.

[16] I. Valiulahi and C. Masouros, "Multi-UAV Deployment for Throughput Maximization in the Presence of Co-Channel Interference," *IEEE Internet of Things Journal,* vol. 8, no. 5, pp. 3605-3618, Mar., 2021.

[17] Y. Zeng, J. Xu and R. Zhang, "Energy Minimization for Wireless Communication with Rotary-Wing UAV," *IEEE Trans. on Wireless Commun.*, vol. 18, no. 4, pp. 2329-2345, April 2019.

[18] Y. Zeng and R. Zhang, "Energy-Efficient UAV Communication With Trajectory Optimization," *IEEE Trans. on Wireless Commun.*, vol. 16, no. 6, pp. 3747-3760, June 2017.

[19] N. Babu, C. B. Papadias and P. Popovski, "Energy-Efficient 3D Deployment of Aerial Access Points in a UAV Communication System," *IEEE Commun. Lett.*, vol. 24, no. 12, pp. 2883-2887, Dec. 2020.

[20] S. Shakoor, Z. Kaleem, M. I. Baig, O. Chughtai, T. Q. Duong and L. D. Nguyen, "Role of UAVs in Public Safety Communications: Energy Efficiency Perspective," *IEEE Access,* vol. 7, pp. 140665-140679, 2019.

[21] L. Chiaraviglio et al., "Minimum Cost Design of Cellular Networks in Rural Areas with UAVs, Optical Rings, Solar Panels, and Batteries," *IEEE Trans. Green Commun. Netw.*, vol. 3, no. 4, pp. 901–918, 2019.

[22] J. Polo, G. Hornero, C. Duijneveld, A. García, and O. Casas, "Design of a low-cost Wireless Sensor Network with UAV mobile node for agricultural applications," *Comput. Electron. Agric.*, vol. 119, pp. 19–32, Nov. 2015.

[23] Li, Ting, et al., "Optimizing the Coverage via the UAVs with Lower Costs for Information-Centric Internet of Things," *IEEE Access*, vol. 7, pp. 15292–15309, 2019.

[24] 3GPP, "Physical layer procedures," , TR 36.213, Sep. 2015, v 10.12.0.

[25] Tóth, G. Fejes, "Thinnest covering of a circle by eight, nine, or ten congruent circles," *Combinatorial and comput. geometry 52.361 (2005).*

[26] A. Goldsmith, *Wireless communications.* Cambridge university press,2005.

[27] Bilal, B. Ould, et al., "Multi-objective design of PV-wind-batteries hybrid systems by minimizing the annualized cost system and the loss of power supply probability (LPSP)," in *2013 IEEE ICIT*, 2013, pp. 861–868.

[28] C. Bouras, A. Kollia and A. Papazois, "Sensitivity analysis of small cells and DAS techno-economic models in mobile 5G," in *2016 IEEE Wireless Communications and Networking Conference*, 2016, pp. 1-6.

[29] N. Omar et al., "Lithium iron phosphate based battery - Assessment of the aging parameters and development of cycle life model," *Appl. Energy*, vol. 113, pp. 1575–1585, Jan. 2014.

[30] Filippone A, "Flight performance of fixed and rotary wing aircraft," *Elsevier*; 2006 May 10.

[31] Tang, Jie, et al., "On the Security–Reliability and Secrecy Throughput of Random Mobile User in Internet of Things," *IEEE Internet of Things J.*, vol. 7, no. 10, pp. 10635-10649, Oct. 2020.

[32] Tang, Jie, et al., "Impact of Mobility on Physical Layer Security Over Wireless Fading Channels," *IEEE Trans. on Wireless Commun.*, vol. 17, no. 12, pp. 7849-7864, Dec. 2018.

Paper E

Energy-Efficient Trajectory Design of a Multi-IRS Assisted Portable Access Point

Nithin Babu, Marco Virgili, Mohammad Al-jarrah, Xiaoye Jing, Emad Alsusa, Petar Popovski, Andrew Forsyth, Christos Masouros, and Constantinos B. Papadias

Under review in
IEEE Transactions on Vehicular Technology.

The layout has been revised.

Abstract

In this work, we propose a framework for energy efficient trajectory design of an unmanned aerial vehicle (UAV)-based portable access point (PAP) deployed to serve a set of ground nodes (GNs). In addition to the PAP and GNs, the system consists of a set of intelligent reflecting surfaces (IRSs) mounted on man-made structures to increase the number of bits transmitted per Joule of energy consumed measured as the global energy efficiency (GEE). The GEE trajectory for the PAP is designed by considering the UAV propulsion energy consumption and the Peukert effect of the PAP battery, which represents an accurate battery discharge profile as a non-linear function of the UAV power consumption profile. The GEE trajectory design problem is solved in two phases: in the first, a path for the PAP and feasible positions for the IRS modules are found using a multi-tier circle packing method, and the required IRS phase shift values are calculated using an alternate optimization method that considers the interdependence between the amplitude and phase responses of an IRS element; in the second phase, the PAP flying velocity and user scheduling are calculated using a novel multi-lap trajectory design algorithm. Numerical evaluations show that: neglecting the Peukert effect overestimates the available flight time of the PAP; after a certain threshold, increasing the battery size reduces the available flight time of the PAP; the presence of IRS modules improves the GEE of the system compared to other baseline scenarios; the multi-lap trajectory saves more energy compared to a single-lap trajectory developed using a combination of sequential convex programming and Dinkelbach algorithm.

1 Introduction

An unmanned aerial vehicle (UAV) carrying a radio access node, hereafter referred to as 'portable access point' (PAP), has been envisioned as a viable solution to save energy or improve user fairness in an Internet-of-Things (IoT) or federated learning application [1] [3]. Moreover, significant progress has been made in the standardization efforts of the Third Generation Partnership Project (3GPP) to define the specifications to utilize aerial platforms for 5G and beyond [2]. The portable feature of a PAP can improve the communication channels of the users, but it is limited by its finite onboard available energy. Hence, the deployment of a PAP to serve a set of users should maximize the number of bits transmitted per Joule of energy consumed, defined as the global energy efficiency (GEE) of the system [4]. One of the goals of this study is the maximization of the GEE, which is achieved with a combination of two sub-goals: decreasing the energy consumption of the PAP while increasing the data rate to users. The first goal exploits the fact that a UAV consumes less energy when flying horizontally at an optimal velocity than when it hovers [6], [5]. The data rate to a user is increased by improving the probability of having a line-of-sight (LoS) channel with the user by flying

the PAP closer to it [7]. However, this strategy also increases the energy consumption of the UAV. Moreover, the flight time is reduced further by the Peukert effect [31], [32], according to which the voltage drop of a PAP's on-board battery is a non-linear function of the power output.

Another way of enhancing the received signal power is represented by intelligent reflecting surfaces (IRSs), a key technology that provides additional paths between the transmitter and the receiver [25]. An IRS is a two-dimensional surface of a finite number of elements made of a meta-material whose properties can be reconfigured using a controller [26]. These elements are sub-wavelength-sized and can apply phase shifts on the incident waves before re-radiating them to the receiver. The direction at which the re-radiated waves add constructively can be controlled by applying suitable bias voltages to the IRS elements using the controller. However, a recent study shows that guaranteeing a constructive interference of signals at the receiver might not always improve the received signal-to-noise ratio (SNR) due to the interdependence of amplitude and phase values of a re-radiated wave from an IRS element [30]. Consequently, the careful addition of IRSs to a PAP system further enhances the received signal at the user end, thereby improving the GEE of PAP communication systems. The main challenge in adding IRSs to a PAP system is finding optimal locations for the IRSs. For instance, a random IRS placement policy would place an IRS in the non-line-of-sight regime of a ground user, thereby limiting its contribution to the GEE improvement. Here we propose a method to find locations for IRSs that guarantee LoS PAP-IRS links, with each user having at least one LoS link to an IRS.

1.1 Related Works

The placement optimization of a UAV-based system has been extensively studied in the literature [3]- [10]. In [3], the authors consider a UAV system deployed to assist slow-learning nodes in a federated learning application. The trajectory optimization problem, formulated to minimize learning time discrepancy among the nodes, is solved using a deep reinforcement learning technique and the sequential convex programming (SCP) technique. The work in [4] finds the optimal hovering altitude of a single-UAV system that maximizes the GEE of the system, whereas [5] considers a fly-hover-communicate protocol to serve a set of ground IoT nodes. The authors of [6] design a trajectory for a rotary-wing UAV that minimizes the UAV propulsion energy consumption. In [7], the authors propose a general probabilistic LoS-non-LoS (NLoS) air to ground channel model and determine the optimal altitude that maximizes the coverage region. The authors of [8] propose a graph-based algorithm to improve the throughput by jointly optimizing the user association, UAV altitude, and transmission direction. In [9] and the references therein, the authors summarize the works that have considered UAV(s) placement problems from an energy efficiency perspective, whereas [10] outlines the works that position UAV(s) to maximize communication-related parameters such as

coverage area and throughput.

Significant efforts have been dedicated by researchers to assess the performance of IRS panels in many wireless applications, such as multi-hop integrated access and backhauling (IAB) [11], localization, physical layer security, and simultaneous wireless and information power transfer (SWIPT) [12]. The works in [13]- [19] consider IRS for aiding the communication in a UAV-based system. In [13], the effect of phase error compensation on the achievable error rate and outage probability is investigated for UAV-IRS systems, and its impact on the achievable capacity is analyzed in [14]. However, the trajectory design of UAVs is not taken into account in these works. In [15] and [16], IRS panels are deployed on high buildings to assist the downlink transmission from a flying base station to a single ground user. The authors consider beamforming at IRS and UAV trajectory design to maximize the average achievable rate and the power received by the user, respectively. The sum-rate maximization problem is addressed in [17], where the joint design of IRS beamforming, IRS scheduling, and UAV trajectory have been considered. In [18], the weighted sum bit error rate (BER) achieved by multiple IRSs is minimized by jointly optimizing the IRS phase shift matrix, the UAV trajectory, and the scheduling of the IRSs. The UAV trajectory design for a UAV-IRS system operating in terahertz (THz) band is considered in [19], where a single IRS panel with ideal phase compensation is assumed. The authors of [20] propose a continuous-time system model for multi-path channels and discuss the optimal IRS configuration with respect to the received power, Doppler spread, and delay spread. Recent studies have also considered the possibility of using backscattering to aid the communication between the nodes [21] [22]. The reconfigurability of IRSs makes them suitable for a UAV-based system.

1.2 Main Contributions and Paper Organization

The work in [3], [6]- [10] and the references therein consider either the maximization of communication-related parameters (sum rate, coverage area), or the minimization of the energy consumed in a UAV-based system. [4] and [5] propose UAV placement policies to maximize the GEE that are suitable for hovering and fly-hover-communicate scenarios, respectively. Here we allow the PAP to serve the users while it is flying. Additionally, the works in [11]- [20] consider scenarios with either a single user with a single IRS panel [15], a single IRS with multiple users [17], or multiple IRSs with a single user [16, 18] to maximize the sum rate or minimize the BER. Moreover, [17] and [19] consider the trajectory design of UAVs assisted by a single IRS operating in a wide-band setting. However, a single IRS with ideal reflection and perfect phase compensation is assumed. Unlike the existing literature, we consider a generalized system model with a multi-user multi-IRS scenario to maximize the number of bits transmitted per Joule of energy consumed. Moreover, practical limitations for IRS design are considered, such as the phase-amplitude relation and discrete phase compensation. It is worth highlighting

that none of the above-mentioned work considers the non-linearity introduced by the Peukert effect on the battery discharge profile of UAVs. Additionally, the relationship between the number of cells of the on-board battery and the maximum flight time of a UAV has not been investigated in the literature. Here we consider the 3GPP-proposed air-to-ground channel model to estimate the UAV-IRS and IRS-user path gains that are later used for IRS positioning. The UAV-user path gain is estimated using the widely accepted LoS-NLoS path loss model proposed in [7]. Our main contributions are summarized as follows:

- A discharge characteristic for Li-ion batteries is obtained by applying a non-linear regression analysis to the discrete data provided in the battery data-sheet. This way, the initial and final voltage and the maximum capacity can be evaluated for all current values with great accuracy. Such an empirical approach differs from analytical models like those in [31] and [32].
- An algorithm to estimate the available flight time of a PAP considering the Peukert effect of the PAP battery, which is usually neglected in studies involving UAVs. For a given flying velocity, the estimation is done by representing the required power as a function of the battery terminal voltage and current using the developed discharge characteristic. Also, we investigate the trade-offs of adding more battery cells to the PAP battery by considering its positive (larger initial capacity) and negative effects (heavier PAP).
- IRS positioning guidelines are introduced considering the 3GPP air-to-ground channel model with the proposed multi-tier circle packing algorithm. Moreover, we optimize the additional phase shift introduced by the elements of an IRS, considering the interdependence of its amplitude and phase responses.
- The estimated available flight time and the determined IRS positions are then utilized in developing an energy-efficient path planning (E2P2) algorithm for a PAP deployed to serve a multi-user multi-IRS system. The algorithm maximizes the global energy efficiency of the system by considering the UAV propulsion energy consumption and the 3GPP air-to-ground channel.

The remainder of this paper is organised as follows. In Section 2, we describe the scenario under consideration, and explain the propagation environment and the PAP power consumption model. Building on this, Section 3 starts by explaining the Peukert effect, then proposes an algorithm to estimate the available flight time of a PAP as a function of its velocity. Then, in Section 3.2, the GEE maximization problem is formulated and solved with a two-phase approach described in Section 3.3 and Section 3.4. The main findings of the numerical evaluation are reported in Section 4.

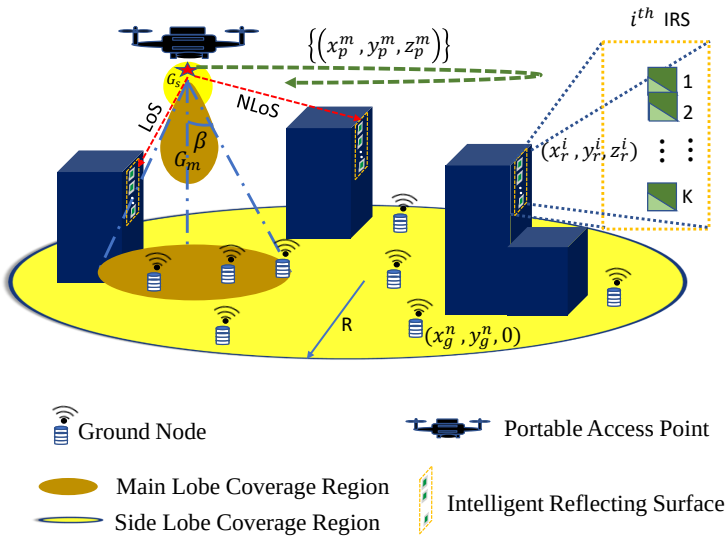

Fig. E.1: PAP deployment scenario.

2 System Model and Definitions

In this work, we consider an unmanned aerial system (UAS) in which a PAP is deployed to deliver Q bits of data to a set of N outdoor ground nodes (GNs) located at $\mathbf{g}_n = [x_{\mathrm{g}}^n, y_{\mathrm{g}}^n, 0]$, $n \in \mathcal{N} = \{1, 2, 3, .., N\}$. In addition to the PAP and the GNs, a set of I IRS modules are deployed. The presence of IRS modules (IRSs) could aid the communication between the PAP and the GNs by providing additional paths for the signal from the PAP to reach the GNs. This improves the GEE of the system by increasing the received signal power at the GNs, thereby reducing the total mission time and energy consumption of the PAP. The PAP is assumed to fly horizontally at an altitude h_{p}. Additionally, we assume the PAP to be equipped with a directional antenna, the gain of which, in the direction (α, ϵ), is given by,

$$G_{\mathrm{a}} = \begin{cases} G_{\mathrm{m}} & -\beta \leq \alpha \leq \beta, -\beta \leq \epsilon \leq \beta, \\ G_{\mathrm{s}} & \text{otherwise}, \end{cases} \tag{E.1}$$

where $G_{\mathrm{m}} = 2.2846/\beta^2$, and G_{s} are the main and side lobe gains of the PAP antenna, respectively [8]; the half-power beamwidth of the antenna in the elevation and the azimuth plane is 2β. The GNs are considered to be equipped with omni-directional antennas.

The trajectory optimization is assumed to happen offline at the ground station prior to the PAP deployment. This requires the ground station to be aware of the positions

of the GNs, which can be done, for instance, using the new radio positioning protocol (NRPPa). We consider a scenario where the ground nodes are static, which relates to practical sensor-centric IoT scenarios. Hence, the offline computed path could be used throughout the mission. Based on the GN scheduling, the bias voltages of the elements of IRSs are varied through control channels existing between the PAP and the IRSs. Furthermore, we assume both the PAP and GNs to be aware of the channel state information, and the backhaul link for the PAP is achievable with the new integration of low earth orbit (LEO) satellites [33]. Hence, not considered in the analysis.

2.1 PAP Trajectory Model

For tractability, the total flying path of the PAP is divided into M segments, represented using $M+1$ way points, whose locations are denoted as $\mathbf{p}_m = [x_{\mathrm{p}}^m, y_{\mathrm{p}}^m, z_{\mathrm{p}}^m]$, $m \in \mathcal{M} = \{1, 2, 3, .., M+1\}$: $z_{\mathrm{p}}^m = h_{\mathrm{p}}\ \forall m$. The length of each segment is constrained to be small enough as to leave the channel between the PAP and ground modules (IRS and GNs) unchanged, while the PAP is in a given path segment [6]:

$$\left\|\mathbf{p}_{m+1} - \mathbf{p}_m\right\| \leq \min\left\{\Delta, T_m v_{\max}\right\}\ \ \forall m \in \mathcal{M}^{'}, \tag{E.2}$$

where $\mathcal{M}^{'} = \mathcal{M} - \{M+1\}$; the segment length Δ is appropriately chosen so that, within each line segment, the PAP can be assumed to fly with a constant velocity v_m, and the distances between the PAP and each GN and IRS modules are approximately unchanged: $\Delta << h_{\mathrm{p}}$; let T_m be the time which the PAP spends in the m^{th} path segment and $v_{\max}$ be the maximum horizontal flying velocity of the PAP. In any given segment, the PAP follows a time-division multiple access (TDMA) scheme to serve the GNs: let T_{mn} be the time allocated to the n^{th} GN while the PAP is in the m^{th} path segment such that,

$$\Sigma_{n=1}^{N} T_{mn} \leq T_m \quad \forall m \in \mathcal{M}^{'}. \tag{E.3}$$

2.2 IRS Model

Each IRS is considered to be a uniform linear array (ULA) of K reflecting elements with dimensions d_{x} and d_{z}, placed along the positive Z axis as shown in Fig. E.2. The first element of each IRS is considered as the reference element and its geometric center is having the coordinates $\mathbf{r}_i = [x_{\mathrm{r}}^i, y_{\mathrm{r}}^i, z_{\mathrm{r}}^i]$, $i \in \mathcal{I} = \{1, 2, 3, .., I\}$. Then, the coordinates of the k^{th} reflecting element of the i^{th} IRS are $\mathbf{r}_i^k = (x_{\mathrm{r}}^i, y_{\mathrm{r}}^i, (z_{\mathrm{r}}^i - (k-1)d_{\mathrm{z}}))$ $\forall k \in [1, K], \forall i \in \mathcal{I}$. Additionally, while considering the channel between the PAP and the n^{th} GN, if either of them is located behind the i^{th} IRS, the IRS is not considered for transmission to the GN. Let $\{b_{\mathrm{pr}}^{m,i}\}$ and $\{b_{\mathrm{rg}}^{i,n}\}$ be the respective binary variables whose value is 1 if the PAP at the m^{th} segment and the n^{th} GN are in front of the i^{th} IRS,

respectively:

$$b_{\mathrm{pr}}^{m,i} = \begin{cases} 1 & \text{if } \alpha_{\mathrm{pr}}^{m,i} = \arctan\left[\dfrac{(y_{\mathrm{p}}^{m} - y_{\mathrm{r}}^{i})}{(x_{\mathrm{p}}^{m} - x_{\mathrm{r}}^{i})}\right] \in [0, -1^{\psi}\pi], \\ 0 & \text{otherwise,} \end{cases} \tag{E.4}$$

$$b_{\mathrm{rg}}^{i,n} = \begin{cases} 1 & \text{if } \alpha_{\mathrm{rg}}^{i,n} = \arctan\left[\dfrac{(y_{\mathrm{g}}^{n} - y_{\mathrm{r}}^{i})}{(x_{g}^{n} - x_{\mathrm{r}}^{i})}\right] \in [0, -1^{\psi}\pi], \\ 0 & \text{otherwise,} \end{cases} \tag{E.5}$$

in which the *arctan* function considers the correct quadrant of the argument. Moreover, a semiconductor device, such as a PIN diode, is used to tune the impedance of a reflecting element of an IRS in real-time without changing the geometrical parameters. This can be done by controlling its biasing voltage using a controller attached to each IRS. The amplitude and phase responses of a reflecting element are mutually dependent. In [30], the authors have presented the relationship in a closed-form as,

$$\mu_{m,i,n}^{k}(\theta_{m,i,n}^{k}) = (1 - \mu_{\min}) \cdot \left(\frac{\sin(\theta_{m,i,n}^{k} - \varrho) + 1}{2}\right)^{\zeta} + \mu_{\min}, \tag{E.6}$$

where $\mu_{\min} \geq 0$, $\varrho \geq 0$, and $\zeta \geq 0$ are the constants related to the circuit implementation of the reflecting element. Let

$$\boldsymbol{\Theta}_{\mathrm{r}}^{m,i,n} = \mathrm{diag}\left(\mu_{m,i,n}^{1}(\theta_{m,i,n}^{1})e^{j\theta_{m,i,n}^{1}}, .., \mu_{m,i,n}^{K}(\theta_{m,i,n}^{K})e^{j\theta_{m,i,n}^{K}}\right), i \in \mathcal{I},\ \theta_{m,i,n}^{k} \in [0, \pi),$$

be the amplitude-phase shift matrix of the i^{th} IRS when the PAP serves the n^{th} GN from the m^{th} segment.

2.3 Propagation Environment

We consider the system to be deployed in an urban environment where the air-to-ground link can be either LoS or NLoS, depending on the blockage profile of the environment and the relative position of the receiver module (IRS/GN) to the transmitter module (PAP/IRS) [7], [27]. Consequently, the mean path loss value of an air-to-ground link has the form,

$$\overline{L}_{c_1}^{c_2,c_3} = \underbrace{P_{c1,1}^{c2,c3} \times L_{c_1,1}^{c_2,c_3}}_{\text{LoS Pathloss}} + \underbrace{(1 - P_{c_1,1}^{c_2,c_3}) \times L_{c_1,2}^{c_2,c_3}}_{\text{NLoS Pathloss}}, \tag{E.7}$$

in which $c_1 \in \{\mathrm{pr}, \mathrm{rg}\}$, $c_2 \in \{m, i_k\}$, $c_3 \in \{i_k, n\}$, where i_k represents the k^{th} element of the i^{th} IRS module.

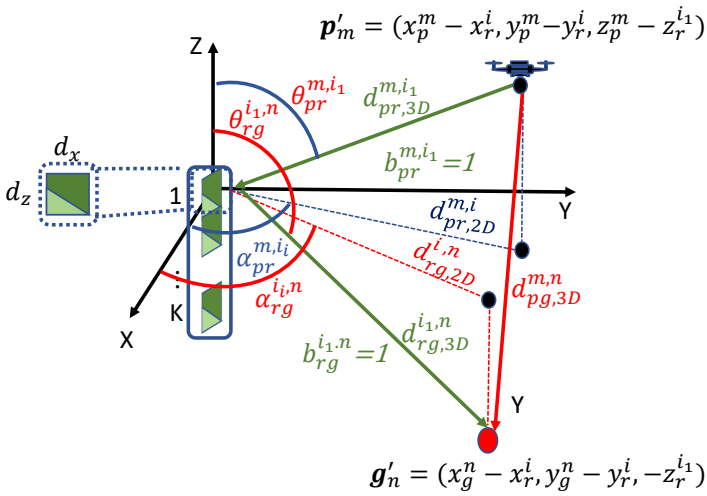

Fig. E.2: Propagation environment considering the m^{th} path segment, i^{th} IRS and n^{th} GN.

PAP-IRS Channel

From the 3GPP report [27], the LoS and NLoS path loss values between the m^{th} path segment and the k^{th} element of the i^{th} IRS can be expressed as,

$$L_{\text{pr},1}^{m,i_k} = 30.9 + (22.25 - 0.5\log h_{\text{p}})\log d_{\text{pr,3D}}^{m,i_k} + F, \tag{E.8}$$

$$L_{\text{pr},2}^{m,i_k} = \max\{L_{\text{pr},1}^{m,i_k}, 32.4 + (43.2 - 7.6\log h_{\text{p}})\log d_{\text{pr,3D}}^{m,i_k} + F\}, \tag{E.9}$$

where $F = 20\log f$, with f being the carrier frequency; $d_{\text{pr,3D}}^{m,i_k} = \|\mathbf{p}_m - \mathbf{r}_i^k\|$. Given that the IRSs are perpendicular to the ground, the azimuth angles for the waves arriving at the reflecting elements of an IRS from the PAP are equal. The corresponding LoS probability is expressed as,

$$P_{\text{pr},1}^{m,i} = \begin{cases} 1 \text{ if } \ d_{\text{pr,2D}}^{m,i} \le d_1, \\ \dfrac{d_1}{d_{\text{pr,2D}}^{m,i}} + \exp\left[\dfrac{-d_{\text{pr,2D}}^{m,i}}{p_1}\right]\left[1 - \dfrac{d_1}{d_{\text{pr,2D}}^{m,i}}\right]; \text{else}, \end{cases} \tag{E.10}$$

where,

$$d_{\text{pr,2D}}^{m,i} = \sqrt{(x_{\text{p}}^m - x_{\text{r}}^i)^2 + (y_{\text{p}}^m - y_{\text{r}}^i)^2}, \tag{E.11}$$

$$p_1 = 233.98\log_{10}(h_{\text{p}}) - 0.95, \tag{E.12}$$

$$d_1 = \max\left(294.05 \cdot \log_{10}(h_{\text{p}}) - 432.94, 18\right). \tag{E.13}$$

Also, (E.8)-(E.13) are valid when $22.5 < h_{\mathrm{p}} \leq 100$m and when the IRSs are located at a height of 10m (for an urban scenario). It is worth pointing out that most of the works in the literature, when considering the relative phase of the incident wave on the ULA elements, assume that the reference element has a phase of 0^o. However, since multiple IRSs are considered in this work, each with different location and reference points, the actual phase should be considered. Hence, the channel gain vector between the i^{th} IRS and the PAP while the PAP is in the m^{th} path segment is represented as,

$$\mathbf{h}_{\mathrm{pr}}^{m,i} = \left(b_{\mathrm{pr}}^{m,i} \sqrt{G_{\mathrm{pr}}^{m,i_k} 10^{-\overline{L}_{\mathrm{pr}}^{m,i_k}/10}} e^{-j\frac{2\pi}{\lambda} d_{\mathrm{pr,3D}}^{m,i_k}} \right)_{k=1,\ldots,K}, \tag{E.14}$$

where $G_{\mathrm{pr}}^{m,i_k} = G_{\mathrm{m}}$ if $\arctan[|((z_{\mathrm{r}}^i - (k-1)d_{\mathrm{z}}) - z_{\mathrm{p}}^m)|/d_{\mathrm{pr,2D}}^{m,i}] \leq \beta$; else G_{s}.

IRS-GN Channel

Similarly to the previous sub-section, from [27], the LoS and NLoS path loss values between the elements of the i^{th} IRS and the n^{th} GN are estimated using,

$$L_{\mathrm{rg},1}^{i_k,n} = \begin{cases} L_1 & \text{if} \quad 10\mathrm{m} \leq d_{\mathrm{rg},2D}^{i_k,n} \leq d_{BP}, \\ L_2 & \text{if} \quad d_{BP} \leq d_{2D}^{i_k,n} \leq 5\mathrm{km}, \end{cases} \tag{E.15}$$

$$L_{\mathrm{rg},2}^{i_k,n} = \max\left(L_{\mathrm{rg},1}^{i_k,n}, L_{\mathrm{rg},2}^{'i_k,n} \right) \quad \text{for} \quad 10\mathrm{m} \leq d_{\mathrm{rg},2D}^{i_k,n} \leq 5\mathrm{km},$$

where $L_1 = 32.4{+}21\log(d_{\mathrm{rg},3D}^{i_k,n}){+}F$ and $L_2 = 32.4{+}40\log(d_{\mathrm{rg},3D}^{i_k,n}){+}F{-}9.5\log\left[(d_{BP})^2 + 72.25\right]$ with $d_{BP} = 18f/c$, $c = 3 \times 10^8$m/s; $L_{\mathrm{rg},2}^{'i_k,n} = 35.3\log_{10}(d_{\mathrm{rg},3D}^{i_k,n}) + 22.4 + 21.3\log_{10}(f)$. The LoS probability is determined using,

$$P_{\mathrm{rg},1}^{i,n} = \begin{cases} 1 \text{ if} \quad d_{\mathrm{rg,2D}}^{i,n} \leq 18\mathrm{m}, \\ \dfrac{18}{d_{\mathrm{rg,\ 2D}}^{i,n}} + \exp\left[\dfrac{-d_{\mathrm{rg,2D}}^{i,n}}{36}\right]\left[1 - \dfrac{18}{d_{\mathrm{rg,2D}}^{i,n}}\right]; \quad \text{else.} \end{cases} \tag{E.16}$$

The channel gain between the i^{th} IRS and the n^{th} GN is given by:

$$\mathbf{h}_{\mathrm{rg}}^{i,n} = \left(b_{\mathrm{rg}}^{i,n} \sqrt{10^{-\overline{L}_{\mathrm{rg}}^{i_k,n}/10}} e^{-j\frac{2\pi}{\lambda} d_{\mathrm{rg,3D}}^{i_k,n}} \right)_{k=1,\ldots,K}. \tag{E.17}$$

PAP-GN channel

The LoS and NLoS path loss values between the m^{th} PAP path segment and the n^{th} GN can be expressed as [7], [5],

$$L_{\text{pg},1}^{m,n} = 20\log d_{\text{pg,3D}}^{m,n} + F + 20\log\left(\frac{4\pi}{c}\right) + \eta_1, \tag{E.18}$$

$$L_{\text{pg},2}^{m,n} = 20\log d_{\text{pg,3D}}^{m,n} + F + 20\log\left(\frac{4\pi}{c}\right) + \eta_2, \tag{E.19}$$

with $d_{\text{pg,3D}}^{m,n} = \|\mathbf{p}_m - \mathbf{g}_n\|$. The corresponding probability of existence of a LoS link between the PAP and the GN is expressed as [7],

$$P_{\text{pg},1}^{m,n} = \frac{1}{1 + a\exp\left[-b(\phi_{\text{pg}}^{m,n} - a)\right]}, \tag{E.20}$$

with $\phi_{\text{pg}}^{m,n} = \arctan\left(z_{\text{p}}^{m}/\sqrt{(x_{\text{p}}^{m} - x_{\text{g}}^{n})^2 + (y_{\text{p}}^{m} - y_{\text{g}}^{n})^2}\right)$; a and b are environment-dependent parameters; η_1 and η_2 are the respective additional path loss values due to long-term channel variations. The corresponding channel gain is expressed as,

$$h_{\text{pg}}^{m,n} = \sqrt{G_{\text{pg}}^{m,n} 10^{-\overline{L}_{\text{pg}}^{m,n}/10}} e^{-j\frac{2\pi}{\lambda} d_{\text{pg,3D}}^{m,n}}. \tag{E.21}$$

where $G_{\text{pg}}^{m,n} = G_{\text{m}}$ if $\phi_{\text{pg}}^{m,n} \leq \beta$; else G_{s}.

The signal transmitted from the PAP reaches a GN through two main paths, PAP-GN link and PAP-IRS link. The received SNR value at the n^{th} GN while the PAP is in the m^{th} path segment is given by,

$$\gamma_{\text{pg}}^{m,n} = \frac{P|h_{\text{pg}}^{m,n} + \sum_{i\in\mathcal{I}} \mathbf{h}_{\text{rg}}^{i,n\,H} \Theta_r^{m,i,n} \mathbf{h}_{\text{pr}}^{m,i}|^2}{\sigma^2}, \tag{E.22}$$

where P is the transmitted power and σ^2 is the additive white Gaussian noise power. Assuming the availability of channel state information (CSI) at both the transmitter and the receiver, the number of bits transmitted-per-second (bps) is given by,

$$D_{\text{pg}}^{m,n} = B_{\text{c}}\log_2\left[1 + \gamma_{\text{pg}}^{m,n}\right] \qquad \forall j \in \mathcal{N}, m \in \mathcal{M}', \tag{E.23}$$

where B_c is the available channel bandwidth for each GN.

2.4 PAP Power Consumption Model

Since the energy consumed by the communication unit is much lower than that consumed by the aerial vehicle, we neglect the communication energy part. The UAV parameters

Table E.1: UAV Parameters [5].

Label	Definition	Value
W	Weight of the UAV in Newton	24.5 N
N_{R}	Number of rotors	4
v_m	UAV's horizontal flying velocity	-
v_{tip}	Tip speed of the rotor	102 m/s
A_{f}	Fuselage area	0.038 m^2
$\rho(h_a)$	Air density	-
C_D	Drag Co-efficient	0.9
A_r	Rotor disc area	0.06 m^2
Δ_p	Profile drag coefficient	0.002
s	Rotor solidity	0.05

used in this section are summarized in Table E.1. The power consumed by a rotary-wing UAV while flying horizontally with a velocity v_m is determined using [5] as,

$$P_{\mathrm{uav}}(v_m) = \underbrace{N_{\mathrm{R}} P_{\mathrm{b}} \left(1 + \frac{3v_m^2}{v_{\mathrm{tip}}^2}\right)}_{P_{\mathrm{blade}}} + \underbrace{\frac{1}{2} C_D A_{\mathrm{f}} \rho(h_{\mathrm{a}}) v_m^3}_{P_{\mathrm{fuselage}}} + \underbrace{W \left(\sqrt{\frac{W^2}{4N_{\mathrm{R}}^2 \rho^2(h_{\mathrm{a}}) A_{\mathrm{r}}^2} + \frac{v_m^4}{4}} - \frac{v_m^2}{2}\right)^{1/2}}_{P_{\mathrm{induce}}}, \tag{E.24}$$

where $P_{\mathrm{b}} = \frac{\Delta}{8} \rho(h_{\mathrm{a}}) s A_{\mathrm{r}} v_{\mathrm{tip}}^3$, $\rho(h_{\mathrm{a}}) = (1 - 2.2558.10^{-5} h_{\mathrm{a}})^{4.2577}$; $W = W_{\mathrm{bt}} + W_{\mathrm{body}}$ is the total weight of the UAV, comprehensive of body and battery unit. P_{blade} and P_{fuselage} are the powers required to overcome the profile drag forces of the rotor blades and the fuselage of the aerial vehicle that oppose its forward movement, respectively. P_{induce} represents the power required to lift the payload. The hovering power is obtained by substituting $v_m = 0$ in (E.24).

2.5 Global Energy Efficiency

The global energy efficiency of a PAP system is defined as the total number of bits transmitted per Joule of energy consumed [4]:

$$\mathrm{GEE[bits/Joule]} = \frac{\sum_{m=1}^{M} \sum_{n=1}^{N} T_{mn} D_{\mathrm{pg}}^{m,n} [\mathrm{bits}]}{\sum_{m=1}^{M} T_m P_{\mathrm{uav}}(v_m) [\mathrm{Joule}]}, \tag{E.25}$$

where the numerator is the total number of data bits transmitted from the PAP to the GNs at the end of the M^{th} path segment and the denominator is the total energy consumed by the PAP during its flight.

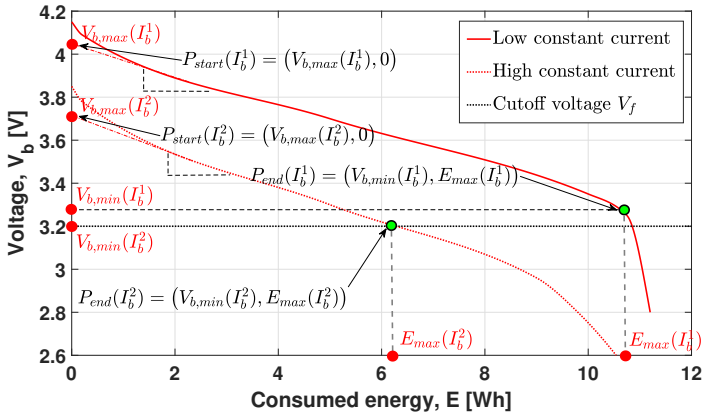

Fig. E.3: Peukert curves for a Li-ion battery cell.

3 GEE PAP Trajectory Design

In this section, we propose an algorithm to estimate the available flight time of a PAP, considering the Peukert effect on the UAV battery. Subsequently, we design a globally energy efficient trajectory for the PAP to deliver data to the GNs.

3.1 Available Flight Time Estimation

The available flight time requires an iterative calculation because it depends on the battery discharge profile, which is a non-linear function of the power drawn by the rotors of the UAV. This non-linear behavior of the UAV battery is defined by the Peukert effect [31], [32].

Peukert Effect

Fig. E.3 portrays the voltage drop of a typical Li-ion battery (commonly used in UAVs) during discharge, in various conditions. As shown in the figure, a battery is useful until the terminal voltage becomes lower than a given threshold (V_{cf}), or the discharge curve comes out of its linear section, whichever happens first. In the example reported in Fig. E.3, the discharge at high current (dotted red curve) reaches the cutoff voltage before the end of its linear section, whereas the opposite is true at low current (continuous red curve). The curves offer a clear explanation of the Peukert effect: as the current drawn from the battery unit increases, the available capacity (time) decreases as a non-linear function of the output current, contrary to what is often assumed in the literature [6]. In the considered scenario, the current drawn from the battery is a function of the power consumed by the PAP, its terminal voltage, and the number of

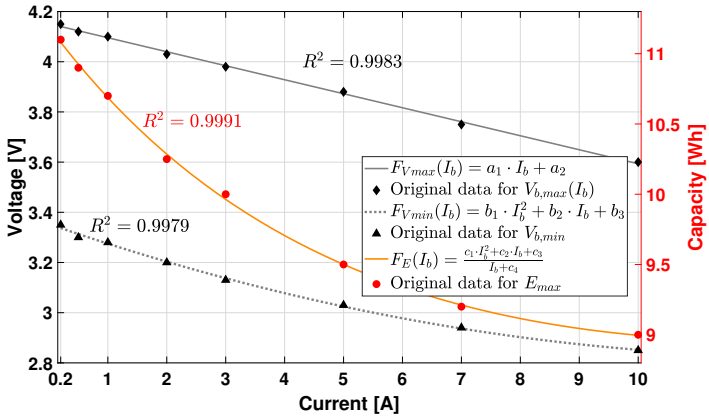

Fig. E.4: Regression functions for $V_{b,max}$, $V_{b,min}$, and E_{max}.

the battery cells n_c that form the battery unit of the PAP:

$$I_b^m = \frac{P_{uav}(v_m)}{V_b^m \cdot n_c} \qquad \forall m \in \mathcal{M}'. \tag{E.26}$$

In practice, the rates at which the battery terminal voltage drops under different conditions are determined experimentally and typically reported in the battery data sheet, like the curves of Fig. E.3. Since data-sheets typically present a limited number of such curves, we propose to simulate this phenomenon for a continuous range of currents by adopting a hybrid approach between those developed in [31] and [32], but based on data from data-sheets rather than analytical models. In particular, as shown in Fig. E.3, we extrapolate discharge curves from the data provided in [29], in order to have information for several current values. The coordinates of two points are registered for each value of discharge current: the voltage and used capacity at the full charge point (taken as a continuation of the linear segment, neglecting the initial voltage drop), $P_{start}(I_b) = (V_{b,max}(I_b), 0)$, and the point where the useful capacity ends, $P_{end}(I_b) = (V_{b,min}(I_b), E_{max}(I_b))$. The latter corresponds to the point after which the curve's slope cannot be considered constant anymore, as shown in Fig. E.3. Between P_{start} and P_{end}, the slope of change of battery terminal voltage is calculated as,

$$k(I_b) = \frac{V_{b,max}(I_b) - V_{b,min}(I_b)}{E_{max}(I_b)}. \tag{E.27}$$

A regression analysis is then carried out using the 'fit' function in MATLAB to generate three functions of the output current: F_{Vmax}, F_{Vmin}, and F_E. These are used to determine the initial and final voltage points, and the maximum capacity for any current value. As reported in Fig. E.4, the maximum voltage is a linear decreasing function F_{Vmax} of current, while F_{Vmin} is quadratic and the capacity function F_E has a rational

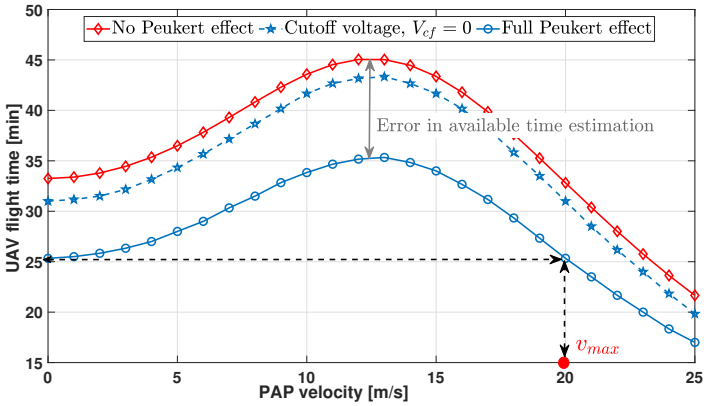

Fig. E.5: Variation of available flight time with PAP velocity and cutoff voltage.

formulation. All three functions represent a great fit for the respective original data, with values of R^2 (an indicator of 'goodness-of-fit' ranging from 0 to 1) next to 1.

If the PAP consumes P_{uav} Watts at all times while active, the available flight time can be estimated using Algorithm E.1. The required power is assumed to be drawn equally from the n_{c} battery cells. The algorithm starts by initializing the parameters of a cell as $V_{\text{b}}^1 = V_{\text{b}}^0$, the rated terminal voltage of a battery cell and current I_{b}^1 determined using (E.26). The total flight time is divided into chunks of small intervals Δt, so that the battery terminal voltage can be assumed constant during this interval. The first operation is the calculation of the slope k of the discharge curve, using (E.28):

$$k(I_{\text{b}}^j) = \frac{F_{\text{Vmax}}(I_{\text{b}}^j) - F_{\text{Vmin}}(I_{\text{b}}^j)}{F_{\text{E}}(I_{\text{b}}^j)}. \tag{E.28}$$

The parameter $k(I_{\text{b}}^j)$ is then used to calculate the voltage at instant $(j+1)$, which, after verifying it is not lower than the cutoff voltage, allows to calculate the current at the $(j+1)^{\text{th}}$ time step. It should be noted that even though the power requirement from the PAP remains the same, the current drawn from each battery cell increases after each step due the drop in terminal voltage. This allows us to calculate the energy consumed in the next time step E_b^{j+1}, the total energy consumed in the mission E_{tot} up to the current slot, and to re-evaluate the maximum available energy $E_{\max}(I_b^{j+1})$. If the total energy consumed is greater than the maximum available energy, the loop stops and the maximum flight time $T(P_{\text{uav}})$ is obtained by multiplying the length of a time step, Δt, with the number of iterations, j.

Fig. E.5 shows how the available flight time of a PAP is affected by its velocity, which is directly related to the power consumption. The flight time is maximized at 13 m/s because this velocity minimizes the UAV power consumption; then it decreases to the hovering level at 20 m/s. Above this velocity, the flight time is lower than in

hovering conditions; the maximum velocity considered is 25 m/s because this allows to show this phenomenon while keeping the current under 10A per cell, the upper limit for this kind of batteries. The figure also shows the relevance of the Peukert effect by comparing the case where it is considered (blue curves) with one where it is neglected (red curve). In the latter, the flight time is calculated by simply dividing the battery capacity by the power consumption [6], [5]. Since they result from a more conservative model, the blue curves are entirely below the red curve by a considerable margin, which is nearly constant when the cutoff voltage V_{cf} is 0 (dashed blue curve). With $V_{\mathrm{cf}} = 3.2V$ (continuous blue curve), the gap with the red curve is variable because the secondary break condition in Algorithm E.1 ($V_j < V_{\mathrm{cf}}$) is prevalent, causing a non-linear relation with the power consumption. The hovering time, assuming a UAV weight of 2 kg (excluding the battery), is estimated to be about 25 minutes, which is a sensible value for a commercial UAV[2].

Algorithm E.1: Available Flight Time Estimation.

Initialize P_{uav}, $j = 1$, E_{tot}, $E_{\max}(I_{\mathrm{b}}^{j})$, V_{b}^{j}, V_{cf}, I_{b}^{j}, Δt, E_{b}^{j}
while $E_{tot} < E_{max}(I_{\mathrm{b}}^{j})$ **do**
  Calculate Slope k with (E.28);
  $V_{\mathrm{b}}^{j+1} = V_{\mathrm{b}}^{j} - k(I_{\mathrm{b}}^{j}) \cdot E_{\mathrm{b}}^{j}$;
  if $V_{\mathrm{b}}^{j+1} < V_{cf}$ **then**
    break;
  $j = j + 1$;
  $I_{\mathrm{b}}^{j} = P_{\mathrm{uav}} / \left(V_{\mathrm{b}}^{j} n_{\mathrm{c}} \right)$;
  $E_{\mathrm{b}}^{j} = \left(I_{\mathrm{b}}^{j} V_{\mathrm{b}}^{j} \right) \Delta t$;
  $E_{\mathrm{tot}} = \sum_{t=1}^{j} E_{\mathrm{b}}^{t}$;
  $E_{\max}(I_{\mathrm{b}}^{j}) = F_{\mathrm{E}} \left(I_{\mathrm{b}}^{j} \right)$;
Output: $T(P_{\mathrm{uav}}) = j\Delta t$.

3.2 Trajectory Design Problem Formulation

The GEE of a PAP system can be increased by increasing the total number of bits transmitted and/or by reducing the PAP energy consumption with an efficient trajectory design. The flying velocity of the PAP affects: a) the PAP energy consumption; b) the discharge profile of its on-board battery; c) the number of bits transmitted, which is a

[2] https://dl.djicdn.com/downloads/m100/M100_User_Manual_EN.pdf

function of the time the PAP spends in the m-th path segment, T_m. The GEE trajectory optimization problem is formulated as,

$$\text{(E:P1)}: \underset{\{\mathbf{p}_m\},\{T_m\},\{T_{mn}\},\{\boldsymbol{\Theta}_{\mathrm{r}}^{m,i,n}\}}{\text{maximize}} \quad \frac{\sum_{m=1}^{M}\sum_{n=1}^{N} T_{mn} D_{\mathrm{pg}}^{m,n}}{\sum_{m=1}^{M} T_m P_{\mathrm{uav}}\left(v_m\right)},$$

$$\text{s.t.} \quad \sum_{m=1}^{M} T_{mn} D_{\mathrm{pg}}^{m,n} \geq Q \qquad \forall n, \tag{E.29}$$

$$-\pi \leq \theta_{m,i,n}^{k} < \pi \qquad \forall m,i,n,k, \tag{E.30}$$

$$\mathbf{p}_{M+1} = \mathbf{p}_{\mathrm{F}}; \mathbf{p}_1 = \mathbf{p}_{\mathrm{I}}, \tag{E.31}$$

$$T_m \geq 0; \quad T_{mn} \geq 0 \qquad \forall m,n, \tag{E.32}$$

$$b_{\mathrm{pr}}^{m,i}, b_{\mathrm{rg}}^{i,n} \in \{0,1\}, \qquad \forall m,i,n, \tag{E.33}$$

$$\sum_{j=1}^{m} T_j P_{\mathrm{uav}}(v_j) \leq E_{\max}(P_{\mathrm{uav}}(v_j)) \quad \forall m, \tag{E.34}$$

$$V_{\mathrm{b}}^{m}(P_{\mathrm{uav}}(v_j)) \geq V_{\mathrm{cf}} \quad \forall m, \tag{E.35}$$

$$\text{(E.2)}, \text{(E.3)}. \tag{E.36}$$

The objective function of (E:P1) is the GEE of the system, the denominator of which is the total energy consumed by the aerial vehicle. Constraint (E.29) demands that the PAP delivers Q bits of data to the GNs by the end of the trajectory; the phase shift constraint associated with the IRS elements is represented by (E.30), whereas (E.31) restrains the initial and final locations of the PAP; (E.32) is the non-negative time constraint whereas (E.34) and (E.35) summarize the Peukert effect.

The solution to (E:P1) is not trivial, mainly due to the following reasons: a) the numerator of the objective function of (E:P1) has binary variables b) the denominator of the objective function and constraint (E.29) are non-convex functions of the trajectory variables; c) the optimal design of phase shifts associated with the IRS elements to maximize the received SNR and the trajectory of the PAP are interlinked; d) the non-tractable form of the constraints (E.34) and (E.35).

To tackle the above issues, we propose a two-phase algorithm: in the first phase, we determine a discretized GEE path that connects a set of *locations-of-interest (LoIs)*, $\{\mathbf{p}_m\}\,\forall m \in \mathcal{M}$; in the second phase, the determined $\{\mathbf{p}_m\}$ are used to obtain the values of binary variables $\{b_{\mathrm{pr}}^{m,i}\}$, $\{b_{\mathrm{rg}}^{i,n}\}$. This allows us to accurately tune the phase shift values of the IRS reflecting elements so as to maximize the received SNR values at the GNs using an alternate optimization algorithm. We then propose a novel multi-lap trajectory design method to efficiently allocate time to the GNs, while considering the Peukert constraints.

3.3 Phase 1: PAP Path Design and IRS beamforming

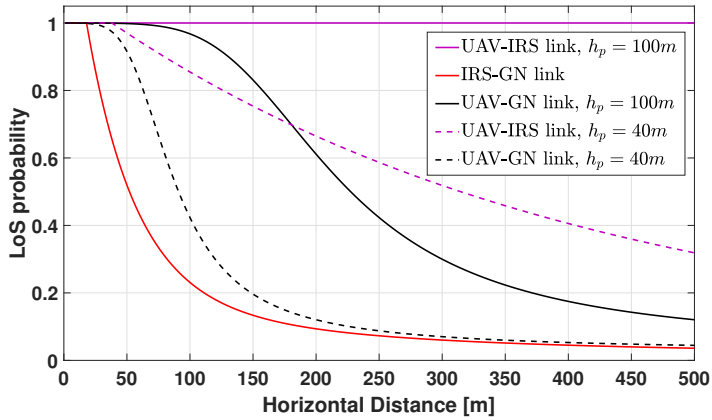

Fig. E.6: LoS probability variation of UAV-IRS, IRS-GN and UAV-GN links, with respect to projected horizontal distance.

Table E.2: Packing Patterns [34].

Number of circles, u	$R^u_{\max} = \Lambda(u) \cdot R_{\text{small}}$
1	$1 \cdot R_{\text{small}}$
2	$1 \cdot R_{\text{small}}$
3	$2/\sqrt{3} \cdot R_{\text{small}}$
4	$\sqrt{2} \cdot R_{\text{small}}$
5	$1.641 \cdot R_{\text{small}}$
6	$1.7988 \cdot R_{\text{small}}$
7	$2 \cdot R_{\text{small}}$
$u = 8, 9, 10$	$[1 + 2\cos(2\pi/(u-1))] \cdot R_{\text{small}}$

PAP Path Design and IRS positioning

The gain achieved by using IRSs to aid the communication between the PAP and a GN is expected to be significant when the PAP-IRS and IRS-GN are LoS links [26]. Fig. E.6 shows the variation of LoS probabilities between the PAP and a GN, the PAP and an IRS, and an IRS and a GN, obtained using (E.20), (E.10), and (E.16), respectively. For the considered urban scenario, a flying altitude of 100 m always guarantees a LoS link between the PAP and an IRS module [27]. Hence, we select the flying altitude $h_{\text{p}} = 100$ m. Additionally, a LoS link between an IRS and a GN can be guaranteed by placing the IRS module at a 2D distance of 20 m from the GN. Consequently, we cover the given geographical area of radius R_{g} by placing a set of small circles of radius 20 m using the proposed multi-tier packing algorithm.

Multi-tier Packing Algorithm: The multi-tier packing algorithm is an extension of the multi-level circle packing algorithm that considers the packing of 5 circles only in

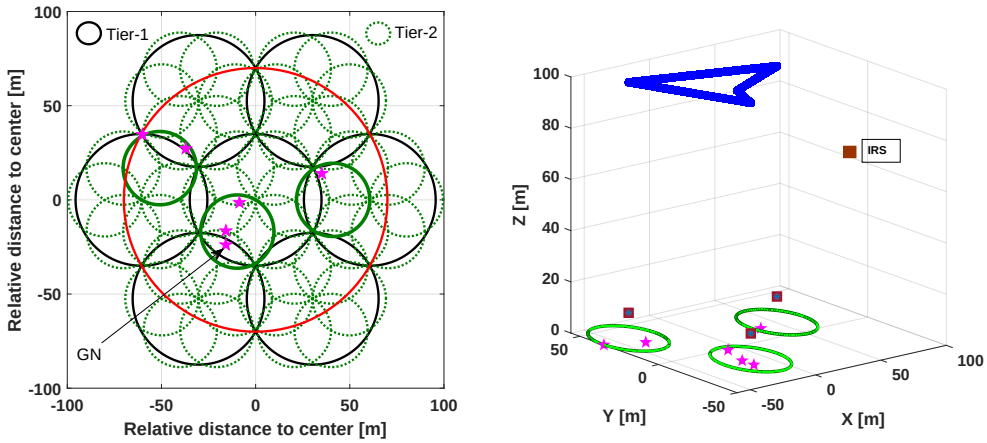

(a) (b)

Fig. E.7: a)Set of LoS circles covering the users; b) PAP path through the LoIs.

each level [Algorithm 2, [5]]. If $R_{\mathrm{g}} > 20$, we need multiple smaller circles to cover the given region. Let $R^{u}_{\max}$ be the maximum radius of the geographical region that u small circles of radius R_{small} can cover. With the available packing patterns, in Table E.2, the maximum radius of the geographical region that can be covered using 10 circles is $2.53 \cdot R_{\mathrm{small}}$. In practice, the considered region could be very large in dimension compared to the radius of the smaller circle ($R_{\mathrm{g}} >> R_{\mathrm{small}}$). Hence, our objective is to find the minimum number of smaller circles and the corresponding locations of their centers required to cover the given geographical area. The multi-tier packing concept is better explained in Fig. E.7a: in the first tier of packing, 7 circles of radius $R_{\mathrm{g}}/\Lambda(7)$ are placed using 7-circle packing; in the second tier, each of these 7 circles is covered by 6 smaller circles of radius $R_{\mathrm{g}}/[\Lambda(7)\Lambda(6)]$, using 6-circle packing.

Proposition E1. *The optimal circle packing pattern that requires the least number of circles of radius R_{small} to cover a region of radius R_t is determined as,*

$$u^{t}_{opt} = \underset{u=1,2,..,10}{argmin}\ u^{\mu(u)}, \tag{E.37}$$

where $\mu(u) = \dfrac{1}{log_2(\Lambda(u))} log_2\left(\dfrac{R_t}{R_{\mathrm{small}}}\right)$, *and* $\Lambda(u)$ *is obtained from Table E.2.*

Proof:

Proof. The proof is a direct extension of the proof of Proposition 1 of [5]. □

Algorithm E.2: Multi-tier packing algorithm.

Input: $t = 1$ $R_t = R_{\mathrm{g}}$, R_{small};
while $R_t \leq R_{\mathrm{small}}$ **do**
    Find the optimal packing pattern for the t^{th} tier using Proposition E1;
    Store the locations of the center of the circles to $\mathbf{l}_t$;
    t=t+1;
    Update the radius $R_t = R_{t-1}/\Lambda(u_{\mathrm{opt}}^{t-1})$
Output: $\mathcal{L} = \mathbf{l}_{t-1}$, the set of locations of the smaller circles to cover the given geographical area.

Algorithm E.2 gives the steps to follow to complete the multi-tier packing procedure. To find the path for the PAP, as shown in Fig. E.7a, we first determine a set of locations using Algorithm E.2 (center of green circles) with $R_{\mathrm{small}} = 20$m: $\{\mathbf{l}_{t-1}\} \equiv \mathcal{L}$, that cover the given geographical area (red circle) entirely using the multi-tier packing method. Next, we consider the *LoIs* as a subset of $\mathcal{L}$: $\mathcal{L}^{'} \subset \mathcal{L}$ for which each of the corresponding circles covers at least one GN (set of solid green circles):

$$\mathcal{L}^{'} \equiv \{\mathbf{l}_{t-1}\} \text{ s.t } \|\mathbf{l}_{t-1} - \mathbf{g}_n\| \leq 20 \text{ for at least one GN.} \tag{E.38}$$

Using $\mathcal{L}^{'}$, an energy-efficient path to cover the GNs in the geographical region is determined by finding the shortest path between points $\{\mathbf{l}_o\} \in \mathcal{L}^{'}$, starting from $\mathbf{p}_{\mathrm{I}}$ and ending at $\mathbf{p}_{\mathrm{F}}$ (constraint (E.31)). The continuous path is then discretized into segments of length Δ (constraint (E.2)), giving a set of way points $\{\mathbf{p}_m\}$, as shown in Fig. E.7b. For a set of way points, the optimum $\mathbf{\Theta}_{\mathrm{r}}^{m,i,n}$ $\forall\{m,i,n\}$ that maximizes the achievable received SNR at a GN can be found as shown below.

IRS Beamforming Design

We consider that the additional phase shift value introduced by an IRS element is limited to a discrete set of phase values due to practical hardware constraints. The possibility of using the i^{th} IRS module to aid the communication between the PAP at the m^{th} path segment and the n^{th} GN is determined by the values of $b_{\mathrm{pr}}^{m,i}$ and $b_{\mathrm{rg}}^{i,n}$. If these are equal to one, the phase of each IRS element should be selected to maximize the GEE value. For a given $\{\mathbf{p}_m\}, \{T_m\}, \{T_{mn}\}$, from (E.22) and (E.23), the optimal $\{\mathbf{\Theta}_{\mathrm{r}}^{m,i,n}\}$ that maximizes the GEE is the one that maximizes the SNR. Ideally, the phases must be adjusted to ensure constructive addition of the signals received through the direct and indirect paths from the PAP at a GN. However, due to the interdependence of the amplitude and phase responses of the IRS elements, as given in (E.6), an additional phase shift introduced by an IRS element that guarantees a constructive addition of the received signals might produce a low amplitude response. Hence, an approximate solution can be determined by using the alternate optimization (AO) proposed in [30].

The AO algorithm finds an approximate solution that maximizes the GEE by iteratively optimizing the phase shift of one of the K reflecting elements with those of the others being fixed at each time, and repeating this procedure for all K elements of an IRS module until the GEE value converges [30]. This process must be repeated for all the IRS modules that satisfy $b_{\text{pr}}^{m,i} = b_{\text{rg}}^{i,n} = 1$. Due to the considered discrete set of available phase values, the convergence of the algorithm is guaranteed. Using the optimal phase values obtained using AO, the value of $D_{\text{pg}}^{m,n}$ $\forall m, n$ can be determined using (E.22) in (E.23).

3.4 Phase 2: Multi-Lap Trajectory Design

In this phase, using the set of way points $\{\mathbf{p}_m\}$ and the determined $D_{\text{pg}}^{m,n}$ values, we design a novel multi-lap trajectory that maximizes the GEE, while scheduling the GNs so that Q bits of data are delivered to each of these by the end of the trajectory. Let us define a lap of the trajectory as the discretized path from $\mathbf{p}_{\text{I}}$ to $\mathbf{p}_{\text{F}}$ through all the LoIs. The PAP takes N_{lap} laps to deliver Q bits of data to the GNs. For a given flying velocity v_m, the GNs can be scheduled by solving the following sub-problem of (E:P1),

$$\text{(E:P1.1)}: \underset{N_{\text{lap}},\{T_{mn}\}}{\text{maximize}} \quad \frac{Q}{N_{\text{lap}} \sum_{m=1}^{M} T_m P_{\text{uav}}(v_m)},$$

$$\text{s.t.} \quad \sum_{m=1}^{M} T_{mn} D_{\text{pg}}^{m,n} \geq Q/N_{\text{lap}} \qquad \forall n \in \mathcal{N}, \tag{E.39}$$

$$T_m = \frac{\Delta}{v_m} \qquad \forall m \in \mathcal{M}', \tag{E.40}$$

$$N_{\text{lap}} + 1 \leq \frac{T_{\max}(v_m)}{M T_m} \qquad \forall \in \mathcal{M}', \tag{E.41}$$

$$\text{(E.3), (E.32).} \tag{E.42}$$

$T_{\max}(v_m)$ is obtained in Algorithm E.1 with the substitution $P_{\text{uav}} = P_{\text{uav}}(v_m)$, given by (E.24). (E:P1.1) is a convex optimization problem and can be solved using any available solvers, such as MATLAB's CVX. In practice, the velocity resolution of a UAV is determined by the on-board flight controller. Hence, we consider a finite set of velocity values that a UAV can take during its mission. (E:P1.1) is solved for different velocity values, and the one that maximizes the objective function is selected. Moreover, flying at a constant velocity avoids the additional power consumption linked to acceleration/deceleration, which is neglected by (E.24). Algorithm E.3 defines the overall energy-efficient path planning (E2P2) algorithm combining phases 1 and 2 of the proposed solution.

Algorithm E.3: E2P2 Algorithm.

Initialize the available phase set and the set of velocity values
Find the discretized path between the LoIs, as explained in Section 3.3: $\{\mathbf{p}_m\}$;
Find $b_{\text{pr}}^{m,i}, b_{\text{rg}}^{i,n}\ \forall i,n$ using $\{\mathbf{p}_m\}$ and $\{\mathbf{g}_n\}$;
Find the optimal amplitude-phase shift matrix of the IRSs ($\{\boldsymbol{\Theta}_{\text{r}}^{m,i,n}\}$) using the AO proposed in [30];
Find $D_{\text{pg}}^{m,n}\ \forall m,n$ using (E.23);
for *each* $v \in \mathcal{V}$ **do**
    $v_m = v, T_m = \frac{\Delta}{v_m}\quad \forall m$, calculate $P_{\text{uav}}(v_m)$ and estimate $T_{\max}(v_m)$ using Algorithm E.1;
    Determine the optimal solution of (E:P1.1): $\{T_{mn}\}$, N_{lap};
    if *GEE does not improve* **then**
        break;
Output: Optimal PAP trajectory variables: $\{\mathbf{p}_m\}, \{T_m\}, \{T_{mn}\}, \{\boldsymbol{\Theta}_{\text{r}}^{m,i,n}\}$, N_{lap}.

4 Numerical Analysis and Discussion

In this section we provide the main findings through numerical evaluation. The parameters used for the simulation are given in Table E.3.

4.1 Battery Design

The model and methodology described in Section 3.1 were used to study several aspects related to the battery design, such as the effect of flight velocity, the battery size and the relevance of the Peukert effect. As explained before, Fig. E.5 shows the relevance of the Peukert effect by comparing the case where it is considered with one where it is neglected.

Fig. E.8 shows how the available hovering time varies with different numbers of battery cells. Under the hypothesis of unconstrained battery size, represented by the dotted line, it is possible to observe the trade-off between the extra capacity and the extra weight provided by each extra cell; the weight of a battery cell is considered as 50 g. The positive effect of a larger battery tends to provide decreasing marginal returns as the battery size grows, until the trend is reversed and a heavier battery starts having a negative impact on the hovering time. In reality, it is not possible to increase the UAV weight indefinitely, because there is a maximum take-off weight the motors can withstand, which is set at 3.6kg in this case (inclusive of UAV and battery). When such constraint is considered, the range of possibilities is restricted to the continuous curve in Fig. E.8, and the hovering time maximization is achieved at its upper boundary, corresponding to 17 battery cells and an hovering time of about 25 minutes, as shown in Fig. E.5. Under the current assumptions, the battery configuration is irrelevant, as it

Table E.3: Simulation Parameters.

Label	Definition	Value
B_c	Channel Bandwidth for each GN	20MHz
σ^2	Noise Power	-101 dBm
h_p	PAP's flying altitude	100 m
β	antenna beamwidth	45^0
$v_{\max}$	Maximum achievable PAP speed	20 m/s
Δ	Path Discretization Interval	1 m
P	Transmission Power	23 dBm
(a, b)	LoS probability constants for Suburban topology	(4.88,0.43)
η_1	additional mean pathloss for LoS group	0.2 dB
η_2	additional mean pathloss for for NLoS group	24 dB

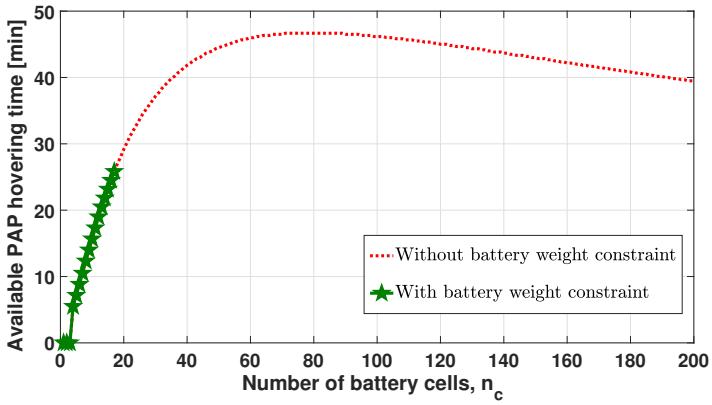

Fig. E.8: Hovering time as a function of battery size, with and without weight constraint.

is evident from step 8 of Algorithm E.1. Nonetheless, 17 is a prime number, so the only way to achieve it is to put all cells either in series or in parallel, which is an unrealistic solution. Therefore, a battery size of 16 cells is a more sensible option.

4.2 IRS Design

Fig. E.9 represents the variation of GEE as a function of the number of elements of a single-IRS-single-user system. The user is placed in the NLoS regime of the PAP position. The figure shows five different cases:

- Case 1: GEE achieved if the IRS phase values are optimized neglecting the amplitude and phase dependency;
- Case 2: The actual received GEE value with the phase optimized according to

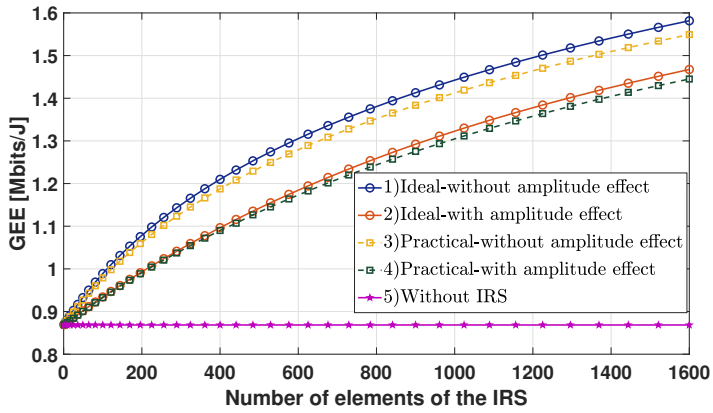

Fig. E.9: GEE vs Number of elements of the IRS.

Case 1;

- Case 3: Each element of the IRS can take any of the available four options: $\{0, \pi/2, -\pi/2, \pi\}$, and the phases are optimized without considering the amplitude effect using the alternate optimization algorithm;
- Case 4: Each element of the IRS has only 4 phase shift options $\{0, \pi/2, -\pi/2, \pi\}$ and the phases are optimized considering the amplitude effect using the alternate optimization algorithm;
- Case 5: GEE of the system without IRS.

As expected, the GEE value improves with the number of elements of the IRSs due to an increase in the number of PAP-IRS and IRS-GN paths. An IRS of area 0.25 m^2 improves the GEE by 63% when the user is in the NLoS regime of the PAP. The figure also shows the effect of considering the interdependence of amplitude and phase responses of the IRS element. Optimizing the IRS phase shift values without considering the amplitude effect could lead to an over-estimation error of 10%. This might result in a trajectory that does not allow the PAP to reach the goal of transmitting Q bits of data to all users, since these are scheduled based on the overestimated spectral efficiency values. Additionally, a discrete set of 4 phase values could achieve a performance comparable to an ideal scenario that allows the IRS elements' phases to be tuned to any value in the interval $[-\pi, \pi)$.

4.3 PAP Trajectory Design

Fig. E.10 compares the total number of circles required to cover a given geographical area according to the proposed multi-tier packing algorithm, with those using 5,7,10

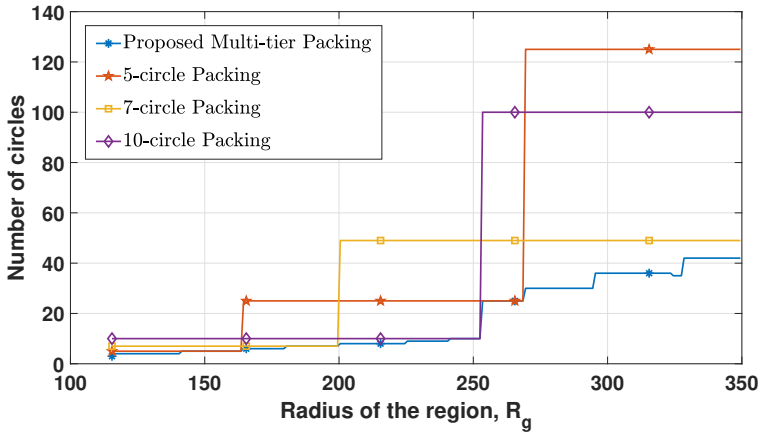

Fig. E.10: Comparison of different packing algorithms.

circles in each level of the multi-level circle packing algorithm, as proposed in [5]. As the figure shows, the proposed method always guarantees the least number of circles, even by a conspicuous margin when the radius of the region to be covered is three or more times the radius of the smaller circle. The radius of the smaller circle, R_{small}, is taken as 100 m. Now, we compare the proposed multi-lap trajectory design with two base scenarios:

- Baseline 1: GEE obtained if the PAP follows a fly-hover-communicate protocol to serve the GNs [5];
- Baseline 2: GEE obtained if the mission is to be completed in a single lap [6].

Single Lap Trajectory Design

In this baseline, the PAP is expected to complete the mission in a single lap. The corresponding optimization problem can be written as,

$$\text{(E:P1.2)}: \underset{\{T_m\},\{T_{mn}\}}{\text{maximize}} \quad \frac{\sum_{m=1}^{M}\sum_{n=1}^{N} T_{mn} D_{\text{pg}}^{m,n}}{\sum_{m=1}^{M} T_m P_{\text{uav}}\left(v_m\right)},$$

$$\text{s.t.} \quad \frac{\Delta}{T_m} \leq v_{\max}, \qquad \forall m \in \mathcal{M}^{'}, \tag{E.43}$$

$$\sum_{m=1}^{M} T_m \leq T_{\max}, \tag{E.44}$$

$$\text{(E.3)}, \text{(E.29)}, \text{(E.32)}. \tag{E.45}$$

Using (E.43) and (E.44), the Peukert constraints are equivalently represented by limiting the PAP flying velocity to $v_{\max}$, such that $P_{\text{uav}}(v_{\max}) \leq P_{\text{uav}}(0)$. Furthermore, the total

trajectory time is constrained to be less than $T_{\max}$; $T_{\max}$ is the maximum available time if the PAP is hovering, determined using Algorithm E.1, as marked in Fig. E.5. Consequently, (E:P1.2) takes the form of a fractional programming problem and can be solved using the Generalized Dinkelbach's Algorithm if the numerator is a concave function and the denominator is a convex function of the optimization variables [4]. Also, all the constraints have to be convex in nature.

The $P_{\text{uav}}(v_m)$ given by (E.24) makes the denominator term of the objective function of (E:P1.2) a non-convex function of the optimization variable T_m. We use the sequential convex programming (SCP) approach to tackle the non-convex objective function. The fundamental idea of the SCP technique is to solve iteratively a sequence of convex approximated problems of the original non-convex problem, so that the feasible solution points converge to the KKT point of the original non-convex problem [4].

Let,

$$E(T_m) = T_m P_{\text{uav}}\left(\frac{\Delta}{T_m}\right), \tag{E.46}$$

$$= C_1\left(T_m + \frac{3\Delta^2}{T_m v_{\text{tip}}^2}\right) + C_2\frac{\Delta^3}{{T_m}^2} + C_3\left(\sqrt{C_4 {T_m}^4 + \frac{\Delta^4}{4}} - \frac{\Delta^2}{2}\right)^{1/2}, \tag{E.47}$$

with $\Delta = \|\mathbf{p}_{m+1} - \mathbf{p}_m\|\ \forall m \in \mathcal{M}'$. By introducing the slack variable z_m such that,

$$z_m^2 = \left(\sqrt{C_4 {T_m}^4 + \frac{\Delta_m^4}{4}} - \frac{\Delta^2}{2}\right), \tag{E.48}$$

where $C_1 = N_R P_b$, $C_2 = \frac{1}{2} C_D A_{\text{f}} \rho(h_{\text{p}})$, $C_3 = W$, and $C_4 = W^2/\{4N_{\text{R}}^2 \rho^2(h_{\text{a}}) A_{\text{r}}^2\}$. By substituting (E.48) in (E.47), (E.47) can be written in the convex form as,

$$E(T_m) = C_1\left(T_m + \frac{3\Delta^2}{T_m v_{\text{tip}}^2}\right) + C_2\frac{\Delta^3}{{T_m}^2} + C_3 z_m, \tag{E.49}$$

such that

$$\frac{{T_m}^4}{z_m^2} \leq \frac{{z_m^l}^2 + 2z_m^l\left(z_m - z_m^l\right) + \Delta^2}{C_4}, \tag{E.50}$$

where (E.50) is the first order Taylor expansion of (E.48) around the point z_m^l. Hence, the optimization problem (E:P1.2) can be rewritten as,

$$\text{(E:P1.3)} \underset{\{T_m\},\{T_{mn}\}}{\text{maximize}} \ \frac{\sum_{m=1}^{M}\sum_{n=1}^{N} T_{mn} D_{pg}^{m,n}}{\sum_{m=1}^{M} E(T_m)}, \quad \text{s.t} \ \ \text{(E.43)} - \text{(E.45)}, \text{(E.50)}. \tag{E.51}$$

The above problem is convex and can be solved using Dinkelbach's algorithm. To find the optimal trajectory, steps 6-10 of Algorithm E.3 are replaced with the Generalized Dinkelbach's algorithm to solve (E:P1.3).

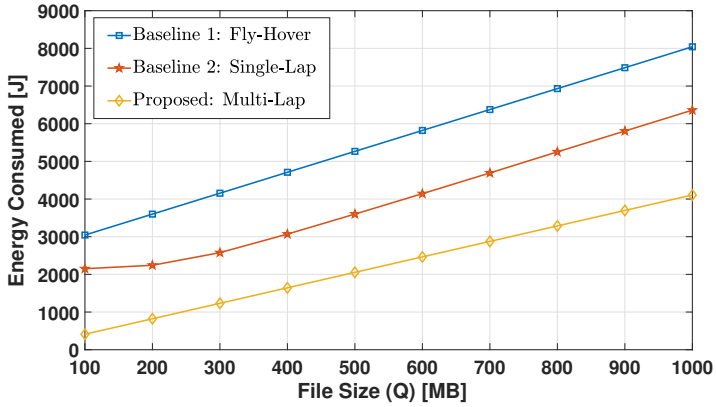

Fig. E.11: Total energy consumed by the PAP as a function of the file size to be delivered to each GN.

Fig. E.11 shows the amount of energy saved by having the the PAP follow the proposed multi-lap trajectory, compared to single-lap and fly-hover communicate policies. The solution is obtained after executing the E2P2 algorithm considering a set of 6 GNs uniformly distributed over a circular area of radius 60 m. Out of the LoS coverage circles obtained using the multi-tier packing algorithm (Algorithm E.2), 3 LoIs are selected that cover the GNs. The shortest path between them, starting and ending at (0,0,100), is determined. In the fly-hover-communicate policy, the PAP hovers at LoIs to serve the GNs with a file of a given size. The PAP is assumed to fly with the maximum velocity between the LoIs. In the single-lap baseline scenario, the velocity with which the PAP covers a path segment and the scheduling of the GNs are calculated by solving (E:P1.3) with the Generalized Dinkelbach's algorithm [4]. The initial feasible value z_m^l to solve (E:P1.3) is taken as the solution of the fly-hover-communicate policy. The amount of energy consumed while following a multi-lap policy is always lower than in the two other baseline scenarios, and the gain scales with the size of the file to be delivered to the GNs. This is because the single-lap policy involves hovering at LoIs for longer to complete the data transmission. In contrast, the multi-lap policy allows the PAP to deliver a file in batches over multiple laps. Since the power consumed during hovering is greater than flying horizontally, the multi-lap policy requires less energy than the single-lap counterpart. The fly-hover-communicate policy is the most energy-hungry, but it has lower complexity than the other two policies.

5 Conclusion

In this work, we proposed an algorithm to design a GEE trajectory for a multi-IRS assisted PAP deployed to deliver a given amount of data to a set of GNs, while taking into account the non-linear discharge behavior of the PAP battery. Furthermore, an algorithm to estimate the available flight time of a PAP for different flying velocities has been provided. The proposed two-phase GEE PAP trajectory design solution allows to consider the interdependence of the phase and amplitude responses of the IRS modules on the received SNR. From the numerical evaluation, it is observed that: adding more battery cells to a PAP battery unit does not always increase the available flight time, since it also increases the weight of the PAP; neglecting the amplitude-phase dependency of IRS elements leads to an overestimation of the GEE of the system. Finally, a fly-communicating PAP system always has a higher GEE compared to the fly-hover-communicate counterpart. The presence of IRS modules enhances the GEE by providing extra separate paths for the signal to reach a GN from the PAP.

The trajectory design for a multi-UAV system, with some UAVs carrying IRS modules on-board and the remaining ones configured as PAPs deployed to serve a set of moving GNs, is left as future work. The same is true for models taking into account the effect of variable temperature on the energy availability of the battery.

References

[1] Mozaffari, Mohammad, et al. "A Tutorial on UAVs for Wireless Networks: Applications, Challenges, and Open Problems," *IEEE communications Surveys and Tutorials 21.3 (2019):* 2334-2360.

[2] 3GPP; Technical Specification Group Services and System Aspects; Unmanned Aerial System (UAS) support in 3GPP; Stage 1; Release 17.

[3] I. Donevski, N. Babu, J. J. Nielsen, P. Popovski and W. Saad, "Federated Learning with a Drone Orchestrator: Path Planning for Minimized Staleness," *IEEE Open Journal of the Commun. Society*, vol. 2, pp. 1000-1014, 2021

[4] N. Babu, K. Ntougias, C. B. Papadias and P. Popovski, "Energy Efficient Altitude Optimization of an Aerial Access Point," in *IEEE 31st Annual International Symposium on Personal, Indoor and Mobile Radio Communications (PIMRC),* 2020, pp. 1-7.

[5] N. Babu, M. Virgili, C. B. Papadias, P. Popovski and A. Forsyth, "Cost- and Energy-Efficient Aerial Communication Networks with Interleaved Hovering and Flying," *IEEE Transactions on Vehicular Technology*, 70(9), pp.9077-9087.

[6] Y. Zeng, J. Xu and R. Zhang, "Energy Minimization for Wireless Communication with Rotary-Wing UAV," *IEEE Trans. on Wireless Commun.*, vol. 18, no. 4, pp. 2329-2345, April 2019.

[7] A. Al-Hourani, S. Kandeepan and S. Lardner, "Optimal LAP Altitude for Maximum Coverage," *IEEE Wireless Communications Letters,* vol. 3, no. 6, pp. 569-572, Dec. 2014

[8] W. Huang, D. M. Kim, W. Ding and P. Popovski, "Joint Optimization of Altitude and Transmission Direction in UAV-Based Two-Way Communication," *IEEE Wireless Commun. Lett.*, vol. 8, no. 4, pp. 984-987, Aug. 2019

[9] S. Shakoor, Z. Kaleem, M. I. Baig, O. Chughtai, T. Q. Duong and L. D. Nguyen, "Role of UAVs in Public Safety Communications: Energy Efficiency Perspective," *IEEE Access,* vol. 7, pp. 140665-140679, 2019.

[10] C. T. Cicek, H. Gultekin, B. Tavli and H. Yanikomeroglu, "UAV Base Station Location Optimization for Next Generation Wireless Networks: Overview and Future Research Directions," in *1st International Conference on UVS, Oman* , 2019.

[11] M. Al-Jarrah, E. Alsusa, A. Al-Dweik and M.-S. Alouini, "Performance Analysis of Wireless Mesh Backhauling Using Intelligent Reflecting Surfaces," *IEEE Trans. Wireless Commun.*, vol. 20, no. 6, pp. 3597-3610, Jun. 2021.

[12] S Q. Wu, S. Zhang, B. Zheng, C. You, and R. Zhang, "Intelligent Reflecting Surface-Aided Wireless Communications: A Tutorial," *IEEE Trans. Commun.*, vol. 69, no. 5, pp. 3313-3351, May 2021.

[13] M. Al-Jarrah, E. Alsusa, A. Al-Dweik and D. K. C. So, "Capacity Analysis of IRS-Based UAV Communications with Imperfect Phase Compensation," *IEEE Wireless Commun. Lett.*, vol. 10, no. 7, pp. 1479-1483, Jul. 2021.

[14] M. Al-Jarrah, A. Al-Dweik, E. Alsusa, Y. Iraqi, and M.-S. Alouini, "On the Performance of IRS-Assisted Multi-Layer UAV Communications with Imperfect Phase Compensation," *IEEE Trans. Commun.*, IEEE early access, 2021.

[15] S. Li, B. Duo, X. Yuan, Y. Liang, and M. Di Renzo, "Reconfigurable Intelligent Surface Assisted UAV Communication: Joint Trajectory Design and Passive Beamforming," *IEEE Wireless Commun. Lett.*, vol. 9, no. 5,pp. 716-720, May 2020.

[16] L. Ge, P. Dong, H. Zhang, J. Wang, and X. You, "Joint Beamforming and Trajectory Optimization for Intelligent Reflecting Surfaces-Assisted UAV Communications," *IEEE Access*, vol. 8, pp. 78702-78712, 2020.

[17] Z. Wei *et al.*, "Sum-Rate Maximization for IRS-Assisted UAV OFDMA Communication Systems," *IEEE Trans. Wireless Commun.*, vol. 20, no. 4, pp. 2530-2550, Apr. 2021.

[18] M. Hua, L. Yang, Q. Wu, C. Pan, C. Li and A. Swindlehurst, "UAV-Assisted Intelligent Reflecting Surface Symbiotic Radio System," *IEEE Trans. Wireless Commun.*, vol. 20, no. 9, pp. 5769-5785, Sep. 2021.

[19] Y. Pan, K. Wang, C. Pan, H. Zhu and J. Wang, "UAV-Assisted and Intelligent Reflecting Surfaces-Supported Terahertz communications," *IEEE Wireless Commun. Lett.*, vol. 10, no. 6, pp. 1256-1260, Jun. 2021.

[20] Matthiesen, Bho, et al. "Intelligent Reflecting Surface Operation under Predictable Receiver Mobility: A continuous time propagation model," *IEEE Wireless Commun. Lett.* 10.2 (2020): 216-220.

[21] Gong, Shimin, et al. "Backscatter-Aided Cooperative Relay Communications in Wireless-Powered Hybrid Radio Networks," *IEEE Network* 33.5 (2019): 234-241.

[22] Gao, Xiaozheng, et al. "Cooperative Scheme for Backscatter-Aided Passive Relay Communications in Wireless-Powered D2D Networks." *IEEE Internet of Things Journal* 9.1 (2021): 152-164.

[23] E. Basar, M. Di Renzo, J. De Rosny, M. Debbah, M.-S. Alouini, and R. Zhang, "Wireless Communications Through Reconfigurable Intelligent Surfaces," *IEEE Access*, vol. 7, pp. 116753–116773, Aug. 2019.

[24] Q. Wu and R. Zhang, "Intelligent Reflecting Surface Enhanced Wireless Network via Joint Active and Passive Beamforming," *IEEE Trans. Wireless Commun.*, vol. 18, no. 11, pp. 5394-5409, Nov. 2019.

[25] W. Tang et al., "Wireless Communications With Reconfigurable Intelligent Surface: Path Loss Modeling and Experimental Measurement," *IEEE Trans. on Wireless Commun.,* vol. 20, no. 1, pp. 421-439, Jan. 2021, doi: 10.1109/TWC.2020.3024887.

[26] Björnson, Emil, et al. "Reconfigurable Intelligent Surfaces: A signal Processing Perspective with Wireless Applications," *IEEE Signal Processing Magazine* 39.2 (2022): 135-158.

[27] "Study on Enhanced LTE Support for Aerial Vehicles (Release 15)," 3GPP, Sophia Antipolis, France, Rep. 3GPP TR 36.777, Dec. 2017.

[28] Filippone A, "Flight performance of Fixed and Rotary Wing Aircraft," *Elsevier*; 2006 May 10.

[29] 3.7V, 3200mAh, GWL Power, LG MH1, 2019 [Online]. Available:https://files.gwl.eu/inc/_doc/attach/StoItem/5230/Datasheet_LG_MH1.pdf.

[30] Abeywickrama, S., Zhang, R., Wu, Q., and Yuen, C., "Intelligent Reflecting Surface: Practical Phase Shift Model and Beamforming Optimization," *IEEE Trans. on Commun.*, 68(9), 5849-5863.

[31] F. Cheng, H. Wang, and P. Cui, "Rotorcraft Flight Endurance Estimation Based on a New Battery Discharge Model," *Chinese J. Aeronaut.,* vol. 30, no. 4, pp. 1561–1569, Aug. 2017.

[32] M. H. Hwang, H. R. Cha, and S. Y. Jung, "Practical Endurance Estimation for Minimizing Energy Consumption of Multirotor Unmanned Aerial Vehicles," *Energies*, vol. 11, no. 9, pp. 1–10, 2018.

[33] Soret, Beatriz, et al. "5G Satellite Networks for Internet of Things: Offloading and Backhauling," *International Journal of Satellite Communications and Networking 39.4 (2021):* 431-444.

[34] Tóth, G. Fejes, "Thinnest Covering of a Circle by Eight, Nine, or Ten Congruent Circles," *Combinatorial and comput. geometry 52.361 (2005)*: 59.

Paper F

Fairness Based Energy-Efficient 3D Path Planning of a Portable Access Point: A Deep Reinforcement Learning Approach

Nithin Babu, Igor Donevski, Alvaro Valcarce, Petar Popovski, Jimmy Jessen Nielsen, and Constantinos B. Papadias

Under review in
IEEE Open Journal of the Communications Society.

The layout has been revised.

Abstract

In this work, we optimize the 3D trajectory of an unmanned aerial vehicle (UAV)-based portable access point (PAP) that provides wireless services to a set of ground nodes (GNs). Moreover, as per the Peukert effect, we consider pragmatic non-linear battery discharge for UAV's battery. Thus, we formulate the problem in a novel manner that represents the maximization of a fairness-based energy efficiency metric and is named fair energy efficiency (FEE). The FEE metric defines a system that lays importance on both the per-user service fairness and the PAP's energy efficiency. The formulated problem takes the form of a non-convex problem with non-tractable constraints. To obtain a solution we represent the problem as a Markov Decision Process (MDP) with continuous state and action spaces. Considering the complexity of the solution space, we use the twin delayed deep deterministic policy gradient (TD3) actor-critic deep reinforcement learning (DRL) framework to learn a policy that maximizes the FEE of the system. We perform two types of RL training to exhibit the effectiveness of our approach: the first (offline) approach keeps the positions of the GNs the same throughout the training phase; the second approach generalizes the learned policy to any arrangement of GNs by changing the positions of GNs after each training episode. Numerical evaluations show that neglecting the Peukert effect overestimates the air-time of the PAP and can be addressed by optimally selecting the PAP's flying speed. Moreover, the user fairness, energy efficiency, and hence the FEE value of the system can be improved by efficiently moving the PAP above the GNs. As such, we notice massive FEE improvements over baseline scenarios of up to 88.31%, 272.34%, and 318.13% for suburban, urban, and dense urban environments, respectively.

1 Introduction

To provide seamless network connectivity, it is expected that future radio access networks implement much denser deployments of small cells, that imply very high deployment costs. A more cost-efficient solution for serving a set of ground nodes (GNs) is to use an unmanned aerial vehicle (UAV) that carries a radio access node, hereafter referred to as a portable access point (PAP) [1]. The third generation partnership project (3GPP) item [2] proposes the architecture and Quality-of-Service (QoS) requirements for such a system. The ability to have a controllable maneuver and the presence of line-of-sight (LoS) dominant air to ground channels [6] make it appropriate for applications such as data collection from wireless sensor networks (WSNs), enhancing the cellular coverage, remote sensing, emergency deployments, and so on [1]. The main drawback of the PAP system is its limited air-time which is a function of the capacity of the onboard battery unit and its power consumption profile. The air-time of a PAP is defined as the duration it remains aloft. The power consumed by a PAP varies with its mode of

flying; for instance, a PAP consumes the maximum amount of power when it climbs vertically up, whereas the power consumption can be the least during a horizontal flight at an certain non-zero velocity [3]. Hence, the air-time of a PAP can be increased by suitably selecting its flying mode and velocity. Moreover, the available capacity of a PAP battery unit is a non-linear function of the power-draw profile of the PAP [4]. Additionally, the air to ground channel LoS probability and the path loss between a PAP and a GN are proportional functions of the elevation angle and 3D distance between them, respectively [6]. Consequently, the trajectory of a PAP can be used as a tool to increase its air-time and improve the channel to a GN. Hence, in this work, we design a 3D trajectory for a PAP that maximizes the number of bits transmitted per Joule of energy consumed while guaranteeing a fair service to the GNs measured in terms of fair energy efficiency (FEE) of the system.

1.1 Related Works

The works in [6]- [29] consider UAV placement optimization and trajectory design problems with main objectives as maximizing coverage area, throughput, air-time, energy efficiency, and minimizing mission time, power consumption, e.t.c. The authors of [6]- [10] consider the 3D placement of UAV(s) to maximize the coverage area. In [6], the authors propose a probabilistic LoS-non-LoS (NLoS) air to ground channel model and use it to find the optimal hovering altitude of a stationary UAV that maximizes the coverage area. [7] and [8] find the optimal altitude that maximizes the coverage area of a multi- and single-UAV system using circle packing theory. [9] uses a combination of exhaustive search and maximal weighted area algorithm to propose an optimal UAV placement method that maximizes the number of users covered, whereas [10] considers the placement optimization of a dynamic standalone drone equipped with a steerable antenna. The work in [11] proposes a power-efficient deployment of multiple UAVs which are used as aerial base stations to collect data from ground Internet of Things (IoT) devices, whereas [12] and [13] consider minimizing the total transmit power of a drone base station by considering a downlink communication scenario.

The authors of [14]- [18] consider the average throughput of a UAV-based aerial communication system as the performance metric. [14] and [15] maximize the minimum average throughput by considering an uplink communication between a set of GNs and a UAV, whereas [16], [17], [18], and [19] consider a downlink communication scenario. In [20]- [24], the authors consider the aerial vehicle's energy consumption while proposing an energy-efficient UAV(s) deployment policy. In [20], the authors propose a tractable power consumption model for a single-rotor rotary-wing UAV and use it to design a 2D trajectory that consumes the least amount of energy. In [24], we extend the model to a multi-rotor UAV and propose a 2D trajectory for a PAP that maximizes the number of bits transmitted per Joule of energy consumed while following a fly-hover-communicate protocol to serve the users. The algorithm given in [21] designs an energy-efficient

2D trajectory for a fixed-wing UAV, while in [22], we determine a set of energy-efficient hovering points using circle packing theory. The works [25]- [27] use a deep reinforcement learning (DRL) technique to design a UAV(s) placement policy that guarantees fair service to the users. [25] uses the UAV trajectory as a tool to achieve fairness in terms of learning staleness, which reflects the learning time discrepancy among the users. The proposed policies of [26] and [27] achieve fairness in terms of coverage and throughput, respectively. Comprehensive lists of works that consider placement optimization of a UAV-based system are available in [28] and [29].

1.2 Main Contributions and Paper Organization

The works in [6]- [17] propose UAV trajectory design algorithms that either maximize communication-related parameters such as the coverage area and sum or average throughput or minimize the transmit power. The works mainly design a 2D trajectory or represent the 3D optimal UAV(s) positioning problems as two subproblems that optimize the vertical and horizontal positioning of the UAV(s) recurrently. Even though the problem formulations to maximize the energy-efficiency in [20]- [24] consider the aerial vehicle's power consumption, the solutions are again 2D flight trajectories. Please note that for an energy-limited system such as a PAP, maximizing the number of bits transmitted per Joule of energy consumed while ensuring user fairness is paramount. Maximizing the throughput for a given energy budget is different from maximizing the energy efficiency since each movement of the UAV should maximize the throughput and minimizes the energy consumption simultaneously. Moreover, a UAV consumes different power during its axial climb and forward flight modes. Neglecting this, as in [18], [19], and [26], falsely overestimates the air-time of a UAV resulting in the initiation of the early-landing procedure before completing the planned trajectory. Furthermore, [18] and [26] propose trajectory planning and resource allocation schemes for high-mobility users in which the trajectory parameters and the resources are allocated to guarantee high instantaneous throughput fairness between all users. Even though the proposed fairness metric is ideal for analyzing the performance of the considered scenario, it might be sub-optimal for an IoT application such as data collection from an IoT network. For such applications, long-term fairness metrics are more suitable. For instance, consider a scenario in which the PAP is deployed to deliver a file of a given size to all the users by the end of the trajectory. In this case, the service fairness could be measured at the end of the trajectory; if all the users are delivered with an equal amount of bits on an average by the end of the trajectory, the fairness between the users will be high.

Suppose the PAP flies near to a user in a given time instant. In that case, it is more efficient to allocate more resources to that user since the communication channel to the user, as well as the throughput, will improve. However, to guarantee a high long-term user fairness, the later segments of the trajectory should be closer to the remaining users. Finally, none of the above works consider the Peukert effect seen in Li-ion batteries that

are typically used in UAVs. Neglecting the Peukert effect overestimates the air-time of the PAP, resulting in initiating the early-landing procedure before completing the planned trajectory. In practice, the PAP will be flying at different velocities resulting in different power consumption; hence the remaining air-time of the PAP varies after each action as a non-linear function of the power consumption. This affects the system's energy efficiency since the number of trajectory segments varies as a non-linear function of the power consumption profile. In essence, the 3D trajectory design of a PAP that maximizes the fairness-based energy efficiency while factoring in the UAV power consumption and the Peukert effect has, to the best of our knowledge, not yet been considered in the literature. The main contributions of this work are summarized as follows:

- We propose a method to model the non-linear Peukert effect of the PAP battery using the data points from a data sheet;
- We additionally propose an algorithm to estimate the air-time of a PAP by considering the Peukert effect and the PAP power consumption profile;
- We introduce a user fairness-based energy efficiency metric called the fair energy efficiency that considers user fairness, sum throughput, and the PAP propulsion power consumption;
- Finally, we implement a twin delayed deep deterministic policy gradient (TD3)-based 3D path planning algorithm to design a 3D trajectory for the PAP that maximizes the FEE value of the system.

This paper is structured as follows: Section 2 explains the system setup, propagation environment, the 3D power consumption model of the PAP, and the FEE metric. In the section, we also detail the Peukert effect of the PAP battery and propose an algorithm to estimate the air-time of the PAP. Section 3 includes the problem formulation to maximize the FEE of the system and the solving methodology. Section 4 presents the main findings through numerical evaluations, and elaborates the significance of the results. Finally, Section 5 summarizes the main findings of this work. All the quantities are in SI units unless otherwise specified.

2 System Model

In this work, we consider a PAP deployed to serve a set of N GNs. Each GN $n \in \mathcal{N} = \{1, 2, 3, .., N\}$ is located at $\mathbf{g}_{\mathrm{n}} = [\mathbf{g}_{\mathrm{h},n}, 0]$ of Cartesian space (x, y, z) with $\mathbf{g}_{\mathrm{h},n} = [g_{\mathrm{x},n}, g_{\mathrm{y},n}]$, as shown in Fig. F.1. The PAP flies along a 3D path to serve the set of GNs. Both the PAP and the GNs are assumed to be equipped with omni-directional antennas.

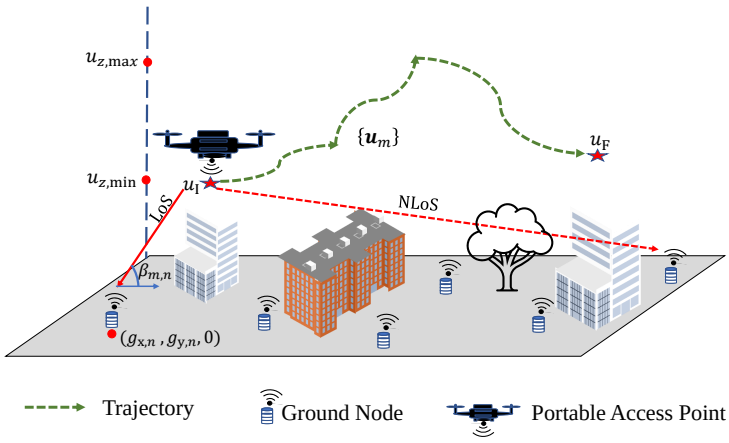

Fig. F.1: Trajectory determination scenario.

2.1 PAP Trajectory Model

The optimal flying path of the PAP is obtained by dividing the total air time T into M time segments of length δ_t each such that $T = M\delta_t$ [20]. The value of δ_t is chosen so that within each segment the PAP can be assumed to fly with a constant velocity, and the change in path loss values between the PAP and each GN is insignificant, i.e., $\delta_t v_{\max} \leq \Delta$ where $v_{\max}$ is the maximum speed of the UAV and Δ is the maximum change in distance below which the path loss values between the PAP and each GN remain stationary. Consequently, the path of the PAP can be represented using $M+1$ points, whose locations are denoted as $\mathbf{u}_m = [\mathbf{u}_{\mathrm{h},m}, u_{\mathrm{z},m}]$, $m \in \mathcal{M} = \{1, 2, 3, .., M+1\}$ where $\mathbf{u}_{\mathrm{h},m} = [u_{\mathrm{x},m}, u_{\mathrm{y},m}]$ is the projection of the PAP location on the horizontal plane. The length of each segment and the maximum PAP velocity are constrained as,

$$\left\|\mathbf{u}_{m+1} - \mathbf{u}_m\right\| = \delta_t v_m \leq \delta_t v_{\max} \leq \Delta \ \forall m \in \mathcal{M}^{'}, \tag{F.1}$$

where $\mathcal{M}^{'} = \{1, 2, ..M\}$. In a particular segment, the PAP follows a time-division multiple access (TDMA) scheme to serve the GNs: let $T_{m,n}$ be the time allocated to the n^{th} GN while the PAP is flying in the m^{th} path segment with a speed of v_m m/s, then,

$$\Sigma_{n=1}^{N} T_{m,n} = \delta_t \quad \forall m \in \mathcal{M}^{'}. \tag{F.2}$$

2.2 Propagation Environment

The communication channel between the PAP and a GN at a given time can be either LoS or NLoS depending on the relative position of the GN with respect to the PAP and

the blockage profile of the environment. The LoS and NLoS path loss values can be expressed as [6]- [11],

$$L_{m,n}^{\text{los}} = 20\log d_{m,n}^{\text{3D}} + 20\log f_c + 20\log\left(\frac{4\pi}{c}\right) + \eta^{\text{los}}, \tag{F.3}$$

$$L_{m,n}^{\text{nlos}} = 20\log d_{m,n}^{\text{3D}} + 20\log f_c + 20\log\left(\frac{4\pi}{c}\right) + \eta^{\text{nlos}}, \tag{F.4}$$

with $d_{m,n}^{\text{3D}} = \sqrt{{d_{m,n}^{\text{2D}}}^2 + u_{\text{z},m}^2}$ and $d_{m,n}^{\text{2D}} = \|\mathbf{u}_{\text{h},m} - \mathbf{g}_{\text{h},n}\|$. f_c and c are the carrier frequency and the velocity of light, respectively. The corresponding probability of existence of a LoS link between the PAP and the n^{th} GN while the PAP is in the m^{th} path segment can be expressed as,

$$P_{m,n}^{\text{los}} = \frac{1}{1 + a\exp\left[-b(\beta_{m,n} - a)\right]}, \tag{F.5}$$

with $\beta_{m,n} = \text{arctand}\left(\frac{u_{\text{z},m}}{d_{m,n}^{\text{2D}}}\right)$; a and b are the environment dependent parameters; η^{los} and η^{nlos} are the mean values of the respective additional path loss values due to long-term channel variations. For a given elevation angle, this additional path loss has a Gaussian distribution [5], and we use its mean value in this work [6]- [8]. The mean value depends on the building profile of the region and it is noticed that the change in the additional path loss within a particular propagation group (LoS/NLoS) is insignificant compared to the change in path loss value from one group to the other [5], [6]. This allows us to model the path loss with a constant gap between the two propagation groups as given in (F.3) and (F.4). Hence, the expected spectral efficiency to the n^{th} GN is given by,

$$\overline{R}_{m,n} = P_{m,n}^{\text{los}} R_{m,n}^{\text{los}} + (1 - P_{m,n}^{\text{los}}) R_{m,n}^{\text{nlos}}, \tag{F.6}$$

where $R_{m,n}^{x} = \log_2\left(1 + \frac{P_t}{\sigma^2 10^{L_{m,n}^{x}/10}}\right)$ $\forall x \in \{\text{los}, \text{nlos}\}$; P_t and σ^2 are the respective transmitted signal and noise power values.

2.3 UAV Power Consumption Model

In this section, we provide the general expressions to calculate the total power consumed by the PAP during a considered time slot. The definitions and values[1] of all the variables used in this section are given in Table F.1. In the m^{th} time slot, the PAP moves from $\mathbf{u}_m$ to $\mathbf{u}_{m+1}$ in δ_t seconds. Then, as shown in Fig. F.2, the PAP velocity vector in the spherical coordinates system can be represented as $\mathbf{v}_m =$

[1] https://dl.djicdn.com/downloads/m100/M100_User_Manual_EN.pdf

Table F.1: UAV's physical properties [24].

Label	Definition	Value
W	Weight of the UAV in Newton	24.5 N
N_{R}	Number of rotors	4
v_m	UAV's horizontal flying velocity	-
v_{tip}	Tip speed of the rotor	102 m/s
A_{f}	Fuselage area	0.038 m^2
$\rho(u_{\mathrm{z},m})$	Air density at $u_{\mathrm{z},m}$	-
C_D	Drag Co-efficient	0.9
A_r	Rotor disc area	0.06 m^2
Δ_p	Profile drag coefficient	0.002
s	Rotor solidity	0.05

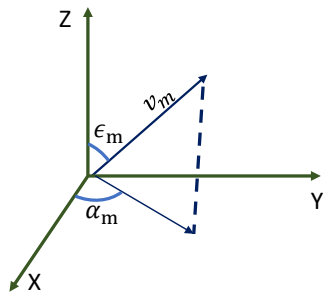

Fig. F.2: Velocity Vector.

$(v_m, \alpha_m, \epsilon_m)$, in which $v_m = \|\mathbf{u}_{m+1} - \mathbf{u}_m\|/\delta_t$ is the speed of the PAP at which it travels from $\mathbf{u}_m$ to $\mathbf{u}_{m+1}$, $\alpha_m = \arctan\left[(u_{\mathrm{y},m+1} - u_{\mathrm{y},m})/(u_{\mathrm{x},m+1} - u_{\mathrm{x},m})\right]$ and $\epsilon_m = \arctan\left[\|\mathbf{u}_{\mathrm{h},m+1} - \mathbf{u}_{\mathrm{h},m}\|/(u_{\mathrm{z},m+1} - u_{\mathrm{z},m})\right]$ are the azimuth and elevation angles of $\mathbf{u}_{m+1}$ with respect to the axes located at $\mathbf{u}_m$. In each time slot, the PAP is in one of the following flight conditions:

Forward Flight ($v_m \neq 0$, $\epsilon_m \neq 0$)

The forward flight condition contains the following PAP flying modes: 1) the PAP moves along a plane that is parallel to the horizontal plane ($v_m \neq 0, \epsilon_m = 90°$) commonly called as level forward flight; 2) forward (inclined) ascent or descent mode in which the PAP moves in the 3D space thereby changing all the 3 coordinates of its position ($v_m \neq 0$, $\epsilon_m \notin \{90°, 0°\}$). The amount of power required to maintain this flight condition can be determined using [24], [3],

$$P_{\text{uav}}^{\text{fwd}}(\mathbf{v}_m) = \underbrace{N_{\text{R}} P_{\text{b}} \left(1 + \frac{3v_m^2}{v_{\text{tip}}^2}\right)}_{P_{\text{blade}}} + \underbrace{\frac{1}{2} C_D A_{\text{f}} \rho(u_{\text{z},m}) v_m^3}_{P_{\text{fuselage}}} + \underbrace{W \left[\sqrt{\left(\sqrt{\frac{W^2}{4N_{\text{R}}^2 \rho^2(u_{\text{z},m}) A_{\text{r}}^2} + \frac{v_m^4}{4}} - \frac{v_m^2}{2}\right)} + \cos\epsilon_m\right]}_{P_{\text{induce}}}, \tag{F.7}$$

where $P_{\text{b}} = \frac{\Delta_p}{8} \rho(u_{\text{z},m}) s A_{\text{r}} v_{\text{tip}}^3$ and $\rho(u_{\text{z},m}) = (1 - 2.2558.10^{-5} u_{\text{z},m})^{4.2577}$. P_{blade} and P_{fuselage} are the powers required to overcome the profile drag forces of the rotor blades and the fuselage of the aerial vehicle that oppose its forward movement, respectively, while P_{induce} represents the induced power from the rotation of rotors.

Hover ($v_m = 0$)

In this mode, the PAP is static and its position is the same as that in the previous time slot. From [24], the hovering power consumption of a PAP is estimated using,

$$P_{\text{uav}}^{\text{hov}} = N_{\text{R}} P_{\text{b}} + \frac{W^{3/2}}{\sqrt{4N_{\text{R}} \rho(u_{\text{z},m}) A_{\text{r}}}}. \tag{F.8}$$

Axial Climb or Descent ($v_m \neq 0$, $\epsilon_m = 0$)

Here, the PAP moves along the +/− z-direction. Using (12.35) of [3], the power required by the PAP to climb vertically ($\epsilon_m = 0$) is expressed as,

$$P_{\text{uav}}^{\text{vert}}(v_m) = \frac{W}{2} \left(v_m + \sqrt{v_m^2 + \frac{2W}{N_{\text{R}} \rho(u_{\text{z},m}) A_{\text{r}}}}\right) + N_{\text{R}} P_{\text{b}}. \tag{F.9}$$

Hence, the total power consumed by the PAP while it flies along the m^{th} path segment is calculated as,

$$P_{\text{uav}}(\mathbf{v}_m) = \begin{cases} P_{\text{uav}}^{\text{fwd}}(\mathbf{v}_m) & \text{if } v_m \neq 0 \,\&\, \epsilon_m \neq 0, \\ P_{\text{uav}}^{\text{hov}} & \text{if } v_m = 0, \\ P_{\text{uav}}^{\text{vert}}(v_m) & \text{if } v_m \neq 0 \,\&\, \epsilon_m = 0. \end{cases} \tag{F.10}$$

2.4 Fair Energy Efficiency

The fair energy efficiency (bits/Joule) of the system is expressed as,

$$\mathrm{FEE}\left(\mathcal{V}_M\right) = \frac{\mathrm{FI}\left(\mathcal{V}_M\right) \sum_{m=1}^{M} \sum_{n=1}^{N} D_{m,n}\left(\mathbf{v}_m\right)}{\sum_{m=1}^{M} \delta_t P_{\mathrm{uav}}(\mathbf{v}_m)}, \tag{F.11}$$

where $D_{m,n}\left(\mathbf{v}_m\right) = BT_{m,n}\overline{R}_{m,n}$ is the number of bits transmitted to the n^{th} GN while the PAP is in the m^{th} segment, and

$$\mathrm{FI}\left(\mathcal{V}_M\right) = \frac{\left[\sum_{n=1}^{N} \overline{\mathrm{D}}_n\left(\mathcal{V}_M\right)\right]^2}{N \sum_{n=1}^{N} \overline{\mathrm{D}}_n^2\left(\mathcal{V}_M\right)}, \tag{F.12}$$

is the fairness index with $\overline{\mathrm{D}}_n\left(\mathcal{V}_M\right) = \sum_{m=1}^{M} \mathrm{D}_{m,n}\left(\mathbf{v}_m\right)/M$ giving the average number of bits transmitted to the n^{th} GN by the end of the trajectory. $\mathrm{FI}\left(\mathcal{V}_M\right) = 1$ means the PAP sends equal number of data bits to the GNs when it completes the trajectory. B is the total available bandwidth; $\mathcal{V}_M = \{\mathbf{v}_m, \forall m \in \mathcal{M}^{'}\}$. Considering the energy efficiency metric alone could allow the PAP to fly above a sub-set of GNs to maximize the energy efficiency by increasing the sum rate. Furthermore, the fairness index can be maximized either by maximizing the average number of bits transmitted to each GN or by minimizing it. The FEE metric defined in (F.11) is a weighted energy efficiency metric, where the weight is the fairness index. This forces the PAP to follow a 3D trajectory that maximizes energy efficiency and per-user fairness.

2.5 The Peukert Effect

A usual approach to estimate the maximum air-time of a PAP is to find the ratio of the initial onboard energy to the sum of instantaneous power consumption values [20]- [24]. This calculation has the fundamental assumption that the available discharge time of the PAP battery remains the same irrespective of the power-draw profile of the PAP. But, in practice, the battery discharge rate affects its available discharge time as shown in Fig. F.3, called the Peukert effect [4].

Let c_o be the rated capacity of a cell of the PAP battery unit in ampere-hours (Ah) and t_o be the rated discharge time in hours (h). This means, if the PAP draws 1A of current from the cell, the cell will be completely discharged after t_o hours. However, in practice, the current drawn by the PAP changes with time as a function of the power required and the terminal voltage of the battery:

$$P_{\mathrm{uav}}(\mathbf{v}_m) = i_m^{\mathrm{b}} \cdot n^{\mathrm{b}} \cdot V_m^{\mathrm{b}} \quad \forall m \in \mathcal{M}^{'}, \tag{F.13}$$

where n^{b} is the number of battery cells connected in series to form the battery unit of the PAP with V_m^{b}, the terminal voltage of a battery cell at the beginning of the m^{th}

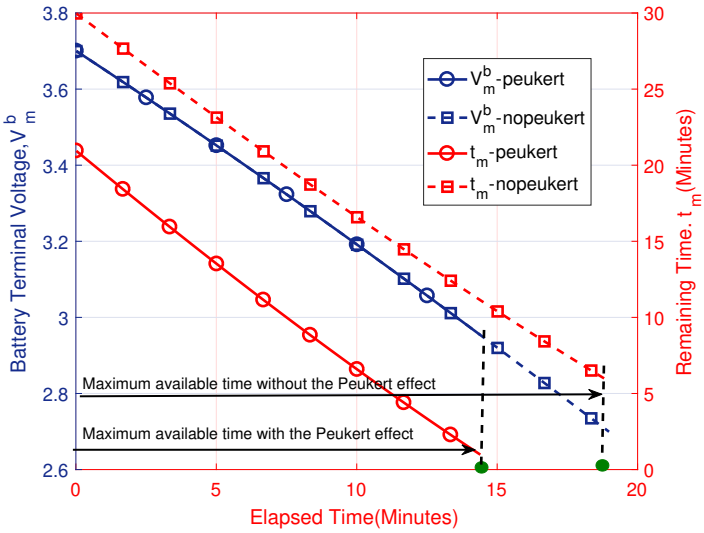

Fig. F.3: Air-time with and without considering the Peukert effect for constant 200W power-draw until the battery discharges completely.

time slot; also, $V_1^{\mathrm{b}} = V_o$ is the nominal voltage of the battery. Hence, the current drawn by the PAP during the m^{th} slot is $i_m^{\mathrm{b}} = P_{\mathrm{uav}}(\mathbf{v}_m)/(n^{\mathrm{b}} \cdot V_m^{\mathrm{b}})$. After the m^{th} slot, the battery terminal voltage drops according to,

$$V_{m+1}^{\mathrm{b}} = V_m^{\mathrm{b}} - s_m^{\mathrm{b}}(i_m^{\mathrm{b}}) \cdot i_m^{\mathrm{b}} \delta_t \ \forall m \in \mathcal{M}^{'}, \tag{F.14}$$

where $s_m^{\mathrm{b}}(i_m^{\mathrm{b}})$ is the rate of change of terminal voltage per Ah that changes as a function of i_m^{b}. In addition to the drop in the battery terminal voltage, the remaining discharge time also changes after each time slot according to,

$$t_{m+1}^{\mathrm{b}} = t_m^{\mathrm{b}} \left(\frac{c_m^{\mathrm{b}} - i_m^{\mathrm{b}} \delta_t}{i_{m+1}^{\mathrm{b}} t_m^{\mathrm{b}}} \right)^{p^{\mathrm{b}}} \qquad \forall m \in \mathcal{M}^{'}, \tag{F.15}$$

with

$$t_1^{\mathrm{b}} = t_o \left(\frac{c_o}{i_1^{\mathrm{b}} t_o} \right)^{p^{\mathrm{b}}}; \tag{F.16}$$

$c_m^{\mathrm{b}} = t_m^{\mathrm{b}} i_m^{\mathrm{b}}$ with $c_1^{\mathrm{b}} = c_o$; $p^{\mathrm{b}} > 1$ is the Peukert coefficient that depends on the type of the battery used; i_{m+1}^{b} is determined by substituting the voltage determined using (F.14) in (F.13) to guarantee a power output of $P_{\mathrm{uav}}(\mathbf{v}_{m+1})$. The PAP should reach the destination either before the value of the terminal voltage reaches V_{cutoff}: $V_{M+1}^{\mathrm{b}} \geq V_{\mathrm{cutoff}}$ or $t_{M+1}^{\mathrm{b}} \geq 0$.

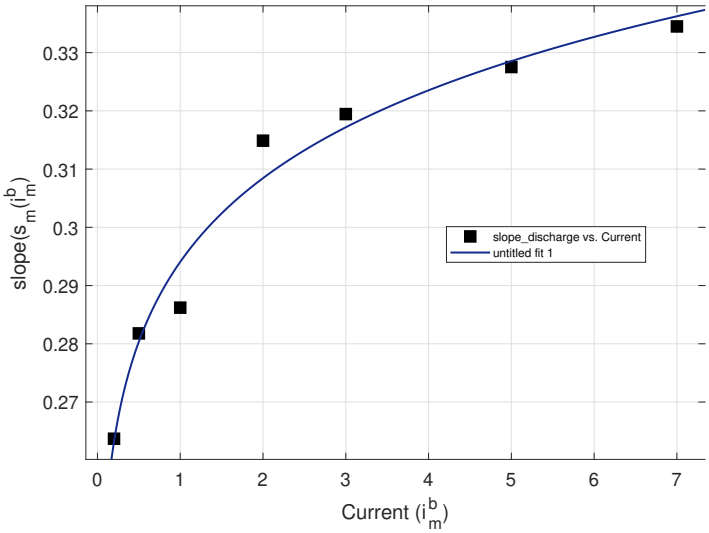

Fig. F.4: Variation of battery discharge slope for different discharge current.

The slope, $s_m^{\mathrm{b}}(i_m^{\mathrm{b}})$ depends on the type of the battery used in the PAP. For a Li-ion battery with $c_o = 3.1$ Ah, $t_o = 3$ h, $i_o = 1$ A, $V_{\text{cutoff}} = 2.5$ V, and $V_o = 3.7$ V, we perform a curve fitting over the variation of $s_m^{\mathrm{b}}(i_m^{\mathrm{b}})$ with regards to i_m^{b} using the data points from the data sheet [30] as shown in Fig. F.4:

$$s_m^{\mathrm{b}}(i_m^{\mathrm{b}}) = f_1^{\mathrm{b}} \cdot {i_m^{\mathrm{b}}}^{f_2^{\mathrm{b}}}, \tag{F.17}$$

where $f_1^{\mathrm{b}} = 0.2941$, and $f_2^{\mathrm{b}} = 0.06888$.

The Peukert effect is better explained in Fig. F.3. The figure shows the voltage drop and the remaining discharge time of a typical Li-ion battery (commonly used in UAVs) during discharge when the PAP draws a power of 200 W continuously. As shown in the figure, a battery is useful until the terminal voltage or the remaining discharge time becomes lower than the corresponding threshold values (2.9 V and 30 Seconds, respectively), whichever happens first. The air-time of the PAP is defined as the time elapsed from the beginning till the battery is useful. As seen in the figure, neglecting the Peukert effect overestimates the air-time of the PAP. Thus a trajectory planned considering the availability of air-time determined without considering the Peukert effect will initiate the early-landing procedure before completing the trajectory. This affects the system's service fairness, sum rate, and energy efficiency. The PAP air-time for a given power profile considering the Peukert effect can be estimated using Algorithm F.1.

Algorithm F.1: PAP Air Time Estimation.

Initialize $m = 1$ $P_{\text{uav}}(\mathbf{v}_m)$, t_o, V_o, c_o, V_{cutoff}, δ_t;
while *1* **do**
  if *($m == 1$)* **then**
    $V_m^{\text{b}} = V_o$; find i_m^{b} from (F.13); find t_m^{b} using (F.16);
  if *($t_m^{\text{b}} \leq 0$)* **then**
    break;
  find $s_m^{\text{b}}(i_m^{\text{b}})$ using (F.17);
  find V_{m+1}^{b} using (F.14);
  if *($V_{m+1}^{\text{b}} < V_{cutoff}$)* **then**
    break;
  $m = m + 1$; update $P_{\text{uav}}(\mathbf{v}_m)$;
  find i_m^{b} from (F.13); t_m^{b} using (F.15);
Output: Air-Time: $T_{\text{uav}} = m\delta_t$.

3 Trajectory Optimization Using DRL Method

In this section, we formulate the problem and use the deep reinforcement learning technique to design an optimal trajectory for the PAP that maximizes the FEE of the system.

3.1 Problem Formulation

The FEE of the considered system can be increased by suitably designing the 3D trajectory of the PAP. The corresponding problem can be formulated as,

$$\text{(F:P1)}: \underset{\mathcal{V}_M}{\text{maximize}} \quad \text{FEE}\left(\mathcal{V}_M\right),$$

$$\text{s.t.} \quad V_{M+1}^{\text{b}} \geq V_{\text{cutoff}}; t_{M+1}^{\text{b}} \geq 0, \tag{F.18}$$

$$u_{\text{x},m+1} = u_{\text{x},m} + \underbrace{\delta_t v_m \sin\epsilon_m \cos\alpha_m}_{\Delta_m^{\text{x}}(\mathbf{v}_m)} \; \forall m \in \mathcal{M}', \tag{F.19}$$

$$u_{\text{y},m+1} = u_{\text{y},m} + \underbrace{\delta_t v_m \sin\epsilon_m \sin\alpha_m}_{\Delta_m^{\text{y}}(\mathbf{v}_m)} \; \forall m \in \mathcal{M}', \tag{F.20}$$

$$u_{\text{z},m+1} = u_{\text{z},m} + \underbrace{\delta_t v_m \cos\epsilon_m}_{\Delta_m^{\text{z}}(\mathbf{v}_m)} \forall m \in \mathcal{M}', \tag{F.21}$$

$$u_{\text{z,min}} \leq u_{\text{z},m} \leq u_{\text{z,max}} \quad \forall m \in \mathcal{M}, \tag{F.22}$$

$$\Sigma_{n=1}^{N} T_{m,n} = \delta_t \quad \forall m \in \mathcal{M}', \tag{F.23}$$

$$\mathbf{u}_{M+1} = \mathbf{u}_{\mathrm{F}}; \mathbf{u}_1 = \mathbf{u}_{\mathrm{I}}, \tag{F.24}$$

$$T_{m,n} \geq 0 \quad \forall m \in \mathcal{M}^{'}, n \in \mathcal{N}. \tag{F.25}$$

The objective function of (F:P1) maximizes the FEE; (F.18) ensures that the PAP will not run out of onboard available battery capacity at any point of the trajectory. The x, y, and z coordinates of the PAP position are changed according to (F.19) – (F.21), respectively. The flying region of the PAP is limited in the z-direction using (F.22) with $u_{\mathrm{z,min}}$ and $u_{\mathrm{z,max}}$ as the respective minimum and maximum permitted flying altitudes. (F.23) is the TDMA scheduling constraint. (F.24) constrains the initial and final positions of the PAP to be $\mathbf{u}_{\mathrm{I}}$ and $\mathbf{u}_{\mathrm{F}}$, respectively. (F:P1) is a non-convex optimization problem with a large number of optimization variables restricting the use of conventional convex optimization methods such as sequential convex programming [31]. Consequently, (F:P1) is equivalently represented as a Markov Decision Process (MDP) with continuous state and action spaces, and a DRL-based algorithm is proposed to design a 3D trajectory for the PAP that maximizes the FEE of the system.

The PAP is considered as an agent of the DRL framework; the framework takes the state observed by the PAP, s_m, and outputs an action, a_m. The agent receives a reward r_m after taking the action a_m that moves it from state s_m to state s_{m+1}. The whole trajectory of the PAP is considered as an episode of the DRL framework; an episode ends (i.e., $m = M+1$) if it runs out of the onboard battery capacity. It should be noted that the value of M is not constant here, and it varies according to the profile of the PAP power consumption. Additionally, to model the FEE solely as a function of the PAP trajectory, we schedule the data transmission to each GN for a time that is proportional to the respective expected spectral efficiency (i.e. $T_{m,n} = \overline{R}_{m,n} / \sum_{n=1}^{N} \overline{R}_{m,n}$, $\forall m \in \mathcal{M}^{'}, n \in \mathcal{N}$).

3.2 PAP Trajectory as an MDP

Since the next state and action of the PAP depend only on the present state of the PAP, we use a standard MDP representation as a 4-tuple $(\mathcal{S}, \mathcal{A}, \mathcal{P}, \mathcal{R})$ with sets: state space $\mathcal{S}$, action space $\mathcal{A}$, probability of transition $\mathcal{P}$, and a state-action reward map $\mathcal{S} \times \mathcal{A} -> \mathcal{R}$.

State Space, $\mathcal{S} = \{s_m\}$

The state of the PAP consists of 3D-coordinates of the PAP location written relative to the destination, the PAP's battery terminal voltage, the total energy consumed, coordinates of the GNs written relative to the horizontal projection of the PAP position, and the number of bits transmitted to each GN until the end of the m^{th} time slot:

$$s_m = \{\{(\mathbf{u}_m - \mathbf{u}_{\mathrm{F}}), V_m^{\mathrm{b}}, E_m, \{(\mathbf{g}_{\mathrm{h},n} - \mathbf{u}_{\mathrm{h},m})\}, \{D_{m,n}^{\mathrm{sum}}\}\}, \tag{F.26}$$

where $D_{m,n}^{\text{sum}} = \sum_{j=1}^{m} D_{j,n}(\mathbf{v}_j, T_{jn})$ is the total number of bits transmitted to the n^{th} GN till the end of the m^{th} time slot; $E_m = \sum_{j=1}^{m} \delta_t P_{\text{uav}}(\mathbf{v}_j)$ is the total energy consumed until the end of the m^{th} time slot. Hence, s_m has $5 + 3 \cdot N$ dimensions.

Action Space $\mathcal{A} = \{a_m\}$

Since all the state dimensions are functions of the 3D movement of the PAP, the action a_m taken by the PAP is velocity-steered and can be expressed as a vector of dimension 3: $a_m = \{c_m^{\text{x}}, c_m^{\text{y}}, c_m^{\text{z}}\} \in [-1, 1]$ such that the components of the velocity vector are given by,

$$v_m = \sqrt{{c_m^{\text{x}}}^2 + {c_m^{\text{y}}}^2 + {c_m^{\text{z}}}^2} \cdot \frac{v_{\max}}{3}, \tag{F.27}$$

$$\epsilon_m = \arctan\left(\frac{\sqrt{{c_m^{\text{x}}}^2 + {c_m^{\text{y}}}^2}}{c_m^{\text{z}}}\right), \tag{F.28}$$

$$\alpha_m = \arctan\left(\frac{c_m^{\text{y}}}{c_m^{\text{x}}}\right). \tag{F.29}$$

Moreover, if the action takes the PAP out of the altitude boundaries, the z-coordinate of the next state is readjusted to the corresponding boundary value.

Reward Space $\mathcal{R} = \{r_m\}$

The reward function determines how fast the PAP finds the optimal trajectory. Here, the primary objectives are to maximize the FEE and let the PAP reach the specified destination before the battery becomes obsolete by satisfying all the constraints of (F:P1). To efficiently map the above objectives, we leverage the reward shaping technique [32]. Hence, the reward r_m is expressed as,

$$r_m = f_m + p_m, \tag{F.30}$$

where,

$$p_m = \begin{cases} \text{FEE}(\mathcal{V}_{m+1}) & \text{if FEE improves,} \\ 0 & \text{otherwise/if m=M+1,} \end{cases} \tag{F.31}$$

is the position reward that encourages the PAP to move in a direction that improves the FEE of the system, and

$$f_m = \begin{cases} \kappa_{\text{f}} \cdot \text{FEE}(\mathcal{V}_M) & \text{if} \quad m = M+1, \\ 0 & \text{else,} \end{cases} \tag{F.32}$$

is the terminal reward. The value of κ_{f} should be selected in a way that ensures the sum of the position rewards is always less than or equal to the terminal reward. κ_{f} is

needed to balance the position and terminal rewards. Otherwise, the position reward would dominate over the terminal reward.

Since the defined MDP is deterministic, no randomness is considered and all transitions follow the agent's decisions [25]. Therefore, the next state is a direct consequence of the current action of the agent.

Episode Termination

The FEE of the system increases when the PAP spends the maximum time over the air to serve the GNs. Hence, an episode is terminated when the remaining air-time (T_{uav}) of the PAP is equal to the minimum time required by the PAP to reach the destination from the current position with a speed of $v_{\max}$: $T^{\min}_{\text{uav},m} = \|\mathbf{u}_m - \mathbf{u}_{\text{F}}\|/v_{\max}$. The remaining air-time of the PAP can be estimated using Algorithm F.1. Consequently, if an action takes the PAP to $\mathbf{u}_{m+1}$ and if $T_{\text{uav}} < T^{\min}_{\text{uav},m+1}$, the action is discarded and the PAP moves to the destination from $\mathbf{u}_m$ with a speed of $v_{\max}$ m/s. Accordingly, the GNs are served for a maximum amount of time while ensuring a safe landing of the PAP at the destination.

The safety check explained above satisfies (F.18) by ensuring sufficient energy available at the PAP to fly back to the destination after each action. The 3D coordinates of the PAP after taking an action are determined by substituting (F.27)-(F.29) in (F.19)-(F.21), satisfying the PAP movement constraints. The altitude constraint (F.22) is satisfied by limiting the action space if such an action violates the constraint. The proposed heuristic time allocation in which the data transmission to each GN is scheduled for a time proportional to the respective expected spectral efficiency satisfies the TDMA constraints (F.23) and (F.25). Finally, all the episodes start and end at $\mathbf{u}_{\text{I}}$ and $\mathbf{u}_{\text{F}}$, respectively satisfying constraint (F.24).

3.3 TD3-Based PAP 3D Path Design

Here, the objective is to find the optimal policy π that takes the current state of the PAP (agent) and gives an action that maximizes the expected return: $R_m = \sum_{i=m}^{M} \gamma^{i-m} r_m$, where γ is a discount factor determining the priority of short-term rewards. The action value of a state, $Q_\pi(s_m, a_m)$, gives the expected return for starting in state s_m, taking action a_m, and then acting according to the policy π forever after. The optimal action-value function is given by the Bellman equation as,

$$Q^*(s_m, a_m) = \left[r_m + \gamma \max_{a_{m+1}} Q^*(s_{m+1}, a_{m+1}) \right]. \tag{F.33}$$

In DRL, $Q^*(s_m, a_m)$ is approximated by a neural network $Q_\phi(s_m, a_m)$ with parameters

Algorithm F.2: Energy Efficient 3D Path Planning.

Initialize the locations of GNs;
Initialize critic networks Q_{ϕ_1}, Q_{ϕ_2}, and actor network μ_θ with random parameters ϕ_1, ϕ_2, θ;
Initialize target networks $\phi_{1,\text{tgt}} \leftarrow \phi_1$, $\phi_{2,\text{tgt}} \leftarrow \phi_2$, $\theta_{\text{tgt}} \leftarrow \theta$
Initialize replay buffer $\mathcal{H}$;
for *each episode* **do**
  Initialize the location of PAP to $\mathbf{u}_I$, $m = 1$, $V_m^b = V_o$, $t_m = t_o$; $d = 1$;
  Formulate the state of the PAP s_m;
  while *the episode is not over* **do**
    The agent takes an action with exploration noise: $a_m = \mu_\theta(s_m) + \epsilon$, observe the reward r_m and new state s_{m+1};
    store (s_m, a_m, r_m, s_{m+1}) in the replay buffer;
    if *replay buffer is sufficient* **then**
      sample mini batch of $|\mathcal{H}^{'}|$ transitions from $\mathcal{H}$;
      compute target actions using (F.41);
      compute target using (F.38);
      update critic networks by one step gradient descent using,
      $$\nabla_{\phi_j} \frac{1}{|\mathcal{H}'|} \sum_{e_i \in \mathcal{H}'} \left(Q_{\phi_j}(s_i, \mu_\theta(s_i)) - y_i \right)^2 \text{ for } j \in \{1, 2\};$$
      if *it is time to update* **then**
        update policy network by one step gradient ascent using,
        $$\frac{\sum_{e_i \in \mathcal{H}'} \nabla_{\mu_\theta(s_i)} Q_{\phi_1}(s_i, \mu_\theta(s_i)) \nabla_\theta \mu_\theta(s_i)}{|\mathcal{H}'|};$$
        update target networks using, $\theta_{\text{tgt}} = \tau\theta_{\text{tgt}} + (1 - \tau\theta)$;
        $\phi_{j,\text{tgt}} = \tau\phi_{j,\text{tgt}} + (1 - \tau\phi_j)$ for $j \in \{1, 2\}$.
    $m = m + 1$;

ϕ. Then the closeness of $Q_\phi(s_m, a_m)$ to $Q^*(s_m, a_m)$ is judged by evaluating the mean-squared Bellman error (MSBE) function:

$$L(\phi, \mathcal{H}) = \underset{\{e_i\}\sim\mathcal{H}}{\mathrm{E}} \left[\left(Q_\phi(s_i, a_i) - y_i \right)^2 \right], \tag{F.34}$$

where

$$y_i = r_i + \gamma(1-d) \max_{a_{i+1}} Q_\phi(s_{i+1}, a_{i+1}), \tag{F.35}$$

is the target value and $d = 1$ represents the terminal state. The expectation in (F.34) is taken over a mini batch of experiences, $\{e_i\} = \{(s_i, a_i, r_i, s_{i+1}, d)\} = \mathcal{H}'$ sampled from the experience replay buffer, $\mathcal{H}$. The parameter ϕ is updated to minimize the MSBE. Since the considered action space is continuous, the evaluation of the MSBE is not trivial because of the $\max_{a_{i+1}} Q_\phi(s_{i+1}, a_{i+1})$ term in the target value where the maximization has to be done over a continuous action space. To tackle this, we use an actor-critic framework-based twin delayed deep deterministic policy gradient (TD3) algorithm [33]. An actor-critic framework uses an actor network that takes the state s_m as input and outputs the action a_m, whereas the Q-value of the taken action a_m at state s_m is estimated by the critic network. At the end of the training, the actor network represents the optimal policy, π. Hence, (F.34) and (F.35) can be rewritten as,

$$L(\phi, \mathcal{H}) = \underset{\{e_i\}\sim\mathcal{H}}{\mathrm{E}} \left[\left(Q_\phi(s_i, \mu_\theta(s_i)) - y_i \right)^2 \right], \tag{F.36}$$

$$y_i = r_i + \gamma(1-d) Q_\phi(s_{i+1}, \mu_\theta(s_{i+1})), \tag{F.37}$$

where μ_θ is the actor network with parameters θ and Q_ϕ is the critic network with parameters ϕ. From (F.36) and (F.37), the target y_i depends on the same parameters we are trying to train: ϕ and θ which makes the MSBE minimization unstable. The solution is to use target networks that have sets of parameters which come close to ϕ and θ, but with a time delay. The parameters of the target network are denoted as ϕ_{tgt} and θ_{tgt}, respectively. In order to avoid the overestimation problem of the deep deterministic policy gradient (DDPG) algorithm [34], the TD3 algorithm proposed in [33] uses:

Clipped Double-Q Learning

in which two critic networks are used instead of one, and uses the smaller of the two Q-values to form the targets in the MSBE functions:

$$y_i = r_i + \gamma(1-d) \min_{j=1,2} Q_{\phi_{j,\mathrm{tgt}}}(s_{i+1}, \mu_{\theta_{\mathrm{tgt}}}(s_{i+1})), \tag{F.38}$$

where $Q_{\phi_{j,\text{tgt}}}$ for $j \in \{1, 2\}$ are the corresponding target critic networks. Both networks are then trained to minimize this target:

$$L(\phi_1, \mathcal{H}) = \underset{\{e_i\}\sim\mathcal{H}}{\text{E}}\left[Q_{\phi_1}(s_i, \mu_\theta(s_i)) - y_i\right]^2, \tag{F.39}$$

$$L(\phi_2, \mathcal{H}) = \underset{\{e_i\}\sim\mathcal{H}}{\text{E}}\left[Q_{\phi_2}(s_i, \mu_\theta(s_i)) - y_i\right]^2, \tag{F.40}$$

that avoids the overestimation problem;

Delayed Policy Updates

through which the TD3 updates the policy (μ_θ) and target networks less frequently than the critic networks (once every K critic networks update);

Target Policy Smoothing

which adds a clipped noise on each dimension of the action produced by the target policy network. After adding the clipped noise, the target action is then clipped to lie in the valid action range: $[a_{\min}, a_{\max}]$,

$$\mu_{\theta_{\text{tgt}}}(s_{i+1}) = \text{clip}\left(\mu_{\theta_{\text{tgt}}}(s_{i+1}) + \text{clip}(\epsilon, -c, c), a_{\min}, a_{\max}\right), \tag{F.41}$$

where $\epsilon \sim \mathcal{N}(0, \sigma)$ and $\text{clip}(x, a, b) = \max(\min(x, b), a)$. This avoids the problem of developing an incorrect sharp peak for some actions by the Q-function approximator. The steps to design a fair energy-efficient 3D trajectory for the PAP using the TD3 framework are given in Algorithm F.2.

4 Numerical Evaluation

In this section, we present our main findings obtained through numerical evaluations. The evaluations consider a square area of 1000×1000 meters with 16 GNs. The values of all the environment-related parameters are listed in Table F.2 [25]. To the best of our knowledge, the same overall setting has not been considered in the literature yet, hence we are comparing our results with the following two baseline scenarios:

1. Baseline 1: the first maneuver executed by the PAP is a diagonal climb from $\mathbf{u}_\text{I}$ up to the center of the region with coordinates $(500, 500, 100)$; hovers there until it only has sufficient energy to reach its destination; and flies reclined to the end of its trajectory $\mathbf{u}_\text{F}$;

Table F.2: Testing environment settings.

Label	Definition	Value
f_c	Channel carrier frequency	5.8 GHz
c	Velocity of light	$3 \cdot 10^8$ m/s
B	Channel bandwidth for each GN	40 MHz
N_0	Noise spectral power	-174 dBm/Hz
$u_{z,\min}$	PAP's minimum flying altitude	20 m
$u_{z,\max}$	PAP's maximum flying altitude	100 m
$v_{\max}$	Maximum achievable PAP speed	24 m/s
δ_t	Time discretization Interval	1 s
P_t	Transmission Power	23 dBm

Table F.3: Network Architecture.

Network(s)	Layer	Depth	Activation
Critic	Input Layer	56	–
Critic	Hidden Layer 1	256	ReLu
Critic	Hidden Layer 2	512	ReLu
Critic	Hidden Layer 3	512	ReLu
Critic	Output Layer	1	ReLu
Actor	Input Layer	53	–
Actor	Hidden Layer 1	256	ReLu
Actor	Hidden Layer 2	512	ReLu
Actor	Hidden Layer 3	512	ReLu
Actor	Output Layer	3	TanH

2. Baseline 2: the first maneuver executed by the PAP is a diagonal climb from $\mathbf{u}_\mathrm{I}$ to (200,200,100). It then continues through the shortest path between the locations of the GNs until it only has sufficient energy to reach its destination. We determine the shortest path using the well known travelling salesman algorithm.

The simulations are done considering 3 different environment scenarios namely, sub-urban, urban and dense urban with $(a, b, \eta^{\mathrm{LoS}}, \eta^{\mathrm{NLoS}})$ parameters $(4.88, 0.43, 0.2, 24)$, $(9.61, 0.16, 1.2, 23)$, and $(12.08, 0.11, 1.8, 26)$, respectively [6].

The architecture of actor and critic networks used in the simulations are listed in Table F.3. After an extensive experimentation, the values of various hyper parameters associated with the networks that give the maximum FEE value after training the networks for 1000 episodes are listed in Table F.4. Fig. F.5 plots the PAP power consumption and air-time as a function of the speed. The vertical flying power consumption increases with speed since the PAP requires more power to overcome the downward drag force. When the PAP is flying horizontally, the power consumption initially decreases

Table F.4: Network Parameters.

Label	Definition	Value
α	Actor learning rate	10^{-4}
β	Critic learning rate	10^{-3}
$\lvert\mathcal{H}^{'}\rvert$	Batch size	64
$\lvert\mathcal{H}\rvert$	Replay buffer size	2×10^5
K	Network update interval	2
τ	Soft update factor	0.001
γ	Discount factor	0.99
κ_{f}	-	1000

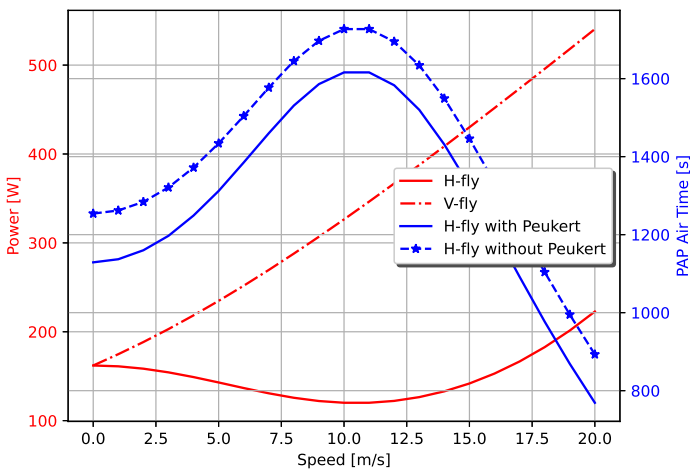

Fig. F.5: Variation of the PAP power consumption and air-time (endurance) as a function of the flying velocity. H-fly represents a level forward flight at the maximum height ($v_m \neq 0$, $\epsilon_m = 90°$); v-fly represents axial climb or descent ($v_m \neq 0$, $\epsilon_m = 0$).

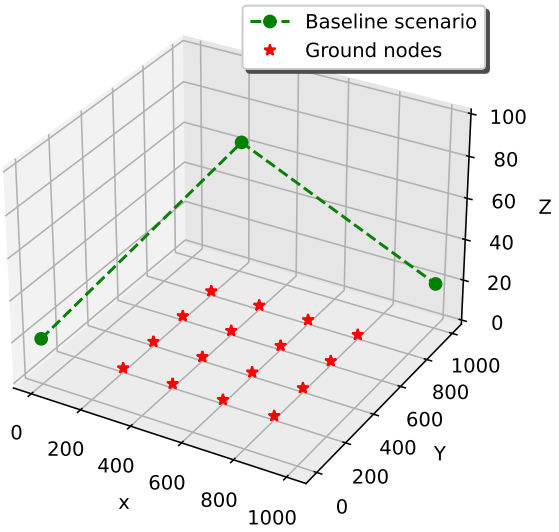

Fig. F.6: Baseline1 scenario to compare the performance; the PAP starts at (0,0,20), flies to the center of the geographical region (500,500,100), hovers there until the battery capacity reaches the threshold value, flies back to the destination (1000,1000,20).

and then increases after 11 m/s: because the magnitude of power required to overcome the rotor-induced drag force decreases with the PAP velocity; in the low-speed regime, it dominates the power consumed to overcome the fuselage and rotor profile drag forces. Correspondingly, the maximum PAP air-time, using Algorithm F.1, is obtained as 1616 seconds (s) when the PAP is flying at a speed of 11 m/s. The figure also shows the importance of considering the Peukert effect during the trajectory planning of the PAP; neglecting the Peukert effect overestimates the air-time of the PAP that could force the PAP to initiate landing procedure before completing the planned trajectory.

Finally, we perform two types of RL training to showcase the effectiveness of our approach in different scenarios. The first (offline) approach assumes the same fixed user positions for both the training and testing part. This analysis is done to evaluate the capability of the actor network to solve problem where all users are uniformly spaced along the x and y directions, as shown in Fig. F.6. This fixed arrangement has very sparse GNs which makes it difficult for the FI problem. The second approach considers random positions, such as in a point process, where the x and y coordinates of each GN are uniformly distributed for each training episode. In this approach the testing is done on a set of random GN arrangements that the agent has not used for training before, which also includes the fixed uniform positions. This is a slightly easier problem when solving fairness problems such as FI due to the likelihood of users to cluster and/or disperse due to the entropy of the system.

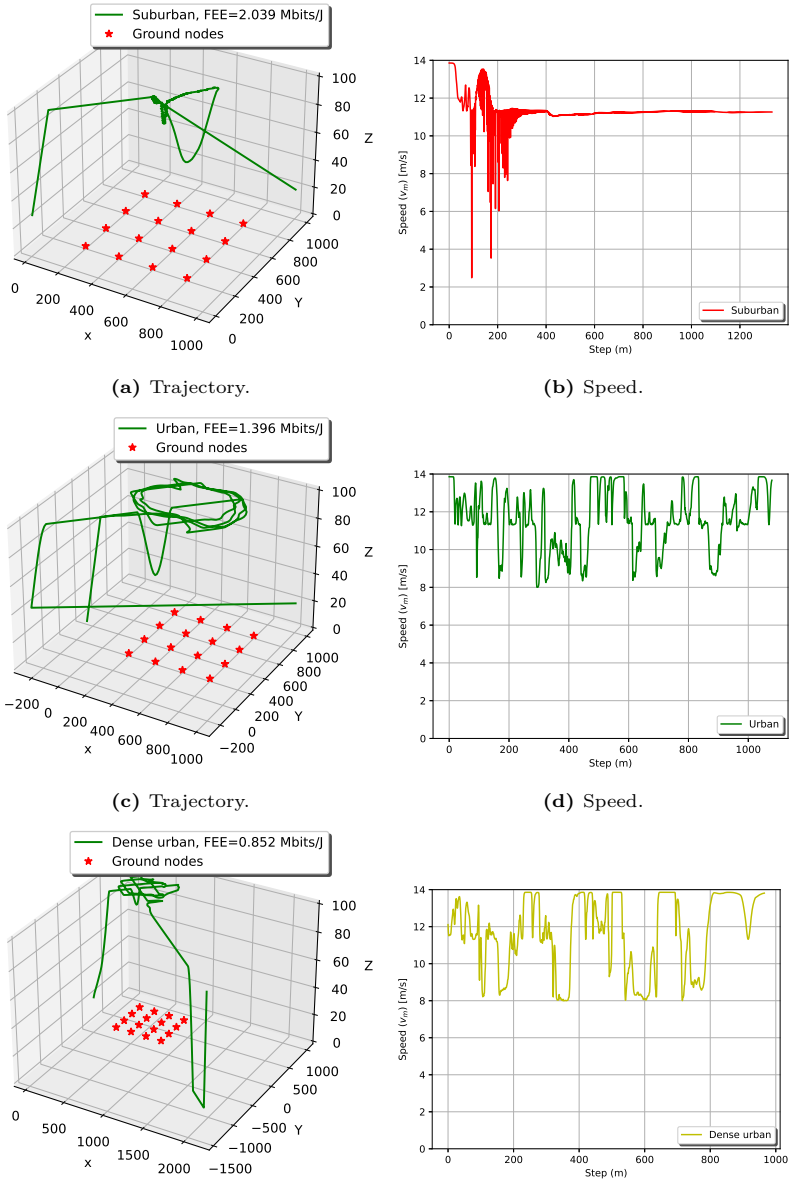

(a) Trajectory. **(b)** Speed.

(c) Trajectory. **(d)** Speed.

(e) Trajectory. **(f)** Speed.

Fig. F.7: Sample PAP trajectories obtained using the trained actor network.

Table F.5: Improvement with respect to the baselines.

		Proposed	Baseline1	Improvement	Baseline2	Improvement
Suburban	FEE	2.039	1.085	87.93 %	1.083	88.27%
	FI	0.896	0.975	-8.1 %	0.985	-9.03%
	EE	2.276	1.113	104.49%	1.098	107.28%
Urban	FEE	1.4	0.376	272.34%	0.508	175.59%
	FI	0.968	0.681	42.14 %	0.971	-0.31%
	EE	0.876	0.552	58.69 %	0.523	67.49%
Dense urban	FEE	0.853	0.204	318.13 %	0.329	159.27%
	FI	0.902	0.617	46.19 %	0.976	-7.58%
	EE	0.946	0.331	185.8 %	0.337	180.71%

4.1 Fixed Uniform User Positions (Offline RL)

The resulting trajectories following the training process of the actor network for the first arrangement are given in Fig. F.7. We notice that in the case of suburban deployments, the TD3 DRL method behaves very similarly to the stop-and-hover baseline deployment. This is due to the very high likelihood of having a LoS with all users and gives less relevance to the position of the PAP. However, opposite to the baseline case, the DRL method performs occasional repositioning to maintain better FEE. Finally, the TD3-DRL implementation keeps the PAP in constant movement with speeds around its most energy efficient velocity. We note that the most energy efficient velocity varies with the aerodynamics of the specific UAV and can thus be different with UAVs from different manufacturers. Opposed to the suburban scenario, in Fig. F.7 we can see in the subplots c) and e) that the PAP maintains much more dynamic movements for the urban and dense urban scenarios respectively. This is a superior approach to the stop-and-hover one, due to the short bursts of better LoS connectivity when the PAP travels above each GN. However, these bursts need to be balanced over the longer period of service and thus the PAP is always kept on the move. Finally, it is noticeable that in these two scenarios, the PAP flies off to a position that is far from the center of the area of service. This is significant for keeping the nodes equally serviced, and thus have improved FEE, in the more challenging propagation environments.

Figs. F.8a-F.8d show the respective improvement in the fair energy efficiency, fairness index, energy efficiency, and PAP air time as the training progresses. As seen in the figures, initially, the agent tries random trajectories to explore the state-action space causing relatively shorter episodes with low FEE, FI, and EE values. Later, this experience helps the ML model to converge to a better policy that improves the optimization metric. Moreover, the testing values (the values after 1000 episodes) using the proposed algorithm outperform the baseline scenarios in all the considered environments, as given in Table F.5. The maximum gain over Baseline1 is achieved when the PAP is deployed in a dense urban scenario. This is because the considered setup places a subset of GNs in the NLoS regime of the PAP's hovering point, thereby giving a low baseline FI value. The proposed algorithm improves the FI value by moving the PAP around the GNs,

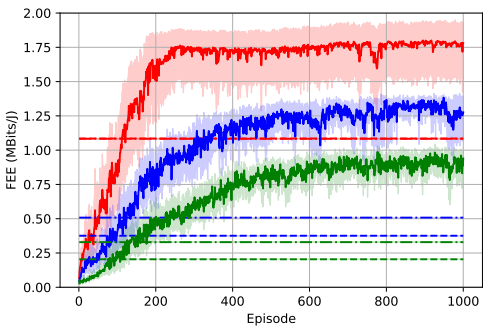

(a) Fair energy efficiency.

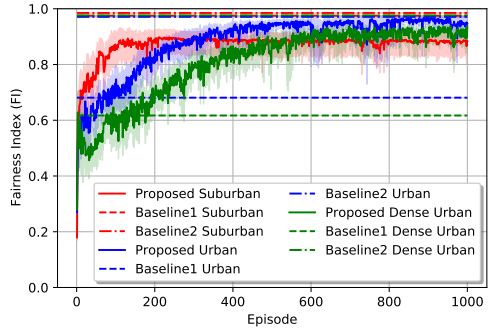

(b) Fairness index.

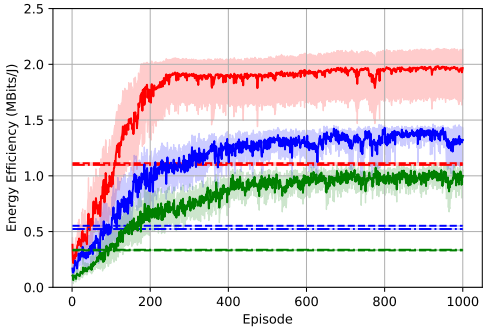

(c) Energy-efficiency.

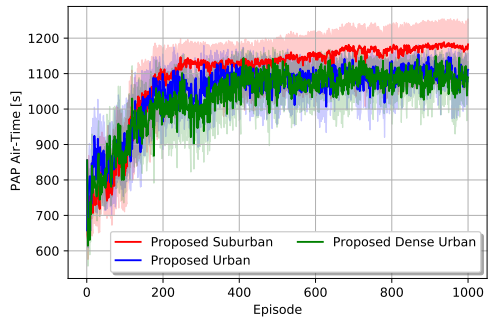

(d) PAP Airtime.

Fig. F.8: FEE, FI, EE, and PAP airtime improvements as the training progresses. The training procedure is repeated for 16 different random seeds. The shadow regions around the plots show a 95% confidence interval across randomized repetitions.

as shown in Fig. F.7e. The performance gain achieved by Baseline2 is competitive in urban and dense urban scenarios, with regards to Baseline1, because the corresponding trajectory improves the service fairness among all the GNs. Interestingly, the FEE performances of Baseline1 and Baseline 2 in a suburban scenario are comparable since all the GNs are in LoS with the PAP throughout the respective placement policy, giving high FI values. This leads us to the conclusion that the suburban environment is not challenging enough for the problem of trajectory with regards to the scale of our implementation. In all the trajectories, the PAP climbs to the maximum altitude after leaving the starting point and then follows a horizontal flight during the remaining endurance: as the altitude increases, the throughput between the PAP and a node increases due to an improved LoS probability between them; furthermore, the PAP power consumption during a vertical flight is much higher compared to a horizontal flight as shown in Fig. F.5. Hence, flying horizontally at the maximum altitude increases the PAP air time as well as the number of bits transmitted to the GNs thereby improving the FEE value of the system. Also, the speed plots of Fig. F.7 show that the actor proposes to fly the PAP at the optimal flying speed that maximizes the air-time of the PAP.

4.2 Randomized Uniform User Positions (Online RL)

In this section, we describe the method adopted from [35] to generalize the training so that the trained actor network performs well for any set of user positions. The system is trained for a fixed number of episodes N_{train}, where the x and y coordinates of each GN are uniformly distributed for each training episode. After every 10 training episodes, we evaluate the actor network on a total of N_{eval} evaluation episodes with disabled learning to assess the current performance of the actor network. We repeat this training procedure for N_{seed} times, each with a different random seed. The average FEE value after each evaluation phase is used as a metric to select the best-performing parameter (θ) of the actor network (μ_θ). At the end of the training procedure, we further evaluate the learned policy by assessing its performance in N_{test} episodes, each with a different placement of GNs that the agent has not seen during the entire training process. Moreover, this test phase happens without exploration and learning.

Fig. F.9 shows the training and testing performances for suburban, urban, and dense urban scenarios with $N_{\text{train}} = 1000$, $N_{\text{eval}} = 16$, and $N_{\text{seed}} = 8$. The shadow regions around the plots show a 95% confidence interval across randomized repetitions. In all the scenarios, the FEE value improves with the training as seen in Fig. F.8a. The mean and median FEE values obtained after testing the learned policy over $N_{\text{test}} = 512$ episodes outperform the mean baseline performances. As observed previously, the maximum and minimum performance gains are observed in dense urban and suburban scenarios, respectively. Additionally, the test performances (with learning disabled) are comparable with the performances at the end of the training phase. Thus the learned policy can be used to design an energy-efficient 3D trajectory for a PAP deployed to

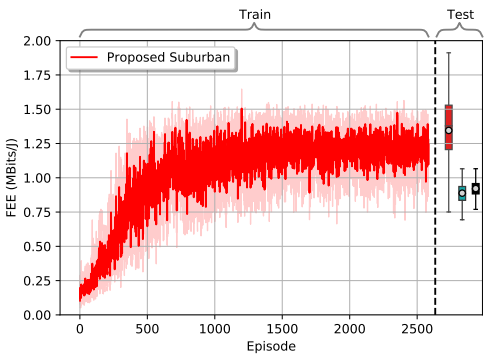

(a) FEE Suburban

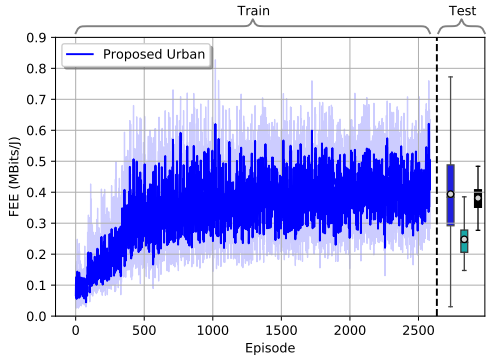

(b) FEE Urban

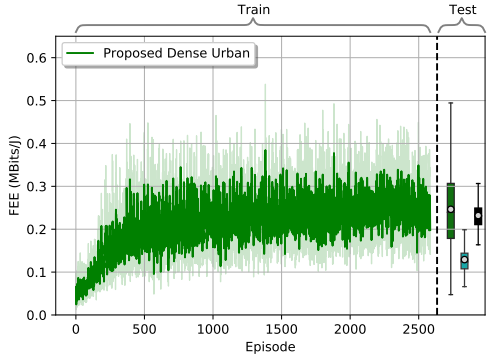

(c) FEE Dense urban

Fig. F.9: Training and testing FEE plots. Circles inside the box plots represent the average test FEE values. The second and third box plots represent Baselines 1 and 2, respectively.

serve any given distribution of the GNs while guaranteeing per-user service fairness.

5 Conclusion

In this paper, we considered a UAV in the role of a portable access point (PAP) that aims to maximize the novel fairness-based energy efficiency metric, fair energy efficiency (FEE). Optimizing the energy-efficiency of PAPs is important but this should not come at the expense of service fairness. The method we propose here strikes a good balance between both. Moreover, we defined a pragmatic non-linear discharge behavior of the PAP battery, as the Peukert effect. As the first work to investigate the Peukert effect in PAP 3D trajectory optimization for wireless IoT services, we initially investigated the impact of the non-linearity of the energy storage. As such, we deducted that neglecting the Peukert effect overestimates the PAP air time which could force the PAP to perform an early landing. Given the non-convex FEE maximization problem with non-tractable constraints we proposed an adapted implementation of a twin delayed deep deterministic policy gradient deep reinforcement learning (TD3-DRL) framework. The optimal solutions provided by TD3-DRL varied by the properties of the propagation environment. The improvements of using the TD3-DRL in suburban scenarios are moderate with a gain up to 80% in suburban over the baseline scenarios and around 200% and 300% in the urban-and dense urban scenarios respectively. Finally, we generalize the network to any set of GN positions. Thus, we can summarize, that our TD3-DRL implementation provides a robust solution for PAP trajectory optimization in both strongly LoS and strongly NLoS environments.

References

[1] Fotouhi, Azade, et al. “Survey on UAV Cellular Communications: Practical Aspects, Standardization Advancements, Regulation, and Security Challenges,” *IEEE Commun. Surv. and Tut. 21.4 (2019)*: 3417-3442.

[2] “Study on Enhanced LTE support for Aerial Vehicles (Release 15),” 3GPP, Sophia Antipolis, France, Rep. 3GPP TR 36.777, Dec. 2017.

[3] Filippone A, “Flight Performance of Fixed and Rotary Wing Aircraft,” *Elsevier*; 2006 May 10.

[4] Khan, K. A., et al. “PKL Electrochemical Cell and the Peukert’s Law,” in *IJARIIE* 4.2 (2018): 4219-4227.

[5] A. Al-Hourani, S. Kandeepan, and A. Jamalipour, “Modeling Air-to-Ground Path Loss for Low Altitude Platforms in Urban Environments,” in *Globecom 2014, Sym-*

posium on Selected Areas in Communications: Satellite & Space Communication, Austin, USA, Dec. 2014.

[6] A. Al-Hourani, S. Kandeepan and S. Lardner, "Optimal LAP Altitude for Maximum Coverage," *IEEE Wireless Communications Letters,* vol. 3, no. 6, pp. 569-572, Dec. 2014

[7] M. Mozaffari, W. Saad, M. Bennis, and M. Debbah, "Efficient Deployment of Multiple Unmanned Aerial Vehicles for Optimal Wireless Coverage," *IEEE Commun. Lett.,* vol. 20, no. 8, pp. 1647–1650, Aug. 2016.

[8] M. Alzenad, A. El-Keyi, F. Lagum, and H. Yanikomeroglu, "3-D Placement of an Unmanned Aerial Vehicle Base Station (UAV-BS) for Energy Efficient Maximal Coverage," *IEEE Wireless Commun. Lett.,* vol. 6, no. 4, pp. 434–437, Aug. 2017.

[9] M. Alzenad, A. El-Keyi and H. Yanikomeroglu, "3-D Placement of an Unmanned Aerial Vehicle Base Station for Maximum Coverage of Users With Different QoS Requirements," *IEEE Wireless Commun. Lett.,* vol. 7, no. 1, pp. 38-41, 2018.

[10] I. Donevski and J. J. Nielsen, "Dynamic Standalone Drone-Mounted Small Cells," in *2020 European Conference on Networks and Communications (EuCNC),* 2020, pp. 342-347, doi: 10.1109/EuCNC48522.2020.9200918.

[11] M. Mozaffari, W. Saad, M. Bennis, and M. Debbah, "Mobile Unmanned Aerial Vehicles (UAVs) for Energy-Efficient Internet of Things Communications," *IEEE Trans. Wireless Commun.,* vol. 16, no. 11, pp. 7574–7589,Nov. 2017.

[12] J. Cui, H. Shakhatreh, B. Hu, S. Chen and C. Wang, "Power-Efficient Deployment of a UAV for Emergency Indoor Wireless Coverage," *IEEE Access,* vol. 6, pp. 73200-73209, 2018.

[13] Q. Zhang, M. Mozaffari, W. Saad, M. Bennis and M. Debbah, "Machine Learning for Predictive On-Demand Deployment of Uavs for Wireless Communications," in *2018 IEEE Global Communications Conference (GLOBECOM),* 2018, pp. 1-6.

[14] S. Eom, H. Lee, J. Park, and I. Lee, "UAV-Aided Wireless Communication Designs with Propulsion Energy Limitations," *IEEE Trans. on Veh. Technol.*, 2019.

[15] C. You and R. Zhang, "Hybrid Offline-Online Design for UAV-Enabled Data Harvesting in Probabilistic LoS Channels," *IEEE Transactions on Wireless Communications,* vol. 19, no. 6, pp. 3753-3768, June 2020.

[16] I. Valiulahi and C. Masouros, "Multi-UAV Deployment for Throughput Maximization in the Presence of Co-Channel Interference," *IEEE Internet of Things Journal,* vol. 8, no. 5, pp. 3605-3618, Mar., 2021.

[17] Wu, Qingqing, and Rui Zhang, "Common Throughput Maximization in UAV-Enabled OFDMA Systems with Delay Consideration," *IEEE Trans. on Commun. 66.12 (2018)*: 6614-6627.

[18] W. Shi, J. Li, H. Wu, C. Zhou, N. Cheng and X. Shen, "Drone-Cell Trajectory Planning and Resource Allocation for Highly Mobile Networks: A Hierarchical DRL Approach," *IEEE Internet of Things Journal,* vol. 8, no. 12, pp. 9800-9813, June 15, 2021.

[19] Wu, H., Lyu, F., Zhou, C., Chen, J., Wang, L., & Shen, X., "Optimal UAV Caching and Trajectory in Aerial-Assisted Vehicular Networks: A Learning-Based Approach," *IEEE Journal on Selected Areas in Communications,* 38(12), 2783-2797, 2020.

[20] Y. Zeng, J. Xu and R. Zhang, "Energy Minimization for Wireless Communication with Rotary-Wing UAV," *IEEE Trans. on Wireless Commun.*, vol. 18, no. 4, pp. 2329-2345, April 2019.

[21] Y. Zeng and R. Zhang, "Energy-Efficient UAV Communication With Trajectory Optimization," *IEEE Trans. on Wireless Commun.*, vol. 16, no. 6, pp. 3747-3760, June 2017.

[22] N. Babu, C. B. Papadias and P. Popovski, "Energy-Efficient 3D Deployment of Aerial Access Points in a UAV Communication System," *IEEE Commun. Lett.*, vol. 24, no. 12, pp. 2883-2887, Dec. 2020.

[23] S. Shakoor, Z. Kaleem, M. I. Baig, O. Chughtai, T. Q. Duong and L. D. Nguyen, "Role of UAVs in Public Safety Communications: Energy Efficiency Perspective," *IEEE Access,* vol. 7, pp. 140665-140679, 2019.

[24] N. Babu, M. Virgili, C. B. Papadias, P. Popovski and A. J. Forsyth, "Cost- and Energy-Efficient Aerial Communication Networks With Interleaved Hovering and Flying," *IEEE Transactions on Vehicular Technology,* vol. 70, no. 9, pp. 9077-9087, Sept. 2021.

[25] I. Donevski, N. Babu, J. J. Nielsen, P. Popovski and W. Saad, "Federated Learning With a Drone Orchestrator: Path Planning for Minimized Staleness," *IEEE Open Journal of the Communications Society,* vol. 2, pp. 1000-1014, 2021.

[26] C. H. Liu, Z. Chen, J. Tang, J. Xu and C. Piao, "Energy-Efficient UAV Control for Effective and Fair Communication Coverage: A Deep Reinforcement Learning Approach," *IEEE Journal on Selected Areas in Communications,* vol. 36, no. 9, pp. 2059-2070, Sept. 2018.

[27] R. Ding, F. Gao and X. S. Shen, "3D UAV Trajectory Design and Frequency Band Allocation for Energy-Efficient and Fair Communication: A Deep Reinforcement Learning Approach," *IEEE Transactions on Wireless Communications,* vol. 19, no. 12, pp. 7796-7809, Dec. 2020.

[28] Mazaherifar A, Mostafavi S., "UAV Placement and Trajectory Design Optimization: A Survey," in *Wireless Personal Communications,* 2021 Dec 1:1-20.

[29] S. Shakoor, Z. Kaleem, M. I. Baig, O. Chughtai, T. Q. Duong and L. D. Nguyen, "Role of UAVs in Public Safety Communications: Energy Efficiency Perspective," *IEEE Access,* vol. 7, pp. 140665-140679, 2019.

[30] https://files.gwl.eu/inc/_doc/attach/StoItem/5230/Datasheet_LG_MH1.pdf

[31] B. R. Marks and G. P. Wright, "Technical Note- A General Inner Approximation Algorithm for Nonconvex Mathematical programs," *Oper.Res.,* vol. 26, no. 4, pp. 681–683, Aug. 1978.

[32] Wang Z, Li H, Wu Z, Wu H, "A Pretrained Proximal Policy Optimization Algorithm with Reward Shaping for Aircraft Guidance to a Moving Destination in Three-Dimensional Continuous Space," *International Journal of Advanced Robotic Systems,* January 2021.

[33] Fujimoto, Scott, Herke Hoof, and David Meger, "Addressing Function Approximation Error in Actor-Critic Methods," *International Conference on Machine Learning, PMLR,* 2018.

[34] Lillicrap, Timothy P., et al. "Continuous Control with Deep Reinforcement Learning," *arXiv preprint arXiv:1509.02971 (2015).*

[35] M. P. Mota, A. Valcarce, J. -M. Gorce and J. Hoydis, "The Emergence of Wireless MAC Protocols with Multi-Agent Reinforcement Learning," in *2021 IEEE Globecom Workshops (GC Wkshps),* 2021, pp. 1-6

Paper G

Cost-Efficient Design of an Energy-Neutral UAV-Based Mobile Network

Marco Virgili, Nithin Babu, Mashid Javidsharifi, Iman Valiulahi, Christos Masouros, Andrew Forsyth, Tamas Kerekes, and Constantinos B. Papadias

Under review in
IEEE Transactions on Communications.

The layout has been revised.

Abstract

This work proposes a framework to design a cost-efficient unmanned aerial vehicle (UAV)-based energy-neutral (EN) system deployed to harvest data from a set of internet-of-things (IoT) nodes. The energy-neutrality refers to the zero-sum balance between energy harvested, stored, and consumed during operation, which is a game-changer when a connection to the electricity grid is not available/feasible. This involves employing an off-grid charging station (CS) comprising of photovoltaic (PV) panels and batteries that provide enough energy to recharge the UAV-based aerial access points (AAPs). The investment cost is determined by the number of AAPs, PV panels, and ground battery units. Its minimization cannot be achieved using conventional optimization tools due to the non-tractable form of the CS load. Therefore, a novel wave-based method is proposed to represent the load profile as a proportional function of the required number of AAPs, so as to directly relate the CS design to the trajectory optimization. Compared to baseline scenarios, the proposed trajectory design can halve the time and energy consumption; the investment cost varies with the time and season of service; the off-grid CS is particularly advantageous in rural areas, while in urban areas its cost is comparable to that of a grid-connected alternative.

1 Introduction

The use of unmanned aerial vehicle(s) (UAVs) provisioned with on-board next-generation small cell radio access node as aerial access point(s) (AAPs) to harvest data from a set of Internet-of-Things (IoT) nodes has gained much attention in the recent years [1]. A separate study item has been released by the third generation partnership project (3GPP) detailing the architecture and link-level requirements of an AAP [2]. If the system is deployed for a short-term event, such as data harvesting from a rural IoT network that is widely spread geographically, deploying a grid-connected fixed infrastructure would be cost-inefficient, since this would require a large number of telco modules with under-utilized capacity. Additionally, a connection node to the electricity grid may not be available in some areas, and installing one might not be feasible due to the high installation costs. A potential solution to this is to employ an off-grid system that harvests (and stores) the required energy from the surrounding environment. In the proposed instance, the system is a UAV-based mobile network that consists of a set of UAVs and a ground charging station (CS). By virtue of limited on-board battery capacity, the available service time of an active (flying) AAP is a function of the on-board battery pack and its trajectory; consequently, in order to guarantee continuity of service beyond the active time of a single AAP, a set of fully charged idle (not active) AAPs is needed, so as to replace the out-of-power AAP(s), as shown in Fig. G.1. Moreover, given the high cost of AAPs, the out-of-power AAP should be recharged while its replacement

is active, thereby justifying the use of a CS. Hence, to guarantee 100% reliability, the load to the CS should be modeled as a function of the UAV-and mission-related time factors, such as the active time of a UAV, time between successive data harvesting from an IoT node, etc. Inspired by the above facts, in this work, we model both the energy demand and supply of an energy-neutral (EN) UAV-based mobile network as respective functions of the mission-related time factors and the solar irradiation. These are then used to develop a general framework that uses the trajectory of the AAP as a tool to minimize the investment cost.

1.1 Related Works

The sizing of a photovoltaic (PV)-battery system for supplying a CS is challenging due to factors such as the associated costs, the volatility of solar irradiation, varying load, and physical location constraints [3]. The focus of the work in [3] - [8] is on supplying the energy required by base stations in mobile networks through PV-battery systems. In [3] and [4], the authors optimize the size of the energy system used to power a fixed telecommunication infrastructure, but they do not control the load profile, which is taken as a design requirement. The works in [5] and [6] model the performance of renewable energy source (RES)-based base stations to size the energy system based on Markovian models. [7] proposes a multi-objective wind-driven optimization (MO-WDO) algorithm to size an off-grid energy system. The number of PV panels and battery cells are optimized based on the 'annual total life cycle cost'. In [8], a genetic algorithm-based methodology is proposed to design a PV-battery system with the objectives of minimizing CAPEX and OPEX. The load profile to the charging station used in [3]- [8] is not suitable for a UAV-based mobile network, since it is not a function of UAV-related time factors.

The articles in [9]- [13] consider an off-grid UAV-based architecture to serve a set of users with the objective of minimizing the investment cost or maximizing the energy storage. In [9] and [10], the authors minimize the installation cost of a UAV-based cellular network in rural areas while considering UAV recharge over time, coverage, and installation constraints. However, the UAVs hover while serving the users, thereby making the proposed frameworks less efficient. The work in [11] proposes a GA-based solution to maximize the energy stored in UAVs and the ground sites while providing cellular coverage to the considered area; there is no attempt to minimize the investment cost. The authors of [12] propose an energy-efficient mission planning for a UAV-based cellular network to minimize the energy consumed by UAVs and ensure cellular coverage to the users. However, [12] does not consider the power constraints related to the recharging sites. Moreover, it uses the results of [10] to design the energy systems of the UAV recharging sites. [13] proposes an optimization framework to minimize the financial cost of a PV-battery-powered off-grid UAV-based cellular telecommunication network by sizing the energy system using the derived power consumption profiles for

three recharging sites. The work uses the results of optimal mission planning in [12] as input to obtain the load profile of each recharging site. However, for real-world IoT applications, the mission planning of the UAVs and the design of the energy system should be investigated as a united problem.

The work in [14] - [26] consider efficient deployment of UAV-based systems to maximize performance metrics such as coverage area, number of covered users, sum rate, and energy efficiency. The placement optimization of a UAV-based communication system can be generally divided into two categories: quasi-stationary deployment and optimal trajectory design. The first scenario determines optimal hovering position(s) of UAV(s) [14] - [19]; in the second scenario, a set of UAVs move along a designed path that maximizes the considered performance metric [20] - [26]. The authors of [14] and [15] use analytical tools to maximize the coverage region of a UAV-based system by varying the altitude of the UAV. In [16] and [17], the authors use circle packing-based algorithms for the optimal quasi-stationary deployment of a multi-UAV system to maximize the global energy efficiency and throughput, respectively. In [18] and [19], the authors provide multi-UAV deployment strategies based on the K-mean and mean-shift algorithms to maximize the coverage region and the minimum achievable rate, respectively. The authors of [20] and [21] design a UAV-enabled system based on covert wireless communications to enable the ground users to hide their transmissions from each other while conveying critical information to the UAV. The work in [20] uses a penalty successive convex approximation (P-SCA) scheme to jointly design the UAV trajectory and its maximum transmit power of the artificial noise (AN), together with the user scheduling strategy subject to covertness constraint, whereas, [21] uses a heuristic approach to optimize the flying location and transmit power. The trajectory design or placement methods proposed in [20] - [25] formulate the problem to either maximize the energy efficiency or throughput as a mixed-integer non-linear problem (MINLP). This is then solved using the sequential convex programming technique. A comprehensive list of papers that consider UAV placement optimization is available in [26].

1.2 Major Contributions and Paper Structure

The work in [3] - [8] consider supplying the power required by a fixed base station using PV and battery storage systems. The load to the energy system is modeled as a function of the traffic demand of the base station. However, the load to the CS in a UAV-based architecture is a function of the service demand of the users, as well as the trajectory of the UAV. Although the works [9]- [13] tackle the cost minimization of a UAV-based architecture, they consider a simple hovering UAV scenario. These are sub-optimal solutions for an IoT application since they do not exploit the mobility of UAVs as a tool to minimize the cost by reducing both their number and the load to the CS. Moreover, the load profiles do not present an interactive formulation that allows us to show its response to the mission and UAV-related time factors, such as the delay

between the successive data harvesting from a node, active and charging time of a UAV, etc. Coverage and energy-efficient UAV deployment strategies are proposed in [14]- [26]. However, the authors do not consider the presence of a ground CS, and all the missions are set to have a duration less than or equal to the active time of a UAV. The objectives are either to determine an optimal altitude that maximizes the coverage area or to find the trajectory parameters that maximize the number of bits transmitted per Joule of Energy consumed. Maximizing the coverage area/ energy efficiency might not always minimize the cost. For instance, the energy efficiency can be improved by flying the AAP at an optimal velocity which is not equal to the maximum velocity. This increases the delay, which forces the system to deploy another AAP if the delay in visiting the same user in succession is greater than the network's time difference of arrival (TDOA), thereby increasing the cost. Therefore the trajectory design to minimize the cost requires further attention. In this work, the objective of cost-efficient design and deployment of a UAV-based system in areas without access to a reliable electricity grid is pursued. The major contributions of this paper can be summarized as follows:

- Proposing a novel wave-based method to generate the load profile of a CS in an EN UAV-based mobile network as a function of the number of AAPs and its mission parameters.
- Designing an efficient AAP path design based on the mean-shift algorithm that minimizes the number of AAPs subject to data harvesting and trajectory constraints. This method makes it possible to solve the problem using convex optimization techniques and can be tweaked to optimize any performance metric.
- Employing the above to minimize the overall cost of deploying an EN UAV-based communication network that harvests data from a set of IoT nodes over set intervals of time.

Section 2 describes the considered scenario and the applied models. Section 3 illustrates the problem formulation and the wave-based load profile modeling, as well as the mean-shift clustering-based trajectory design. The main findings of this paper are summarized in Section 4.

2 System Model and Definitions

In this work, a delay-tolerant IoT network is considered, in which a UAV-based EN system is deployed to collect Q bits of data from a set of ground users (GUs) every T_{period} seconds. In practice, T_{period} is the time difference of arrival (TDOA) of the IoT network, and is a function of the memory capacity of the IoT sensor nodes. The EN system, as shown in Fig. G.1, consists of a flock of AAPs, and a CS on the ground to harvest and store the required energy for the AAPs. The CS is formed by two elements:

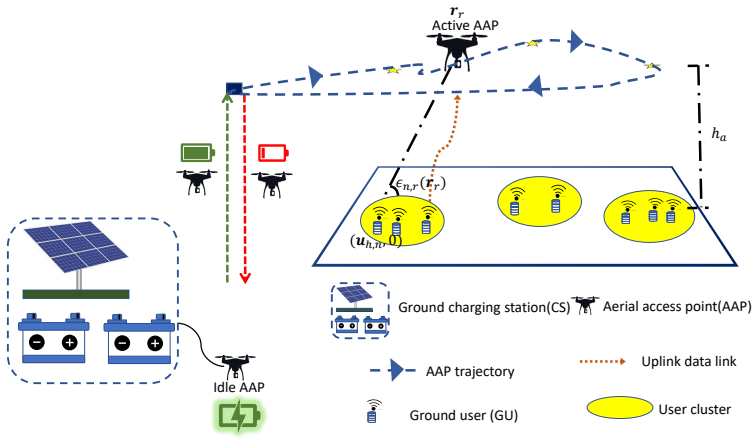

Fig. G.1: Considered application scenario: the AAP(s) is (are) deployed to collect data from a set of ground IoT nodes; an active AAP with little energy left is replaced by a fully charged idle AAP.

- an energy harvesting PV system, consisting of a number N_{pv} of solar panels, each of cost C_{pv} €, that harvest energy from solar irradiation;
- a battery unit of N_{bt} units, each costing C_{bt} €, to store the energy harvested in surplus and use it to supplement the PV module when this cannot sustain the load by itself.

A flying AAP is called *active* AAP, whereas one at the CS, either charging or waiting to be deployed, is called *idle* AAP. The system is assumed to work for an amount of time T_{service}, measured in hours, within a given time slot of a day: $\mathcal{T} \equiv [T_{\text{start}}, T_{\text{start}} + T_{\text{service}}]$, where T_{start} is the time of the day, thus ranging from from 00:00 hrs to $(24{:}00 - T_{\text{service}})$ hrs. For tractability, the trajectory of the AAP corresponding to one data harvesting cycle is divided into R path segments, represented using $R+1$ waypoints [23]. The length of each segment is constrained to be small enough as to assume the channels between the AAP and each GU to remain stationary:

$$\left\|\mathbf{r}_{\text{h},r+1} - \mathbf{r}_{\text{h},r}\right\| \leq \min\left\{\delta, T_r \cdot v_{\max}\right\} \ \forall r \in \mathcal{R} = \{1, 2, ..R\}, \tag{G.1}$$

where δ is chosen so that, within each path segment, the AAP can be assumed to either hover or fly at a constant velocity v_r, which cannot be higher than the maximum AAP velocity $v_{\max}$. $\mathbf{r}_{\text{h},r} = (x_r, y_r)$ represents the horizontal-plane coordinates of the 3D position of the r^{th} path segment of the AAP $\mathbf{r}_r = (\mathbf{r}_{\text{h},r}, \mathbf{r}_{\text{v},r})$, in which $r_{\text{v},r}$ corresponds to the vertical coordinate of the AAP; the AAP is assumed to fly at a constant altitude: $r_{\text{v},r} = h_{\text{a}} \, \forall r \in \mathcal{R}$. The AAP schedules one GU at a time for data uplinking, thereby following a time division multiple access (TDMA) scheme to serve the GUs. If T_r is the time that the AAP spends in the r^{th} path segment, and $T_{n,r}$ is the time allocated to

the n^{th} GU when the AAP is in the r^{th} path segment, then $T_{\text{Hcycle}} = \sum_{r=1}^{R} T_r$ is the time it takes the AAP to harvest Q bits of data from N GUs such that,

$$\sum_{n=1}^{N} T_{n,r} \leq T_r \qquad \forall r \in \mathcal{R}. \tag{G.2}$$

Also, the n^{th} GU is located at ground level with the corresponding horizontal plane coordinates $\mathbf{u}_{\text{h},n} = (x_n, y_n)\, \forall n \in \mathcal{N} = \{1, 2, ..N\}$.

2.1 How is Data Harvested from the GUs?

At T_{start}, a fully charged AAP ascends from the CS and follows the optimal trajectory (designed as explained in Section 3.2). If the time it takes the AAP to complete one cycle of data harvesting is greater than the TDOA of the network ($T_{\text{Hcycle}} > T_{\text{period}}$), then a second AAP from the ground station is deployed at $T_{\text{start}} + (T_{\text{period}}/3600)$ hours, following the same trajectory as that of the previously deployed AAP[1]. This data harvesting cycle continues for T_{service} hrs. The AAPs are assumed to be operating in orthogonal frequency bands to minimize the inter-user interference (e.g., narrow-band frequency division multiple access systems [34]). The frequency reuse technique used in the conventional fixed-telecommunication system can be used to accommodate any number of AAPs without increasing the available bandwidth. Additionally, at the beginning of each cycle of data harvesting, the on-board battery of the AAP is checked to guarantee that it has enough energy to complete the cycle; if not, it returns to the CS for recharging, and it is replaced by a fully recharged AAP, as shown in Fig. G.1.

2.2 Propagation Environment

The communication channel between the AAP and a GU can be either line-of-sight (LoS) or non-LoS (NLoS), depending on the relative position of the GU with respect to the AAP and the building profile of the region [14]- [25]. Hence, the probability of having a LoS channel between the n^{th} GU and the AAP while the AAP is in the r^{th} path segment is determined using,

$$\mathbb{P}^{\text{los}}_{n,r}(\mathbf{r}_r) = \frac{1}{1 + a \cdot \exp\left\{-b \cdot [\epsilon_{n,r}(\mathbf{r}_r) - a)\right]\}}, \tag{G.3}$$

where a, b are the environment-dependent parameters that are fundamentally decided by the building profile of the region [14], and $\epsilon_{n,r}(\mathbf{r}_r) = (180/\pi)\tan^{-1}\left[\frac{h_{\text{a}}}{\|\mathbf{r}_{\text{h},r} - \mathbf{u}_{\text{h},n}\|}\right]$ is the corresponding elevation angle. The LoS and NLoS path loss values in dB are expressed

[1]In this work, we are not considering the case $T_{\text{period}} = 0$; when $T_{\text{period}} = 0$, a suitable aerial cell planning is required to minimize the number of AAPs, as proposed in [17] and [25].

as [14], [17], [25],

$$L^{\mathrm{g}}_{n,r}(\mathbf{r}_r) = 20 \cdot \log d_{n,r}(\mathbf{r}_r) + 20 \cdot \log f + 20 \cdot \log\left(\frac{4\pi}{v_{\mathrm{light}}}\right) + \eta^{\mathrm{g}}, \tag{G.4}$$

where $g \in \{\mathrm{los}, \mathrm{nlos}\}$, $d_{n,r}(\mathbf{r}_r) = \sqrt{\|\mathbf{r}_{\mathrm{h},r} - \mathbf{u}_{\mathrm{h},n}\|^2 + h_{\mathrm{a}^2}}$; f and v_{light} are the respective signal frequency and the velocity of light; η^{los} and η^{nlos} are the mean values of the additional path loss for LoS and NLoS links due to the environment, respectively. For a given elevation angle, this additional loss has a Gaussian distribution [27], and it depends on the building profile of the region. However, from [27], it is noticed that the change in the additional path loss within a particular propagation group (LoS/NLoS) is insignificant compared to the change in path loss value from one group to the other: the NLoS path loss value depends on the scattering and reflections from the surrounding buildings which depend largely on the frequency of operation and the building profile of the region rather than the distance. This allows us to model the path loss with a constant gap between the two propagation groups. Consequently, the average amount of exchanged data in bits-per-seconds-per-Hertz (bps/Hz) is given by,

$$D_{n,r}(\mathbf{r}_r) = \mathbb{P}^{\mathrm{los}}_{n,r}(\mathbf{r}_r)\log_2\left(1 + \frac{P}{\sigma^2 10^{L^{\mathrm{los}}_{n,r}(\mathbf{r}_r)/10}}\right) + \mathbb{P}^{\mathrm{nlos}}_{n,r}(\mathbf{r}_r)\log_2\left(1 + \frac{P}{\sigma^2 10^{L^{\mathrm{nlos}}_{n,r}(\mathbf{r}_r)/10}}\right), \tag{G.5}$$

where $\mathbb{P}^{\mathrm{nlos}}_{n,r}(\mathbf{r}_r) = 1 - \mathbb{P}^{\mathrm{los}}_{n,r}(\mathbf{r}_r)$, and P and σ^2 are the signal and noise power, respectively. The principal reason for considering a probabilistic LoS-NLoS air to ground channel model is the lack of the building map of the region. If the building map of the region is available, the value of $\mathbb{P}^{\mathrm{los}}_{n,r}(\mathbf{r}_r)$ can be determined using ray tracing methods, and (G.5) can be modified accordingly. Hence, the mean shift clustering-based trajectory design we propose in Section III-B can be used for several scenarios, including a channel estimated using a deep neural network [28].

2.3 UAV Power Consumption Model

In the considered system, the AAP takes off vertically from the CS to replace an out-of-power AAP, then the latter descends vertically for recharging; during data harvesting, the AAP flies horizontally or hovers to collect the data from the users. The total power

Table G.1: UAV Parameters [25].

Label	Definition	Value	Label	Definition	Value
W	Weight of the UAV	32.34 N	$\rho(h_a)$	Air density	-
N_{rotor}	Number of rotors	4	U_{d}	Drag coefficient	0.9
v_r	UAV's horizontal flying velocity	-	A_{rotor}	Rotor disc area	0.06 m^2
Δ	Profile drag coefficient	0.002	v_{tip}	Tip speed of the rotor	102 m/s
s	Rotor solidity	0.05	A_{f}	Fuselage area	0.038 m^2
v_{c}	ascent/descent velocity	5 m/s			

consumption of the AAP is the sum of the power consumed by the UAV and the radio access node; since the power consumed by the radio access node is negligible compared that consumed by the UAV (by two orders of magnitude) [17], [23], it is assumed that the power consumption of the whole AAP is equal to that of the UAV. The UAV parameters are summarized in Table G.1. From [25], the power required by the AAP for flying horizontally and vertically is given by (G.6) and (G.7), respectively:

$$P_{\mathrm{h}}(v_r) = \underbrace{N_{\mathrm{rotor}} P_{\mathrm{b}} \left(1 + \frac{3v_r^2}{v_{\mathrm{tip}}^2}\right)}_{P_{\mathrm{blade}}} + \underbrace{\frac{1}{2} U_{\mathrm{d}} A_{\mathrm{f}} \rho(h_{\mathrm{a}}) v_r^3}_{P_{\mathrm{fuselage}}} + \underbrace{W \left(\sqrt{\frac{W^2}{4N_{\mathrm{rotor}}^2 \rho^2(h_{\mathrm{a}}) A_{\mathrm{rotor}}^2} + \frac{v_r^4}{4}} - \frac{v_r^2}{2}\right)^{1/2}}_{P_{\mathrm{induce}}}, \tag{G.6}$$

$$P_{\mathrm{v}}(v_{\mathrm{c}}) = \frac{W}{2} \left(v_{\mathrm{c}} + \sqrt{v_{\mathrm{c}}^2 + \frac{2W}{N_{\mathrm{rotor}} \rho(h_{\mathrm{a}}) A_{\mathrm{rotor}}}}\right) + N_{\mathrm{rotor}} P_{\mathrm{b}}. \tag{G.7}$$

where $P_{\mathrm{b}} = \frac{\Delta}{8} \rho(h_{\mathrm{a}}) s A_{\mathrm{rotor}} v_{\mathrm{tip}}^3$, $\rho(h_{\mathrm{a}}) = (1 - 2.2558.10^{-5} h_{\mathrm{a}})^{4.2577}$. P_{blade} and P_{fuselage} are the power levels required to overcome, respectively, the profile drag forces of the rotor blades and the fuselage of the aerial vehicle opposite to its forward movement; P_{induce} represents the power required to lift the payload. Replacing $v_r = 0$ in (G.6) gives the power level required for hovering.

2.4 PV-Battery System Modeling

PV Modeling

The considered model for the PV power generation has the following expression:

$$P_{\mathrm{pv}}(N_{\mathrm{pv}}, t) = I_{\mathrm{irr}}(t) \cdot A_{\mathrm{pv}} \cdot N_{\mathrm{pv}} \cdot \eta_{\mathrm{pv}}, \tag{G.8}$$

where $I_{\mathrm{irr}}(t)$ is the solar irradiance at time t on a south-oriented plane with tilt angle of 30°, measured in W/m^2; A_{pv} is the panel area (m^2), and η_{pv} is the panel efficiency (assumed constant).

Ground Battery Modeling

Battery storage devices are combined with RESs, such as PV panels, to offset the intermittency of these resources. The power needed by the CS to recharge the AAPs is supplied by either the PV panels or the ground battery, depending on the availability of

the solar energy. If there is a surplus of power generation, the extra power is redirected towards recharging the batteries of the charging station, as long as their capacity allows it. If, on the other hand, the power generation is not sufficient, the remaining power is drawn from the ground battery. The battery model, including its boundary conditions, is adapted from that in [32], and it is the following:

$$E_{\mathrm{bt}}(t) = E_{\mathrm{bt}}(t-\Delta t) + P_{\mathrm{bt}}(t)\cdot\Delta t\cdot\eta_{\mathrm{bt}}(P_{\mathrm{bt}}), \tag{G.9}$$

$$E_{\mathrm{bt}}(0) = N_{\mathrm{bt}}\beta_{\mathrm{module}}\mathrm{SOC}_{\mathrm{max}}, \tag{G.10}$$

$$N_{\mathrm{bt}}\beta_{\mathrm{module}}\mathrm{SOC}_{\mathrm{min}} \le E_{\mathrm{bt}}(t) \le N_{\mathrm{bt}}\beta_{\mathrm{module}}\mathrm{SOC}_{\mathrm{max}}, \tag{G.11}$$

$$P_{\mathrm{bt}}(t) \le P_{\mathrm{Ch,max}}, \quad \text{when } P_{\mathrm{bt}}(t) > 0, \tag{G.12}$$

$$|P_{\mathrm{bt}}(t)| \le P_{\mathrm{DCh,max}}, \quad \text{when } P_{\mathrm{bt}}(t) < 0, \tag{G.13}$$

where $E_{\mathrm{bt}}(t)$ is the energy stored in the battery at time t; $P_{\mathrm{bt}}(t)$ is the power flowing into the battery (negative when the battery is discharging); Δt is the time interval considered, and $\eta_{\mathrm{bt}}(P_{\mathrm{bt}})$ is the battery efficiency, which depends on the sign of P_{bt} because charging and discharging efficiencies are different. As per the constraints, N_{bt} is the number of battery modules, β_{module} is the capacity of one battery module, $\mathrm{SOC}_{\mathrm{min}}$ and $\mathrm{SOC}_{\mathrm{max}}$ are the minimum and maximum State-of-Charge (SOC) of the battery, which indicates the level of charge relative to the capacity. Hence, conditions (G.10) and (G.11) mean that the battery pack is initially fully charged, ($\mathrm{SOC} = \mathrm{SOC}_{\mathrm{max}}$), while the battery is considered depleted when $\mathrm{SOC} = \mathrm{SOC}_{\mathrm{min}}$. Finally, (G.12) and (G.13) impose maximum input and output powers, as specified in the battery data-sheet.

2.5 AAP Mission Breakdown

The time intervals that define the work cycle of an AAP during a mission are displayed in Fig. G.2, and are defined as follows:

- T_{active} is the active time of an AAP, i.e., the total time it spends flying before recharging. T_{active} is given by the sum of the horizontal flying time T_{fly} and the exchange time T_{ex}:

$$T_{\mathrm{active}} = \underbrace{N_{\mathrm{Hcycle}}\cdot T_{\mathrm{Hcycle}}}_{T_{\mathrm{fly}}} + \underbrace{T_{\mathrm{descent}} + T_{\mathrm{ascent}}}_{T_{\mathrm{ex}}}, \tag{G.14}$$

  where T_{fly} is the product of the duration of a cycle of data harvesting and the number of cycles, N_{Hcycle}, an AAP can withstand before running out of energy; T_{ex} is the time spent in the exchange process, from when the substitute AAP leaves the CS to when the discharged AAP reaches the CS. It is obtained by summing the descent and ascent times, T_{descent} and T_{ascent}, which are, respectively, the time an AAP needs to return to and to leave the CS.

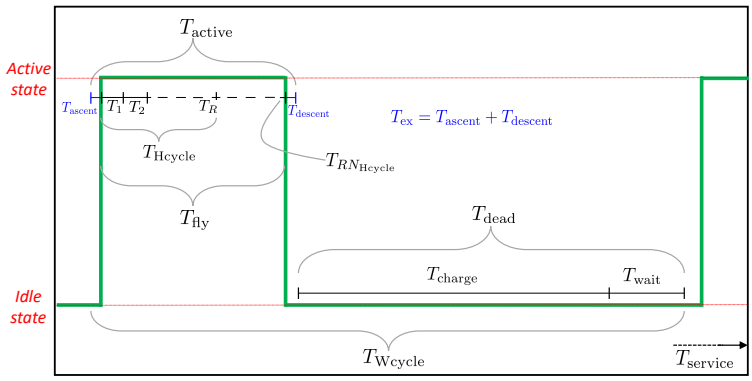

Fig. G.2: Time components of an AAP work cycle.

- T_{charge} is the time needed to fully recharge an AAP, which is calculated based on the capacity of each AAP's on-board battery β_{aap}, its Depth-of-Discharge DOD_{aap} (the proportion of capacity that is used during each work cycle), and its average charging power P_{charge}:

$$T_{\text{charge}} = \beta_{\text{aap}} \text{DOD}_{\text{aap}} P_{\text{charge}}. \tag{G.15}$$

- T_{wait} is the interval in which an AAP is charged, but it is waiting for the an active AAP to finish its mission before being deployed. Its value is determined by using the two definitions of T_{Wcycle}, one referring to a single AAP, and the other to a whole flock, as follows:

$$\begin{aligned} T_{\text{Wcycle}} = T_{\text{active}} + T_{\text{charge}} + T_{\text{wait}} &= N_{\text{aap}} \left(T_{\text{active}} - \frac{T_{\text{ex}}}{2} \right), \\ \rightarrow T_{\text{wait}} &= (N_{\text{aap}} - 1)\, T_{\text{active}} - T_{\text{charge}} - N_{\text{aap}} \frac{T_{\text{ex}}}{2}. \end{aligned} \tag{G.16}$$

- The period T_{Wcycle} is the interval corresponding to a full AAP work cycle, given by the sum of the time the AAP spends in each of the three states: active, charging, and idle,

$$T_{\text{Wcycle}} = T_{\text{active}} + T_{\text{charge}} + T_{\text{wait}}. \tag{G.17}$$

3 Optimal Design of an Energy-Neutral System

In this section, it is explained how a cost-efficient EN system is achieved by optimally designing the trajectory of the AAP and efficiently selecting the configuration of the

CS. The corresponding optimization problem can be formulated as,

$$\text{(G:P1)}: \underset{N_{\text{pv}},N_{\text{bt}},\{\mathbf{r}_r\},\{T_r\},\{T_{n,r}\}}{\text{minimize}} \quad C_{\text{inv}}\left[N_{\text{pv}}, N_{\text{bt}}, N_{\text{aap}}(\{T_r\})\right], \tag{G.18}$$

$$P_{\text{pv}}(N_{\text{pv}}, t) + P_{\text{bt}}(N_{\text{bt}}, t)\eta_{\text{bt}} \geq P_{\text{ld}}\left[N_{\text{aap}}(\{T_r\}), t\right], \forall t, \tag{G.19}$$

$$\frac{\delta}{T_r} \leq v_{\max} \qquad \forall r, \tag{G.20}$$

$$\sum_{r=1}^{R} T_{n,r} BD_{n,r}(\mathbf{r}_r) \geq Q \quad \forall n, \tag{G.21}$$

$$\mathbf{r}_{\text{h},1} = \mathbf{r}_{\text{h},c(R+1)} = \mathbf{r}_{\text{CS}}, \quad \forall c \in \{1, 2, ..., N_{\text{Hcycle}}\}, \tag{G.22}$$

$$\text{(G.1)}, \text{(G.2)}, \text{(G.8)} - \text{(G.13)}. \tag{G.23}$$

The objective function of (G:P1) is the total investment cost, consisting in the costs of the PV panels, battery units, and the AAPs:

$$C_{\text{inv}}(N_{\text{pv}}, N_{\text{bt}}, N_{\text{aap}}(\{T_r\})) = N_{\text{pv}}C_{\text{pv}} + N_{\text{bt}}C_{\text{bt}} + N_{\text{aap}}(\{T_r\})C_{\text{aap}}, \tag{G.24}$$

where $N_{\text{aap}}(\{T_r\})$ is the total number of AAPs, each costing C_{aap} €; $N_{\text{aap}}(\{T_r\})$ is the sum of idle and active AAPs, where the number of active AAPs is determined by the TDOA of the network T_{period} and the time it takes an AAP to complete one cycle of data harvesting:

$$N_{\text{active}}(\{T_r\}) = \left\lceil \frac{\sum_{r=1}^{R} T_r}{T_{\text{period}}} \right\rceil, \tag{G.25}$$

where $\lceil x \rceil$ rounds x to the nearest integer greater than or equal to x. Therefore, the total number of AAPs required to guarantee that there is always a fully charged AAP ready to be deployed to replace a depleted AAP is determined as [25],

$$N_{\text{aap}}(\{T_r\}) = \left\lceil \left(\frac{T_{\text{dead}}}{T_{\text{active}}} + 1 \right) N_{\text{active}}(\{T_r\}) \right\rceil, \tag{G.26}$$

with T_{dead} defined as the sum of charging and wait times, $T_{\text{dead}} = T_{\text{charge}} + T_{\text{wait}}$. T_{active} is obtained from the data-sheet [2] of the UAV used. Usually, the UAV manufacturers specify T_{active} as the hovering time for a given payload. Since the hovering power is greater than the horizontal flying power of the UAV until a particular velocity value, the maximum AAPs flying speed is set to be $v_{\max}$ in (G.20), where $v_{\max}$ is obtained from the power profile of the AAP, as shown in Fig. G.3. This ensures that T_{active} will be greater than or equal to the hovering time indicated in the data-sheet. The corresponding number of idle AAPs is then determined as $N_{\text{idle}}(\{T_r\}) = N_{\text{aap}}(\{T_r\}) - N_{\text{active}}(\{T_r\})$. Constraint (G.19) is the energy neutrality constraint, which guarantees that the CS

[2] https://dl.djicdn.com/downloads/m100/M100_User_Manual_EN.pdf

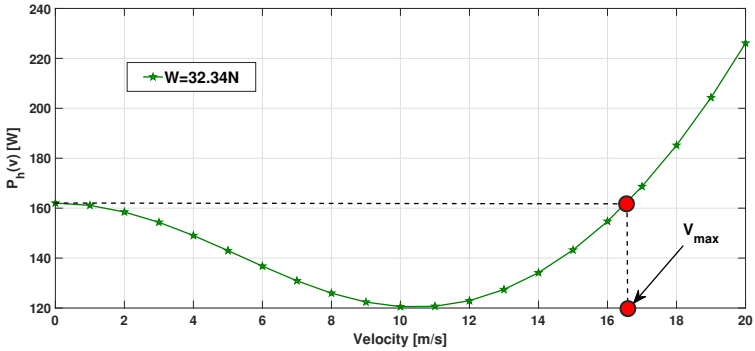

Fig. G.3: UAV power consumption as a function of the velocity.

load power requirement is always satisfied, regardless of whether power is provided by the PV panels or the ground battery. One of the challenges in solving (G:P1) is the difficulty in representing the load to the CS at a given time t as a function of T_{period}, T_{Hcycle}, T_{active}, and T_{dead}. In Section 3.1, a novel model is developed to represent the load, $P_{\text{ld}}\left[N_{\text{aap}}(\{T_r\}), t\right]$, as a function of the number of AAPs. (G.21) guarantees the delivery of Q bits of data from all the GUs to the AAP within T_{Hcycle}s, with B being the available bandwidth. (G.22) ensures that each data harvesting cycle starts and ends above the charging station location, $\mathbf{r}_{\text{CS}}$.

3.1 Wave-Based Load Profile Modeling of the CS

From the point of view of the CS, an AAP can only be in two alternative states: charging or not charging. In the previously described scenario, these two states will periodically repeat themselves within a given period of time. Let, $K_{\text{aap},i}(t)$ be the function describing the state of the i^{th} AAP at time t, such that:

$$K_{\text{aap},i}(t) \equiv \begin{cases} = 0, & \text{when the AAP begins/finishes charging;} \quad \text{(G.27a)} \\ > 0, & \text{when the AAP is charging;} \quad \text{(G.27b)} \\ < 0, & \text{when the AAP is not charging;} \quad \text{(G.27c)} \\ & \text{is periodical with period } T_{\text{Wcycle}}. \quad \text{(G.27d)} \end{cases}$$

The above conditions can be met by modeling $K_{\text{aap},i}(t)$ as a function of the following variables:

$$K_{\text{aap},i}(t) = F\left(T_{\text{period}}, T_{\text{Wcycle}}, T_{\text{Hcycle}}, T_{\text{active}}, T_{\text{charge}}\right). \quad \text{(G.28)}$$

The solution to model F, inspired by the modulation of power electronics, is to use a sinusoidal function that can be converted into a square wave at a later stage, using a comparative function. This approach allows synthetic expression for whatever number

of cycles and even AAPs, and it is easy to implement in any programming language. Its expression is the following:

$$K_{\text{aap},i}(t) = \alpha \sin\left\{\omega(T_{\text{Wcycle}})\left[t + \phi(T_{\text{active}}, T_{\text{charge}}) - \zeta_i(T_{\text{Hcycle}}, T_{\text{period}})\right]\right\} + \gamma(T_{\text{Wcycle}}, T_{\text{charge}}). \tag{G.29}$$

In order to meet the conditions described in (G.27a)-(G.27d), the shape of (G.29) can be adjusted by tweaking its five coefficients, as follows:

- α is the amplitude of the wave, but in this case it is only used to specify the sign of the function. Its value is $\alpha = -1$ if the cycle starts with an already charged AAP (or vice-versa);
- $\omega(T_{\text{Wcycle}})$ is the period of the sine wave, which can be calculated as $\omega(T_{\text{Wcycle}}) = \frac{2\pi}{T_{\text{Wcycle}}}$, as a consequence of the definition of period applied to condition (G.27d);
- $\phi(T_{\text{active}}, T_{\text{charge}})$ is the phase of the wave, which establishes the shape of the function. It is found by imposing (G.27a) at $t = T_{\text{active}}$ and $t = T_{\text{active}} + T_{\text{charge}}$, resulting in $\phi(T_{\text{active}}, T_{\text{charge}}) = \frac{\arcsin\left(-\frac{C}{A}\right)}{\omega} - T_{\text{active}}$;
- $\zeta_i(T_{\text{Hcycle}}, T_{\text{period}})$ is the delay between the launch of the first and the i^{th} AAP, as explained in Section 2.1:

$$\zeta_i(T_{\text{Hcycle}}, T_{\text{period}}) = \begin{cases} 0 & \text{if} \quad i = 1, \\ (i-1) \cdot \frac{T_{\text{period}}}{\left\lceil \frac{T_{\text{Hcycle}}}{T_{\text{period}}} \right\rceil}, & \text{if} \quad T_{\text{Hcycle}} \geq T_{\text{period}}, \forall i, \\ T_{\text{active}}, & \text{if} \quad T_{\text{Hcycle}} < T_{\text{period}}. \end{cases} \tag{G.30}$$

- $\gamma(T_{\text{Wcycle}}, T_{\text{charge}})$ is a constant that can shift the wave upwards or downwards without affecting its shape. For $\gamma(T_{\text{Wcycle}}, T_{\text{charge}}) = 0$, the ratio between T_{charge} and T_{Wcycle} would be 0.5, while for $\gamma(T_{\text{Wcycle}}, T_{\text{charge}}) = 1$ the AAP would be charging the whole time. Thus, the general formulation is $\gamma(T_{\text{Wcycle}}, T_{\text{charge}}) = \frac{T_{\text{charge}}}{2T_{\text{Wcycle}}} - 1$.

Now, all the cycle functions $K_{\text{aap},i}(t)$ are transformed into state functions $S_{\text{aap,i}}(t)$ of value 1 when the AAP is charging, 0 when it is not, consistently with the convention adopted initially:

$$S_{\text{aap},i}(t) = \begin{cases} 1, & \text{if} \quad K_{\text{aap},i}(t) > 0, \\ 0, & \text{if} \quad K_{\text{aap},i}(t) \leq 0. \end{cases} \tag{G.31}$$

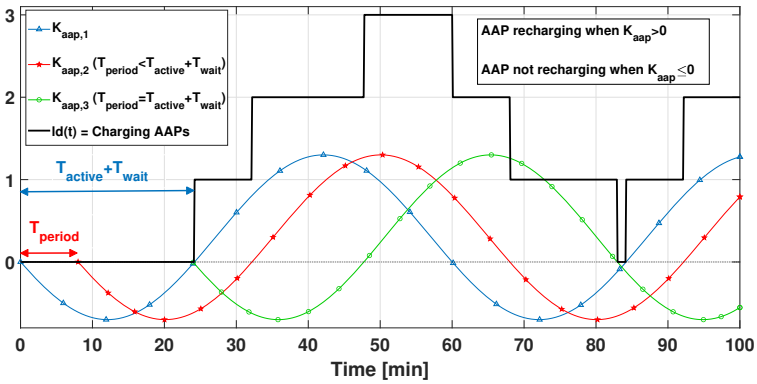

Fig. G.4: Visualization of three AAP state functions, and the consequent load on the charging station.

Then, the sum of all the state functions S_{aap} provides the number of AAPs recharging at the same time:

$$\text{ld}\left[N_{\text{aap}}(\{T_r\}), t\right] = \sum_{i=1}^{N_{\text{aap}}(\{T_r\})} S_{\text{aap},i}(t). \tag{G.32}$$

The resulting curves are visualised in Fig. G.4, where three AAP curves exemplify two cases: one where a single active AAP is enough to satisfy the delay constraint, and one where at least two AAPs must be active at the same time. It is shown in grey the load function defined by (G.32), i.e., the number of AAPs connected to the CS at any given time. It can be observed how the steps of the load function correspond with the intersection between a state function K and the Time = 0 axis. Finally, the load on the CS can be calculated by multiplying the number of charging AAPs by the power consumed to charge a single AAP, $\frac{P_{\text{charge}}}{\eta_{\text{aap}}}$. Hence, the RHS of (G.19) becomes:

$$P_{\text{ld}}\left[N_{\text{aap}}(\{T_r\}), t\right] = \frac{P_{\text{charge}}}{\eta_{\text{aap}}} \cdot \text{ld}\left[N_{\text{aap}}(\{T_r\}), t\right] + \Psi(t). \tag{G.33}$$

The function Ψ represents the power consumption associated with recalculating the optimal trajectory locally, a binary function assuming the value of computational power when the computation is executed, and zero at all other times. Since the charging power was assumed to be a constant, $P_{\text{ld}}\left[N_{\text{aap}}(\{T_r\}), t\right]$ will have the same shape as $\text{ld}\left[N_{\text{aap}}(\{T_r\}), t\right]$, but it will be expressed in Watts. For a given T_{period}, from (G.19), the number of required PV panels and battery units is proportional to the load profile on the CS; from (G.33), the load profile of the CS is in turn a function of the number of AAPs. Therefore, the size of the AAP fleet has an impact on the number of PV panels and battery units. Thus, from (G.19) and (G.33), minimizing the number of AAPs means minimizing the objective function of (G:P1). Once the minimum number

of AAPs required to harvest Q bits of data from N GUs within T_{period} is determined, the cost-efficient combination of PV panels and battery units is directly consequential.

3.2 Minimum Number of AAPs

In this section we design a trajectory that minimizes the number of AAPs required to harvest data from the GUs every T_{period} during T_{service}. The corresponding problem is formulated as,

$$(\text{G:P1.1}): \underset{\{\mathbf{r}_r\},\{T_{n,r}\},\{T_r\}}{\text{minimize}} \quad N_{\text{aap}}(\{T_r\}), \tag{G.34}$$

$$N_{\text{aap}}(\{T_r\}) \geq \left(\frac{T_{\text{dead}}}{T_{\text{active}}} + 1\right) N_{\text{active}}(\{T_r\}), \tag{G.35}$$

$$N_{\text{active}}(\{T_r\}) \geq \frac{\sum_{r=1}^{r} T_r}{T_{\text{period}}}, \tag{G.36}$$

$$(\text{G.1}), (\text{G.20}) - (\text{G.22}). \tag{G.37}$$

In (G:P1.1), we have relaxed the integer constraint on the number of active and total AAPs. After determining the trajectory variables, the values will be rounded to the nearest greater integer. (G:P1.1) is a non-convex optimization problem due to the non-convex form of $D_{n,r}(\mathbf{r}_r)$, used in (G.21). Hence, the solution is found by dividing the problem into two sub-problems: 1) AAP path design using mean-shift clustering; 2) update of $\{T_r\}$ and $\{T_{n,r}\}$ for the obtained AAP path.

In practice, the number of GUs is large, or they are likely to form clusters. Thus, to find the cluster properties of user distributions, one can exploit the mean-shift algorithm proposed in [19] to identify the locations with the highest density of users. When the number of users is high, the cluster centers are potential points for the AAP trajectory. In addition, in cases where the users form clusters in advance, such as in rural areas, referring to these centers prevents the AAP from visiting locations where there are no GUs. The cluster centers obtained from Algorithm 1 of [19] are the potential points through which the AAP must pass. Since the active number of AAPs can be reduced by minimizing $\sum_{r=1}^{R} T_r$, the shortest path between the potential points is determined using the traveling salesman algorithm [30]. The resulting continuous path between cluster centers is then discretized into small segments, each of length δ, satisfying constraint (G.1), and providing the set of waypoints $\{\mathbf{r}_r\}$. The values of $D_{n,r}(\mathbf{r}_r)$ are then calculated using (G.5). The scheduling problem now takes the following form:

$$(\text{G:P1.2}): \underset{\{T_{n,r}\},\{T_r\}}{\text{minimize}} \quad N_{\text{aap}}(\{T_r\}), \tag{G.38}$$

$$(\text{G.20}) - (\text{G.22}), (\text{G.35}), (\text{G.36}). \tag{G.39}$$

Problem (G:P1.2) is a convex optimization problem, and can be solved with solvers like CVX.

3.3 Cost-Efficient CS Design

In the previous section, the load to the CS was represented as a function of the number of AAPs. Also, a trajectory was found that minimizes the number of AAPs, thereby minimizing the load on the CS and the economic impact of purchasing AAPs. In this section, efforts are directed towards minimizing the number of PV panels and ground battery units of the CS, N_{pv} and N_{bt}, while satisfying the power requirement of the CS. The corresponding problem is formulated as,

$$(\text{G:P1.3}): \underset{N_{\mathrm{pv}}, N_{\mathrm{bt}}}{\text{minimize}} \quad C_{\mathrm{inv}}\left[N_{\mathrm{pv}}, N_{\mathrm{bt}}, N_{\mathrm{aap}}(\{T_r\})\right], \tag{G.40}$$

$$P_{\mathrm{pv}}(N_{\mathrm{pv}}, t) + P_{\mathrm{DCh}}(N_{\mathrm{bt}}, t)\eta_{\mathrm{bt}} \geq P_{\mathrm{ld}}\left[N_{\mathrm{aap}}(\{T_r\}), t\right], \forall t, \tag{G.41}$$

$$(\text{G.8}) - (\text{G.13}). \tag{G.42}$$

Constrained Search Algorithm

Algorithm G.1: Cost-Efficient EN System Design.

1 Initialize the locations of GNs;
2 Find the user-cluster centers using the mean-shift algorithm;
3 Find the shortest path between the centers using the travelling salesman algorithm;
4 Segment the path into R segments of length δ and find $\{D_{n,r}(\mathbf{r}_r)\}$ using (G.5);
5 Solve (G:P1.2) to get the trajectory variables, the GU scheduling, and the minimum number of AAPs;
6 Model the load to the CS using (G.32);
7 Use the constrained search algorithm to find the minimum number of PV and battery units that allows to meet the load requirement.

The constrained search algorithm proposed to solve (G:P1.3) is an enhanced version of a classic 'brute force' algorithm. Brute force methods, also known as exhaustive search, offer a forthright and very accurate optimization approach of solving problems, visiting all possible search points in the design space, in order to find the global optimum within a given search space [33].Their main drawback is the high computational load, but, in the present application, this is acceptable due to the simple form of problem (G:P1.3). Since the trajectory optimization is now decoupled from the CS design, this can be carried out by manipulating only two variables: N_{pv} and N_{bt}. With a classic extensive search, all the solutions generated from the combination of these two variables would be simulated to evaluate their cost and power profile. The ones not satisfying constraint (G.41) would be simply discarded, and the remaining ones compared by their cost to find the global minimum. However, the constrained search algorithm achieves the same result with less iterations: for each number of PV panels, the size of the battery

Table G.2: Simulation Settings.

Label	Definition	Value	Label	Definition	Value
A_{pv}	Area of PV panel	1.63 m^2	η_{pv}	Average efficiency of PV panel	17.1%
β_{module}	Energy capacity of a battery module	37.44 Wh	η_{bt}	Average efficiency of ground battery	90%
SOCmin	Minimum battery State-of-Charge	5%	T_{active}	Active time of an AAP	1320 s
SOCmax	Maximum ground battery State-of-Charge	95%	v_{c}	AAP climbing velocity	5 m/s
β_{aap}	On-board battery capacity of an AAP	100 Wh	P_{charge}	AAP nominal charging power	180 W
DOD_{aap}	Depth-of-Discharge of AAP battery	90%	η_{aap}	Average efficiency of AAP battery	85%
f	Channel carrier frequency	5.8 GHz	Q	Data size	-
B	Channel bandwidth	20 MHz	a	P^{los} Constant for suburban topology	4.88
N_0	Noise spectral power	-174 dBm/Hz	b	P^{nlos} Constant for suburban topology	0.43
v_{max}	AAP's maximum speed	17 m/s	η^{loS}	additional mean path loss for LoS group	0.2
δ	Path discretization interval	1 m	η^{nloS}	additional mean path loss for NLoS group	24
P	Transmission power	23 dBm	h_{a}	Flying altitude of an AAP	50 m

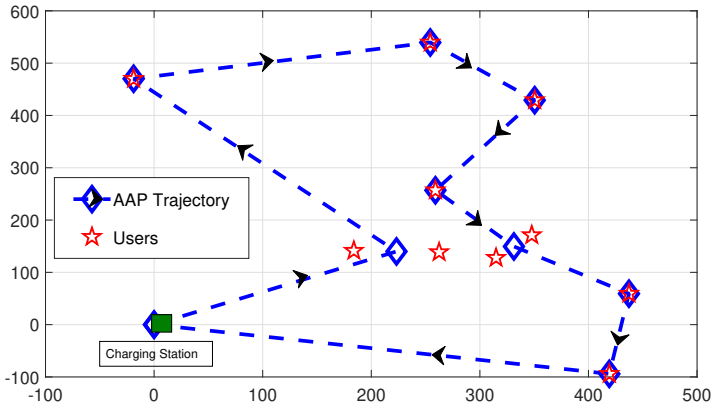

Fig. G.5: Horizontal projection of a sample AAP trajectory to collect 200 Mbits of data from 10 randomly distributed users.

is progressively increased until the condition posed by constraint (G.41) is met. This skips the simulation of several configurations that would be later discarded for their excessive cost. Algorithm G.1 summarizes the steps involved in designing a UAV-based cost-efficient EN system to serve a set of IoT ground units.

4 Results and Discussion

The simulation parameters used to generate the results described in this section are listed in Table G.2. In Section 4.1, the results related to the trajectory design are discussed, and in Section 4.2 the results of the cost-efficient system design are presented.

4.1 AAP Trajectory

Fig. G.5 shows a sample path an AAP follows to collect 200 Mbits of data from a set of 10 users, uniformly distributed over a square region of side 600m. The CS is placed at

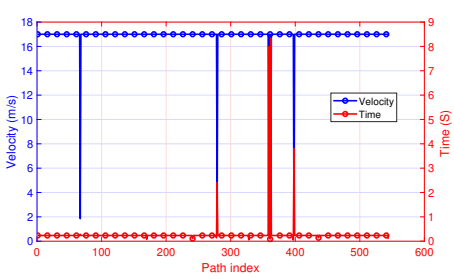

(a) Velocity- Time profile.

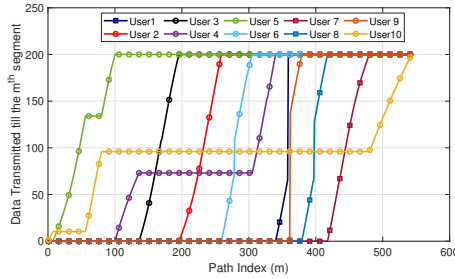

(b) Scheduling.

Fig. G.6: a)The total time and energy to collect the data is 148 seconds; and 6.9133 Wh, respectively; b)AAP collects 200 Mbits of data from all the users by the end of the trajectory.

$(0, 0, 0)$. The set of feasible points the AAP should pass through are determined using the mean-shift algorithm. Fig. G.6a and Fig. G.6b show the trajectory parameters and the user scheduling obtained by solving (G:P1.2); the flying velocity of the AAP in each path segment shows how this AAP trajectory satisfies the maximum velocity constraint (G.20); also, by the end of the trajectory, all the users have delivered 200 Mbits of data, thereby satisfying the data harvesting constraint (G.21). Moreover, the horizontal projection of the trajectory starts and ends above the CS location (G.22). Fig. G.7 shows the advantage of the suggested mean-shift method path design when compared to two baseline scenarios:

1. the AAP flies at its maximum velocity to each user and hovers right on top of it to complete the data transmission. This is widely known as fly-hover-communicate protocol [23], [25];

2. the AAP hovers at the center of the coverage region (hover-communicate) [14], [15].

As seen in Fig. G.7, the proposed method outperforms the two baseline scenarios in terms of both time and energy an AAP needs to complete a cycle of data harvesting. The hover-communicate scenario has the worst performance because the mobility of the AAP is not exploited to optimize the channels between AAP and users. The benefits of user clustering are maximized when the number of users is large. Since the expected number of user nodes in an IoT network is very large, the proposed path design is an ideal candidate for an IoT data harvesting application.

4.2 Charging Station Design

This section explains the findings related to the design of the CS using the trajectory information from the previous section. A $T_{\text{period}} = 600$s is considered, resulting in $N_{\text{active}}(\{T_r\}) = 1$ from (G.25); $T_{\text{dead}} = 600$s, giving $N_{\text{aap}}\{T_r\}) = 3$. The irradiation data used in the simulations is obtained from the online database in [31], which refers to

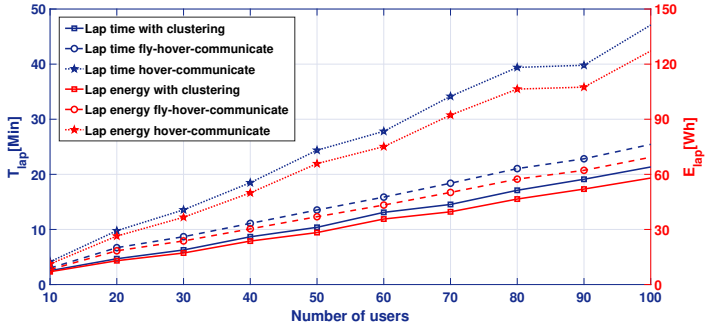

Fig. G.7: AAP lap time energy consumption: the proposed method versus the baseline scenarios.

the area of Milan, Italy. This is provided with intervals of one minute, so the irradiation was assumed to stay constant over a single interval. The solar panels[3] considered in this study have a unit price C_{pv} of 129.80€. Each battery unit is represented by a pack of 4 Li-ion cells[4], with a unit cost C_{bt} of 39.59€. The load to the CS corresponding to $N_{\text{aap}}(\{T_r\}) = 3$, $T_{\text{period}} = 2580$s, $T_{\text{Wcycle}} = 3900$s, $T_{\text{Hcycle}} = 148$s, $T_{\text{active}} = 1320$s, and $T_{\text{charge}} = 1800$s is then modeled using the the methodology described in Section 3.3, and the result is shown in Fig. G.8. The cost-efficient PV-battery combination that serves the load while satisfying the battery constraints (G.9)- (G.13) is determined by solving (G:P1.3) with the constrained search algorithm. The effect of the battery constraints can be observed indirectly in Fig. G.8, as they produce a slightly over-sized battery, which is not fully exploited, at least on an average day. Fig. G.8 shows the operation of the designed CS with $T_{\text{start}} = 11:15$ and $T_{\text{service}} = 2$ hrs: as the irradiation starts to grow, the solar panels begin to generate power, which goes all towards charging the battery, since the load is nil until 11:00, when the optimal trajectory is computed. This process takes one minute using an average laptop with a power consumption of 50 W, and it does not impact the system significantly. After 11:15, when the mission starts, the generated power is not enough to supply the load alone, so the battery kicks in, as the drop in its SOC shows. It can be noticed in Fig. G.8 how the power consumption profile actually extends beyond the mission duration T_{service}. This is because it is assumed that the AAPs are fully charged in the morning, so they need to be recharged in the evening. However, this can be done slowly, so as to avoid unnecessary peaks of power consumption. For this reason, the number of AAPs simultaneously recharging during this phase was arbitrarily set equal to the number of active AAPs. When this 'constant consumption' phase begins, the solar panels are still producing enough power to recharge the battery. This example, representing a day when the irradiation is particularly low, shows how power constraint (G.41) is always satisfied.

[3] https://www.futurasun.com/wp-content/uploads/2020/10/2020_FuturaSun_60p_260-285W_en.pdf?x78774

[4] http://www.farnell.com/datasheets/3170915.pdf

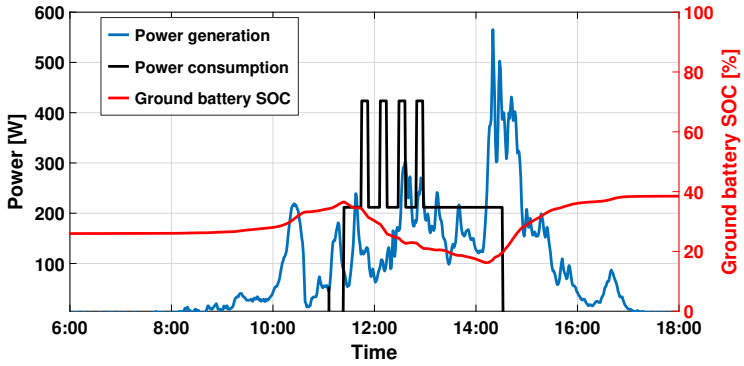

Fig. G.8: Power profiles and ground battery SOC for a 2 hours mission starting at 11:15 in February.

The optimization of the CS design is repeated using different values of the following variables:

- *mission duration*, which measures the amount of time during which the network is continuously operated;
- *starting time*, which indicates at what time the network starts operating (this is assumed to be the same every day);
- *season*, which is a binary variable: 'winter' goes from the 21$^{\text{st}}$ of September to the 21$^{\text{st}}$ of March, while 'summer' covers the remaining time.

These variables influence the CS design in different ways: the first modifies the power profile shape shown in Fig. G.4, whereas starting time and season affect the irradiation data $I_{\text{rr}}(t)$. This sensitivity analysis is summarized in Figs. G.9a and G.9b, which show how the cost of the system is affected by the three aforementioned variables, respectively for the winter and summer scenarios. The dotted line is included for comparison with the grid-connected case in a urban scenario, which is explained in more depth in Fig. G.11. In both seasons, the effect of the mission duration is particularly marked if the mission starts in the afternoon. This is because, when the solar irradiation is low, the task of satisfying the load is left to the battery pack alone, which, as a result, must be made larger. More in general, the greater the mismatch between energy generation and load profile, the larger the battery will need to be. The minimum point of the curves shifts to an earlier starting time as the mission duration grows, suggesting that the cost minimization can only be achieved as a combination of these two variables. While short missions are feasible at almost any time of the day even in winter, longer missions at later times make the system cost soar at a growing pace, due to the decreasing marginal returns of designing a larger ground battery. Apart from this aspect, the curves look similar in winter and summer, with a downward shift in the latter case. However, more pronounced differences can be expected if the 'summer' season is restricted to the actual

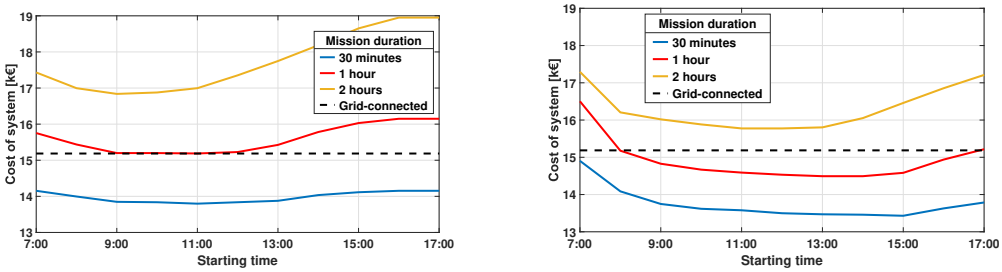

(a) Winter **(b)** Summer

Fig. G.9: Cost of the whole system, with 20 users and $Q = 200$ Mb, compared to grid-connected urban scenario.

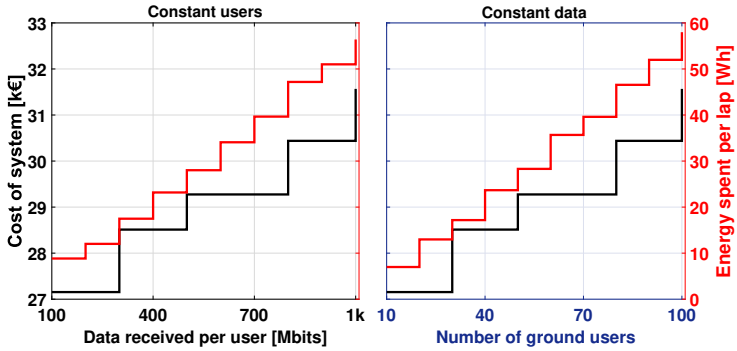

Fig. G.10: Cost of charging station and energy consumption trends as a function of variable data size and number of users.

summer, instead of half a year. Fig. G.10 shows how the cost of the system and the energy spent per data harvesting cycle change according with the number of ground users and the amount of data to be received from each of these. Both variables have similar effects: the energy spent by an AAP to complete a data harvesting cycle grows at a quasi-constant pace, whereas the charging station cost grows intermittently, together with the number of active AAPs. The latter represents the main voice of expense for the system.

A cost comparison is presented in Fig. G.11 between the off-grid system described in this work and a grid-connected scenario with the same modes of operation (UAV-based, mission of 2 hours, starting at 11:15). The left hand side of the histogram shows the cost breakdown of the energy-neutral CS, while the right hand side shows the voices of expense for the grid-connected scenario, namely the cost of connecting to the electricity grid and that of the consumed energy. The cost of the UAVs is the same on both sides, so the y-axis is cut to improve readability. The cost of energy was calculated as a cumulative sum on 10 years, assuming a fixed cost of 0.17€/kWh (average cost

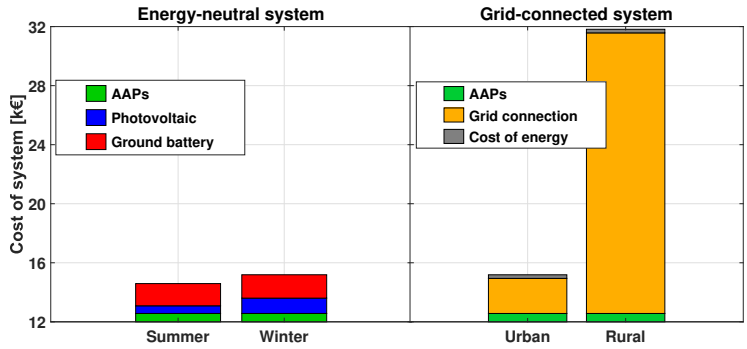

Fig. G.11: Cost comparison between EN system designed for summer or winter and a grid-connected one in urban or rural area.

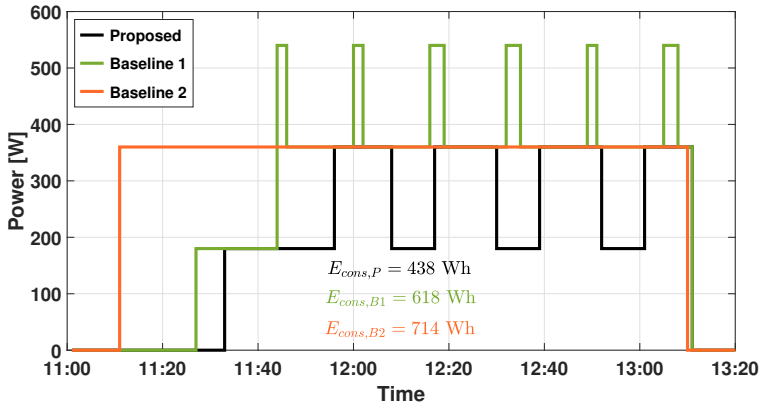

Fig. G.12: Load profiles comparison between the proposed method and the two baselines.

of electricity in the UK). The cost of connecting the system to the electricity grid was estimated using an online tool provided by an electricity provider in the UK[5], assuming a distance from the substation of 10 meters both in the rural and the urban scenarios. It can be deduced that the installation of a PV-based off-grid charging station is particularly advantageous in rural areas, while the two options have comparable costs in urban areas. It can be observed in Fig. G.9 how short missions taking place during the day make the off-grid option less expensive than a grid-connected urban scenario. For longer missions, or when these start later in the day, the EN charging station is only advantageous when compared to the rural scenario, which would be feasible for continuous or nearly-continuous service.

A cost comparison is carried out between the proposed method and two baseline

[5] https://www.northernpowergrid.com/quick-calculator

Table G.3: Numerical comparison between proposed methodology and two baseline scenarios.

	N_{aap}	N_{pv}	Battery capacity [Wh]	Total cost [£]
Proposed	3	2	936	13,814.85
Baseline 1	4	3	1273	18,489.46
Baseline 2	3	3	1498	14,538.50

scenarios considering the same target area, UAV type, and mission duration:

- Baseline 1: The load profile is formed by considering UAVs hovering all the time [12];
- Baseline 2: The CS is designed considering a constant power consumption, corresponding to 2 tethered UAVs [11].

The resulting load profiles can be observed in Fig. G.12: the green and orange curves represent the load profiles from Baselines 1 and 2, respectively. In Baseline 1, the UAVs are hovering all the time, thereby reducing their active time, with higher peaks of power consumption and the need for an extra UAV; As reported in the figure, the proposed solution has the lowest value of energy consumption by a margin of over 50%, which could be even higher for longer missions. Furthermore, as reported in Table G.3, the higher load profiles clearly affect the initial cost, either due to the larger CS or to the larger fleet of UAVs. However, the effect of the latter is prominent due to the high cost of UAVs. This explains why, despite consuming less energy than Baseline 2, Baseline 1 is by far the most expensive option.

5 Conclusion and Future Work

In this article, a holistic design methodology was proposed for a cost-efficient UAV-based EN system for the data harvesting of IoT nodes. This methodology minimizes the investment cost by acting on the planning (how), scheduling (when), and energy supply of the AAP mission.

The main engineering insights derived from the results of this study are listed below:

- The clustering protocol adopted in this study reduces the time and energy an AAP needs to complete a cycle of data harvesting, compared to other benchmark protocols. This gap gets wider for higher numbers of users, up to a 50% energy and time saving in our simulation setups. The same is true for the cost of the system, which has a linear relation with the data exchange.
- For short missions (30 minutes) the investment cost of the system is minimized when the mission starts in the late morning in winter, or in the early afternoon in summer. Earlier times are preferred with longer missions. These cost variations

between seasons are mainly due to the PV size required, while mission duration and time mostly affect the ground battery size. However, the larger portion of the investment cost is represented by the AAPs.

- In an urban setting, an EN UAV-based system has an investment cost comparable to that of a grid-connected one, whereas it is much cheaper in rural areas, even for long missions.

The optimal solution is highly dependant on the aforementioned time variables, and the EN option becomes anti-economical when long missions are planned, especially in winter or at night. These issues could be tackled by diversifying the energy sources, which would complicate both the system design and operation, thus representing an interesting topic for future work.

References

[1] Fotouhi, Azade, et al. "Survey on UAV Cellular Communications: Practical Aspects, Standardization Advancements, Regulation, and Security Challenges," *IEEE Commun. Surv. and Tut. 21.4 (2019)*: 3417-3442.

[2] 3GPP; Technical Specification Group Services and System Aspects; "Unmanned Aerial System (UAS) Support in 3GPP"; Stage 1; Release 17.

[3] Javidsharifi, Mahshid, et al. "Optimum Sizing of Photovoltaic and Energy Storage Systems for Powering Green Base Stations in Cellular Networks," *Energies 14.7 (2021):* 1895.

[4] Marsan, Marco Ajmone, et al. "Towards Zero Grid Electricity Networking: Powering BSs with Renewable Energy Sources," in *IEEE international conf. on commun. workshops (ICC),* IEEE, 2013.

[5] Song J, Krishnamurthy V, Kwasinski A, Sharma R, "Development of a Markov-Chain-Based Energy Storage Model for Power Supply Availability Assessment of Photovoltaic Generation Plants," *IEEE Trans. on Sustain. Energy. 2012 Sep 10;4(2):*491-500.

[6] Chamola V, Sikdar B, "Outage Estimation for Solar Powered Cellular Base Stations," in *Proceedings of the 2015 IEEE Int. Conf. on Commun. (ICC),* London, UK, 8–12 June 2015; pp. 172–177.

[7] Ibrahim Anwar, et al. "A Novel Sizing Method of a Standalone Photovoltaic System for Powering a Mobile Network Base Station using a Multi-Objective Wind Driven Optimization Algorithm," *Energy Conversion and Management 238 (2021):* 114179.

[8] M. Virgili, A. J. Forysth and P. James, "A Multi-Objective Genetic Algorithm Methodology for the Design of Standalone Energy Systems," in *2021 IEEE Design Methodologies Conf. (DMC),* 2021, pp. 1-6.

[9] Chiaraviglio, Luca, et al. "Minimum Cost Design of Cellular Networks in Rural Areas with UAVs, Optical Rings, Solar Panels, and Batteries," *IEEE Trans. on Green Commun. and Netw. 3.4 (2019):* 901-918.

[10] Chiaraviglio, Luca, et al. "Optimal Design of 5G Networks in Rural Zones with UAVs, Optical Rings, Solar Panels and Batteries," in *Proceedings of the 20th International Conf. on Transparent Optical Networks (ICTON), Bucharest, Romania, 1–5 July 2018;* pp. 1–4.

[11] Amorosi, L.; Chiaraviglio, L.; Galan-Jimenez, J. "Optimal Energy Management of UAV-Based Cellular Networks Powered by Solar Panels and Batteries: Formulation and Solutions," *IEEE Access 2019, 7:* 53698–53717.

[12] Galán-Jiménez J, Moguel E, García-Alonso, J, Berrocal J, "Energy-Efficient and Solar Powered Mission Planning of UAV Swarms to Reduce the Coverage Gap in Rural Areas: The 3D case," in *Ad Hoc Netw. 2021, 118, 102517.*

[13] Javidsharifi, Mahshid, et al. "Optimum Sizing of Photovoltaic-Battery Power Supply for Drone-Based Cellular Networks." *Drones 5.4 (2021):* 138.

[14] A. Al-Hourani, S. Kandeepan, and S. Lardner, "Optimal LAP Altitude for Maximum Coverage," *IEEE Wireless Commun. Lett.*, vol. 3, no. 6, pp. 569–572, Dec. 2014.

[15] M. Alzenad, A. El-Keyi, F. Lagum, and H. Yanikomeroglu, "3-D Placement of an Unmanned Aerial Vehicle Base Station (UAV-BS) for Energy-Efficient Maximal Coverage," *IEEE Wireless Commun. Lett.*, vol. 6, no. 4, pp. 434–437, Aug. 2017.

[16] M. Mozaffari, W. Saad, M. Bennis, and M. Debbah, "Efficient Deployment of Multiple Unmanned Aerial Vehicles for Optimal Wireless Coverage," *IEEE Commun. Lett.,* vol. 20, no. 8, pp. 1647–1650, Aug. 2016. 69.5 (2021): 3352-3366.

[17] N. Babu, C. B. Papadias and P. Popovski, "Energy-Efficient 3D Deployment of Aerial Access Points in a UAV Communication System," *IEEE Commun. Lett.*, vol. 24, no. 12, pp. 2883-2887, Dec. 2020.

[18] J. Sun and C. Masouros, "Deployment Strategies of Multiple Aerial BSs for User Coverage and Power Efficiency Maximization," *IEEE Trans. Commun.,* vol. 67, no. 4, pp. 2981–2994, Apr. 2019.

[19] Valiulahi, Iman, and Christos Masouros. "Multi-UAV Deployment for Throughput Maximization in the Presence of Co-Channel Interference," *IEEE Internet of Things Journal* 8.5 (2020): 3605-3618.

[20] Zhou X, Yan S, Shu F, Chen R, Li J, "UAV-Enabled Covert Wireless Data Collection," *IEEE Journal on Selected Areas in Commun. 2021 Jun 14;39(11):*3348-62.

[21] Yan S, Hanly SV, Collings IB, "Optimal Transmit Power and Flying Location for UAV Covert Wireless Communications," *IEEE Journal on Selected Areas in Commun. 2021 Jun 16;39(11):*3321-33.

[22] N. Zhao et al., "Joint Trajectory and Precoding Optimization for UAV-Assisted NOMA Networks," *IEEE Trans. on Commun.,* vol. 67, no. 5, pp. 3723-3735, May 2019.

[23] Zeng Y, Xu J, Zhang R. "Energy Minimization for Wireless Communication with Rotary-Wing UAV," *IEEE Transactions on Wireless Commun.*, 2019 Mar 8;18(4):2329-45.

[24] X. Jing, J. Sun and C. Masouros, "Energy Aware Trajectory Optimization for Aerial Base Stations," *IEEE Transactions on Communications,* vol. 69, no. 5, pp. 3352-3366, May 2021.

[25] N. Babu, M. Virgili, C. B. Papadias, P. Popovski and A. J. Forsyth, "Cost- and Energy-Efficient Aerial Communication Networks With Interleaved Hovering and Flying," *IEEE Trans. on Vehicular Technology,* vol. 70, no. 9, pp. 9077-9087, Sept. 2021.

[26] Mazaherifar A, Mostafavi S, "UAV Placement and Trajectory Design Optimization: A Survey," in *Wireless Personal Commun. 2021 Dec* 1:1-20.

[27] J. Holis and P. Pechac, "Elevation Dependent Shadowing Model for Mobile Communications via High Altitude Platforms in Built-Up Areas," *IEEE Trans. on Antennas and Propagation, vol. 56, no. 4, pp. 1078-1084, April 2008.*

[28] P. Yang, X. Xi, T. Q. S. Quek, J. Chen and X. Cao, "Power Control for a URLLC-Enabled UAV System Incorporated With DNN-Based Channel Estimation," *IEEE Wireless Commun. Lett., vol. 10, no. 5, pp. 1018-1022, May 2021.*

[29] Rokrok E, Javidsharifi M, Pourroshanfekr H, Javidsharifi B, "Adaptive Nonlinear Control Scheme for Three-Phase Grid-Connected PV Central Inverters," in *Proceedings of 29th Int. Power System Conf. (PSC), Terhan, Iran,* 27 October 2014; pp. 1-7.

[30] "Travelling Salesman Problem", availabe online at `https://www.mathworks.com/matlabcentral/fileexchange/46629-tsp-zip`.

[31] Sonia Leva, Alfredo Nespoli, Silvia Pretto, Marco Mussetta, Emanuele Ogliari, September 23, 2020, "Photovoltaic Power and Weather Parameters," in *IEEE Dataport, doi: https://dx.doi.org/10.21227/42v0-jz14.*

[32] Javidsharifi, Mahshid, et al, "Effect of Battery Degradation on the Probabilistic Optimal Operation of Renewable-Based Microgrids," *Electricity 2022, 3, 53-74.*

[33] Berliner, H. J. "An Examination of Brute Force Intelligence," in *In IJCAI* (pp. 581-587), 1981, August.

[34] A. Goldsmith, Wireless communications. Cambridge university press, 2005.

Paper H

Sustainable Wireless Services with UAV Swarms Tailored to Renewable Energy Sources

Igor Donevski, Marco Virgili, Nithin Babu, Jimmy Jessen Nielsen, Andrew Forsyth, Constantinos B. Papadias, and Petar Popovski

Under review in
IEEE Transactions on Smart Grid.

The layout has been revised.

Abstract

Unmanned Aerial Vehicle (UAV) swarms are often required in off-grid scenarios, and require balancing of the energy expenditure. Considering a main battery fed from two renewable sources, wind and solar, we scale such a system based on the financial budget, environmental characteristics, and seasonal variations. We maximize the cost efficiency of coverage in the area as a combinatorial optimization problem with a multivariate energy generation system under a non-convex criteria. We devised a customized algorithm by lowering the processing complexity and reducing the solution space through sampling. Evaluation is done with real-world data on wind, solar energy, traffic load, and vendor provided prices. Since UAV hovering becomes more laborious in strong winds, the energy source is correlated with the energy expenditure. Therefore, best results were achieved in areas with mild wind and reliable solar irradiation, while areas with strong winds and unreliable solar intensity require higher CAPEX.

1 Introduction

The use of UAVs, in particular the multi-copter drones, has been praised for the ability of providing modular, adaptable and scalable wireless communications services as they can easily be redeployed, target specific users and load balance existing cellular architectures, [1, 2]. However, safety, privacy and noise concerns are diminishing the vision of having UAV-mounted small base stations (UAVSBSs) as a replacement to traditional base stations. In addition, multi-copter UAVs are generally extremely power hungry, and require a lot of energy (usually stored in the form of a lithium battery) in order to maintain their aerial position. Due to this, UAVSBSs cannot be considered as a viable alternative for upgrading the local cellular infrastructure. Nonetheless, UAVSBSs are crucial in scenarios that result in service outages such as war-torn or disaster struck areas [3, 4] and traffic surges in weakly serviced areas [5]. In these cases, it should be expected that the existing infrastructure is unable to support the energy requirements of the UAVSBS system. Moreover, to satisfy the service constraints of the area, that generally vary during the day [6], the deployments require multiple UAVs (a.k.a. swarm). Thus, the goal of this work is to provide a financially feasible deployment of a UAV swarm to enable long-term persistent (uninterrupted) communications in an area. Moreover, we maximize the coverage area in off-grid areas that rely entirely on renewable energy.

1.1 Literature Overview

The effects of using UAVSBSs that are positioned to offer service to ground customers has already been well investigated in [2, 7–14]. In [7–9] the focus is on improving spectral efficiency when exploiting the temporal and spatial mobility of UAVs for servicing

user hotspots. In our previous works [10, 11], we demonstrated the benefit of horizontally positioning a standalone UAVSBS, equipped with a tilting directional antenna. Moreover, the work in [12] focused on the energy efficiency for UAVSBS deployment, while the authors in [15] and [16] studied the problem of placement optimization of a single cell and interference-limited multi UAVSBS deployments, respectively. While the aforementioned works are concerned with optimizing deployment locations of the UAVs once they are in the air, they generally ignore the problem of short service durations.

Ever since the proliferation of drones into the mass market there has been a strive towards persistent UAV services [17, 18] with several methods. The most prominent method assumes automated battery swapping [19]. In [20] the authors solve the optimal trajectory for patrolling UAVs that exactly exploit the battery swapping mechanism that is connected to the grid mains. In [21] the authors consider a mothership-like UAV that houses and orchestrates the deployment of a swarm of smaller UAVs, where the mothership ensures that the energy requirements for the entire system is satisfied. While such mothership systems are genuinely useful for achieving unlimited mobility, the creation of one is complex and assume technical innovation on several fronts which would become very costly to implement. On the other hand, the authors of [22] consider a ground based central unit that serves as a backbone to the UAVs and has solar panels to manage the energy requirements on the ground. In [23] the authors propose a cost efficient UAV system for data harvesting from IoT systems. In [24] we previously investigated the optimal arrangement for UAVs that need to provide persistent service by interleaved recharging at a ground station.

We note that per [2], UAV Base Stations are able to alleviate capital and operating expenditures (CAPEX & OPEX) of telecom operators up to 52% and 42% respectively, through only diminishing site management costs and complexity that can become particularly overwhelming in developing countries. For such investigations to be applicable to disaster struck, remote, or underdeveloped areas, we focus on works that involve dimensioning sustainable energy generation systems for wireless communications. As such, the authors of [25] and [26] proposed alleviating the energy requirements of multi-tier cellular implementations supported with renewable energy. The work of [27] comes the closest to our goal of providing cellular connectivity in rural zones. Moreover, the authors consider an architecture composed of UAV-based BSs to provide cellular coverage, ground sites to connect the UAVs with the rest of the network, Solar Panels (SPs) and batteries to recharge the UAVs. And finally, the work [28] follows a similar groundwork for a mothership-orchestrated UAV swarm for wireless communications, where the goal is to minimize the overall weighted distance traveled by the mothership when the UAVs come back to the housing area to recharge.

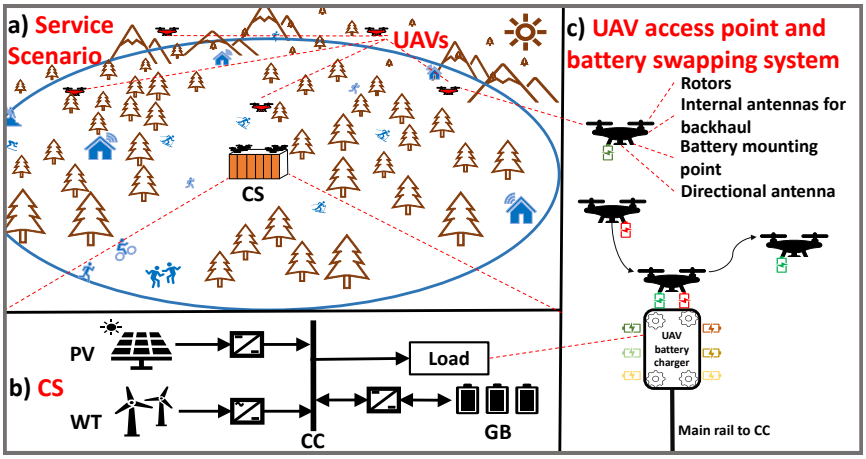

Fig. H.1: Schematic of the energy system at the central station (CS) that consists of wind turbines (WT), photovoltaic (PV) panels, a central circuit (CC), ground battery (GB) and a UAV battery charger (UAVBC) that represents the load. The service scenario illustrates a deployment in a mountainous region.

1.2 Off-grid Redeployable UAV Communications System

The communications system that we propose is shown in Fig. H.1 and inspired by [27]. Though in Fig. H.1 it is illustrated in a remote mountainous region its utility extends to rural, suburban and low-rise urban settings, especially if such areas have an ongoing humanitarian crisis. It is envisioned to provide persistent service by deploying a central station (CS) that coordinates and manages the UAV deployment process, while it also serves as a recharging station for the UAVs. Upon placing the CS, a swarm of UAVs is deployed, and position themselves in designated hovering points to provide the desired service rate to the whole area. When a UAV nearly depletes its battery, it flies back to the CS for recharging. As in [29], we consider an automatic battery swapping mechanism that replaces the depleted battery for a full one, after which the UAV can immediately fly back to the designated hovering position.

To ensure a long-term persistent deployment of the service-providing UAVs, the system needs to compensate the power requirements for operation of the entire system. As Illustrated in Fig. H.1, our considered implementation of a CS has five energy modules. The wind turbine (WT) and photovoltaic (PV) panels generate energy to be stored into a ground battery (GB) that acts as a central energy storage module. The system is interconnected by a central circuit (CC) module that directly links the load from the energy management components. The load of the system is an automatic UAV battery charger (UAVBC) that charges the hot-swappable UAV batteries, where the system automatically queues a full battery to be swapped for the depleted one on a landed UAV. Finally, we assume that the CS acts as a sink/middlehaul for the wireless service that

the UAVs offer, and that the backhaul link is overprovisioned and thus not included in the analysis that follows. This is achievable with the new integration of low earth orbit (LEO) satellites [30]. Finally, we note that the system is sensitive to stormy weather which would cause a total outage altogether.

1.3 Main Contributions & Paper Outline

This work provides a fresh perspective on UAV swarm implementations for persistent wireless service such as:

- We consider long-term standalone deployment of UAVs for remote areas by having a realistic model of the impact of wind intensity on the energy consumption of the UAVs. As such, we consider the hourly wind intensity as a function of elevation and terrain roughness, and account for its impact on long duration UAV hovering.
- We model the system as totally self-sustainable and including PV- and WT-based energy generation modules, where the WTs have the capability of offsetting the UAV's energy expenditure due to wind strength.
- We formulate the problem as CAPEX efficient coverage area maximization, which is a multi-variate optimization problem for solving the load profile based on real world data, where the energy generation comes from two sources, wind and solar, that are also modeled on real world data.
- We propose a computationally light algorithm that uses greedy sampling and binary search to find the optimal configuration that is a combination of wind turbines, PV panels, cells in the ground battery, and UAVs in the swarm.

The rest of the paper is organized in the following manner. In Section 2 we describe the communications service environment, the UAV orchestration, and the energy cost of satisfying the aforementioned service. This is followed by a detailed elaboration of the energy generation and management system in Section 3. We define both the formal problem and the proposed algorithmic solution in Section 4. The simulation analysis, and the results of the implementation are contained in Section 5. Finally, in Section 6 the work is summarized and future directions are drawn.

2 Modeling UAV Service and Energy

The coverage area (CA), a circle with radius $D_{\max}$, contains an arbitrary number of users that we model in terms of zonal datarate density (ZDD). The ZDD is defined as λ_h which represents the requested datarate per unit of area, for hour of the day $h = 1, 2...24$, that is uniform for the entire area and can be described in unit Mbps/m^2. The goal for modelling the traffic in terms of area instead of per user is to properly scale

it for larger time-lengths in the order of hours such as in [6, 31], and to easily adapt the traffic requirements depending on the residency type of the area in question. Note that we do not consider different rates between days of the year $i = 1, 2, ..365$, since such a metric is strongly dependent on the area in question and such data is private and difficult to request in advance of a deployment. Therefore, we consider the data requested per unit of area as a random variable for a stochastic process with expected data rate of λ_h. Moreover, since the goal of the work is coverage maximization through $D_{\max}$, ZDD helps us scale the traffic demand for different $D_{\max}$, without having to assume a stochastic point process. As a result, the minimum datarate requested for the entire CA $R_{h,\min}$, for hour h, scales with its area as:

$$R_{h,\min}(D_{\max}) = \lambda_h \pi D_{\max}^2. \tag{H.1}$$

Considering a fleet of available drones n_{UAV}, a swarm size of $k_h \leq n_{\text{UAV}}$ UAVs is released so that each UAV j is given an equal amount of area to serve with rate $R(k_h, D_{\max})$. We can thus linearly scale the traffic load on each UAV with the swarm size, so that it satisfies:

$$\frac{R_{h,\min}(D_{\max})}{k_h} \leq R(k_h, D_{\max}) \ \forall h, \tag{H.2}$$

under the condition that $\max_h (R_{h,\min}) \leq n_{\text{UAV}} \cdot R(n_{\text{UAV}}, D_{\max})$ is satisfied. We note that the serviced data rate is a function of both k_h and $D_{\max}$. This is due to the radius of coverage for each UAV $0 < D(k_h, D_{\max}) \leq D_{\max}$ being dependent on the number of UAVs we deploy for the entire hour h as well as the size of the cell that the UAVs need to cover.

2.1 UAV Hovering Locations

The coverage region for each UAV in the swarm is a circle of radius $D(k_h, D_{\max})$ which is derived from a packing algorithm [32]. In order to avoid leaving any part of the area without service, the circles of individual UAV coverage are packed in an overlapping manner that fully covers the CA. Making each UAV $j \in \{1, 2, .. k_h\}$ equally relevant, we assign the same radius $D(k_h, D_{\max}) = D_j \ \forall j$. Thus, as per the packing provided in [32], the radius $D(k_h, D_{\max})$ occupies discrete values and is given in Table H.1.

Setting the center of the CA as the center of our coordinate system (0,0), the centers of the $k_h = \{3, 4, 5, 6\}$ circles are located at $\{\mathbf{p}_j(k_h, D_{\max}) = (x_j, y_j)\}$ where,

$$x_j = D(k_h, D_{\max}) \cos\left(\frac{2\pi(j-1)}{k_h - 1}\right) \ \forall j \in \{1, 2, ...k_h\}, \tag{H.3}$$

$$y_j = D(k_h, D_{\max}) \sin\left(\frac{2\pi(j-1)}{k_h - 1}\right) \ \forall j \in \{1, 2, ...k_h\}. \tag{H.4}$$

For the case of 7, the centers of the smaller circles of radius $D(7, D_{\max})$ that cover the

Table H.1: Packing Patterns [32].

k_h	$D(k_h, D_{\max})$
1	$D_{\max}$
2	$D_{\max}$
3	$\frac{D_{\max}}{1.1547}$
4	$\frac{D_{\max}}{\sqrt{2}}$
5	$\frac{D_{\max}}{1.641}$
6	$\frac{D_{\max}}{1.7988}$
7	$\frac{D_{\max}}{2}$
$k_h = 8, 9, 10$	$\frac{D_{\max}}{1+2\cos\left(\frac{2\pi}{k_h-1}\right)}$

region have coordinates $\{\mathbf{p}_j(7, D_{\max}) = (x_j, y_j)\}$ where,

$$x_j = D(7, D_{\max})\sqrt{3}\cos(\frac{2\pi(j-1)}{6}) \; \forall \, j \in \{1, 2, ...6\}\,, \tag{H.5}$$

$$y_j = D(7, D_{\max})\sqrt{3}\sin(\frac{2\pi(j-1)}{6}) \; \forall \, j \in \{1, 2, ...6\}\,, \tag{H.6}$$

$$(x_7, y_7) = (0, 0). \tag{H.7}$$

As such, the horizontal distance from the CS can be calculated as $d_j(k_h, D_{\max}) = \sqrt{x_j^2 + y_j^2}$. Finally, for $k_h = \{8, 9, 10\}$, one circle is concentric with the region and the centers of the other circles are situated in the vertices of a regular $(n-1)$-gon at a distance of $d_j(k_h) = 2\sin(\frac{\pi}{(j-1)})$ for $j \in \{1, 2, ...(k_h - 1)\}$ from the center of the region. The circle packing formations are shown in Fig. H.2. In order to achieve coverage regions with radius $D(k_h, D_{\max})$ we adjust the UAV hovering height $H(k_h, D_{\max})$, which is dependent on the propagation environment in the CA and it is covered below.

2.2 Propagation Characteristics with a Directional Antenna

UAV based communication links discriminate two propagation groups, users with direct line-of-sight (LoS) or no-LoS (NLoS). As such, the path loss ℓ is a sum of the free space path loss (FSPL) and the additional large-scale shadowing coefficient for each one of the propagation groups. The mean large scale fading coefficients for each propagation group are η_{LoS} and η_{NLoS} and come as a consequence of the typology's features [13]. Thus, the path loss between a user at horizontal distance D and a UAV with altitude

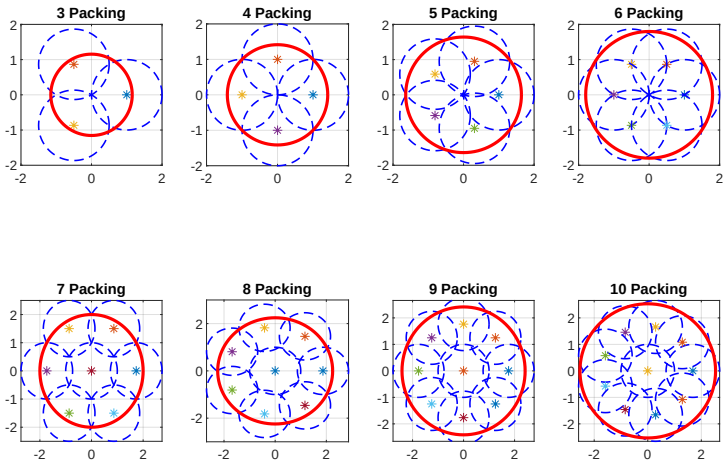

Fig. H.2: Different packing patterns used in this paper. The blue circles represent UAV coverage regions of radius $D(k_h, D_{\max})$ whereas the red circles represent the CA with radius $D_{\max}$.

H can be expressed as:

$$\ell_{\text{LoS}} = -10\log(G_{\text{t}}) + 20\log(\sqrt{D^2 + H^2}) + C + \eta_{\text{LoS}}, \tag{H.8}$$

$$\ell_{\text{NLoS}} = -10\log(G_{\text{t}}) + 20\log(\sqrt{D^2 + H^2}) + C + \eta_{\text{NLoS}}, \tag{H.9}$$

where, G_{t} is the antenna gain, log is a shortened version of the common logarithm $\log_{10}$, and the term C is a substitute for the carrier frequency f_{c} constant in FSPL $C = 20\log\left(\frac{f_{\text{c}} 4\pi}{c}\right)$. Finally, averaging the two propagation groups by the probability of a LoS occurring gives:

$$10\log[L] = \ell_{\text{LoS}} \cdot P_{\text{LoS}} \tag{H.10}$$

$$+ \ell_{\text{NLoS}} \cdot P_{\text{NLoS}} \tag{H.11}$$

$$= P_{\text{LoS}}(\eta_{\text{LoS}} - \eta_{\text{NLoS}}) + \ell_{\text{NLoS}}, \tag{H.12}$$

where the LoS probability is given by the s-curve model [14]:

$$P_{\text{LoS}} = \frac{1}{1 + a\exp(-b[\arctan\left(\frac{H}{D}\right) - a])}, \tag{H.13}$$

where a and b are constants dependent on the topological setting.

Each UAV has a downwards facing antenna with gain $G_{\text{t}} = A_{\text{eff}} 10\log(G_{\text{I}})$, where the ideal conical antenna has gain:

$$G_{\text{I}} = \frac{2}{1 - \sin\left(\theta\frac{\pi}{180}\right)}, \tag{H.14}$$

where $\theta = \arctan(\frac{H}{D})$ is the elevation angle at the cell edge and A_{eff} is the antennas' effectiveness in fitting an ideal conical beamwidth. This results in the final path loss expression:

$$10\log(L) = \frac{\eta_{\text{LoS}} - \eta_{\text{NLoS}}}{1 + a\exp\{-b[\theta - a]\}} + 20\log\left(\sqrt{D^2 + H^2}\right) - A_{\text{eff}} 10\log\left[\frac{2}{1 - \sin(\theta\frac{\pi}{180})}\right] + C + \eta_{\text{NLoS}}. \quad \text{(H.15)}$$

In order for all the users within the area with radius D to be served, we optimize the elevation angle of $\theta = \arctan(\frac{H}{D})$ from the perspective of a user located exactly at distance D. Thus, as in [10] we can extract an optimal ratio of D and H, through the angle θ, by solving:

$$0 = \frac{\pi\tan(\theta\frac{\pi}{180})}{9\log(10)} + \frac{a\,b(\eta_{\text{LoS}} - \eta_{\text{NLoS}})\exp(-b(\theta - a))}{a\exp(-b(\theta - a) + 1)^2} - A_{\text{eff}}\frac{\pi\cos(\theta\frac{\pi}{180})}{18\log(10)(1 - \sin(\theta\frac{\pi}{180}))}. \quad \text{(H.16)}$$

This makes it easy to calculate the hovering height as $H = D\tan(\theta)$, which formulates the pathloss only as a function of the horizontal distance $L(D)$. Finally, the serving rate for a user at distance $D = D(k_h, D_{\max})$ becomes:

$$R(k_h, D_{\max}) = B\log_2\left[1 + \frac{P_{\text{t}}}{BN_0 L(D(k_h, D_{\max}))}\right], \quad \text{(H.17)}$$

where P_{t} is the transmission power that is assumed to be identical at both user and UAV side, while N_0 is the noise spectral density linearly scaling the noise with the channel bandwidth B. Since the packing is done in an overlapping manner, we must account for a total available spectrum of $B_{\text{tot}} \geq 3 \cdot B$ to avoid inter-UAV-cell interference. Finally, we note that even though the coverage circles of two UAVs using the same bandwidth may overlap, such overlap occurs outside both coverage regions, and is thus not harmful towards the spectrum reuse in the packing algorithm, as it can be seen in Fig. H.2.

2.3 UAV Power Consumption Model

Most of the UAV's power consumption is absorbed by its rotors, while the power dedicated to the communications is negligible. Initially, the UAV ascends vertically with a velocity of v_{c} to the designated height $H(k_h, D_{\max})$, and flies horizontally with a velocity of v_{hfly} to reach position $\mathbf{p}_j(k_h, D_{\max})$ that is at horizontal distance $d_j(k_h, D_{\max})$. Once the UAV reaches the hovering spot, it maintains its position for a designated amount of time, and then returns to the CS. Since the UAV may have to counteract the wind speed

Table H.2: UAV Flight Parameters.

Label	Definition	Value
W	Weight of the UAV in Newton	23.84 N
N_{R}	Number of rotors	4
F_{n}	Upward thrust by the n^{th} rotor	-
v_{hfly}	UAV's horizontal flying velocity	-
v_{tip}	Tip speed of the rotor	102 m/s
A_{f}	Fuselage area	0.038 m^2
$\rho(H(k_h, D_{\max}))$	Air density	-
C_{D}	Drag Co-efficient	0.9
A_{r}	Rotor disc area	0.06 m^2
Δ	Profile drag coefficient	0.002
s	Rotor solidity	0.05

$v_{h,i}^{\mathrm{wind}}$, for hour h at day i to achieve net zero speed, the hovering process is remarked as flying horizontally with non-zero velocity. Here we differentiate the wind intensity with regards to the daily variations since such data is readily available, and has very strict seasons. We also expect that the horizontal speed required to counteract the wind speed increases with altitude [33]:

$$v_{\mathrm{hov},h,i} = v_{h,i}^{\mathrm{wind}} \left[\frac{H(k_h, D_{\max})}{H_0} \right]^{E_{\mathrm{w}}}, \tag{H.18}$$

where H_0 is the measurement altitude of the wind velocity $v_{h,i}^{\mathrm{wind}}$, and E_{w} is the empirically measured indicator derived from the roughness of the surface in the area. Therefore, we note that sometimes the maximum tolerable wind speed is exceeded, forcing all active UAVs to return to the CS, or to decrease their flight altitude until the wind speed is within a tolerable range. Finally, the UAV descends with the same (but negative) vertical speed as it ascended v_{c} to represent negative velocity with regards to the coordinate system.

All the parameters used in the following equations are defined in Table. H.2, and with the goal to reduce equation clutter swarm size dependent variables $H(k_h, D_{\max})$ and $d_j(k_h, D_{\max})$ are reduced to H and d_j respectively. The power consumed by the UAV when flying horizontally with speed v is derived using the axial momentum theory, while assuming identical rotors [24], and is given by,

$$P_{\mathrm{hfly}}(v) = \underbrace{N_{\mathrm{R}} P_{\mathrm{b}} \left(1 + \frac{3v^2}{v_{\mathrm{tip}}^2} \right)}_{P_{\mathrm{blade}}} + \underbrace{\frac{1}{2} C_{\mathrm{D}} A_{\mathrm{f}} \rho(H) v^3}_{P_{\mathrm{fuselage}}}$$

$$+ \underbrace{W\left(\sqrt{\frac{W^2}{4N_{\mathrm{R}}^2\rho^2(H)A_{\mathrm{r}}^2}+\frac{v^4}{4}}-\frac{v^2}{2}\right)^{\frac{1}{2}}}_{P_{\mathrm{induce}}}, \tag{H.19}$$

where $P_{\mathrm{b}} = \frac{\Delta}{8}\rho(H)sA_{\mathrm{r}}v_{\mathrm{tip}}^3$, $\rho(H) = (1 - 2.2558.10^{-5}H)^{4.2577}$. P_{blade} and P_{fuselage} are the powers required to overcome the profile drag forces of the rotor blades and the fuselage of the aerial vehicle that oppose its forward movement, respectively, while P_{induce} represents the power required to lift the payload.

The power required by the aerial vehicle to climb vertically with a rate v_{c} m/s is expressed as,

$$P_{\mathrm{vfly}}(v_{\mathrm{c}}) = \frac{W}{2}\left(v_{\mathrm{c}}+\sqrt{v_{\mathrm{c}}^2+\frac{2W}{N_{\mathrm{R}}\rho(H)A_{\mathrm{r}}}}\right)+N_{\mathrm{R}}P_{\mathrm{b}}. \tag{H.20}$$

The energy consumption for the entire flight of UAV j occuring at hour h, day i, is $E_{j,h,i}(k_h, D_{\max})$ and can be thus segmented into the three parts, ascent, hovering, and descent:

$$\begin{aligned} E_{j,h,i}(k_h, D_{\max}) = & \underbrace{P_{\mathrm{vfly}}(v_{\mathrm{c}})\frac{H}{v_{\mathrm{c}}}+P_{\mathrm{hfly}}(v_{\mathrm{hfly}})\frac{d_j}{v_{\mathrm{hfly}}}}_{\text{ascent}} \\ & + \underbrace{P_{\mathrm{vfly}}(-v_{\mathrm{c}})\frac{H}{v_{\mathrm{c}}}+P_{\mathrm{hfly}}(v_{\mathrm{hfly}})\frac{d_j}{v_{\mathrm{hfly}}}}_{\text{descent}} \\ & + \underbrace{P_{\mathrm{hfly}}(v_{\mathrm{hov},h,i})\cdot\left(\tau_{\mathrm{fly}}-2\left(\frac{H}{v_{\mathrm{c}}}+\frac{d_j}{v_{\mathrm{hfly}}}\right)\right)}_{\text{hover}}, \end{aligned} \tag{H.21}$$

where τ_{fly} is the designated flight time that the UAV must complete. For convenience, we use a flight duration τ_{fly} of half an hour, which is reasonable for state-of-the-art UAV models, since our wind, solar and traffic data are quantized at each hour of the day. This means that at hour h on day i the UAV consumes a total energy of:

$$E_{\mathrm{UAVs},h,i}(k_h) = \frac{1}{\tau_{\mathrm{fly}}}\sum_{j=1}^{k_h}E_{j,h,i}(k_h). \tag{H.22}$$

Finally, we note that some of the flight time is spent on flying to and back from designated hovering positions. The UAVs are made to hover instead of glide/course in order to maintain stable coverage regions and avoid drastically increasing user handover

overhead. In order to avoid service outage in such cases, we assume that the process of positioning occurs at different times for each UAV, which also serves as additional leeway in the duration of the process of battery swapping. Such system needs to account for one spare UAV to afford the mobility.

3 Energy Generation and Management at the Central Unit

Since the CS is not connected to the electrical grid, it relies on two sources of energy: wind harvested by WTs and solar harvested by PV panels. The productivity of each source is tied to the geographical location of the CS and the time of year. Therefore, we use measurement-driven data provided by the European Commision's Photovoltaic Geographical Information System[1] to extract the annual measurements, sampled per hour. Moreover, we expect solar irradiation and wind speed to be inversely correlated, as per the study in [34]. The electricity generated and stored in this system is proportional to its size, and therefore financial budget. The service availability detailed in the previous section thus becomes a function of the CAPEX budget, which is spent on energy generation and storage systems for the CS.

Load

Once the UAV lands on the CS, after spending τ_{fly} time in the air, it releases its depleted battery through an automated battery exchange system and receives a new, fully charged one. The old battery is then charged until full, when it becomes ready to be swapped back into a UAV. Thus, each recharge cycle duration is driven by the supported charging rate of each UAV battery and its size as:

$$\tau_{\text{charge}} = \frac{C_{\text{bat}}}{P_{\text{charge}}}, \tag{H.23}$$

where C_{bat} is the battery capacity, and P_{charge} is the charger power. These are lithium polymer (commonly referred as LiPo) batteries, which have a predominantly linear charging behaviour [35]. Therefore, the power drawn by a single battery unit is assumed to be constant, and the overall load profile will look like a step function directly dependent on the number of batteries recharging at the same time. The time required for each battery to be guaranteed operational for a full half hour must satisfy:

$$\max\left(E_{j,h,i}(k_h, D_{\max})\right) \leq C_{\text{bat}} \quad \forall\, j, h, i. \tag{H.24}$$

Since carrying extra weight in the form of extra battery capacity is unnecessary, we aim to have the lowest C_{bat} possible that satisfies the boundary with some margin.

[1] https://re.jrc.ec.europa.eu/pvg_tools/en/#MR

Therefore, the number of UAV batteries per single UAV that are required by the system is defined by the $\tau_{\text{charge}}/\tau_{\text{fly}}$ ratio. The maximum number of UAV replaceable batteries is:

$$b_{\max} = \left\lceil n_{\text{UAV}} \left(\frac{\tau_{\text{charge}}}{\tau_{\text{fly}}} + 1 \right) \right\rceil . \tag{H.25}$$

It is essential for the price of spare batteries to be reflected in the purchasing price per UAV in the fleet. For this reason, we assume that the sufficient amount of batteries per UAV are purchased at the time of purchasing the UAVs.

PV

One of the energy generation units is represented by a set of photovoltaic (PV) panels placed in parallel, all of the same type [36] and with the same working conditions. All parameters used in these equations are summarized in Table H.3. Their behaviour is simulated using a simplified version of the 5 parameters model [37], which neglects the shunt resistance and allows to calculate the maximum power voltage (V_{m}) and current (I_{m}) provided at any irradiation (G^{irr}) and ambient temperature (T_{a}) conditions. This is made possible using the conservative assumption of a maximum power point tracker (MPPT) with average efficiency $\epsilon_{\text{MPPT}} = 95\%$ [38].

$$V_{\text{m},h,i} = V_{\text{m,ST}} - \beta \left(T_{\text{C},h,i} - T_{\text{ST}} \right) + V_{\text{t},h,i} \log \frac{G^{\text{irr}}_{h,i}}{G^{\text{irr}}_{\text{ST}}}, \tag{H.26}$$

$$V_{\text{t},h,i} = n_{\text{cells}} \frac{k_{\text{b}} n_{\text{I}} T_{\text{C},h,i}}{q}, \tag{H.27}$$

$$I_{\text{m},h,i} = I_{\text{m,ST}} \left(\frac{G^{\text{irr}}_{\text{ST}}}{G^{\text{irr}}_{h,i}} \right) + \alpha \left(T_{\text{C},h,i} - T_{C,\text{ST}} \right), \tag{H.28}$$

$$T_{\text{C},h,i} = T_{\text{a},h,i} + \frac{T_{\text{C,NOC}} - T_{\text{a,NOC}}}{G^{\text{irr}}_{\text{NOC}}} G^{\text{irr}}_{h,i}. \tag{H.29}$$

Knowing V_{m} and I_{m} from (H.26) and (H.28), as well as the cell temperature T_{C}, allows to calculate the output power as:

$$P_{\text{PV},h,i}(n_{\text{PV}}) = n_{\text{PV}} \cdot V_{\text{m},h,i} \cdot I_{\text{m},h,i} \cdot \epsilon_{\text{conv}} \cdot \epsilon_{\text{MPPT}}. \tag{H.30}$$

In the above equations, the subscript ST means standard test conditions ($G^{\text{irr}}_{\text{ST}} = 1000W/m^2$, $T_{\text{a,ST}} = 25°\text{C}$), whereas NOC stands for nominal operating conditions ($G^{\text{irr}}_{\text{NOC}} = 800\ \text{W/m}^2$, $T_{\text{a,NOC}} = 20°\text{C}$). The cell temperature at standard test conditions T_{ST}, was calculated using (H.29), but using $T_{\text{a,SC}}$ and $G^{\text{irr}}_{\text{ST}}$ instead of T_{a} and G. The list price for a single panel, pre-VAT, is €202 resulting in a PV system cost that scales linearly with the number of solar panels n_{PV}, as $F_{\text{PV}} = 202 \cdot n_{\text{PV}}$.

Table H.3: PV Parameters from [36].

Label	Definition	Value
α	Thermal coefficient of SC current	0.0474 %/°C
β	Thermal coefficient of OC voltage	-0.285 %/°C
ϵ_{conv}	Converter efficiency	95%
n_{cells}	Number of PV cells	60
n_{I}	Diode ideality factor	1.5
k_{b}	Boltzmann constant	$1.380649 \cdot 10^{-23}$ J/K
q	Electrical charge of an electron	$1.602176634 \cdot 10^{-19}$ C
$G^{\text{irr}}_{\text{NOC}}$	Irradiation at NOC	800 W/m^2
$G^{\text{irr}}_{\text{ST}}$	Irradiation at ST	1000 W/m^2
$I_{\text{m,ST}}$	Maximum power current at ST	8.85 A
$T_{\text{a,NOC}}$	Ambient temperature at NOC	20°C
$T_{\text{C,NOC}}$	Cell temperature at NOC	45°C
$T_{\text{C,ST}}$	Ambient temperature at ST	25°C
$V_{\text{m,ST}}$	Maximum power voltage at ST	31.8 V

Wind

The power output of a wind turbine is not calculated using an analytical model, but the interpolation of power curves found in the data sheet [39]. This choice is justified by the improved precision. The result is a series of linear segments that cover the non-integer values of velocity that are not provided in the data sheet, as shown with blue in Fig. H.3. Two types of wind turbines are considered and treated as distinct elements of the system:

- A vertical axis small WT with standard power output of 500W (unit cost $F_{\text{W500}} = €1,429.95$);
- A vertical axis medium WT with standard power output of 1kW (unit cost $F_{\text{W1000}} = €2,738.76$);

The list prices displayed above are pre-VAT, and were provided by Aeolos Wind Energy Ltd [39], and include a 9 m pole, as well as a rectifier and control system. Finally, the total power output of the system is scaled to:

$$P_{\text{WT},h,i}(n_{\text{W500}}, n_{\text{W1000}}) = \sum_a n_a P_a(v_{w,h,i}), \tag{H.31}$$

where $a \in \{\text{W500}, \text{W1000}\}$ depicts the type of the turbine out of the two suggested ones, and n_a is the number of turbines of each type, giving a total financial cost of $F_{\text{WT}} = \sum_a F_a \cdot n_a$.

Ground Battery

In order to provide continuous service, an energy storage system with capacity E_{cap} is needed. The load is powered by the generation elements when possible, with the storage

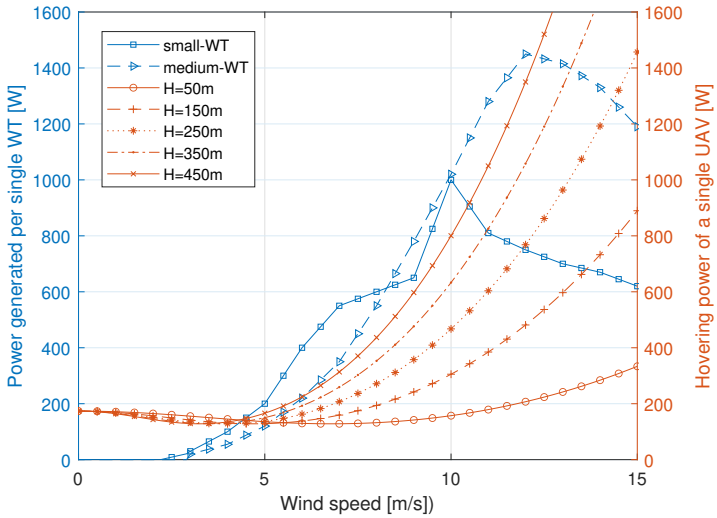

Fig. H.3: The wind power curves for two types of horizontal-axis WTs and UAV power consumption for hovering at different altitudes.

elements receiving any excess energy and providing back-up when the generation rate is too low. Therefore, at the end of the timeslot the net energy in the system is:

$$E_{\text{net},h,i} = \left[P_{\text{PV},h,i}(n_{\text{PV}}) + P_{\text{WT},h,i}(n_{\text{W500}}, n_{\text{W1000}})\right]\delta_t - E_{\text{UAVs},h,i}(k), \quad \text{(H.32)}$$

where $\delta_t = 2\tau_{\text{fly}}$ is the length of the time interval. Thus, in case of net positive or negative energy, the battery capacity at the next time step $E_{(h+1)\%24,i+(h+1)/24}$ (where % is the modulo operator and / is integer division) will increase or decrease by:

$$\min(E_{\text{cap}}(n_{\text{cell}}), E_{h,i} + \epsilon_{\text{b},h,i} E_{\text{net},h,i}), \quad \text{(H.33)}$$

with,

$$\epsilon_{\text{b},h,i} = \begin{cases} \epsilon_{\text{conv}}, & E_{\text{net},h,i} \geq 0; \\ \frac{1}{\epsilon_{\text{conv}}}, & E_{\text{net,h,i}} < 0; \end{cases} \quad \text{(H.34)}$$

where, E_{cap} is the total capacity of the battery as a function of the number of cells in the system n_{cell}, and $\epsilon_{\text{b},h,i}$ is the overall efficiency of the storage system, which, as shown in (H.34), can be lower or higher than 1, depending on whether the battery is being charged or discharged. The Li-ion battery cells are cylindrical LG MJ1, with unit cost of €5.75 and capacity of 12.6 Wh. The choice of such a small incremental step was made to improve the precision when the budget is low. A maximum ground battery (GB) capacity equal to $E_{\text{cap}} = 12.6 \cdot n_{\text{cell}}$ requires an expense of $F_{\text{E}} = 5.75 \cdot n_{\text{cell}}$.

4 Problem Definition and Methodology

The goal of this paper is to find the best value for providing as much coverage as possible in a geographical region, where the cost of the system comes from three separate sub-systems: the communications load, the energy generation, and the energy storage. Therefore, in this section we consider the problem of sizing the entire system as a combination of six variables: 1) number of communication UAVs in the fleet n_{UAV}; 2) number of 500W WTs n_{W500}; 3) number of 1kW WTs n_{W1000}; 4) number of PV panels n_{PV}; 5) number of battery cells in the GB n_{cell}; and 6) the radius of the circular CA $D_{\max}$. In order to evaluate the quality of the system, we use the area $\pi D_{\max}^2$, in which the guaranteed communications rate is satisfied, and the total upfront cost F for the system needed to provide that service.

Given that accurately calculating the total cost of the system is crucial, we note that the size and cost of the UAV swarm plays a big role. The price per UAV can vary vastly between manufacturers. However, since we use the DJI matrice 100/200 models as a reference, we take a reference price of €4000 per UAV, resulting in a total cost for UAV equipment of $F_{\mathrm{UAV}} = 4000 \cdot n_{\mathrm{UAV}}$. Moreover, this budget also covers spare batteries $b_{\max}$ that are required for battery swapping. Finally, to guarantee operability in case of defects in one of the UAVs in the fleet, and to offer better interleaving for battery swapping [24], there needs to be one spare UAV in the fleet $n_{\mathrm{UAV}} \geq 2$.

Since the eligibility of the entire system depends on the financial capital available for spending, we chose an optimization criteria that maximizes the coverage potential of the deployment normalized by the CAPEX of such a system.

$$
\begin{aligned}
\text{(H:P1)}: \quad & \underset{\{n_{\mathrm{PV}}, n_{\mathrm{W500}}, n_{\mathrm{W1000}}, n_{\mathrm{cell}}, n_{\mathrm{UAV}}, D_{\max}\}}{\text{maximize}} \quad \frac{\pi D_{\max}^2}{F}, \\
\text{s.t.} \quad & R(k_h, D_{\max}) \leq R_{\min,h}(D_{\max}), && \text{(H.35)} \\
& 11 \geq n_{\mathrm{UAV}} \geq 2, && \text{(H.36)} \\
& n_{\mathrm{UAV}} \geq \max_h (k_h) + 1, && \text{(H.37)} \\
& E_{h,i} \geq 0, && \text{(H.38)} \\
& F = F_{\mathrm{PV}} + F_{\mathrm{WT}} + F_{\mathrm{UAV}} + F_{\mathrm{E}} \leq F_{\max}, && \text{(H.39)} \\
& D_{\max} \geq D_{\mathrm{lb}}, && \text{(H.40)} \\
& D_{\max} \leq D_{\mathrm{ub}}. && \text{(H.41)}
\end{aligned}
$$

The (H:P1) objective function maximizes the coverage of the deployment normalized by its CAPEX; (H.35) guarantees the quality of service for the whole area; (H.36) maintains eligibility of the number of UAVs in the swarm; (H.37) defines the size of the swarm; (H.38) guarantees no system outage due to lack of energy; (H.39) defines the financial budget; (H.40) and (H.41) define the minimum and maximum required coverage. We note that if the problem is infeasible, the system is inadequate for the

application scenario. Finally, as per (H.35) and (H.38) the system does not account for any outage tolerance given the yearly evolution for sun, wind and data traffic for that location. This is because a mismanagement of energy allocation will not result in total outage but reduced QoS. Since our goal is to provide average service, accounting for outage would not be aimed towards constraining outage for that hour altogether, but a separate problem of QoS maximization instead of coverage maximization (i.e. missing the QoS target at nighttime or daytime should not be equally weighted). So, assuming non-average performance of the system, the system will still operate in best-effort QoS for that hour and equalize over the span of a whole year.

Given a fixed coverage area, the problem can be separated into two sub-problems that construct the CAPEX efficient coverage maximization and thus solution-searching can be done iteratively. The easier problem of the two is searching for the minimum energy load (MEL).

$$\begin{aligned}(\text{MEL}): \underset{\{k_h\}}{\text{minimize}} \quad & \min_{k_h} E_{\text{UAVs},h,i}(k_h, D_{\max}) \ \forall\, h, i, \\ \text{s.t.} \quad & R(k_h, D_{\max}) \leq R_{\min,h}(D_{\max}), && \text{(H.42)} \\ & 10 \geq k_h \geq 1. && \text{(H.43)}\end{aligned}$$

The MEL problem guarantees coverage for a specific area by satisfying the lower QoS bound. In this way, QoS is guaranteed for any user on the ground. Extracting the load profile of the entire system for a single area size is a constant complexity operation, since the number of hours and days for coverage are fixed. As such, the search of the entire space of eligible coverage areas has linear complexity where the complexity of that operation scales with the size of the eligible space between both boundaries (H.35) and (H.36).

The second sub-problem is finding the cheapest combination of energy elements (CCEE) W500 and W1000 WTs, PVs, and battery cells that satisfies the load profile. An exhaustive search on the CEEE problem has quartic complexity, which, summed with an exhaustively searched MEL, create an unreasonably complex problem. In addition, checking the MEL + CCEE sub-problems for every possible coverage multiplies the complexity by the size of the space $D_{\text{lb}} \leq D_{\max} \leq D_{\text{ub}}$. Therefore, it is necessary to find a more efficient way to solve (H:P1). We approach this by performing greedy sparse search to reduce the solution space, and simpler algorithms to find near-optimal solutions. Approximate methods, such as Genetic Algorithms implemented in [40], did not yield a satisfying performance and are thus left out of this work.

4.1 Greedy and Sparse Search (GSS) Algorithm

We define a search algorithm that uses sparse searching of coverage areas where maximum coverage per unit cost is likely to occur, and uncover a simplified way to solve CCEE. Specifically, we investigate the energy efficiency of annual coverage (EEAC) for

Algorithm H.1: GSS.

IMPORT: {MEL, BINARY-SEARCH, SAMPLE-mono, SAMPLE-2ndder , SAMPLE-comb}
Input: all-constants, all-data, D_{lb}, D_{ub} max_budget;
j=0
$D_{\max} = D_{\text{lb}}$
step_size=1;
while $D_{max} \leq D_{ub}$ *&&* $k_h \leq n_{UAV}$ **do**
    j=j+1
    ($\text{load}_{h,i}$ [j] ,F_{UAV} [j])
    =**MEL**($E_{\text{UAVs},h,i}(k_h, D_{\max})\ \forall h, i$)
    EEAC [j]= $\pi D^2_{\max}/\sum_{h,i} \text{load}_{h,i}$ [j]
    $D_{\max} = D_{\max}$ + step_size
SAMPLE-mono (EEAC,EEAC*):
$\text{EEAC}_{mnt} \leftarrow$ monotonic samples
SAMPLE-2ndder (EEAC_{mnt},EEAC*):
$D_{\text{max\_sparse}}, \text{addr} \leftarrow$ positive 2^{nd} derivatives
j=0
for D_{max} **in** D_{max_sparse} **do**
    j=j+1
    $\text{load}_{h,i} = \text{load}_{h,i}$ [addr[j]]
    $F_{\text{UAV}} = F_{\text{UAV}}$ [addr[j]]
    $F_{\text{comb}} = 0$
    $F =$ max_budget
    solutions = []
    flag==True
    while *flag==True* **do**
        $(n_{\text{PV}}, n_{\text{W500}}, n_{\text{W1000}})$, flag $\leftarrow$ **SAMPLE-comb**
        $F_{\text{comb}} = F_{\text{PV}} + F_{\text{WT}} + F_{\text{UAV}}$
        $n_{\text{cell}} = \lfloor (F - F_{\text{comb}})/5.75 \rfloor$
        if $E_{h,i}(n_{cell}, n_{PV}, n_{W500}, n_{W1000}, load) \geq 0$ **then**
            BINARY-SEARCH$_{\text{minimize}}$ n_{cell} **s.t.**
              $E_{h,i}(n_{\text{cell}}, n_{\text{PV}}, n_{\text{W500}}, n_{\text{W1000}}, \text{load}) \geq 0$
            $F_{\text{comb}} = F_{\text{PV}} + F_{\text{WT}} + F_{\text{UAV}} + F_{\text{E}}$
            APPEND $(D_{\max}, n_{\text{cell}}, n_{\text{PV}}, n_{\text{W500}}, n_{\text{W1000}}, n_{\text{UAV}}, F_{\text{comb}})$
            TO solutions
            $F = F_{\text{comb}}$
    fin_sols[j] = $\min_{F_{\text{comb}}}$(solutions)
Output: fin_sols

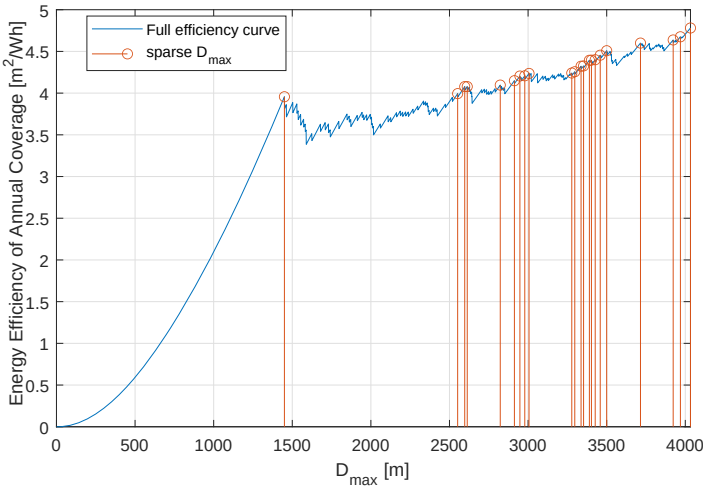

Fig. H.4: EEAC for servicing coverage area, at a suburban/remote setting, in the presence of weak wind with expected velocity of 3.6 m/s, overlay.

each size of coverage area as a proxy-heuristic metric:

$$\text{EEAC} = \frac{\pi D_{\max}^2}{\sum_{h,i} E_{\text{UAVS},h,i}}, \tag{H.44}$$

where $E_{\text{UAVS},h,i}$ is given by the MEL problem. Looking at Fig. H.4, it is noticeable that EEAC is not a monotonic nor a convex function of the coverage area, but it has an increasing trend nonetheless. Therefore, it is convenient to sparsely search for a solution where the coverage per energy efficiency is improving, and drop the cases where an increase in the area does not yield an improvement in the efficiency. Furthermore, we can use a greedy approach to shrink the number of samples that will be searched for optimal combinations to the ones that offer the best improvement with regards to the last sample. Thus we select only the samples whose second order derivative is larger than zero. In this way we still solve the MEL problem for the whole $D_{\text{lb}} \leq D_{\max} \leq D_{\text{ub}}$ space beforehand with the goal of reducing the search space for the multi-variate CCEE sub-problem by a significant factor ranging between 100-1000, depending on the scenario we investigate.

The CCEE problem is harder to simplify. However, we can exploit the fact that the leftover budget can be dedicated to two different purposes: energy generation and storage. We can easily reduce the complexity of searching the viability of storage once we have sufficient energy generation supporting the system. Thus, we decrease the dimensionality of the space by increasing the budget until battery storage becomes relevant, i.e. the power generation profile is able to keep up with the load profile. And since we are looking to minimize the financial cost, the first eligible solution where

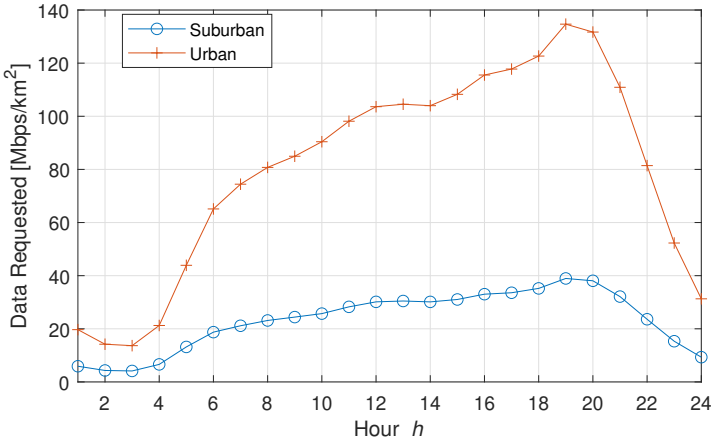

Fig. H.5: Daily evolution of traffic data requested.

battery storage becomes relevant becomes our new and smaller space. A simplified representation of the algorithm is shown in Alg. H.1.

The GSS approach guarantees finding the global minimum for the combination of WTs, PVs, cells, and n_{UAV} given a coverage radius of $D_{\max}$. It however does not guarantee to always find the global maximum for the coverage area due to the sampling of $D_{\max}$. Nonetheless, GSS managed to find the global optimum for all the scenarios that we tested.

5 Numerical Results and Case Analysis

In order to investigate the feasibility of the system, we perform an analysis onto several locations for different deployment scenarios. Although we aim for a realistic representation of a period spanning seasons or years, the data for the traffic requested by the local population is only reflected on a daily cycle. This is due to the unavailability of the sensitive data, especially spanning different locations across different countries. Therefore, we follow the hourly average of incoming traffic λ_h as presented in [6, 31] and shown in Fig. H.5. Moreover, we distinguish two possible types of areas that may need coverage: Suburban and Urban. These have the $(a, b, \eta^{\text{LoS}}, \eta^{\text{NLoS}})$ parameters of values $(4.88, 0.43, 0.2, 24)$ and $(9.61, 0.16, 1.2, 23)$, respectively [13]. We omit the usability of this deployment in more densely populated areas, such as Dense Urban or High-Rise locations, because the traffic demand might be too high for a UAV based system, and these are usually already served by reliable networks and the electricity grid. This is even more true for long term solutions in such environments, where our system would compete with the electricity grid, local MNOs, and internet service providers (ISPs).

Both solar irradiation and wind speed data are taken from the European Commi-

Table H.4: Simulation Parameters. [41, 42]

Label	Definition	Value
f_c	Channel carrier frequency	5.8 GHz
c	Velocity of light	$3 \cdot 10^8$ m/s
B	Channel bandwidth	80 MHz
H_0	Nominal height for wind measurements	10 m
E_w	Environment roughness coefficient	0.335
B_{tot}	Available spectral width	480 MHz
N_0	Noise spectral power	-174 dBm/Hz
P_t	Transmission Power	23 dBm
D_{lb}	Lower bound of coverage size	0 m
D_{ub}	Upper bound of coverage size	∞ m
P_{charge}	Power of the charger	180 W
F_{max}	Total expendable budget	€100000

sion's Photovoltaic Geographical Information System. The data are divided in yearly blocks, from which we use the 2015 measurements for four specific testing locations. Two locations are in regions that are prone to grid and system failures, like the earthquake ridden region around the Italian town of Amatrice and the fjord/floodplains of Western Denmark. We also suggest the placement of the system in common off-grid locations, such as sparsely populated areas in Western Texas and the touristic region of the Faroe Islands. The four locations represent very diverse environments for both wind speed and solar irradiation.

The testing parameters are included in Table H.4. We consider antenna directivity as a split variable and not just another variable in the optimization problem, since mounting an antenna would impact the aerodynamics of the UAV in ways that the power consumption model cannot predict. To elaborate, we expect that one would have a choice to choose between several different antennas to mount on the UAV. Therefore, finding the optimal A_{eff} would not really matter and would be a waste of computational resources, when the system integrator can just input the directivity as a system variable. In Fig. H.6 we illustrate the coverage efficiency across the four different testing scenarios for 4 different antenna directivity coefficients A_{eff}. In this analysis it is obvious that there is a trade-off in mounting better antennas to UAV BSs when maximizing coverage in a packed area. This relationship is a product of the packing algorithm that also decides the altitude of the swarm. More efficient antennas expect higher optimal altitudes, thus consuming more energy for vertical flights and expecting higher wind velocities. Larger areas of coverage expect denser deployments, which decrease the flying altitude of the UAVs. As discussed in the previous section, thanks to the aerodynamics of the UAV, the presence of horizontal wind reduces the power consumption for hovering and proves beneficial for the flying swarm. This effect provides interesting results in the case of the more windy locations, such as the Faroe Islands, which present a distinct improvement in energy efficiency for the coverage of areas with $3500\,\text{m} \leq D_{max} \leq 4250\,\text{m}$. We note

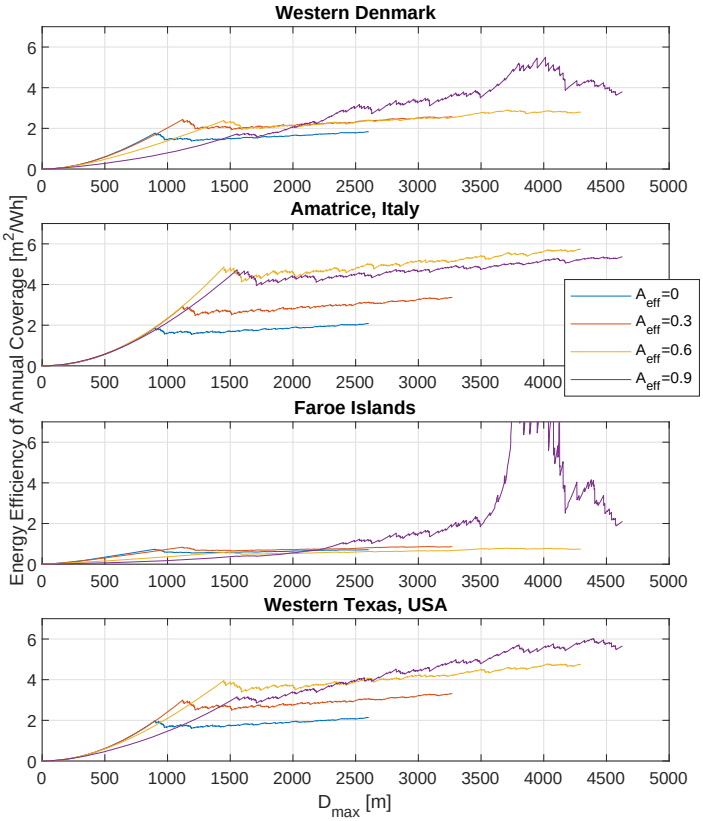

Fig. H.6: EEAC of UAV based wireless coverage for the considered different geographical areas of the suburban type.

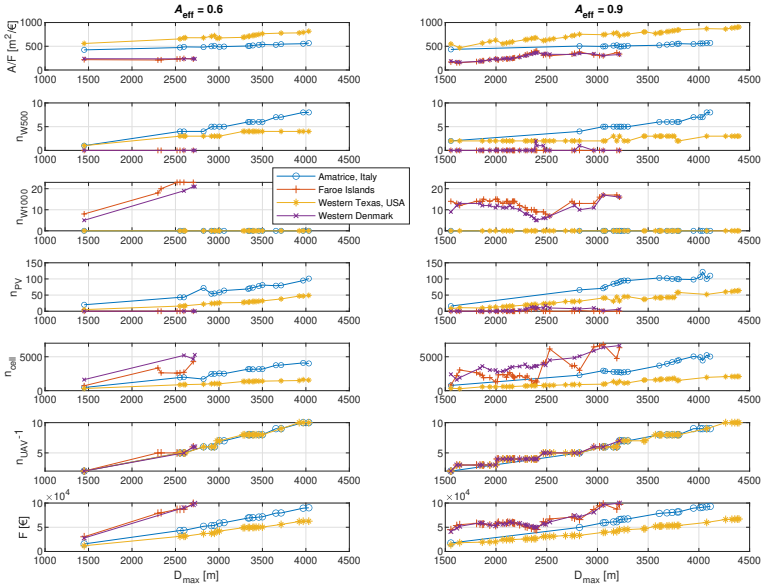

Fig. H.7: Implementation feasibility of the off-grid system in a suburban environment.

that this is under the assumption that the downward facing antenna has negligible impact to the UAVs' aerodynamics.

We start the testing of the off-grid system by segmenting the four testing locations in the group of windy places, Faroe Islands and Western Denmark, and Sunny Places, Amatrice and Western Texas. As per Fig. H.7 there is an obvious advantage of having the setup in an area where the use of solar panels is feasible. In the sunny locations, the cost-feasibility of the system is massively improving by being better at allocating the available budget, which in turn allows for exploiting the improved packing efficiency when using bigger swarms. The most cost efficient deployments are found in the Texian planes where energy can be captured through both wind and solar. Namely, bigger deployments in this setting do not need as much PV panels nor wind turbines as the other three locations, to satisfy the energy requirements of the UAV deployment. Both windy locations do not find use for PV panels and only use the bigger 1000W turbines. We note that even though the 1000W gives the impression of just providing double the power output than the 500W WTs, the behaviour is in fact not linear (it has a specific profile) and can operate efficiently in higher winds, as it was presented back in Fig. H.3.

As we can see in Fig. H.7 the results are not so clear in the case where the UAVs have antennas with high directivity $A_{\text{eff}} = 0.9$. In accord, deployment efficiency between the windy and the sunny locations is much closer, highly due to the better wind effects on the higher altitudes of the UAVs. Nonetheless, UAV swarm deployments are more costly in windy locations and generally require much higher budget than the €100000

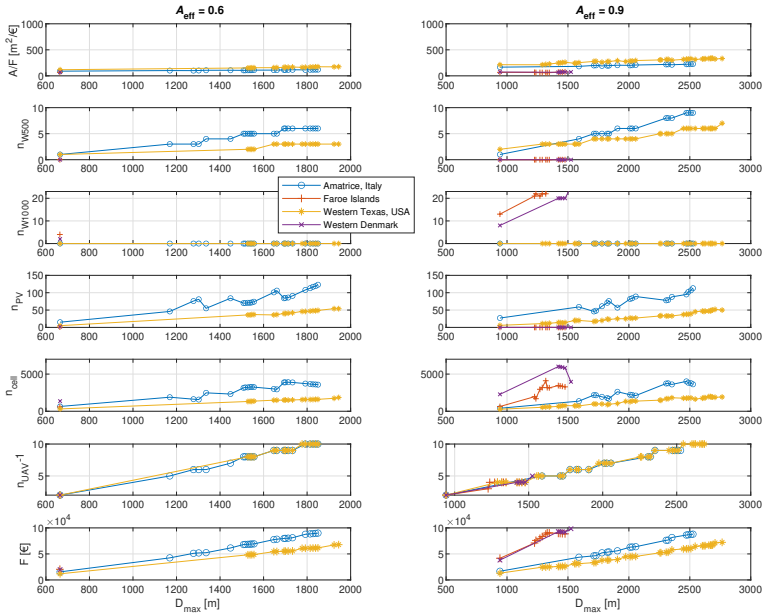

Fig. H.8: Implementation feasibility of the off-grid system in an urban environment.

to achieve coverages bigger than 2700 m or 3200 m when using $A_{\text{eff}} = 0.6$ or $A_{\text{eff}} = 0.9$ respectively. We note that this is an already high cost and thus we do not recommend the use of UAV swarm wireless communications for covering big areas. In contrast, the scenario in Western Texas is not limited by the upper limit on CAPEX but the size of the swarm, which is limited to a total of 11 UAVs. This is due to the mild wind present in the area in addition to the strong and reliable solar irradiation.

Moving over to the Urban environment, Fig. H.8 shows that the implementations' efficiency between the windy and sunny locations are much closer in non-swarm deployments ($n_{\text{UAV}} = 2$). However, the budget of scaling the system to a bigger coverage area, takes a great toll on our CAPEX and exceeds the initial allocation of $F = €100\,000$. Thus, serving windy urban areas sees no use for the case of $A_{\text{eff}} = 0.6$. Again, as seen in Fig. H.8 the performance for the windy location improves when using better antennas and allows for bigger swarms. We note that due to the increased user density and the worse propagation environment, the coverage for the urban implementations usually have much smaller coverages of radius between $2000 - 2700$ m.

6 Conclusion

In this paper we considered deploying a UAV swarm that offers persistent wireless services in an entirely off-grid setting. We formulated the problem as CAPEX efficient

coverage area maximization, which is a multi-variate optimization problem for solving the load profile based on real world data. We considered energy generation from two sources, wind and solar, that are also taken from real world data. In this paper we have emphasized the importance of accounting for the impact of wind onto the deployment. Moreover, we consider the hourly wind intensity as a function of elevation and terrain roughness, and account for its impact on UAV deployments for long duration hover. We have proposed the GSS algorithm that is computationally easy, combining greedy sampling and binary search to find the optimal combination of wind turbines, PV panels, cells in the ground battery, and UAVs in the swarm. Using GSS we have calculated the feasibility of the system in four different locations where the deployment would have to balance wind or solar power generation. This work opens a plethora of directions for future works such as investigating the feasibility in very specific areas, specific short term periods, and different types of UAVs.

References

[1] M. Mozaffari, W. Saad, M. Bennis, Y. Nam, and M. Debbah, "A Tutorial on UAVs for Wireless Networks: Applications, Challenges, and Open Problems," *IEEE Communications Surveys Tutorials*, vol. 21, no. 3, pp. 2334–2360, Mar. , 2019.

[2] A. Fotouhi, H. Qiang, M. Ding, M. Hassan, L. G. Giordano, A. Garcia-Rodriguez, and J. Yuan, "Survey on UAV Cellular Communications: Practical Aspects, Standardization Advancements, Regulation, and Security Challenges," *IEEE Communications Surveys Tutorials*, vol. 21, no. 4, pp. 3417–3442, Mar. , 2019.

[3] M. Erdelj and E. Natalizio, "UAV-Assisted Disaster Management: Applications and Open Issues," in *2016 International Conference on Computing, Networking and Communications (ICNC)*, 2016, pp. 1–5.

[4] S. ur Rahman, G.-H. Kim, Y.-Z. Cho, and A. Khan, "Positioning of UAVs for Throughput Maximization in Software-Defined Disaster Area UAV Communication Networks," *Journal of Communications and Networks*, vol. 20, no. 5, pp. 452–463, Nov. 2018.

[5] S. Sekander, H. Tabassum, and E. Hossain, "Multi-Tier Drone Architecture for 5G/B5G Cellular Networks: Challenges, Trends, and Prospects," *IEEE Communications Magazine*, vol. 56, no. 3, pp. 96–103, 2018.

[6] I. Donevski, G. Vallero, and M. A. Marsan, "Neural Networks for Cellular Base Station Switching," in *Proc. of IEEE INFOCOM 2019-IEEE Conference on Computer Communications Workshops*, Paris, France, Apr. , 2019, pp. 738–743.

[7] A. Fotouhi, M. Ding, and M. Hassan, "Dynamic Base Station Repositioning to Improve Performance of Drone Small Cells," in *Proc. of IEEE Globecom Workshops (GC Wkshps)*, Washington DC, Dec. , 2016, pp. 1–6.

[8] B. Galkin, J. Kibiłda, and L. A. DaSilva, "A Stochastic Model for UAV Networks Positioned Above Demand Hotspots in Urban Environments," *IEEE Transactions on Vehicular Technology*, vol. 68, no. 7, pp. 6985–6996, Jul. 2019.

[9] M. Mozaffari, A. Taleb Zadeh Kasgari, W. Saad, M. Bennis, and M. Debbah, "Beyond 5G With UAVs: Foundations of a 3D Wireless Cellular Network," *IEEE Transactions on Wireless Communications*, vol. 18, no. 1, pp. 357–372, Jan. 2019.

[10] I. Donevski and J. J. Nielsen, "Dynamic Standalone Drone-Mounted Small Cells," in *Proc. of European Conference on Networks and Communications (EuCNC)*, Dubrovnik, Croatia, Sep. , 2020, pp. 342–347.

[11] I. Donevski, J. J. Nielsen, and P. Popovski, "Standalone Deployment of a Dynamic Drone Cell for Wireless Connectivity of Two Services," in *2021 IEEE Wireless Communications and Networking Conference (WCNC)*. IEEE, 2021, pp. 1–7.

[12] M. Alzenad, A. El-Keyi, F. Lagum, and H. Yanikomeroglu, "3-D Placement of an Unmanned Aerial Vehicle Base Station (UAV-BS) for Energy-Efficient Maximal Coverage," *IEEE Wireless Communications Letters*, vol. 6, no. 4, pp. 434–437, Aug. , 2017.

[13] A. Al-Hourani, S. Kandeepan, and A. Jamalipour, "Modeling Air-to-Ground Path Loss for Low Altitude Platforms in Urban Environments," in *Proc. of IEEE Global Communications Conference*, Austin, TX, Oct. , 2014, pp. 2898–2904.

[14] A. Al-Hourani, S. Kandeepan, and S. Lardner, "Optimal LAP Altitude for Maximum Coverage," *IEEE Wireless Communications Letters*, vol. 3, no. 6, pp. 569–572, Dec. , 2014.

[15] N. Babu, K. Ntougias, C. B. Papadias, and P. Popovski, "Energy Efficient Altitude Optimization of an Aerial Access Point," in *Proc. of IEEE 31st Annual International Symposium on Personal, Indoor and Mobile Radio Communications*, London, Sep. , 2020, pp. 1–7.

[16] N. Babu, C. B. Papadias, and P. Popovski, "Energy-Efficient 3-D Deployment of Aerial Access Points in a UAV Communication System," *IEEE Communications Letters*, vol. 24, no. 12, pp. 2883–2887, Aug. , 2020.

[17] B. Bethke, J. How, and J. Vian, "Multi-UAV Persistent Surveillance with Communication Constraints and Health Management," in *AIAA Guidance, Navigation, and Control Conference*, 2009, p. 5654.

[18] J. Scherer and B. Rinner, "Persistent Multi-UAV Surveillance with Energy and Communication constraints," in *2016 IEEE International Conference on Automation Science and Engineering (CASE)*, 2016, pp. 1225–1230.

[19] B. Michini, T. Toksoz, J. Redding, M. Michini, J. How, M. Vavrina, and J. Vian, "Automated Battery Swap and Recharge to Enable Persistent UAV Missions," in *Infotech@ Aerospace 2011*, Jun, 2011, p. 1405.

[20] X. Zhang and L. Duan, "Optimal Patrolling Trajectory Design for Multi-UAV Wireless Servicing and Battery Swapping," in *2019 IEEE Globecom Workshops (GC Wkshps)*, 2019, pp. 1–6.

[21] D. S. Lakew, W. Na, N.-N. Dao, and S. Cho, "Aerial Energy Orchestration for Heterogeneous UAV-Assisted Wireless Communications," *IEEE Systems Journal*, pp. 1–12, May 2021.

[22] J. Galán-Jiménez, E. Moguel, J. García-Alonso, and J. Berrocal, "Energy-Efficient and Solar Powered Mission Planning of UAV Swarms to Reduce the Coverage Gap in Rural Areas: The 3D Case," *Ad Hoc Networks*, vol. 118, p. 102517, Jul. 2021. [Online]. Available: https://www.sciencedirect.com/science/article/pii/S157087052100072X

[23] T. Li, K. Ota, T. Wang, X. Li, Z. Cai, and A. Liu, "Optimizing the Coverage via the UAVs with Lower Costs for Information-Centric Internet of Things," *IEEE Access*, vol. 7, pp. 15 292–15 309, Feb. 2019.

[24] N. Babu, M. Virgili, C. B. Papadias, P. Popovski, and A. J. Forsyth, "Cost- and Energy-Efficient Aerial Communication Networks with Interleaved Hovering and Flying," *IEEE Transactions on Vehicular Technology*, vol. 70, no. 9, pp. 9077–9087, Jul. 2021.

[25] G. Piro, M. Miozzo, G. Forte, N. Baldo, L. A. Grieco, G. Boggia, and P. Dini, "HetNets Powered by Renewable Energy Sources: Sustainable Next-Generation Cellular Networks," *IEEE Internet Computing*, vol. 17, no. 1, pp. 32–39, Feb. 2013.

[26] M. A. Marsan, G. Bucalo, A. Di Caro, M. Meo, and Y. Zhang, "Towards Zero Grid Electricity Networking: Powering BSs with Renewable Energy Sources," in *2013 IEEE International Conference on Communications Workshops (ICC)*, 2013, pp. 596–601.

[27] L. Chiaraviglio, L. Amorosi, N. Blefari-Melazzi, P. Dell'Olmo, A. Lo Mastro, C. Natalino, and P. Monti, "Minimum Cost Design of Cellular Networks in Rural Areas With UAVs, Optical Rings, Solar Panels, and Batteries," *IEEE Transactions on Green Communications and Networking*, vol. 3, no. 4, pp. 901–918, Aug. 2019.

[28] L. Amorosi, J. Puerto, and C. Valverde, "Coordinating Drones with Mothership Vehicles: The Mothership and Multiple Drones Routing Problem with Graphs," 2021.

[29] K. Fujii, K. Higuchi, and J. Rekimoto, "Endless Flyer: A Continuous Flying Drone with Automatic Battery Replacement," in *2013 IEEE 10th International Conference on Ubiquitous Intelligence and Computing and 2013 IEEE 10th International Conference on Autonomic and Trusted Computing*, 2013, pp. 216–223.

[30] B. Soret, I. Leyva-Mayorga, S. Cioni, and P. Popovski, "5G Satellite Networks for Internet of Things: Offloading and Backhauling," *International Journal of Satellite Communications and Networking*, vol. 39, no. 4, pp. 431–444, Jul. 2021.

[31] A. P. Couto da Silva, D. Renga, M. Meo, and M. Ajmone Marsan, "The Impact of Quantization on the Design of Solar Power Systems for Cellular Base Stations," *IEEE Transactions on Green Communications and Networking*, vol. 2, no. 1, pp. 260–274, Oct, 2018.

[32] G. F. Tóth, "Thinnest Covering of a Circle by Eight, Nine, or Ten Congruent Circles," *Combinatorial and computational geometry*, vol. 52, no. 361, p. 59, 2005.

[33] *Wind Characteristics and Resources.* John Wiley & Sons, Ltd, 2009, ch. 2, pp. 23–89. [Online]. Available: https://onlinelibrary.wiley.com/doi/abs/10.1002/9781119994367.ch2

[34] J. Widén, "Correlations Between Large-Scale Solar and Wind Power in a Future Scenario for Sweden," *IEEE transactions on sustainable energy*, vol. 2, no. 2, pp. 177–184, Apr. 2011.

[35] S. Alessandrini, E. Rizzuto, and Z. Del Prete, "Characterizing Different Types of Lithium Ion Cells with an Automated Measurement System," *Journal of Energy Storage*, vol. 7, pp. 244–251, aug 2016.

[36] Futurasun, 280wp, polycrystalline photovoltaic module, fu 280p. [Online]. Available: https://www.futurasun.com/wp-content/uploads/2020/10/2020_FuturaSun_60p_260-285W_en.pdf?x97762

[37] A. Chouder, S. Silvestre, N. Sadaoui, and L. Rahmani, "Modeling and Simulation of a Grid Connected PV System Based on the Evaluation of Main PV Module Parameters," *Simulation Modelling Practice and Theory*, vol. 20, no. 1, pp. 46–58, jan 2012.

[38] M. Valentini, A. Raducu, D. Sera, and R. Teodorescu, "PV Inverter Test Setup for European Efficiency, Static and Dynamic MPPT Efficiency Evaluation," in *2008 11th International Conference on Optimization of Electrical and Electronic Equipment*, 2008, pp. 433–438.

[39] Aeolos wind energy ltd. [Online]. Available: http://www.windturbinestar.com

[40] M. Virgili, A. J. Forysth, and P. James, "A Multi-Objective Genetic Algorithm Methodology for the Design of Standalone Energy Systems," in *2021 IEEE Design Methodologies Conference (DMC)*, Jul. 2021, pp. 1–6.

[41] C. She, C. Liu, T. Q. Quek, C. Yang, and Y. Li, "Ultra-Reliable and Low-Latency Communications in Unmanned Aerial Vehicle Communication Systems," *IEEE Transactions on Communications*, vol. 67, no. 5, pp. 3768–3781, May. , 2019.

[42] I. Donevski, N. Babu, J. J. Nielsen, P. Popovski, and W. Saad, "Federated Learning with a Drone Orchestrator: Path Planning for Minimized Staleness," *IEEE Open Journal of the Communications Society*, vol. 2, pp. 1000–1014, Apr. 2021.

ISSN (online): 2446-1628
ISBN (online): 978-87-7573-865-6

AALBORG UNIVERSITY PRESS